Stress-Induced Permeability Evolution in Limestone Rocks

by

Adrian Głowacki

Department of Civil Engineering and Applied Mechanics
McGill University, Montréal

January, 2017

A thesis submitted to
McGill University
in partial fulfillment of the requirements of the degree of
Doctor of Philosophy

DEDICATION

This thesis is dedicated to my late father, Krzysztof.

ABSTRACT

This thesis investigates the stress-state dependent evolution of permeability of rocks in a laboratory setting. The focus was primarily on Indiana Limestone and Cobourg Limestone. The selected topics for this thesis have a direct impact on current geotechnical endeavours such as the deep geologic disposal of heat-emitting nuclear fuel wastes, the extraction of geothermal energy, oil and gas recovery, as well as the geologic sequestration of carbon dioxide in supercritical form.

The laboratory methods for testing permeability were limited to steady state and hydraulic pulse tests. This thesis outlines specific innovative experimental configurations that were developed to test large rock samples. The investigations on the evolution of permeability in Indiana Limestone with stress state show that as the compressive stresses increased, including post-failure, the permeability decreased. In contrast, for the low porosity Cobourg Limestone the permeability increased with increasing triaxial stress states until failure, after which the permeability increased further. The results obtained from both rocks were used to develop empirical relationships for the variation of permeability with principal stress states. The empirical results were also used in a computational model to analyse seepage into a circular tunnel and the results were compared with situations where the permeability experienced no change. Additionally, the experiments on permeability in rocks were extended to examine factors that influence the results, including the degree of saturation, temperature, trapped air in the experimental configuration, etc. Special diffusing disks were developed to allow permeability testing of rocks subjected to triaxial stresses. The specific permeability studies of the heterogeneous phases found in the Cobourg Limestone was investigated in detail. It was determined that the dark grey argillaceous phase was more permeable (by one order of magnitude) than the light gray carbonate phase.

RÉSUMÉ

Ce travail de thèse s'intéresse à l'évolution de la perméabilité sous contrainte de roches poreuses (le Calcaire de l'Indiana) et peu poreuses (le Calcaire de Cobourg) en laboratoire. Les apports d'un tel travail sont multiples et concernent aussi bien la science fondamentale (structure des roches, comportement de la lithosphère) que le domaine appliqué (stockage en couche géologique profonde de déchets radioactifs à moyenne et longue durée de vie, séquestration du dioxyde de carbonate en conditions subcritique, gestion des géoressources en eau et des énergies fossiles).

De nouvelles configurations expérimentales innovatrices ont été développées autour de deux approches complémentaires pour l'étude de la perméabilité: des mesures à charge constante et des mesures par pulsations hydraulique.

Selon la roche considérée, les résultats montrent deux comportement différents de l'évolution de la perméabilité sous contrainte en configuration triaxiale classique: (1) La perméabilité diminue avec l'augmentation de contrainte dans le calcaire de l'Indiana, au cours de la compaction et dans le domaine inélastique de post-rupture; et (2) la perméabilité augmente de manière continue avec l'augmentation de contrainte dans le calcaire de Cobourg, que ce soit dans le domaine élastique ou dans le domaine inélastique de post-rupture.

Des modèles d'évolution simples de la perméabilité avec les contraintes et basés sur les résultats expérimentaux sont proposés, ainsi que des modélisations numériques plus abouties. Ces derniers consistent à modéliser un écoulement laminaire dans des environnements similaires à des tubes circulaires, en les comparants à des situations où la perméabilité reste constante au cours de la déformation.

Enfin, plusieurs configurations expérimentales ont été mises en œuvre afin d'examiner les facteurs pouvant influencer la perméabilité (hétérogénéité de la roche, taux de saturation, température, régime diphasique air-eau, composition chimique du fluide saturant) ainsi que leur sensibilité respective. De plus, une étude approfondie des deux phases hétérogènes présentes dans le calcaire de Cobourg montre que la phase argilo-calcaire (gris foncé), ou marneuse, est plus perméable (d'environ un ordre de grandeur) que la phase calcaire (gris pâle).

ACKNOWLEDGEMENTS

The author would like to express his appreciation to his supervisor, Professor A.P.S. Selvadurai for suggesting the topic of the research, continuous and extensive guidance and mentoring and support throughout the entire thesis program. The author is grateful to his colleagues in the Environmental Geomechanics Laboratory (EGL): Ariel Gallagher, Benjamin Hekimi, Luc Jenner, Meysam Najari at the Department of Civil Engineering and Applied Mechanics, McGill University for their support and assistance, as well as a friendly and motivating environment. The author would also like to acknowledge the extensive technical assistance he received from Mr. J. Bartczak and Dr. W. Cook, Michael Boyd, in the design, fabrication and assembly of the experimental facilities he used over the course of the research.

The author would also like to thank Mr. Michel Preda in the Département des Sciences de la Terre et de l'Atmosphère, Faculté des Sciences, Université du Québec à Montréal for performing XRF and XRD analysis. Special thanks are due to Mrs. Sally Selvadurai for her extensive editorial corrections of all the papers that resulted from this research.

The research conducted in this thesis was supported by NSERC Strategic and Discovery Grants awarded to Professor A.P.S. Selvadurai. Additional, financial support came from the Nuclear Waste Management Organization (NWMO) of Ontario. The author also wishes to acknowledge his gratitude for allowing him to pursue this program and for the financial support he received from Société de l'Assurance Automobile du Québec (SAAQ), McGill Engineering Doctoral Awards (MEDA) and Fonds de recherche du Québec – Nature et technologies (FQRNT).

Finally, the author would like to express his deepest thanks to his wife Margarita Róża and his children Stanisław Henryk, Sebastian Adrian, Sofia Maria and Julian Piotr who provided him with nothing but support and love throughout the course of this research.

Table of Contents

CHAPTER 8 150

STRESS-INDUCED PERMEABILITY EVOLUTION IN THE COBOURG LIMESTONE 150

LIST OF TABLES

LIST OF FIGURES

Publications Resulting from this Research

Journal Publications (Published/Accepted for Publication)

Selvadurai, A.P.S. and Głowacki, A. (2017) Stress-induced permeability alterations in an argillaceous limestone. *Rock Mechanics and Rock Engineering,* DOI 10.1007/s00603-016-1153-3.

Głowacki, A. and Selvadurai, A.P.S. (2017) On some factors influencing the laboratory measurement of permeability of rock. *Géotechnique Letters* **7**: 1–6, http://dx.doi.org/10.1680/jgele.16.00133

Głowacki, A. and Selvadurai, A.P.S. (2016) Stress-induced permeability changes in Indiana limestone. *Engineering Geology*, http://dx.doi.org/10.1016/j.enggeo.2016.10.015

Journal Publications (Paper in Preparation)

Selvadurai, A.P.S. and Głowacki, A. (2017) Multi-Scale Estimates for the Permeability of a Heterogeneous Argillaceous Limestone.

Conference Publications (Published and Pending Publication)

Selvadurai, A.P.S. and Głowacki, A. (2016) Fluid transport in extensively fractured rocks, *International Geotechnics Symposium cum International Meeting of CSRME 14th Biennial National Congress:* on December 14-17, 2016 in Hong Kong, China.

Głowacki, A. and Selvadurai, A.P.S. (2015) The effect of flow reversal on permeability measurement in rocks, *68th Canadian Geotechnical Conference and 7th Canadian Permafrost Conference*: GéoQuébec 2015: Challenges from North to South, Quebec City, Canada, (ABS286).

CHAPTER 1

INTRODUCTION AND LITERATURE REVIEW

1.1 General

The laboratory and field studies of fluid and gas transport in rocks have several applications of importance to modern environmental geomechanics and groundwater resource management projects. These include the extraction and recharge of the groundwater regime (Bouwer, 2000; Liu *et al.* 2008; Pedretti *et al*. 2012), groundwater restoration post termination of in-situ leach mining operations for uranium (Davis and Curtis, 2007), the deep geological disposal of hazardous and toxic substances (Bredehoeft *et al*., 1978, Gnirk 1993; Selvadurai and Nguyen 1996; Selvadurai, 2004, 2006; Tsang *et al.* 2008), recovery and extraction of energy resources such as shale gas (Boyer *et al.* 2006; Gregory *et al.* 2011) contamination of ground water due to directional drilling and hydraulic-fracturing technologies (Harrison 1983; Osborn *et al*. 2011; Jackson *et al.* 2011), geological sequestration of greenhouse gases in fluidized form (Bachu *et al*., 2000; Lemieux, 2011; Selvadurai, 2012), induced seismicity (Healy *et al*., 1968; Pearson, 1981; Rubinstein and Mahani, 2015), and karst formation and evolution in carbonate rocks (Hasenmueller *et al*., 2003; Ford and Williams 2007).

Experimental investigations of geotechnical parameters, particularly the estimation of rock permeability provide important information that can influence computational modelling and design approaches to the geoenvironmental problems (McClure and Horne, 2011). Hence, establishing a reliable and accurate method for estimating the permeability of a particular rock at *in situ* conditions is important. Permeability estimations in the laboratory or the field can be costly, complex and time consuming. In addition, samples collected from boreholes or quarries can be subjected to sample disturbance that can influence the permeability of rocks through the generation of defects at various scales of the rock fabric. These can include inter-granular and intra-granular defects, the mechanical behavior of which can include irreversible processes that can also influence the permeability estimation (Kowallis and Wang, 1983; Morrow and Lockner, 1997; Géraud and Gaviglio, 2000). Estimation of the geotechnical parameters of rocks can also be influenced by internal scales present in the rock fabric. The Representative Volume Element (RVE) chosen for laboratory testing should be able to adequately duplicate the fabric of the rock (i.e. heterogeneity and anisotropy) such that the experiments give meaningful values. Sample dimensions are of particular importance when permeability is expected to be both anisotropic and heterogeneous (Neuman, 1994). In relation to the permeability testing of the Cobourg Limestone, Vilks and Miller (2007) note that the sample length required to achieve a RVE depends upon the texture of the sample being studied (i.e. a coarse grained rock requires a longer sample length than fine grained rocks because larger grains produce a greater variability in pore geometry in a given rock volume), particularly if fossils are present. The rationale would be to select the largest sample for laboratory testing in order to have the intact rock matrix, the defects (i.e. cracks) and stratification (i.e. deposition layers), that are representative of the in-situ rock (Bernaix, 1969). The size of the sample used for laboratory testing cannot be increased without limit since this will entail expensive testing arrangements particularly if stresses are applied to test specimens. Typically, the laboratory experimental investigations of rock (i.e. Indiana Limestone and Cobourg Limestone) in a triaxial cell were limited to sample sizes in the range of

25 to 50 mm in diameter and varying length (Suri *et al.*, 1997; Vilks and Miller, 2007; Akbarnejad and Ghassemi, 2009; Nasseri *et al.*, 2013;). However, in this research, the samples of Indiana Limestone and Cobourg Limestone, ranged from 50 mm to 100 mm in diameter and 25 mm to 170 mm in length. This increase in size has ensured that the samples are more likely to achieve the RVE for the study of permeability. It is worth noting that in the study by Selvadurai *et al.* (2011), permeability tests were conducted on the Cobourg Limestone, 85 mm in diameter, subjected to isotropic stress states. The current study extends these tests to include deviatoric stress states and post-failure permeability evolution in Cobourg Limestone.

The investigation of the permeability of the Cobourg Limestone is based on the potential use of this particular rock formation as the host rock for the creation of a Deep Geologic Repository (DGR) to be located at the Ontario Bruce Nuclear Power Plant complex in the municipality of Kincardine (see Figure 1.1). The proposed DGR is to be located at a depth of approximately 680 m below surface. At this depth, the total vertical stress is estimated to be approximately 18 MPa. The horizontal stress at this depth is estimated to be approximately 36 MPa (NWMO, 2015b). The ground temperature at this depth is approximately 22^{o}C (OPG, 2011a). The static ground water pressures obtained from borehole testing at this depth is 6.8 MPa, which corresponds to hydrostatic conditions (OPG, 2011a). The DGR should provide a safe environment for the storage of low-and intermediate level nuclear wastes, such that the stored waste will not pose a threat to groundwater contamination due to an accidental release of radionuclides from the repository to the surficial aquifers (OPG, 2011a). While several barriers (metal containers, clay seals, etc.) are being planned to minimize the release of radionuclides to the geo-environment, the rock mass is expected to serve as the main natural geological barrier for retarding the movement of radionuclides for long periods until their radioactivity is reduced to an environmentally acceptable levels or the public dose criterion limit of 0.3 mSv/a (OPG, 2011a). In the case of the proposed DGR in Ontario, Canada, it is predicted that the total amount of radioactivity, generated by the low and intermediate level nuclear wastes remaining in the repository after 10 000 years, will be less than that occurring naturally in the overlying shale rock that will enclose the DGR (OPG, 2016).

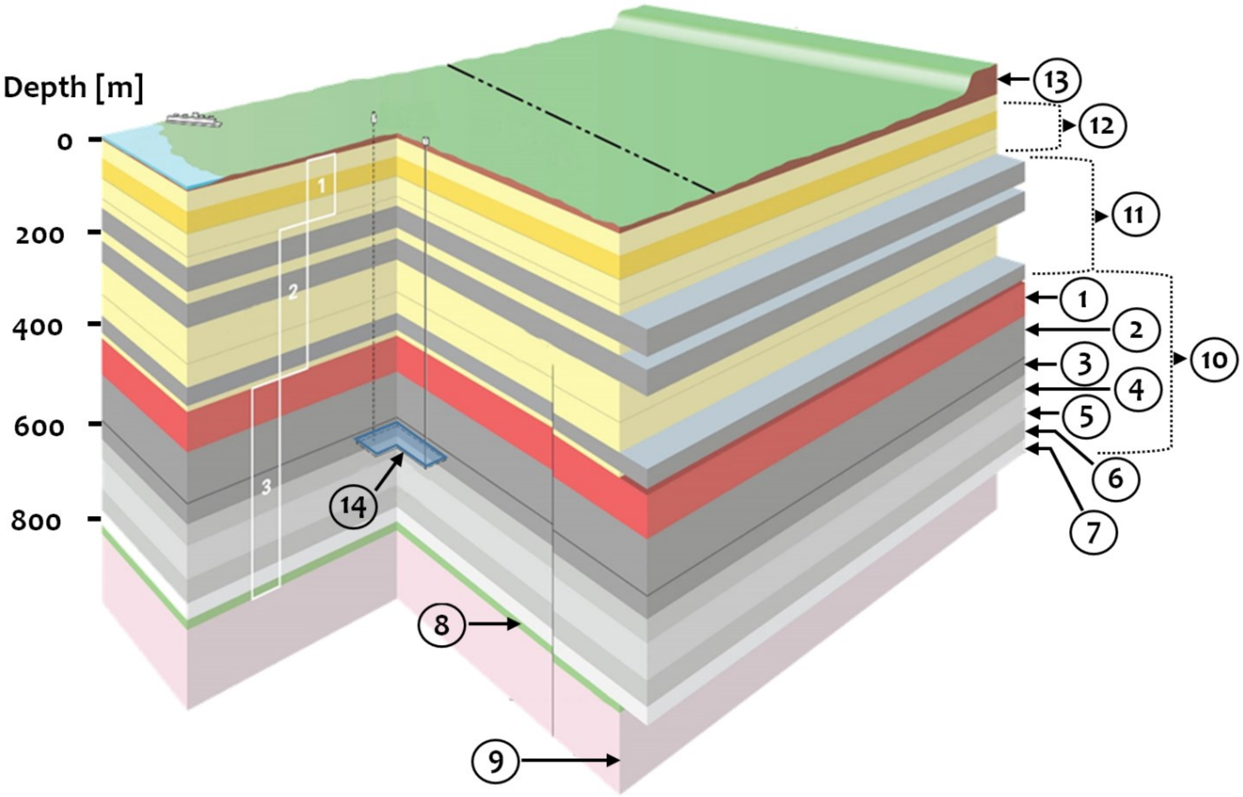

Figure 1.1: Geologic composition of area below the planned repository at the Bruce Nuclear plant in Ontario; 1. Queenston; 2. Georgian Bay; 3. Collingwood; 4. Lindsay; 5. Verulam; 6. Bobcaygeon; 7. Gull River and Shadow Lake; 8. Cambrian Sandstone; 9. Pre-Cambrian Basement; 10. Ordovician; 11. Silurian; 12. Devonian; 13. Overburden; 14. Proposed DGR location.

However, before embarking on an extensive experimental research program for the measurement of the permeability characteristics of the Cobourg Limestone reliable experimental facilities and accurate test procedures had to be established. Hence, a series of experimental investigations, at unstressed conditions, were first conducted on different rock types (limestone, sandstone, granite); these included examination of factors such as initial saturation, flow reversal, de-aired water, etc. that could influence the measurement of rock permeability in a laboratory setting. Furthermore, the permeability evolution with triaxial stress states in Indiana Limestone was investigated prior to testing the Cobourg Limestone. The study of Indiana Limestone allowed experimental investigations of a limestone rock that was previously extensively studied by several investigators in the EGL at McGill (Głowacki, 2006; Selvadurai and Głowacki, 2008; Mattar, 2009; Selvadurai, 2010) and culminated in improvements to both the test procedures and the laboratory equipment, which were necessary for the experimental study of the Cobourg Limestone. The major physical differences between the Cobourg Limestone and the Indiana Limestone are the low porosity and the apparent heterogeneity of the Cobourg Limestone.

1.2 Permeability and Isotropic Stress State

Since a major emphasis of the research is relates to the estimation of the influence of stress states on the evolution of permeability, a literature review was conducted to review those experimental investigations that studied water flow through a porous medium subjected to varying stress states, particularly the rocks that were selected for this thesis (i.e. Indiana Limestone and Cobourg Limestone). The motivation was to determine (i) how does permeability evolve with the application of compressive triaxial stresses, (ii) what factors dominate the permeability estimation, (iii) what are the methods used to conduct the experiments and (iv) what conclusions were derived from these studies. The following is a chronological account of key experimental research dealing with permeability conducted on rocks. In order to support the reader in comparing results from different researches, the following conversion should be used for permeability measurements made with water at room temperature $(20^{\circ}\mathrm{C})$: $1\,\mathrm{Darcy} \approx 1.0\mathrm{E}-3\,\mathrm{cm/s} \approx 1.0\mathrm{E}-12\,\mathrm{m}^2$. The earliest experiments to examine the influence of stress states on permeability are due to Fatt and Davis (1952) and Fatt (1953). These authors conducted experimental permeability measurement on sandstones, with porosities ranging from 15% to 22 %, during the application of isotropic compression in which a decaying permeability was attributed to effects such as pore collapse and fabric compaction (see Figure 1.2).

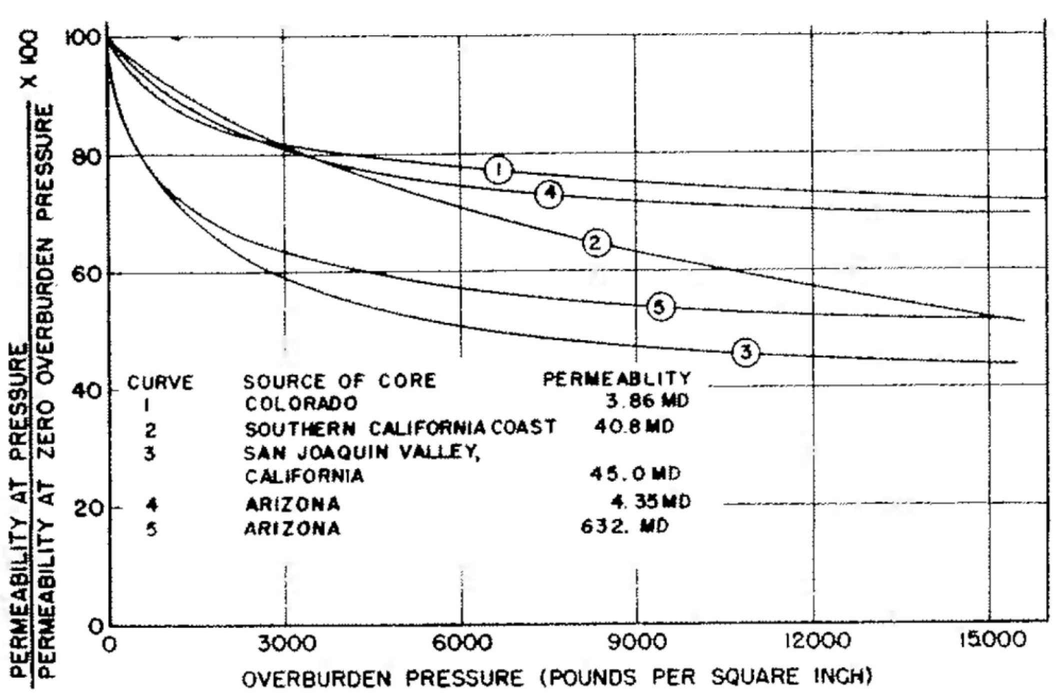

Figure 1.2: Change of permeability with confining pressure (Fatt and Davis, 1952).

Wyble (1958) designed a pressure cell (see Figure 1.3) capable of applying radial stresses to sandstone samples, 19 mm in diameter and 38 mm in height, to estimate axial permeability evolution in samples cored normal and parallel to the bedding planes, during the application of a radial compression of 0 MPa to 24 MPa. The results show that with increasing radial stress the estimated permeability decreased asymptotically, and there was no significant difference in the estimated permeabilities between samples tested either parallel or normal to the bedding directions.

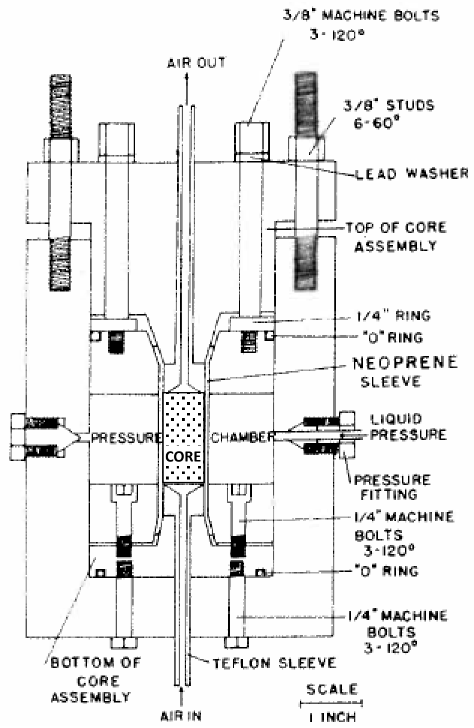

Figure 1.3: Pressure chamber schematic view (Wyble, 1958).

The investigation by Brace *et al.* (1968) dealt with the permeability changes in Westerly Granite samples, 16 mm in height and 25 mm in diameter, obtained by the pulse decay method during the application of confining stresses ranging from 10 MPa to 400 MPa and pore pressure from 15 to 40 MPa. The proposed pulse decay method involved two rigid reservoirs (i.e. V_1 and V_2) located on each side of the rock sample (see Figure 1.4), where one reservoir had the pressure increased to a specific value and was allowed to decay whereas on the opposite side, the receiving reservoir, the pressure increased until both reservoirs stabilized at around the same pressure. By comparing the recorded pressure-time histories in both the reservoirs with the behaviour predicted theoretically, the permeability was estimated at a specific confining stress. It was observed that there was a reduction of permeability with increasing confining stresses, which ranged between: $3.2\mathrm{E}-19\,\mathrm{m}^2$ at 10 MPa to $4.0\mathrm{E}-21\,\mathrm{m}^2$ at 400 MPa.

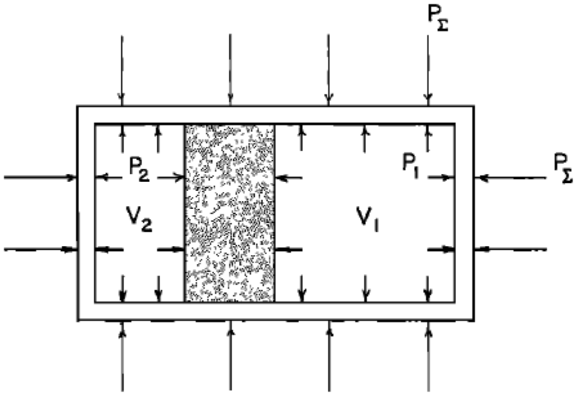

Figure 1.4: Schematic experimental arrangement (Brace, 1968).

Radial hydraulic conductivity tests were conducted by Bernaix (1969) on miliolite limestone from St.Vaast (France) and on gneiss from Malpasset (France) (with micro-fractures and macro-fractures), The samples were 60 mm in diameter and 150 mm in length and contained a cored axial cavity of 12 mm diameter and 125 mm in length which terminated 25 mm from the base of the sample (see Figure 1.5).

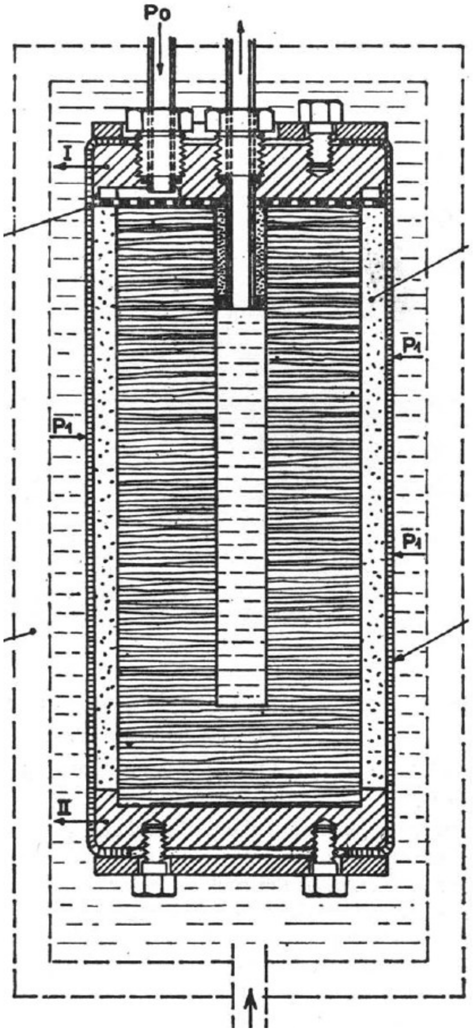

Figure 1.5: Schematic view of experimental setup (Bernaix, 1969).

The flow tests were either inward towards the cavity when the water pressure was applied to the outer surfaces of the sample, or outward when the water within the cavity was under pressure. The results showed that the effective stresses (tensional and compressive) had similar effects on the estimated permeability in both rocks; however, the gneiss, which had considerable discontinuities, showed greater variations in permeability in the tensional and compressive stress states (see Figure 1.6).

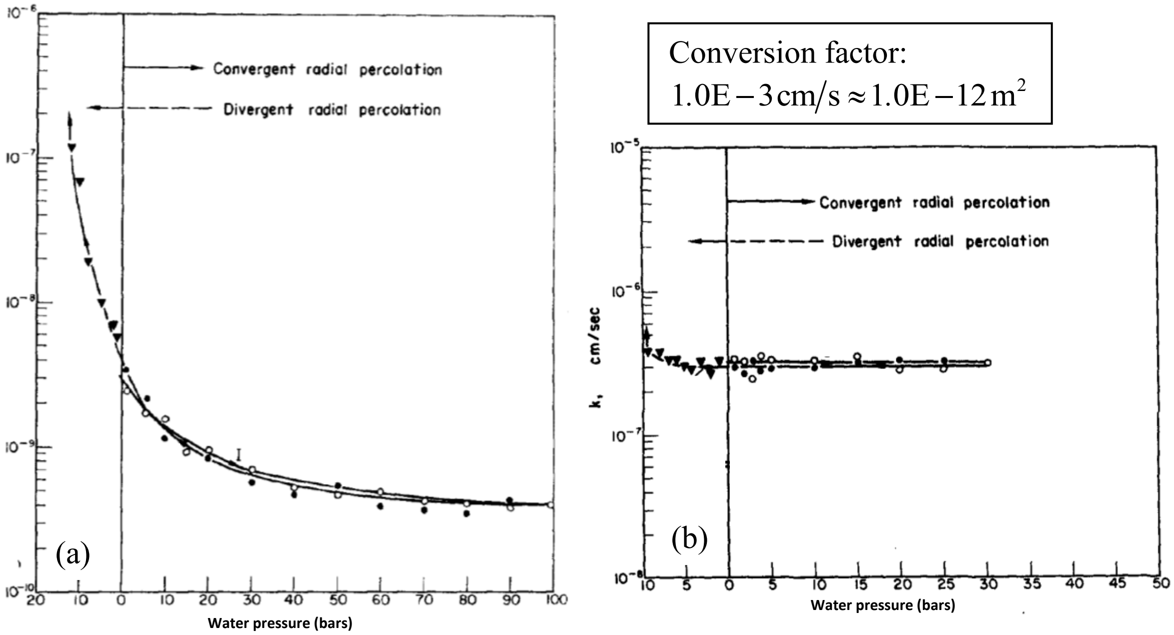

Conversion factor:
$1.0\text{E}-3\,\text{cm/s} \approx 1.0\text{E}-12\,\text{m}^2$

Figure 1.6: Permeability vs. water pressure gradient: (a) gneiss from Malpasset and (b) limestone from St.Vaast (Bernaix, 1969).

Shiping *et al.* (1994) conducted permeability evolution tests at varying strains using a pressure cell on Yinzhuang Sandstone samples (China), 54 mm in diameter and 40 mm to 100 mm in length, subjected to confining pressures of 5 MPa to 40 MPa and pore pressure from 1 MPa to 24 MPa. The results showed an increase in permeability of an order of magnitude for all combinations of stress states. The reduction in radial and axial permeability with isotropic compression (0.2 MPa and 1.5 MPa) was observed by Wright *et al*. (2002) on limestone samples from Bolivar in the Northern Adelaide Plains (South Australia). In order to conduct the axial and radial permeability tests, a new triaxial cell was developed (see Figure 1.7) that was able to test samples 100 mm in diameter and 200 mm in length. The results show that the average axial permeability was 6 times higher than the radial permeability.

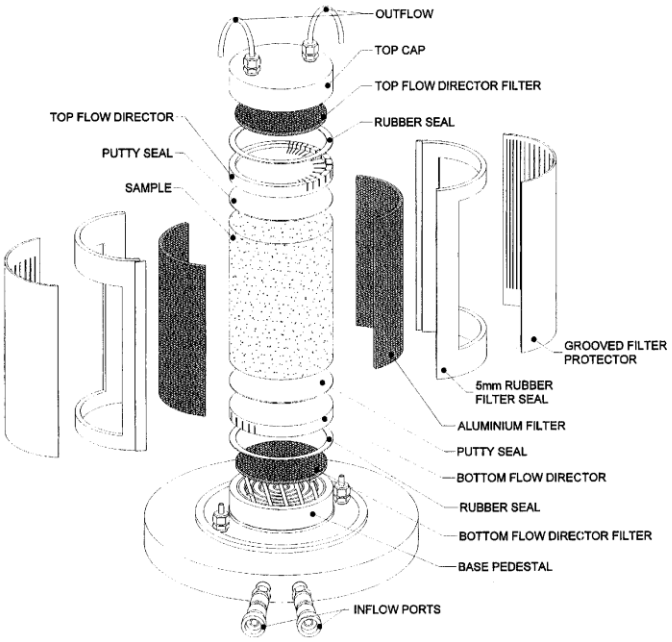

Figure 1.7: Components of the horizontal hydraulic conductivity apparatus shown in an exploded view (Wright *et al.*, 2002).

A series of isotropic compression tests was conducted by Ghabezloo *et al.* (2008) on Limestone from Nîmes, France, with an average porosity of 0.157, with isotropic confining stresses $\left(\sigma_3\right)$ ranging from 2 MPa to 12 MPa; these experiments indicated that a pore pressure increase (from 1 MPa to 3 MPa) and a confining stress increase (from 2 MPa to 12 MPa) resulted in an decrease in permeability from $2.5\mathrm{E}-17\,\mathrm{m}^2$ to $1.0\mathrm{E}-17\,\mathrm{m}^2$. Steady state flow laboratory experiments by Selvadurai and Głowacki (2008) showed a permeability reduction of one order in magnitude with increasing isotropic compression up to 60 MPa on Indiana Limestone samples measuring 100 mm in diameter and 200 mm in length. Permeability hysteresis during unloading and reloading was observed in the confining stress state range of 5 MPa to 60 MPa. Although the typical behaviour of a decrease in permeability with increasing confining stress was previously presented, when heterogeneous geological media, such as the Cobourg Limestone are tested, the external application of isotropic compression can also lead to the development of non-uniform stress states in the internal fabric of the geological medium that can result in an *increase* in permeability with isotropic compression. An example of permeability increase, obtained from pulse decay tests on Cobourg Limestone samples with isotropic compression is given by Selvadurai *et al.* (2011). The experiments were done in a pressure cell with confining pressures in the range of 5 MPa to 20 MPa, on samples 100 mm in diameter and 200 mm in length. The results show an irreversible increase in permeability when the samples were unloaded as well as an increase in permeability with increasing hydrostatic pressures (see Figure 1.8).

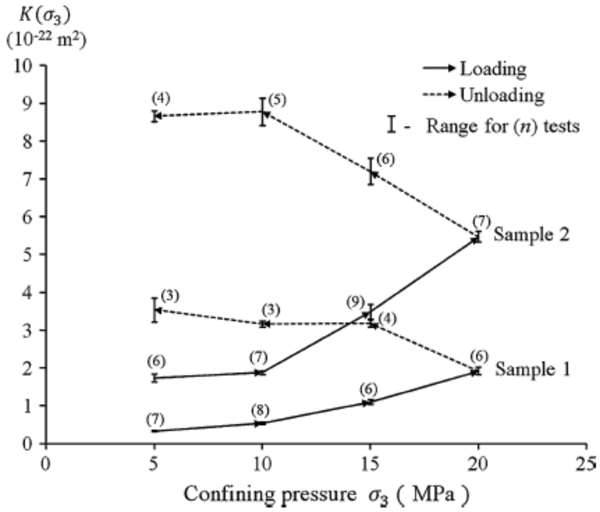

Figure 1.8: Permeability vs confining pressure of the Cobourg Limestone: results derived from 81 pulse tests conducted on two samples (Selvadurai *et al.*, 2011).

1.3 Permeability and Triaxial Stress State

The following sections present, in chorological order, key research related to the estimation of permeability evolution in rocks subject to triaxial stress states. In general, permeability test on rocks subjected to triaxial stresses are more limited than the hydrostatic ones due to the complexities associated with experimental configurations. In general, when the stresses applied to a rock sample deviate from isotropic compression, the resulting permeability is influenced by the triaxial stress states; this can lead to the development of micro-cracks which can alter the permeability of the rock. The studies by Zoback and Byerlee (1975) estimated the permeability of Westerly Granite samples, 25 mm in diameter and 64 mm in length, with argon as the permeating fluid, using the pulse decay method (see Figure 1.9). Samples were subjected to pre-failure triaxial stresses only, up to 95% of failure stresses, with pore pressures ranging from 11 MPa to 24 MPa. The results show that permeability initially decreased during the application of deviatoric stresses and increased due to dilatancy thereafter with a significant hysteresis upon unloading (see Figure 1.10).

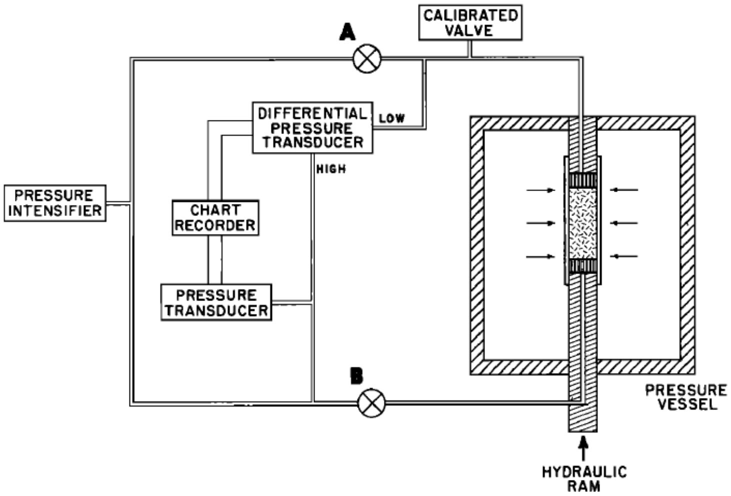

Figure 1.9: Schematic view of the triaxial cell and experimental setup (Zoback and Byerlee, 1975).

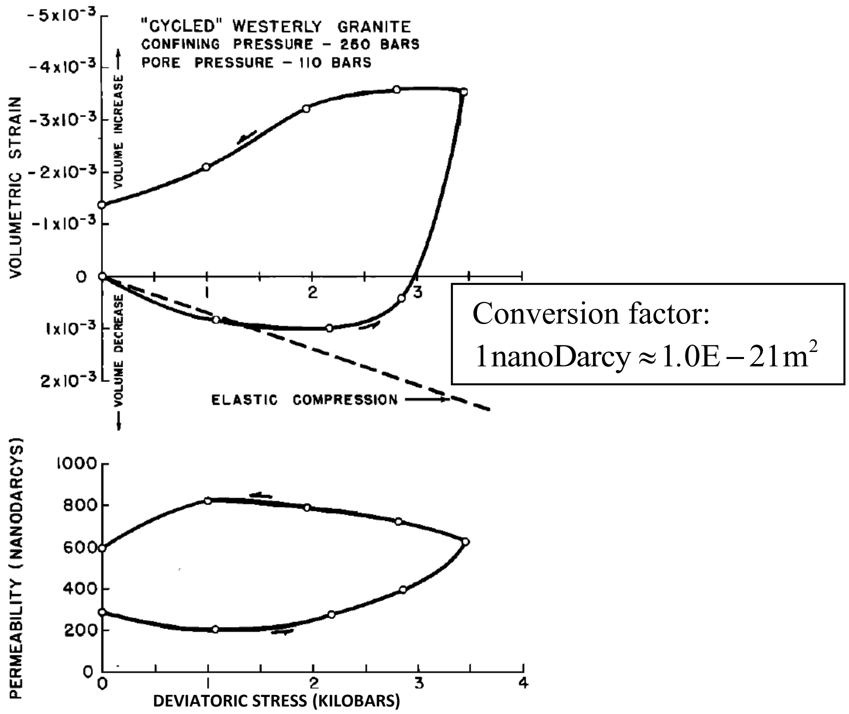

Conversion factor:
$1\,\mathrm{nanoDarcy} \approx 1.0\mathrm{E}-21\mathrm{m}^2$

Figure 1.10: Volumetric strain and permeability vs deviatoric stress (Zoback and Byerlee, 1975).

The important addition of triaxial stress states on permeability evolution is that it allows for the study of the influence of failure regimes on the effective permeability of rocks. Kiyama *et al.* (1996) performed a series of hydrostatic and triaxial permeability tests on Inada Granite samples, 50 mm in diameter and 100 mm in length, using the transient pulse method. For all tests the confining pressure was kept at 10 MPa and the pore pressure at 5 MPa. The results from the triaxial tests show a slight decrease in hydraulic conductivity in the pre-failure tests due to micro-crack closure and a three order of magnitude increase in hydraulic conductivity after failure (see Figure 1.11).

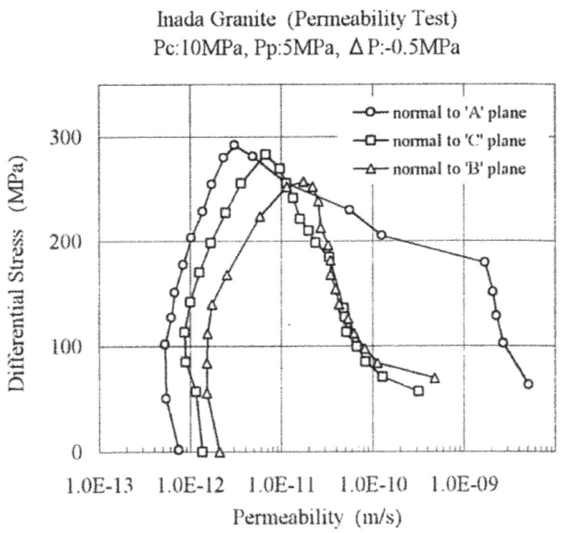

Figure 1.11: Differential stress vs hydraulic conductivity under triaxial conditions (Kiyama *et al.*, 1996).

Hydrostatic and triaxial tests were performed by Suri *et al.* (1997) on Indiana Limestone samples, 54 mm in diameter and 108 mm in length, using the oscillating pulse technique to estimate the permeability. The triaxial tests were performed at confining pressures of 6.9 MPa to 48 MPa with deviatoric stresses up to failure. The results show that permeability decreases until the initiation of dilatancy, at which point there was an increase in permeability; however, at higher confining pressures, dilatancy is suppressed and the permeability decrease continues largely due to pore compaction. The experimental permeability studies that were conducted by Zhu and Wong (1997) on Adamswilier, Berea, Boise, Darley Dale, and Rothbach sandstones (with varying porosities: 15% to 35%) in the *brittle* and *ductile* failure regimes with water as the permeating fluid. The prepared samples, 18 mm in diameter and 38 mm in length, were subjected to confining pressure in the rage of 13 MPa to 55 MPa and a pore pressure of 10 MPa. In their experimental setup all samples were jacketed with a copper foil membrane and a minimum differential pressure of 3 MPa was always kept between the confining and pore pressures to avoid leakage along the sample-membrane interface. The results for permeability differ greatly and whether there is a decrease or an increase in permeability is dependent on the initial porosity and the mode of failure. In general, all sandstones had a decreasing permeability with increasing mean effective stress up to the compactive yield stress. Keaney *et al.* (1998) conducted permeability tests in a triaxial cell on Tennessee Sandstone; the samples were 15 mm diameter and 45 mm length and were subjected to confining stresses varying from 50 MPa to 130 MPa and a pore pressure of 30 MPa. They demonstrated that in the “brittle faulting regime”, under deviatoric compressive stresses, the permeability decreases until failure, after which the increase or decrease of effective permeability is controlled by the properties of the fracture. Dautriat *et al.* (2011) conducted axial and radial permeability experiments on Estaillades Limestone in a triaxial cell (see Figure 1.12). The samples were 38 mm in diameter and 80 mm in length, with a NaCl brine solution as pore fluid. The pore pressure was kept constant at 1 MPa during the experiments. Permeabilities were measured in the pre- and post-failure stress states, in brittle and ductile failure regimes. A summary of the measured permeabilities in shown in Figure 1.13, showing a general trend of a decrease in the estimated permeability for all stress states. Furthermore, the results show that upon unloading all the samples experienced a 10% to 60% reduction in permeability when compared to the initial measurement.

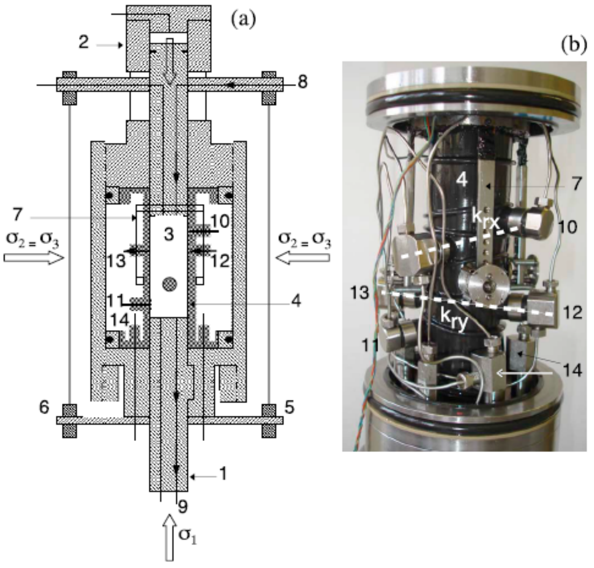

Figure 1.12: (a) Simplified sketch of the triaxial cell. (b) Picture of the equipped core sleeve with radial flow ports (Dautriat *et al.*, 2011).

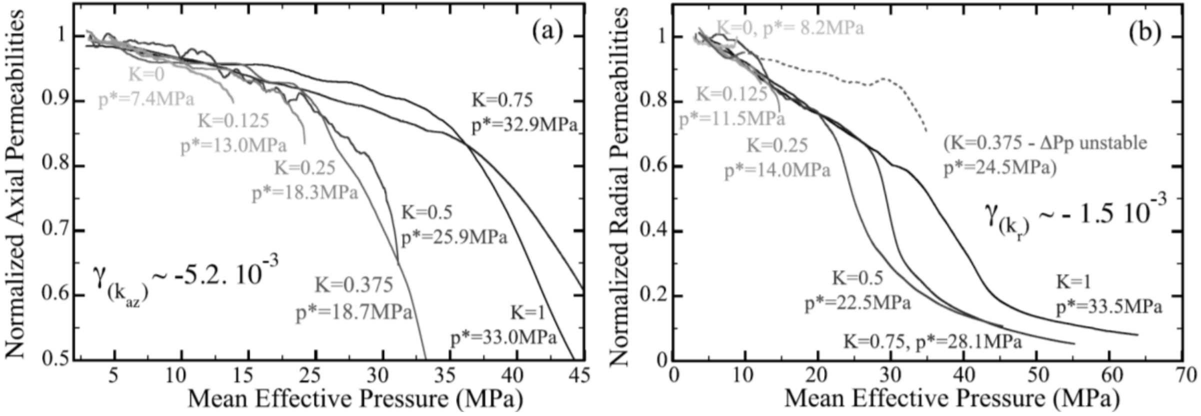

Figure 1.13: (a) axial and (b) radial permeabilities with the effective pressure for the seven investigated stress paths (K). For each test, the values of failure pressure p* (Dautriat *et al.*, 2011).

The change in permeability in the vicinity of excavation damage zones (EDZ) is also an important consideration with regard to fluid movement in repositories constructed for the deep geological storage of hazardous materials (Tsang *et al.* 2012). The research on whether permeability increases or decreases with increasing compressive deviatoric stresses is split, including post-failure. The research by Souley *et al*. (2001) examined the excavation damage-induced alterations in permeability of granite from the Canadian Shield conducted with the use of a packer system (see Figure 1.14). A model was proposed to predict permeability changes with damage stages in the rock corresponding to four distinct regions (I–IV): closure of pre-existing microcracks (region I); elastic behaviour zone (region II); stable crack growth (region III); and unstable crack growth (region IV). The results obtained from the experimental investigation conducted inside the tunnel, at a depth of 420 m, were compared to the proposed model (Figure 1.15).

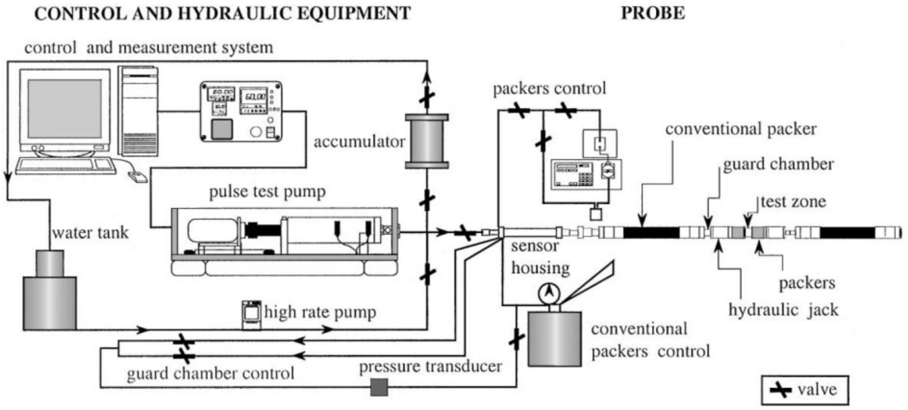

Figure 1.14: Schematic view of the experimental setup (Souley *et al.*, 2001).

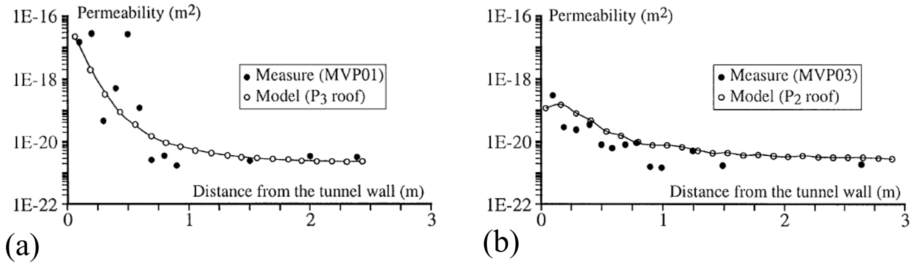

Figure 1.15: Comparison between predicted and in-situ measured permeability vs distance from tunnel wall: (a) in the direction of initial minor stress; (b) in the direction of initial intermediate stress (Souley *et al.*, 2001).

The work of Meier *et al*. (2002) focused on the self-healing of the Excavation Damage Zones (EDZ) in the shaley formation, Opalinus Clay, at the Mont Terri rock laboratory in Switzerland. The results showed one order of magnitude decrease in transmissivity after one year, which was attributed to the self-healing of the argillaceous formation in the EDZ. In summary, tit should be noted that the majority of the studies in the published literature were conducted on small samples (25 mm to 55 mm in diameter and 50 to 100 mm in length) subject to large pore pressures (in the MPa range), which is in contrast to the research performed for this thesis.

1.4 Models for Permeability Evolution with Stress State

The results for permeability evolution with stress state obtained from experiments need to be adapted for use in design and modelling. Such adaptations of experimental results take the form of empirical relationships that use rock-specific parameters to predict the permeability. Gangi (1978) gives an overview of developed empirical models for the permeability reduction in intact and fractured rocks; the model proposed for the intact rock subjected to hydrostatic stresses is based on the Hertz theory for the deformation of spheres by spheres, whereas, the equation for effective permeability of fractured rock is based on the bed of nail model (see Figure 1.16).

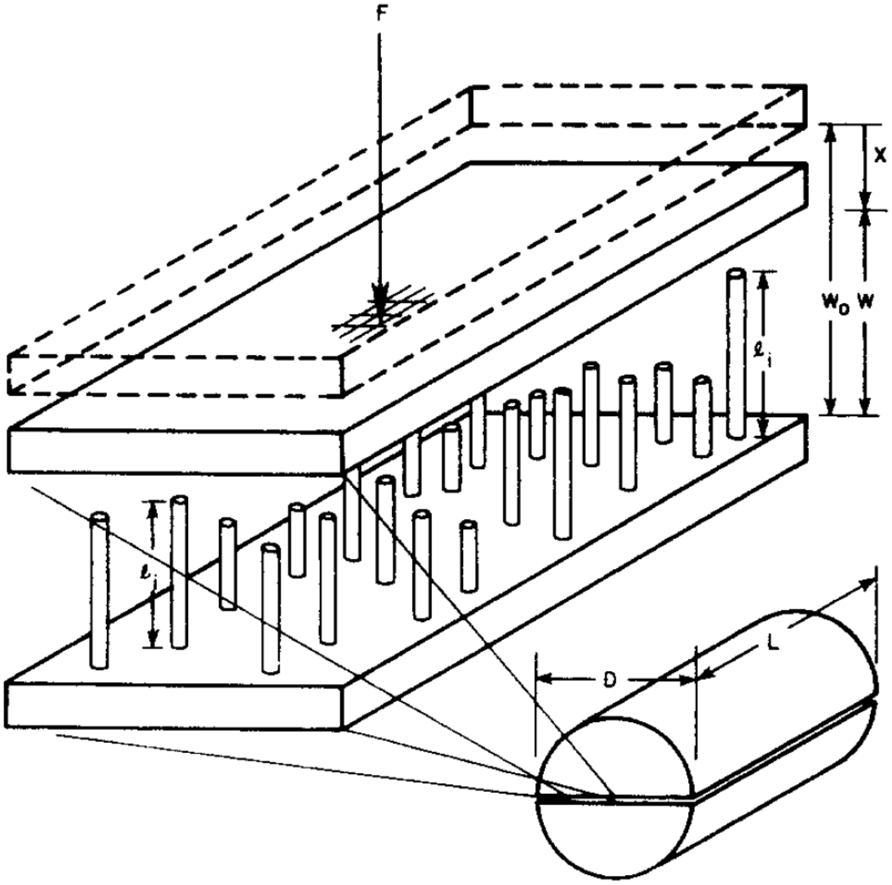

Figure 1.16: Bed of nails model for permeability estimations in fractured rocks (Gangi, 1978)

The review by Guéguen *et al*. (1996) looked into different published models that interpreted permeability from: equivalent channel model; mean radius-statistical models, effective radius-effective media model; networks and critical radius models. These models relied on experimental data obtained from the following techniques: image analysis from thin sections, mercury porosimetry and nitrogen adsorption. However, the review points out that these models are not adapted to take into account important effects on permeability such as stress states, temperature and sample scale (i.e. defects), which based on their literature review present experimental challenges. Shao *et al*. (2005) proposed a fully coupled constitutive model to predict the induced mechanical damage and permeability evolution in brittle rocks subjected to compressive stresses by relation to microcrack growth (i.e. penny-shaped cracks). The proposed model results were compared with experimental data from Lac du Bonnet granite that show good agreement in terms of predicting both the increase in permeability and the mechanical behaviour that occurs at failure state. Massart and Selvadurai (2012) proposed a model to predict the induced permeability in damaged granitic rocks. The proposed model is based on multiscale computational and homogenization techniques which consist of extracting the averaged properties of a heterogeneous material from the properties of their constituents. The proposed model was then verified against experimental data and showed good agreement in predicting the permeability evolution with deviatoric stresses at different confining pressures (see Figure 1.17).

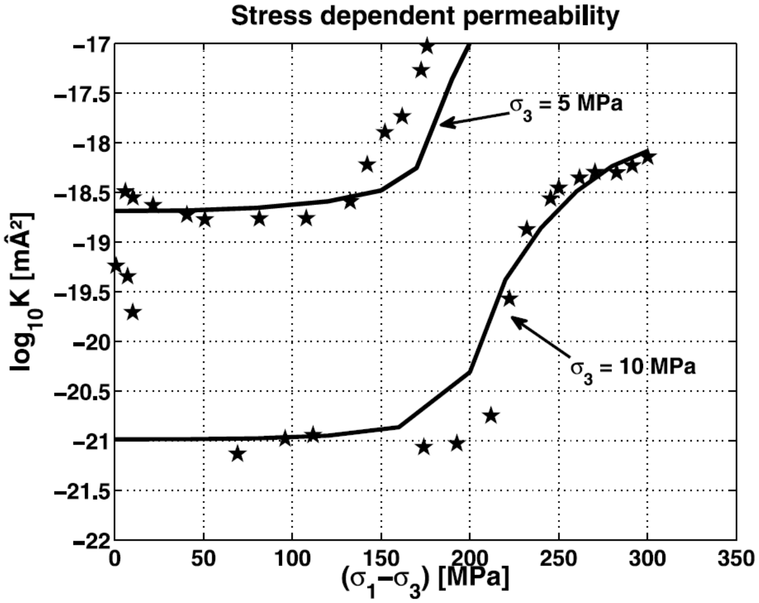

Figure 1.17: Axial permeability evolution vs deviatoric stress for a confining pressures of 5 MPa and 10 MPa. Star points represent experimental results by Souley *et al.*, 2001 (Massart and Selvadurai, 2012).

1.5 Objectives and Scope of the Research

The research presented in this thesis is focused on the experimental and computational study of the permeability of rocks. The majority of the experiments were conducted on Indiana Limestone and Cobourg Limestone samples under unstressed and stressed conditions, with results covering both the pre-failure and the post-failure permeability response. Other rocks tested as complementary investigations included Rudna Sandstone (Cieślik, 2015) and Stanstead Granite (Selvadurai and Najari, 2013). In summary, the novelty of this research is: (i) the use of rocks that can exhibit large scale heterogeneity and therefore required dimensionally large samples (typically 85 mm in diameter and 170 mm in height), which were tested under triaxial stress states; (ii) development of empirical models to characterize the evolution of permeability with triaxial stress states for Indiana Limestone and Cobourg Limestone; (iii) a correlation is proposed between peak and residual steady state hydraulic gradients for unstressed rock samples; (iv) permeability heterogeneity of the two phases found in the Cobourg Limestone is investigated.

In the initial stages of this research the physical and mechanical properties of the rocks were investigated. Chemical analysis was also performed on the rock matrix in order to establish the elements and minerals forming their structure.

In order to properly assess the experimental facilities and methods for testing permeability of rocks various checks had to be performed: (i) assess full saturation of the rock and whether this saturation made a significant difference to the results; (ii) prepare and analyze the permeating fluid used in permeability experiments in order to standardize and obtain satisfactory testing results; (iii) perform a chemical analysis of the outflow fluid (iv) examine the influence of machining particulates no the porous matrix of the rock and how they affect the permeability results; (v) control the temperature of the laboratory and permeating fluid in order to keep temperature fluctuations to a minimum so that they do not affect the estimated permeabilities.

The finite element code (COMSOL Multiphysics^{TM}) was used throughout this research to estimate the permeabilities from hydraulic pulse test results as well as to integrate proposed empirical relationships, based on permeabilities obtained from experiments, into a computational model for examining typical engineering geotechnical problems.

CHAPTER 2

THE CHARACTERIZATION OF THE INDIANA LIMESTONE AND THE COBOURG LIMESTONE

This chapter presents the main physical and mechanical properties relevant to the current investigations of the Indiana Limestone and the Cobourg Limestone. The Cobourg Limestone is a more visually heterogeneous rock when compared to the Indiana Limestone, and both rocks mechanical and fluid transport properties were investigated in the Environmental Geomechanics Laboratory (EGL) at McGill University. Additionally, several different porous materials have been extensively studied in the past at the EGL: cement grout (Selvadurai and Carnaffan, 1997), granite (Selvadurai and Najari, 2013) Cobourg Limestone (Selvadurai *et al*., 2011; Selvadurai and Jenner, 2013; and Selvadurai and Najari, 2015) and Indiana Limestone (Selvadurai and Głowacki, 2008; Selvadurai and Selvadurai, 2010). All past research gives the laboratory substantial repository of collected data on the tested materials, as well as extensive experimental on laboratory equipment and feasible laboratory procedures.

2.1 Indiana Limestone

The Indiana Limestone used in this research was supplied by Les Carrières Ducharme Inc, Québec, in the form of blocks measuring 35 cm x 47 cm x 91 cm. It was quarried from the Salem

Formation, located in Indiana (USA) that was formed during the Mississippian age, more than 300 million years ago (ILIA, 2007). The Indiana Limestone blocks were cored at McGill University, using a diamond bit corer, to produce cylindrical samples of different sizes (50 mm up to 100 mm in diameter and 20 mm up to 200 mm in length, Figure 2.1).

2.1.1 Chemical composition

The XRF analysis of the Indiana Limestone was performed on the Philips PW2440 4kW X-ray fluorescence (XRF) spectrometer system with a PW2540 VRC 168 sample autochanger at Earth and Planetary Sciences Department at McGill University. These instruments allow the determination of element concentrations in solid samples, using either homogenized lithium borate fusion beads or pressed powder pellets, the latter being used in this analysis. Detection limits are as low as 1 part per million (ppm) for some elements (TEAL, 2015). The results of weight percentage of the major compounds as well as the part per million trace elements are shown in Table 2.1. The results obtained compare well with the chemical composition presented in the handbook of Indiana Limestone Institute (ILIA, 2007) (see Table 2.2). The Indiana Limestone is described as mainly composed of calcite-cemented grainstone made up of fossil fragments and oolites, see a typical sample in Figure 2.1 (ILIA, 2007). The chemical analysis has shown that Indiana Limestone is mainly composed of calcium carbonate (98.3%). In Table 2.1, based on the XRF analysis, the calcium carbonate ($CaCO_3$) fraction can be estimated at 98.3% by adding the CaO fraction and the “lost on ignition” (LOI) fraction.

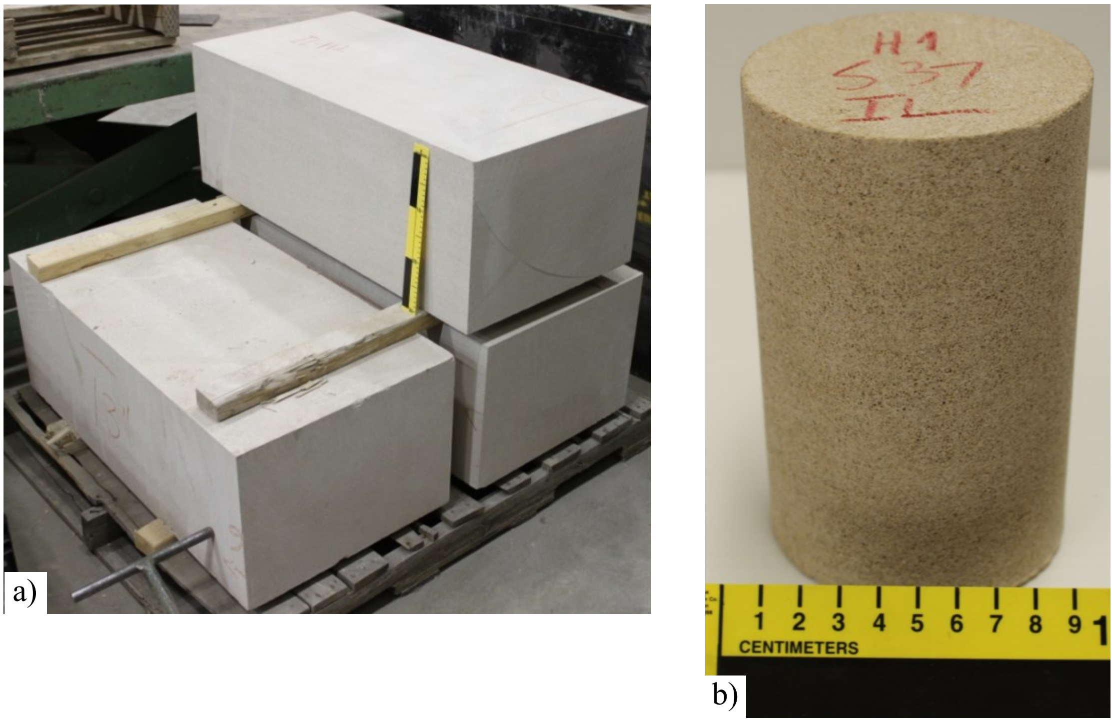

Figure 2.1: Photograph of a) the Indiana Limestone block and b) a cored cylindrical sample.

Table 2.1: Chemical analysis of Indiana Limestone performed at the Earth and Planetary Sciences Department, McGill University.

Indiana Limestone	**Units**	
	wt%	**ppm**
CaO	54.087	
MgO	0.450	
SiO_2	0.553	
Al_2O_3	0.173	
Fe_2O_3	0.123	
TiO_2	0.015	
MnO	0.007	
Na_2O	0.013	
K_2O	0.010	
P_2O_5	0.013	
BaO		-
Ce		-
Co		-
Cr_2O_3		23.0
Cu		24.0
Ni		-
Sc		-
V		10.1
Zn		23.0
LOI	44.217	

Table 2.2: Chemical analysis of two different pigmentations of Indiana Limestone (ILIA, 2007).

	Indiana Limestone	
	Buff wt%	Grey wt%
Calcium Carbonate ($CaCO_3$)	97.39	97.07
Magnesium Cabonate ($MgCO_3$)	1.20	1.20
Silicon dioxide (SiO_2)	0.69	0.80
Aluminium Oxide (Al_2O_3)	0.44	0.68
Iron Oxide (Fe_2O_3)	0.18	0.12
Water and Loss	0.10	0.13

2.1.2 Physical and mechanical properties of Indiana Limestone

The physical and mechanical properties of Indiana Limestone are based on tests performed at the Environmental Geomechanics Laboratories, McGill University. The compressive strengths were determined using the International Society of Rock Mechanics Standard (ISRM, 2007). The estimates for porosity (n)were obtained using the Mercury Intrusion Porosimetry (MIP) technique performed at the Civil Engineering Laboratory, Concordia University, Montréal, Québec. The results from the MIP tests gave a value of $n = 0.144$, which compares well with the value of $n = 0.160$, shown in Table 2.3, obtained using a vacuum water saturation technique (see Chapter 4: Vacuum saturation 4.4). The compressive strengths were determined using the ISRM (2007) Standard. The samples (six dry and five saturated) were tested on the MTS load frame (MTS Systems Corporation 315.03 Load Frame), with a loading rate of 0.2 mm/min until failure; strains were measured with stain gauges and extensometers. Four disk samples (50 mm in diameter by 27 mm in height) were used to measure the tensile strength of the Indiana Limestone using the Brazilian Test method (ISRM, 2007); the ensuing results can be found in Table 2.3. The Brazilian splitting tests generates a state of tension within the test specimen by applying a compressive line load which is distributed over a section of the circular surface and allows to determine the tensile strength of the sample with the following formula:

$$\sigma_t = 2P_o / \pi LD \tag{2.1}$$

where σ_t is the tensile strength of the material, P_o is the maximum axial compressive load, L is the length of the and D is diameter of the sample.

The tensile splitting tests were complemented with a series of plug tests, which infer tensile stress state in an annular cylinder sample by compressing an axially positioned rubber plug inside the central cavity. The method was developed by Selvadurai and Benson (2011), and was adopted by Hekimi (2012) to determine the tensile strength of Indiana Limestone. The tensile strength can be obtain by considering that the hollow cylindrical sample dimensions (i.e. the wall thickness is too large to treat it as a surface) dictate that the solution for the circumferential and radial stresses with no external stresses can be interpreted with the following Lame's stress equations (tensional stresses are taken as + ve) (see Timoshenko and Goodier, 1951):

$$\sigma_{\theta\theta} = \frac{a^2 p}{\left(b^2 - a^2\right)}\left(1 + \frac{b^2}{r^2}\right); \ \sigma_{rr} = \frac{a^2 p}{\left(b^2 - a^2\right)}\left(1 - \frac{b^2}{r^2}\right) \tag{2.2}$$

where $\sigma_{\theta\theta}$ and σ_{rr} are the circumferential and radial stress respectively (MPa), p is the internal pressure (MPa), r is the radius, a and b are respectively the internal and external radii of the thick-walled cylinder. The test results from the plug test for the maximum tensile strength using the Lame's stress equation were estimated at 14.4±0.4MPa.

Table 2.3: Geomechanical and physical properties of the Indiana Limestone (NWMO, 2015a)

Property	**State**	**Dimensions**	**Value**
Height	N/A	[mm]	122.6±0.1
Diameter	N/A	[mm]	49.1±0.1
Unit Weight (γ)	N/A	[kN/m^3]	22.0±0.2
Porosity (n)	N/A	Non-Dimensional	0.16±0.01
Unconfined Compressive Strength (σ_C)	Dry	[MPa]	37.9±1.5
	Saturated	[MPa]	30.5±2.4
Tensile Strength (σ_t)	Dry	[MPa]	3.7±1.2
Young's Modulus (E)	Dry	[GPa]	33.2±2.5
	Saturated	[GPa]	31.1±3.7
Poisson's Ratio (v)	Dry	Non-Dimensional	0.28±0.01
	Saturated	Non-Dimensional	0.33±0.04
Cohesion (c)	Dry	[MPa]	9.8
Angle of internal friction (ϕ)	Dry	Non-Dimensional	33.4

2.1.3 Triaxial compression tests

The results of triaxial compression tests conducted on the Indiana Limestone are shown in Figure 2.2; an inspection of these results indicates that when radial stress $\sigma_3 \in (0,\ 5)\,\mathrm{MPa}$, the failure process is *brittle*. When $\sigma_3 \in (5,\ 20)\,\mathrm{MPa}$ the behaviour at failure exhibits some *ductility* and can be considered to be in a transitional state. At confining stresses $\sigma_3 > 20\,\mathrm{MPa}$, the stress-strain behaviour is generally *ductile*. A similar post-failure response was observed by Chitty *et al.* (1994) on Indiana Limestone. The typical sample, in the ductile failure mode, exhibited no observable (at least to the naked eye) signs of localization, damage or compaction band development. Similarly, laboratory tests made by Vajdova *et al.* (2012) on triaxially stressed Indiana Limestone showed that at confining stresses between 5 MPa and 10 MPa the samples failed by brittle faulting accompanied by dilatancy and strain softening, whereas compactive cataclastic flow occurred at confining stresses above 20 MPa.

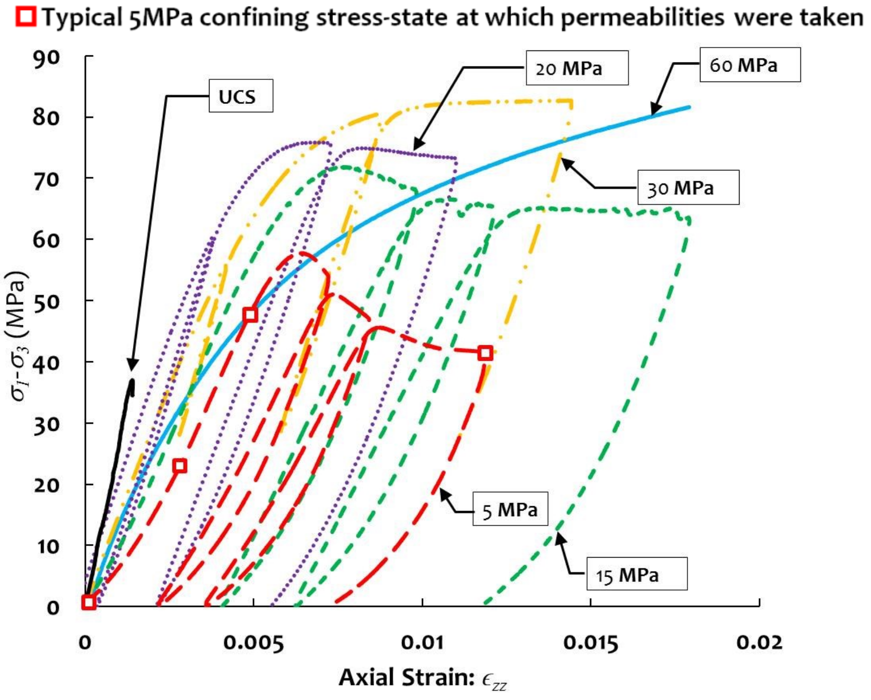

Figure 2.2: Results for deviatoric stress vs. axial strain for Indiana Limestone at different confining stress states.

The apparent cohesion (c) and the angle of internal friction (ϕ) were obtained from triaxial tests using an Obert-Hoek Cell at confining stresses ranging from 5 MPa up to 60 MPa by considering the Mohr–Coulomb failure criterion which represents the linear envelope that is obtained from a plot of the shear strength of a material versus the applied normal stress. The results of the triaxial tests were then plotted on a q vs p graph (see Figure 2.3figure 2.3); where the angle of internal friction and the apparent cohesion are obtained from the following relationships:

$$\phi = \sin^{-1}\left(\tan\left(\alpha\right)\right) \tag{2.3}$$

$$c = \mathrm{d}/\cos\left(\phi\right) \tag{2.4}$$

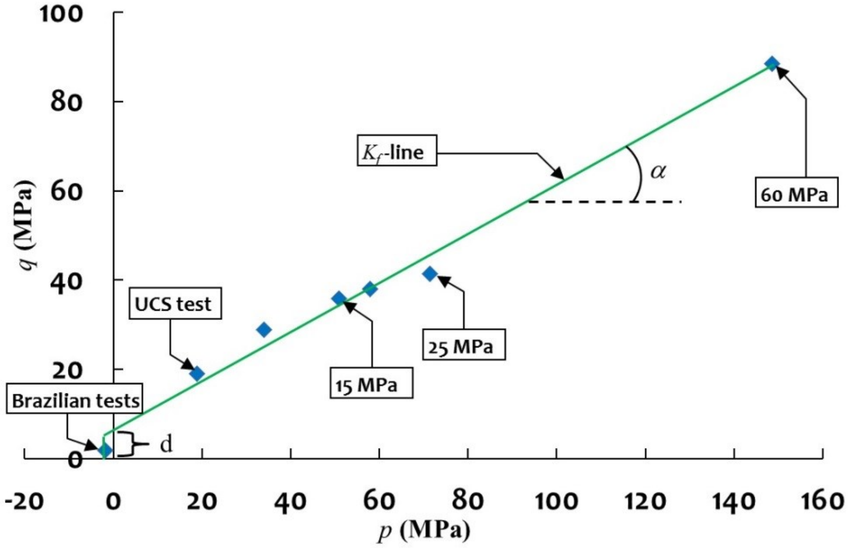

Figure 2.3: Failure line on a q vs p plot for dry Indiana Limestone

2.2 Cobourg Limestone

Large block sample of the Cobourg Limestone used in this research were obtained from Saint Mary's Quarry in Bowmanville, Ontario, Canada. The Cobourg Limestone belongs to the Middle Ordovician carbonate formation located in southern Ontario, in the Great Lakes region.

The Cobourg Limestone is characterized as an argillaceous limestone with a mineralogy composed of calcite with minor amounts of dolomite, quartz and illite with traces of chlorite, pyrite and feldspar (INTERA, 2011). It is heterogeneous in color (see Figure 2.4) with dark to light grey coarse grained patches and clearly identifiable bedding planes of shale (INTERA 2011). These two distinctive phases are primarily composed of a light grey carbonate nodular material and a dark grey argillaceous material. Clay mineral content, illite and mica, for the Ordovician limestones is variable and ranges from 12% to 0% (decreasing with depth) in the Cobourg formation (INTERA, 2011).

Figure 2.4: Photograph of the Cobourg Limestone surface presenting the typical visually heterogeneous matrix phases.

The limestone from Southern Ontario is also referred to as Lindsay Limestone as is described in the studies by Selvadurai *et al*. (2011) and Selvadurai and Jenner (2013).

2.2.1 Chemical composition

A petrographic confirmation and identification study was performed at Département des Sciences de la Terre et de l'Atmosphère, Université du Québec à Montréal (UQAM) using X-ray diffraction (XRD). Additionally, an optical microscopy (OM) and scanning electron microscopy coupled with an energy dispersive spectrometer (SEM–EDS) study was made at Earth and Planetary Sciences, McGill University. From the XRD study it can be concluded that the rock is mostly composed of calcite as the main component (see Table 2.4).

Table 2.4: Summary of mineral analysis of Cobourg Limestone [Current study].

Minerals	CLS1-34 mm %	CLS1-34 mm %
Calcite	79.3	85.5
Quartz	14.8	9.5
Illite	3.3	3.2
Kaolinite	0.5	0.2
Chlorite	1.1	0.5
Pyrite	0.3	0.3
Microcline	0.4	0.5
Albite	0.3	0.3

Table 2.5: Summary of Elemental Geochemical Analyses of Cobourg Limestone cores (INTERA, 2011).

Minerals	**%**
Calcite	81
Dolomite	8
Quartz	3
Sheet silicates*	6

* All clay minerals are grouped togheter (mica, muscovite,clinochlore (chlorite), glauconite and palygorskite.

The chemical analysis results compared well with the results from the literature (Table 2.5) confirming that the rock samples obtained from the Saint Mary's Quarry accurately represent, at least in chemical composition, the host rock formation located at the site of the future DGR at the Bruce Nuclear Plant Complex, Ontario.

2.2.1.1 Chemical composition heterogeneity

Due to the visually apparent heterogeneity of the Cobourg Limestone, a chemical analysis was performed in order to characterize the light grey (referred in this research as: light grey carbonate phase) and dark grey (referred in this research as: dark grey argillaceous phase) phases of the rock matrix and to properly assess the clay content in each phase. Samples, typically representing only the light grey or dark grey phases were prepared for analysis. In summary, the results show that the light grey phase is composed of: calcite (85%), quartz (8%) and dolomite (5%), whereas the dark grey phase contains: calcite (51%), quartz (22%), dolomite

(16%), albite (3%), microcline (3%) and muscovite (1.5%). In the dark phase (referred to as argillaceous) the clay content was established at 2.4% whereas in the light grey (referred to as carbonate) it was 0.3%. Details of the procedure, analysis and experimental procedures are given in Appendix A.

2.2.2 Physical and mechanical properties of Cobourg Limestone

The physical and mechanical properties were based on tests done by the research group in EGL at McGill University. The unconfined compressive strength was determined using the ISRM (2007) Standard. The porosity (n) shown in Table 2.6 was obtained using the vacuum water saturation technique with the value of $n = 0.006$ (see Section 4.4).

Table 2.6: Geomechanical and physical properties of the Cobourg Limestone

Property	Units	Value	Literature	References
Unit Weight (γ)	[kN/m^3]	26.6		
Porosity (n)	N/A	0.006	0.014±0.001	Selvadurai et al 2011, INTERA 2011
Unconfined Compressive Strength (σ_C)	[MPa]		113±25	OPG 2011b
Tensile Strength (σ_t)	[MPa]		6.5	INTERA 2011
Young's Modulus (E)	[GPa]	35	21;35;39	Selvadurai et al 2011; Golder Associates 2003; OPG 2011b
Poisson's Ratio (ν)	N/A	0.25	0.25;0.30	Selvadurai et al 2011; Golder Associates 2003
Shear strength (τ)	[MPa]		1.3	OPG 2011b

2.2.3 Thermal expansion of the heterogeneous phase in Cobourg Limestone

A series of thermal expansion tests were performed on small cylindrical samples of Cobourg Limestone measuring 24.1 mm in diameter and 37.6 mm in length. The cylindrical samples were selected to represent, ideally, only the carbonate light grey or argillaceous dark grey phase. In total, four samples with two strain gauges on each sample were prepared. The thermal expansion coefficient was measured using a set of strain gauges (Tokyo Sokki™ Kenkyujo Co., Ltd: 120 ohm, 5 mm length) that were bonded to specific phases of the sample using epoxying cyanoacrylate epoxy (see Figure 2.5).

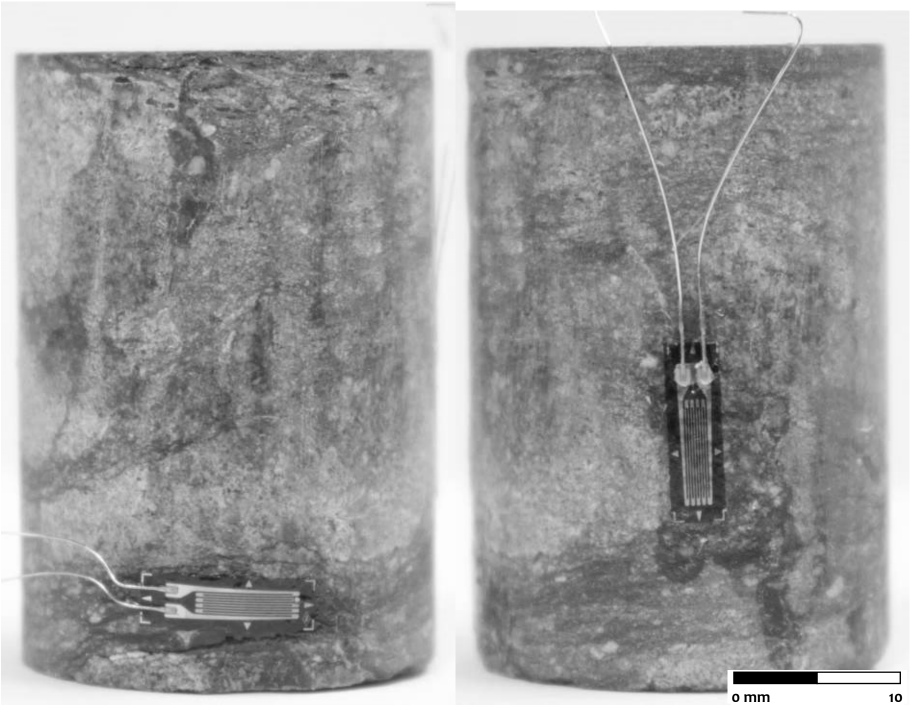

Figure 2.5: Photograph of the Cobourg Limestone samples used in thermal expansion tests with epoxied strain gauges to specific phases.

In order to ensure proper bonding between the strain gauge and the sample, two layers, with drying periods of 24 hours between each layer, were applied to the rock surface before finally epoxying the strain gauge. Samples with epoxied strain gauges were then placed into a pre-heated oven and subjected to 75±3°C. Strains were recorded with time during a period of 3 hours. The result for the coefficient of thermal expansion of the light grey carbonate phase was $\alpha_T^L = \left[2.9\times10^{-5} \pm 5.5\times10^{-5}\right] / {}^{o}\mathrm{C}$ whereas for the dark grey argillaceous phase it was $\alpha_T^D = \left[3.5\times10^{-5} \pm 1.3\times10^{-6}\right]/{}^{\circ}\mathrm{C}$. For comparison, in the interval of $20^{\circ}\mathrm{C}$ and $80^{\circ}\mathrm{C}$ the thermal expansion coefficient of Illinois Limestones given by Harvey (1968) was $8.1\times10^{-6}/{}^{\circ}\mathrm{C}$.

The equation used to determine the coefficient of thermal expansion with the strain gauges that were not self-temperature-compensated was :

$$\alpha_S - \alpha_R = \frac{\left(\varepsilon_{(G/S)} - \varepsilon_{(G/R)}\right)}{\Delta T} \tag{2.5}$$

where α_S is the unknown coefficient of thermal expansion $(1/\mathrm{T})$, α_R is the reference material (i.e. Invar: a nickel–iron alloy) known coefficient of thermal expansion $(1/\mathrm{T})$, $\varepsilon_{(G/S)}$ is the thermal output in strain units of the specimen material, $\varepsilon_{(G/R)}$ is the thermal output in strain units of the reference material and ΔT is the temperature change (i.e. Invar).

Additional information on the derivation of equation 2.5 and the measurement of the coefficient of thermal expansion can be found in Micro-Measurements (2010).

CHAPTER 3

LABORATORY PERMEABILITY MEASUREMENT IN ROCKS

3. Introduction

Permeability is an intrinsic physical property of a rock or soil that describes the ability of fluids to migrate through the accessible interconnected pore space under a hydraulic gradient. The pioneering study that describes the property of hydraulic conductivity of a porous medium is due to Darcy (1856), who used the concepts to provide a water supply scheme for the city of Dijon in France. The terms permeability and hydraulic conductivity are used to describe similar properties and are related by the permeating fluid properties (see equation 3.1).

$$K = \frac{\mu k}{\gamma_w} \tag{3.1}$$

where K is the permeability $\left(\mathrm{L}^2\right)$, k is the hydraulic conductivity $\left(\mathrm{L/T}\right)$, γ_w is the unit weight of water $\left(\mathrm{M/L^2T^2}\right)$ and μ is the dynamic viscosity of water $\left(\mathrm{M/TL}\right)$.

There are many methods for the estimation of permeability of rocks which can be found in literature, including: (i) oscillating pulse technique (Kranz *et al.*, 1990; Azeemuddin *et al.* 1995; Suri *et al.*, 1997), (ii) pore size distribution (Yang and Aplin, 1998) and (iii) CT-scan and X-Ray porosimetry (Grader *et al.*, 2009). The oscillating pulse method (i) consists of solving the same equations as the hydraulic pulse decay method (see Section 3.2) except that the upstream boundary condition is different. The measured data is the steady pressure amplitude ratio between upstream and downstream reservoirs as well as the phase difference between peak pressures in the two reservoirs. This technique has the benefit of obtaining the permeability as well as the diffusivity constants for the porous medium, although, for rocks, such as granite, with low permeability ($1\text{E}-19\,\text{m}^2$) Kranz *et al.* (1990) was not able to collect accurate data to calculate the permeability. Moreover, the method requires subjecting the rock sample to high pore pressures and a substantial effort is needed to calibrate the oscillation frequency and the measuring system for each and every rock type to make accurate measurements. But once the method is properly setup in a reservoir borehole it has the potential to detect changes in storage and interconnected porosity provided those changes are slow with respect to the oscillation frequency (see e.g. Kranz *et al.*, 1990). The flow properties of a porous material (ii) are related to microstructure of the pore and grain structure of the porous material (Shepherd, 1989). Therefore, the estimation of permeability uses the properties of porosity and porous matrix structure. Well established equations such as the Kozeny-Carman (Bear, 1972) can be used to estimate the permeability:

$$K=\left(\frac{\rho g}{\mu}\right)\frac{D_m^2 n^3}{\left(1-n\right)^2 180} \tag{3.2}$$

where g is the gravitational acceleration $\left(\text{L}/\text{T}^2\right)$, ρ is the permeating fluid density $\left(\text{M}/\text{L}^3\right)$, μ is the dynamic viscosity of the permeating fluid $\left(\text{M/TL}\right)$, n is the porosity and D_m is the mean particle size of the mixture $\left(\text{L}\right)$.

In the recent years advancements in digital imaging (CT-scans and X-ray) allow researchers to correctly assess and build 3D models of the pore space, grain structure and interconnectivity of pores. These models (iii) are then combined with computational models for fluid flow to determine the flow properties of the porous material (i.e. permeability) (Auzerais *et al.*, 1996;

Knackstedt *et al*., 2009). These imaging methods do suffer from problems such as small sample size (3.5 mm in diameter), poor spatial resolution of the simulation as well as the numerous assumptions that are subjective, with respect to the selecting the boundary between the pore and the solid. The most common methods for measuring permeability are however the direct methods, which can be categorized as follows: the steady state and the pulse decay (transient) methods. The steady state methods, either constant flow or constant pressure, are naturally occurring and more reliable, since the only measurements needed to estimate the permeability are the hydraulic potential difference, flow rate and the geometry of the flow domain (Boulin *et al*., 2012). The steady state methods are typically applicable to rocks with permeabilities in the range $1.0\mathrm{E}-14\,\mathrm{m}^2$ to $1.0\mathrm{E}-18\,\mathrm{m}^2$ and typically relevant to rocks such as sandstones, limestones and rocks with fractures (Heystee and Roegiers, 1981; Zhu and Wong, 1997; Selvadurai and Głowacki, 2008; Selvadurai and Selvadurai, 2010). These permeability limits are, however, constantly expanding as more sophisticated and more precise equipment (i.e. pumps) becomes available, which allows the successful testing and estimation of low permeability materials. Boulin *et al*. (2012) conducted steady state experiments on tight rocks using a high precision pump and were able to obtain permeabilities as low as $7.8\mathrm{E}-22\,\mathrm{m}^2$. Additionally, by performing steady state flow tests on Illinois granite, Morrow and Lockner (1997) measured permeabilities as low as $1.0\mathrm{E}-23\,\mathrm{m}^2$. One major limitation with the steady state methods is the time required to attain steady conditions. Furthermore, proving that steady state conditions are attained entails accurately measuring the inflow and outflow volume of fluid migrating through the sample, which in some experimental setups, especially for low permeability rocks, it is not feasible or is very difficult. Hence, for tight rocks the preferred method to measure permeability is the pulse decay method, in which the measurement of pressure decay is far more accurate than the measurement of flow rate. One of the first published accounts of the use of the hydraulic pulse method was due to Brace *et al*. (1968) who used the technique to estimate the permeability of Westerly Granite. This method was then used on various geomaterials and improved by Lin (1977), Hsieh *et al*. (1981), Neuzil *et al*. (1981), Bernabe (1986), Selvadurai and Carnaffan (1997), Selvadurai and Najari (2015) and others. A major uncertainty while using the pulse decay method, relates to the estimation of the specific storage of the porous material (Giot *et al*. 2011). This chapter discusses in more detail the steady state method and the pulse decay method that were used in this research to estimate the permeability in a laboratory setting.

3.1 Steady State Method

The fundamental law governing fluid flow through a porous medium was proposed by Darcy (1856). The steady state fluid flow in a saturated porous medium is governed by the gradient in the reduced Bernoulli potential $\varphi(\mathbf{x})$ which consists of the pressure potential $\varphi_P(\mathbf{x})$ and the datum potential $\varphi_D(\mathbf{x})$, while the velocity potential is neglected in relation to these. In a hydraulically isotropic porous medium, the permeability is defined by K. The Darcy's Law can be written as (Bear 1972; Selvadurai, 2000):

$$\mathbf{v}(\mathbf{x}) = -\frac{K\gamma_w}{\mu}\nabla\varphi(\mathbf{x}) \qquad (3.3)$$

where K is the permeability (L^2), $\mathbf{v}(\mathbf{x})$ is the velocity vector $(\mathrm{L/T})$, γ_w is the unit weight of water $(\mathrm{M/L^2T^2})$, ∇ is the gradient operator and $\mathbf{x}$ is a position vector.

In order to describe the flow of a fluid through a porous medium the Laplace equation can be used. The Laplace equation is developed by combining the mass conservation equation and

Darcy's law. Hence, in a porous medium and a Cartesian coordinate system the mass conservation, in three dimensions, can be obtained as:

$$\frac{\partial v_x}{\partial x}+\frac{\partial v_y}{\partial y}+\frac{\partial v_z}{\partial z}=0 \qquad \text{or} \quad \nabla\bullet \tag{3.4}$$

where v_x, v_y, v_z are the velocities in the respective x, y, z direction.

In the mass equation 3.4 it is assumed that the fluid is incompressible, the porous matrix is rigid and isotropic.

For a hydraulically isotropic medium the Darcy's Law can be expressed as:

$$v_x=-\frac{K\gamma_w}{\mu}\frac{\partial\varphi}{\partial x};\ v_y=-\frac{K\gamma_w}{\mu}\frac{\partial\varphi}{\partial y};\ v_z=-\frac{K\gamma_w}{\mu}\frac{\partial\varphi}{\partial z} \tag{3.5}$$

The flow velocities through the porous medium are influenced only by the hydraulic gradient. Therefore, the Darcy's law, equation 3.5, can be substituted into the mass conservation equation 3.4 to obtain the general form of the Laplace's equation for fluid flow through an isotropic material:

$$\frac{\partial^2\varphi}{\partial x^2}+\frac{\partial^2\varphi}{\partial y^2}+\frac{\partial^2\varphi}{\partial z^2}=0 \qquad \text{or} \quad \nabla^2\bullet \tag{3.6}$$

Since, in this research the measurement of permeability is limited to experiments conducted in one direction, typically *z*-axis*,* Laplace's equation 3.6 can be simplified:

$$\frac{d^2\varphi}{dz^2}=0 \tag{3.7}$$

The general solution for of equation 3.7 is:

$$\varphi(x)=C_1x+C_2 \tag{3.8}$$

where C_1 and C_2 are constants, which can be determined from boundary conditions. An example which involves the axial flow through a porous material can be regarded as a typical experimental setup in this thesis, is shown in Figure 3.1.

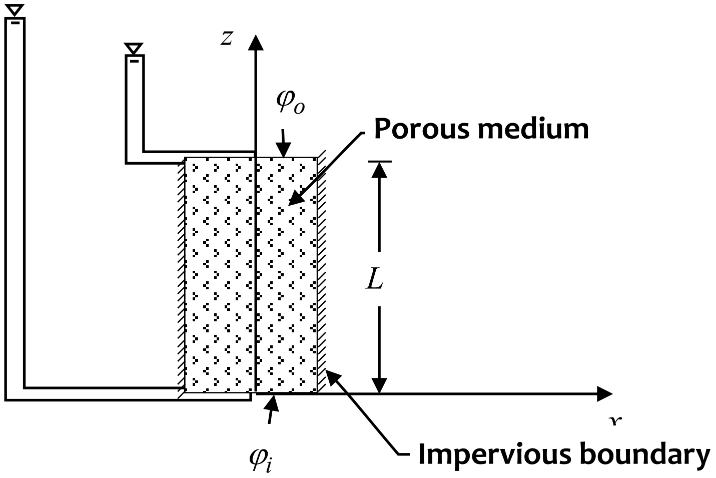

Figure 3.1: One-dimensional flow in a porous medium.

By examining the boundary conditions in Figure 3.1 for the hydraulic potential we get:

$$\varphi(0) = \varphi_i \text{ and } \varphi(L) = \varphi_o \tag{3.9}$$

This gives a hydraulic potential distribution thought the sample of length L as:

$$\varphi(z) = \varphi_i - \frac{z}{L}(\varphi_i - \varphi_o) \tag{3.10}$$

Substituting this result in equation 3.5, the axial velocity in the z-axis direction is given by:

$$v_z(z) = \frac{K\gamma_w}{\mu}\frac{(\varphi_i - \varphi_o)}{L} \tag{3.11}$$

In an axial one-dimensional steady state flow experimental setup, a known flow rate is applied to area surface base of a cylindrical sample and the inflow pressure required to maintain the steady flow is recorded. All other constants are known; therefore the equation (3.11) can rearranged to give permeability:

$$K = \frac{Q\mu L}{A\left(p_i - p_o\right)} \tag{3.12}$$

where Q is the flow rate $\left(\mathrm{L}^3/\mathrm{T}\right)$, L is the length of the sample $\left(L\right)$, A is the cross sectional area of the sample perpendicular to the flow $\left(\mathrm{L}^2\right)$, p_o and p_i are the outflow and inflow pressure of the water respectively $\left(\mathrm{M}/\mathrm{T}^2\mathrm{L}\right)$.

In order to ascertain that a steady state flow was established, a constant pressure plateau is necessary as well as the measurement of the outflow with time.

In addition, the use of Darcy's Law can be extended to an inhomogeneous rock by assuming that, at a local scale, (i.e. near a drilled cavity into the surface of a rock) the permeability is isotropic; justification for this was be further examined in the research conducted by Selvadurai (2011) and reported in the papers by Selvadurai and Selvadurai (2010, 2014).

3.2 Pulse Decay Method

The fluid transport characteristics of low permeability rocks can be estimated by using the pulse decay method. The pulse decay method is more convenient than steady state method because the prolonged time duration required to reach steady state conditions is avoided. However, the pulse decay method requires the knowledge of additional parameters (i.e. porosity, storativity, etc.) in order estimate the permeability of a porous medium from a pulse decay tests. Ideally, the fluid flow problem through a porous medium subjected to elastic deformations should be solved using the differential equations proposed by Biot (1941):

$$G\nabla^2\mathbf{u}+\left(K_{eff}+\frac{G}{3}\right)\nabla^2\bullet \qquad : 0 \tag{3.13}$$

$$\frac{K}{\mu}\nabla^2 p - S^*\frac{\partial p}{\partial t} - \alpha\frac{\partial}{\partial t}\big(\nabla\bullet \tag{3.14}$$

where G is the shear modulus, K_{eff} is the bulk modulus of the porous skeleton, $\mathbf{u}(z,t)$ is the skeletal deformation, $p(z,t)$ is the pore fluid pressure, S^* is the storativity term and α is the *Biot Coefficient*.

The solution of such coupled differential equations would require the formulation of an initial boundary value problem with exact conditions relevant to an experimental configuration where consistent initial and boundary conditions are applied to all the dependent variables (Selvadurai and Najari, 2013). Hence, in order to conduct pulse decay tests and obtain reliable results a method was pioneered by Brace (1968) to obtain the permeability of the Westerly Granite under high confining pressures. Brace (1968) used the partial differential equation for the transient flow of a compressible fluid through the accessible pore space of a porous medium with a porous skeletal compressibility C_{eff} and solid grain compressibility C_s :

$$\frac{K}{\mu}\nabla^2 p = S\frac{\partial p}{\partial t} \tag{3.15}$$

where p is the fluid pressure, S is the storativity $\left(\mathrm{LT}^2/\mathrm{M}\right)$ and t is the time (T).

The equation (3.15), commonly referred to as the piezo-conduction equation, is applicable to a deformable porous medium composed of a compressible pore fluid (C_w), compressible porous skeleton (C_{eff}) and compressible solid grains (C_s) that make up the porous medium. The simplification that is introduced into the piezo-conduction equation over the Biot (1941) equations is that in the hydro-mechanical coupling the time-dependent variations in the skeletal mean stresses are neglected (Selvadurai and Najari, 2015).

The storativity S is expressed as:

$$S = nC_w + C_{eff} - (n+1)C_s \tag{3.16}$$

where n is the porosity of the medium.

The compressibility of the porous skeleton is estimated by the following equation:

$$C_{eff} = \frac{3(1-2v)}{E} \tag{3.17}$$

Where E is the Young's modulus $(\mathrm{M/T^2L})$ and v is the Poisson's ratio.

The compressibility of the porous skeleton and the compressibility of the solid grains are related by the Biot coefficient:

$$\alpha = \left(1 - \frac{C_s}{C_{eff}}\right) \tag{3.18}$$

A Biot coefficient of 1.0 would mean that the grains are incompressible.

By combining the equations 3.16 and 3.18, we obtain a new storativity equation:

$$S_N = \left\{nC_w + C_{eff}\left[\alpha + n(\alpha - 1)\right]\right\} \tag{3.19}$$

The solution to the piezo-conduction equation (3.15) for an axial flow condition can be obtained when the following boundary conditions (see Figure 3.2) are applied to a semi-infinite region (see: Selvadurai, 2009; Selvadurai *et al.*, 2011):

$$\hat{p}(0) = \hat{p}_o \tag{3.20}$$

$$\Phi\left(\frac{\partial p}{\partial z}\right)_{z=0} = \left(\frac{\partial p}{\partial t}\right)_{z=0} \; ; \; p(\infty, t) = 0 \tag{3.21}$$

$$p(z,0) = 0 \tag{3.22}$$

where $\hat{p}(t)$ is the position independent fluid chamber pressure $(\mathrm{M}/\mathrm{T}^2\mathrm{L})$, which is a function of time only and $\hat{p}_o$ is the initial pressure inside chamber at the start of the axial flow pulse test $(\mathrm{M}/\mathrm{T}^2\mathrm{L})$ on the inlet side.

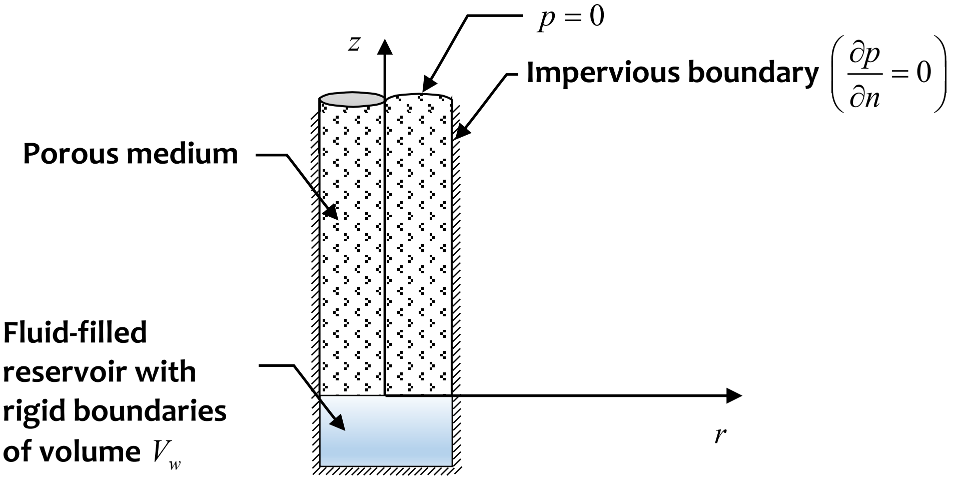

Figure 3.2: Diffusion of fluid pressure in a one-dimensional semi-infinite porous medium.

In equation 3.21, Φ is:

$$\Phi=\left(\frac{AK}{\mu V_w C_w}\right) \tag{3.23}$$

where A is the cross-sectional area of the one-dimensional semi-infinite domain (L^2) and V_w is the volume of the pressurized inlet fluid for the pulse decay test (L^3).

Since the estimation of axial permeability is focused on rocks of low permeability with a finite extent, it can be assumed that the far field boundary conditions have negligible effect on the pulse decay tests for a relatively short duration of time. Therefore, the second part of the boundary condition equation (3.21) is possible because the regularity condition is satisfied $p(z,t)\rightarrow 0$ as $z\rightarrow\infty$. The rationale for this simplification in the axial flow problem can be found in the work of Hsieh *et al.* (1981). The rationale for the use of semi-infinite region and its validity for the radially symmetric case can be found in the work of Selvadurai and Carnaffan (1997).

The solution of the initial boundary value problem for equation (3.15) can be obtained and is expressed as:

$$\frac{\hat{p}(t)}{\hat{p}_o} = \exp\left(\Omega^2 t\right)\mathrm{Erfc}\left(\sqrt{\Omega^2 t}\right) \tag{3.24}$$

where

$$\Omega = \Phi\omega \;\; ; \;\; \omega^2 = \frac{S_N \mu}{K} \tag{3.25}$$

where the Erfc is the complementary error function defined as:

$$\mathrm{Erfc}(x) = \frac{2}{\sqrt{\pi}}\int_x^\infty \exp\left(-\xi^2\right)\mathrm{d}\xi \tag{3.26}$$

In the experimental setup, the pressure in a closed volume, is raised and suddenly released to the saturated surface of the porous medium, creating a hydraulic pulse that will propagate through the medium. The initial pulse pressure prescribed at the inlet $\hat{p}(t)$ is monitored with time as it decays. This experimental pressure decay is then compared to the analytical solution for pressure obtained with equation 3.24, and permeability is obtained when the theoretical results match with the experimental data (see Section 6.5.1).

3.2.1 Pulse decay method with air in the pressurized cavity

The basic assumption in the modelling of the hydraulic pulse tests is that the fluid both within the pressurized cavity and in the pore space of the tested medium is fully saturated with a fluid with a compressibility corresponding to that of pure water. This assumption will be violated if any air is present or introduced during the sample saturation and experimental preparation. Selvadurai and Ichikawa (2013) have investigated the influence of air in the pore space on the performance of the hydraulic pulse tests. If there is trapped air in the pressurized volume of water V_w including the connections (i.e. tubing, valves, etc.), then the compressibility of the air-water mixture should be accounted for. The presence of air bubbles in the pressurized system will slow down the decay of the hydraulic pulse, resulting in a decrease in the estimated permeability. Selvadurai and Najari (2015) first proposed a procedure for incorporating the air content in order to account for the compressibility of the gas–fluid mixture :

$$C_{eq} = \frac{\phi + h(1-\phi)}{P} + (1-\phi)C_w \tag{3.27}$$

where C_{eq} is the compressibility of the fluid within the pressurized cavity and connections $(\mathrm{LT^2/M})$, ϕ is the air fraction (non-dimensional) defined as volume of air bubble fraction divided by the sum of the volume of pure water and air bubble fraction, h is Henry's constant (i.e. for air at a temperature of 25°C and atmospheric pressure, it is 0.01708) and P is the absolute air pressure $(\mathrm{M/T^2L})$.

The equation (3.27) can only be used if the pressurized fluid, on the inlet side, is contained in a very rigid system. This means that the pressurization of the fluid is quick and there are no flexible/expandable elements in the inlet connections (i.e. rubber, plastic tubing). Equation (3.27) can be further simplified by assuming that the Henry's constant is zero, because the rate of dissolution of air in the water is slower than the absolute pressure change in the system. It is important to note that equation (3.27) neglects the influence of solubility of air in water, the surface tension of water and the vapor pressure.

The experimental procedure and setup that presents the estimation of air fraction is given in section 6.5.1. In this research, the method used to estimate the air fraction in the pressurized cavity with rigid boundaries (i.e. pressurized rigid reservoir: stainless steel tubing, valves, pump pistons and connections) follows the procedure given by Selvadurai and Najari (2015): (i) the volume of water $\left(V_w\right)$ was accurately measured by both weight measurement and geometry; (ii) the time required to pressurize the volume $\left(V_w\right)$ was recorded and used in the numerical modelling to determine the air fraction by assigning the compressibility of the gas–fluid mixture $\left(C_{eq}\right)$ for the volume $\left(V_w\right)$.

CHAPTER 4

PERMEABILITY MEASUREMENT IN ROCKS: TESTING FACILITIES

This chapter presents the experimental facilities that were developed and used to conduct the experimental investigations set forth in this thesis for the rock samples. There are sections that present particular procedures (i.e saturation method, de-aired water system) which were specifically developed for the study of permeability in rocks. All major testing was done at the Environmental Geomechanics Laboratories and the Structural EngineeringLaboratories in the Department of Civil Engineering and Applied Mechanics, McGill University.

4.1 Obert-Hoek Cell

The triaxial test cell used in this research was an initially developed by Obert (1963) and later it was adapted by Hoek and Franklin, (1968) to determine the compressive triaxial strength of rocks. The cell was capable of testing rock samples up to 67 MPa radial pressures, which were applied to the cylindrical surface of the sample via a flexible membrane (see Figure 4.1).

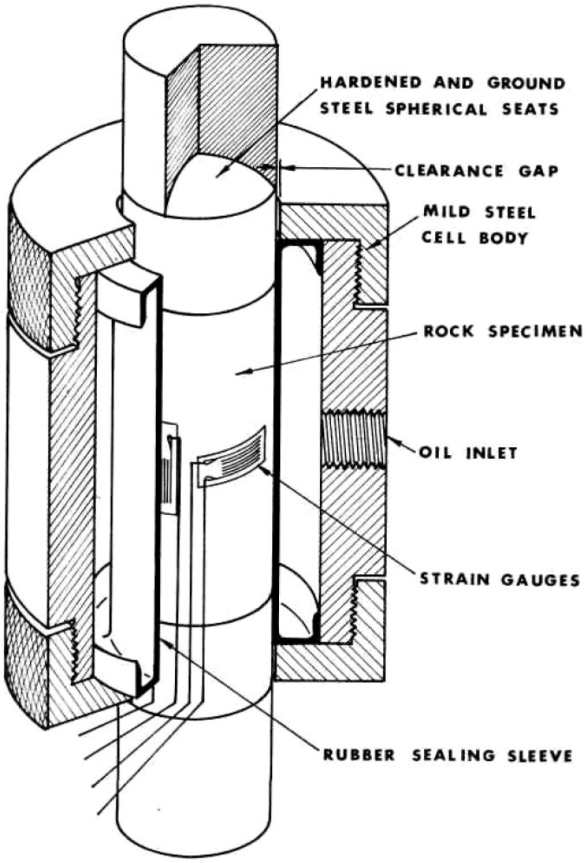

Figure 4.1: Cutaway view of the Obert-Hoek Cell (Hoek and Franklin, 1968).

An adaptation of the Obert-Hoek triaxial cell can also be found in Alsayed (2002), where in which it was used to measure the deformability and failure characteristics of hollow rocks subjected to triaxial compressive and tensional stress states. In the current research, the Obert-Hoek Cell was adapted to measure permeability of the Indiana Limestone and Cobourg Limestone subjected to triaxial stresses with samples of 85 mm in diameter and 170 mm in height and a maximum confining stress of 65 MPa. A schematic view of the modified Obert-Hoek Cell is shown in Figure 4.2, the modification is detailed in the following Section 4.2. The radial stress is applied through the pressurization of the internal rubber membrane and the axial stress is applied via the upper and lower stainless steel loading platens. The modification relates to the provision of a sealing ring to ensure contact between the membrane and the cell via an O-ring. The method of application of the radial and axial stresses can be configured to simulate conditions encountered in a stress-controlled conventional triaxial cell. The radial stresses applied to the sample were supplied by a manual hydraulic pump and then maintained at a prescribed value using a digitally-controlled servo-hydraulic system (GDS Instruments, Controller 2, pressure-rated for 65 MPa) (see Figure 4.3). Similarly, the axial stress was applied using the electric hydraulic pump and maintained at a prescribed values using a digitally-controlled servo-hydraulic system (GDS Instruments, Controller 1, pressure-rated for 65 MPa).

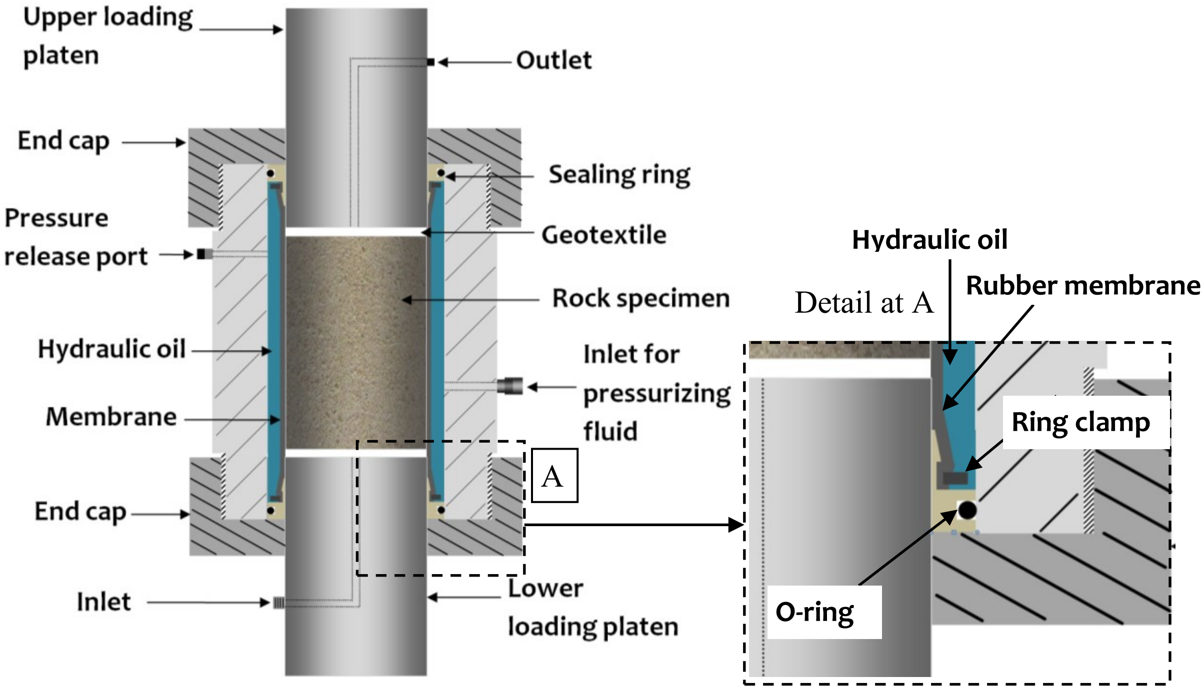

Figure 4.2: Cross-sectional detail of the modified Obert-Hoek Cell, with detail at A.

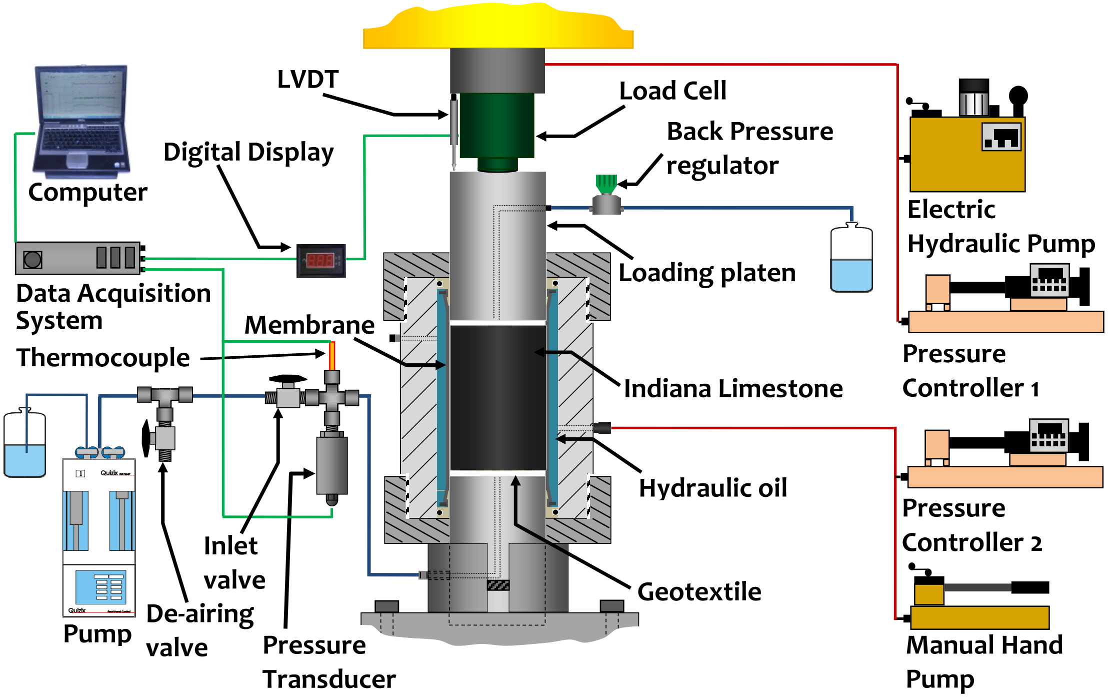

Figure 4.3: Schematic view of the experimental arrangement with Indiana Limestone.

The test specimen was contained between upper and lower stainless steel loading platens. A set of stainless steel loading platens was designed and machined to provide a seal that would allow conducting one dimensional flow permeability tests. The machined platens contained entry ports to provide water inflow and outflow. In this arrangement, the sample can be subjected to both axial and radial stresses and a fluid flow through the sample at a known hydraulic gradient can be maintained by using a back pressure regulator at the outflow. The contact surfaces between the plane ends of the loading platens and the sample contained geotextile layers (Texel™: F-200), which served to (i) distribute/collect the flowing water and (ii) reduce friction between the sample and the loading platens. The geotextile experiences significant compression as well as a reduction in its permeability characteristics. However, even the reduced permeability created by compression is significantly higher ($\approx 2.3\text{x}10^{-7}$ m^2) than the permeability of the Indiana Limestone ($\approx 1.6\text{x}10^{-14}$ m^2) at a reference confining pressure of 5 MPa (Selvadurai and Głowacki, 2008). Since, each loading platen had one central port to distribute/collect water, a stainless steel porous disc, 86 mm in diameter and 4.5 mm in length, was placed to avoid a concentrated point distribution of water (see Figure 4.4). This was especially important when higher axial loads were applied and a more impervious rock, like the Cobourg Limestone, was being tested. The stainless steel disks were placed between the loading platen and the geotextile (see Figure 4.5).

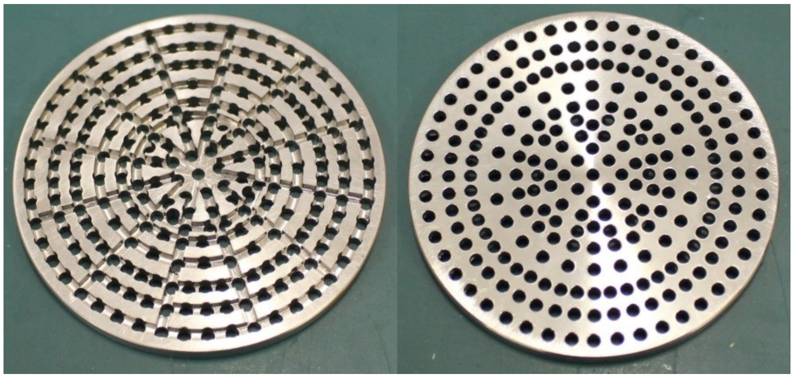

Figure 4.4: Stainless steel porous disks machined for use in the modified Obert-Hoek Cell; all holes had diameter of 2.8 mm, the channels were 2 mm wide and had a depth of 1.8 mm.

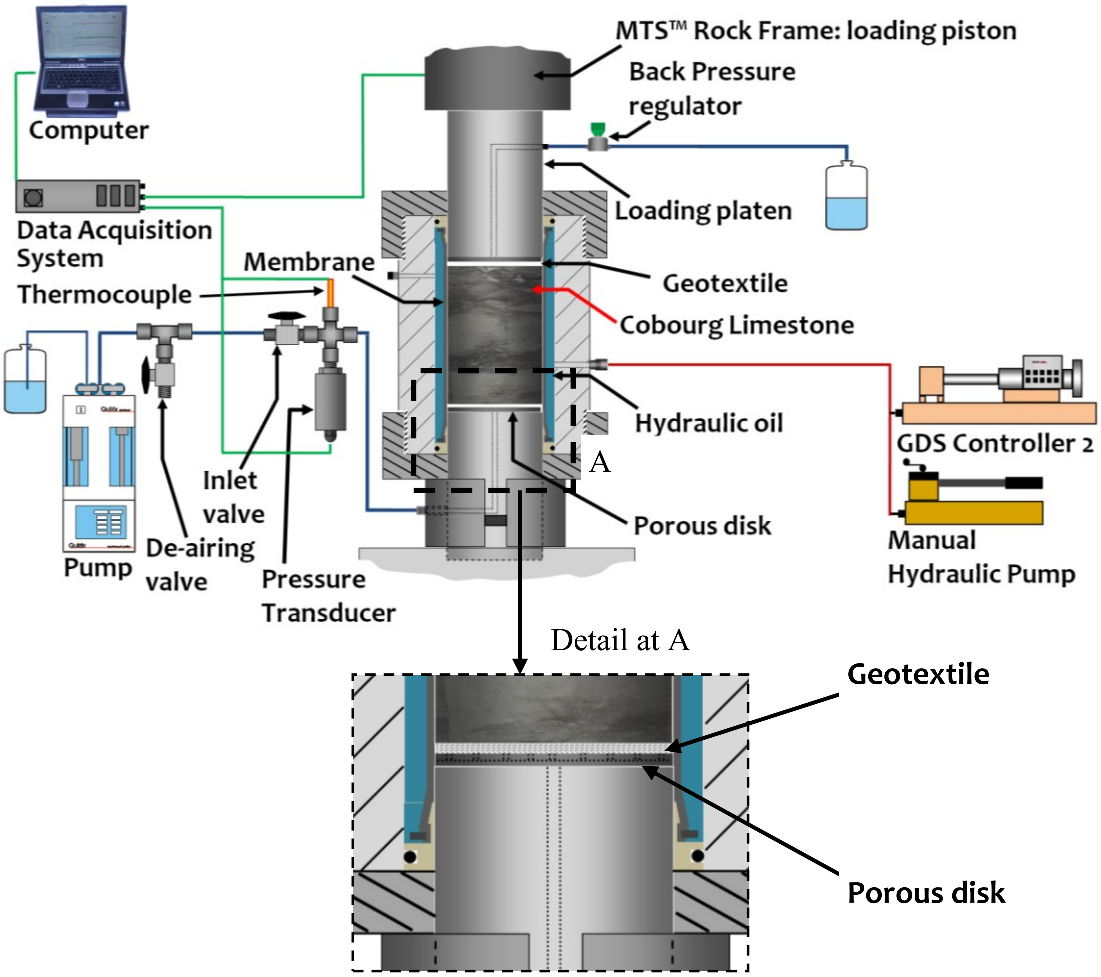

Figure 4.5: Schematic view of the experimental arrangement with Cobourg Limestone; detail at A of geotextile and porous disk.

In order to verify that no interface flow took place between the sample and the rubber membrane during the permeability tests, a machined aluminum cylinder measuring 85 mm in diameter and 170 mm in length was placed in the modified Obert-Hoek Cell and subjected to a minimum radial stress of 5 MPa. In this condition, the upstream end of the cylinder was pressurized to 1500 kPa and maintained for 2 hours with no appreciable pressure drop (less than 0.1%).

The initial membrane (Adiprene™ LF-950: see Appendix C) supplied with the original Obert-

Hoek Cell proved to be inadequate for permeability testing because leakage of the confining hydraulic oil was noticed on to the surface of the sample. Hence, work was initiated to remedy this situation and modification to the Obert-Hoek Cell was necessary. More details on this topic are found in Section 4.2.

4.2 Obert-Hoek Cell Modification

The Obert-Hoek Cell was acquired from Roctest Ltd. based in St-Lambert, Quebec. Early during its service life at EGL (McGill), the Obert-Hoek Cell was used to characterize the deformability and failure characteristics of the Cobourg Limestone. Upon completion of these tests, the Obert-Hoek Cell was fitted with loading stainless steel platens with water entry ports and installed in the High Capacity Load Controlled Testing Facility (HCLC), see Section 4.3, in order to conduct permeability tests on Indiana Limestone subjected to axial and radial stresses. During the initial testing stages it was noted that the Obert-Hoek Cell was not performing adequately in terms of sealing the radial pressure. It was observed that the membrane supplied by the manufacturers was leaking hydraulic oil at the interface between the steel caps of the Hoek Cell and the membrane. Thus contaminating the sample and creating a mixture as permeating fluid. The exact reasons of the leakage could not be established, two possible hypotheses were: (i) that at the low confining stresses some oil leakage was occurring as there was not enough pressure to seal against the Obert-Hoek Cell steel caps; (ii) the upper loading piston was pulling down the membrane, effectively removing the seal between the membrane and the end cap, as the compressive axial load was applied. In order to remedy this situation and after several redesign attempts the original membrane was replaced with a rubber membrane (Nitrile; thickness 2.4 mm) supplemented with two specially designed stainless steel sealing rings fitted with an O-ring (see Figure 4.6). The direct consequence of such modification was on the length of the future samples that were tested; the length had to be reduced from 170 mm to 130 mm in order to accommodate the sealing arrangement. The rubber membrane used to seal the sample was capable of withstanding the applied peak cell pressures, up 60 MPa, without rupture through contact with either the cylindrical surface of the Indiana Limestone or Cobourg Limestone samples or the interfaces layers (geotextile/porous disks). However, it was important to carefully machine the cylindrical surface on all the samples in order to avoid any surface cavities, dents and protrusions, which could result in the puncture of the membrane. The seal capability of the modified Obert-Hoek Cell, brought upon the modifications mentioned previously, was verified by performing a series of sealing tests with an aluminum cylinder.

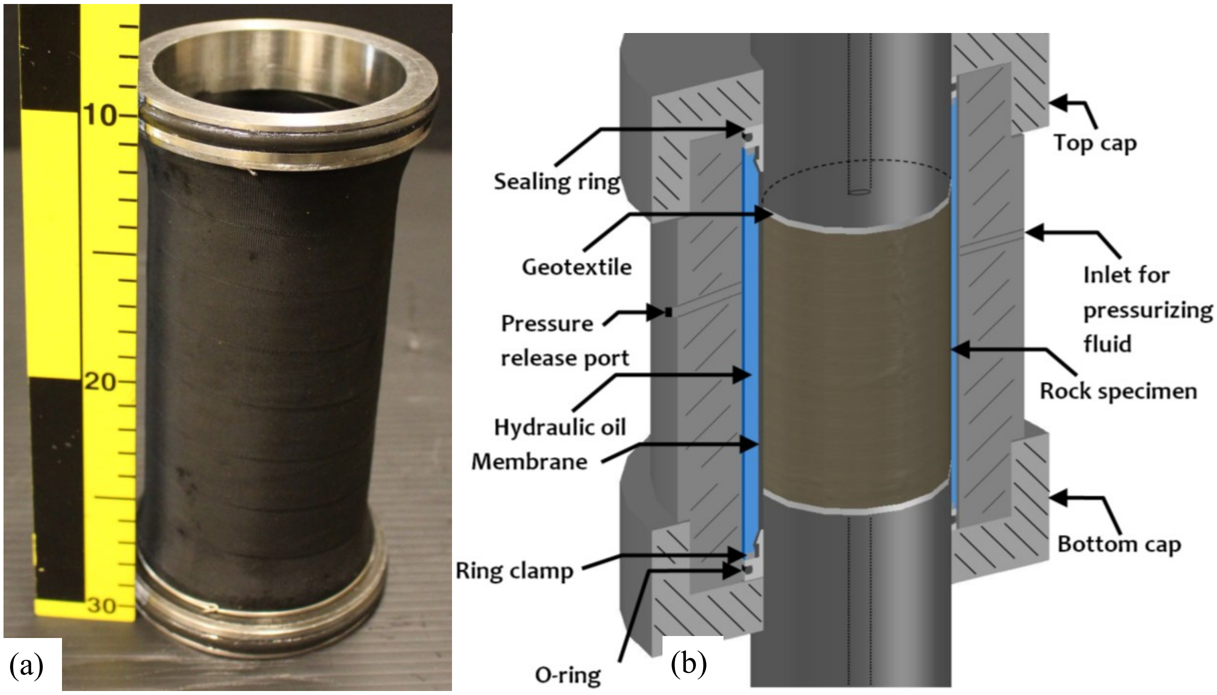

Figure 4.6: (a) Stainless steel sealing rings with rubber membrane use in the modified Obert-Hoek Cell; (b) Cutaway view of the position of the membrane with sealing rings inside the modified Obert-Hoek Cell.

4.2.1 Friction tests

The surfaces of the rock specimen used in the modified Obert-Hoek Cell are machined to a smooth finish. The contact surface between the sealing rubber membrane and the loading platens can be subjected to frictional forces during the application of axial stresses in the presence of large radial stresses.

In order to obtain a preliminary estimate of the frictional axial forces from the loading platen, a set of tests were conducted using only a stainless steel cylinder (85mm in diameter and 445mm in height). In such a configuration the surface on which the friction was applied was the entire surface on the inside of the membrane (area = 85 mm x π x 215 mm = 0.057m^2), whereas in the real experimental setup only the upper and lower platens would have an initial contact surface area of around = 0.012m^2. Hence, these experimental results would represent the upper bound of friction that can be developed by the loading platens.

The stainless steel cylinder used in the experiment to estimate the friction occupied the entire length of the loading platens and the test specimen. The cylinder was not in contact with the bottom loading pedestal of the MTS™ rock frame, a gap of 25 mm was provided at the bottom in order to accommodate for the necessary displacement to generate the friction (see Figure 4.7a). Based on the triaxial tests results on the Indiana and Cobourg Limestones the greatest displacement during failure occurred at around 4 mm (at 60 MPa of radial stress applied to Cobourg Limestone), therefore friction test cycles were limited to end after 4 mm of axial loading piston displacement. The original triaxial tests on Cobourg Limestone used only the MTS™ load cell (capacity 4665 kN) and a confining pressure between 5 and 60 MPa, hence the friction tests were performed in an identical manner. However, due to the very small loads needed to achieve the desired displacement of 4 mm and the intrinsic resistance to movement of the O-ring seals in the axial loading piston of the MTS rock frame, the frictions tests were done using a more accurate 67 kN external load cell (see Figure 4.7b).

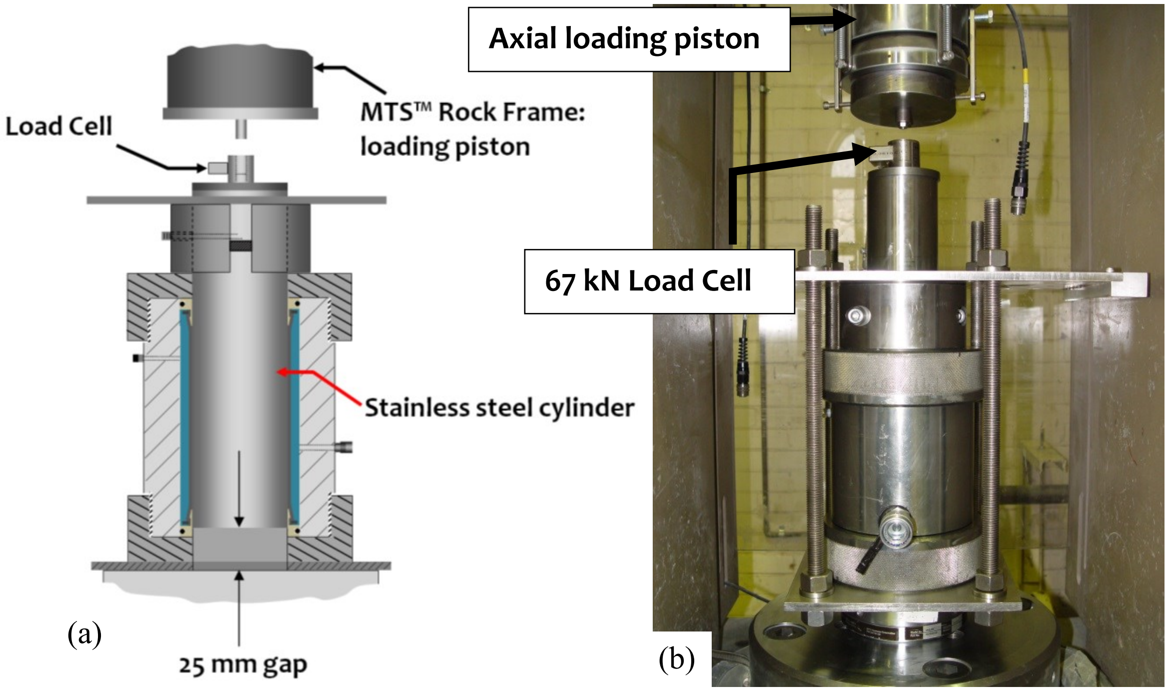

Figure 4.7: (a) Schematic view of the setup to test the friction with the stainless steel cylinder; (b) Setup in the MTS™ rock frame test system with the 67 kN load cell.

The results show that for a confining stress of 60 MPa the load necessary to overcome the friction would be at most 24 kN**,** if the displacements were around 4-5mm. This friction resistive load represents a very small portion of the total failure load for Cobourg Limestones (24kN/1900kN=1.2%) when sample are tested in the failure range.

Additionally, three tests were performed at 3 different radial stresses (5, 20 and 40 MPa) to establish the frictional axial force that could develop during testing of the Cobourg Limestone in the modified Obert-Hoek Cell. A sample of Cobourg Limestone of dimensions 85.1 mm diameter and 300 mm length was placed in the modified Obert-Hoek Cell without the upper and lower loading platens. The length of the sample allowed it to protrude from the top of the Obert-Hoek Cell, establish contact with the entire surface of the pressurizing membrane and had a clearance of 15 mm between the base of the sample and the lower loading platen of the MTS rock frame (see Figure 4.8).

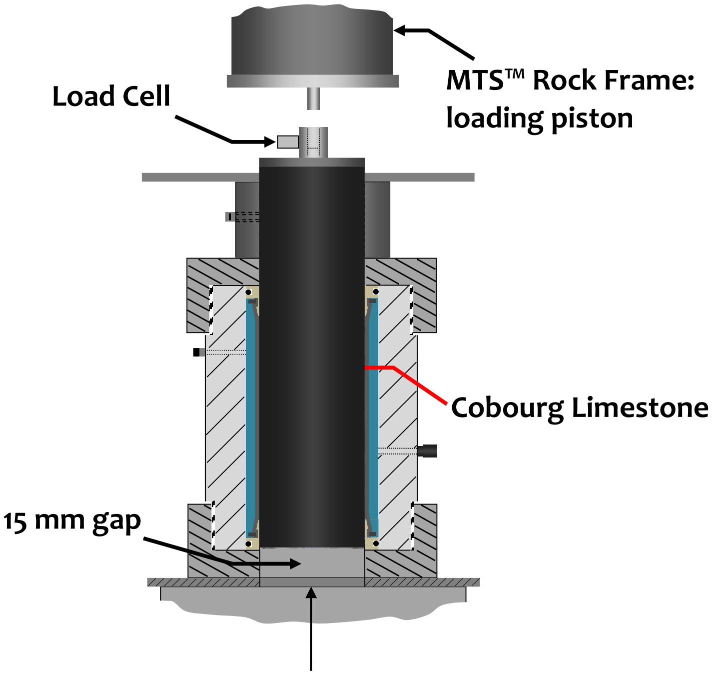

Figure 4.8: Cutaway view of modified Obert-Hoek Cell in the MTS™ rock frame test system with the 300 mm long Cobourg Limestone.

During installation and positioning of the modified Obert-Hoek Cell in the MTS rock frame for estimating friction losses the sample was held in position by a nominal radial stress of 300 kPa. The 15 mm clearance at the base of the sample allowed it to be displaced in the downward direction without any obstruction. This procedure allowed the measurement of axial contact load generated between the external cylindrical surface of the Cobourg Limestone sample and the rubber membrane at a given radial stress. The loading rate for all tests was set at 0.2 mm/min, which corresponded to the same loading rate that was used when testing Coburg Limestone samples were tested to failure. It was observed that a true Coulomb-frictional non-linear elastic type sliding did not occur as the axial load was increased; instead it was more of a non-linear elastic deformation of the membrane. When the applied axial load was reduced to zero the sample returned back to its original position. The same behavior was assumed applicable to the Indiana Limestone, which due to its high porosity, would have had a higher friction coefficient and adhered more to the membrane.

Furthermore, the results from these tests indicate that around 10 kN of the applied axial load, at 4 mm displacement of the MTS™ loading piston, is due to the intrinsic resistance to movement of the O-ring seals in loading piston of the MTS™ rock frame (see Figure 4.9). This additional load was determined with the use of an external 67 kN load cell. Hence, the combined results obtained from these tests show that at a confining stress of 30 MPa it can be expected that 3 % of the applied failure load is a result of “friction losses". Taking into consideration the magnitude of loads applied to cause failure in the rock, the overestimation of the contact area between the platen and the membrane as well as the variability of the compressive resistance of the Cobourg Limestone, it can be concluded that these friction losses can be assumed as negligible. Furthermore, all permeability tests performed using the modified Obert-Hoek Cell were limited to confining stresses of 30 MPa. A relationship was developed to account for the frictional losses when using the modified Obert-Hoek Cell and the MTS rock frame (see Figure 4.10).

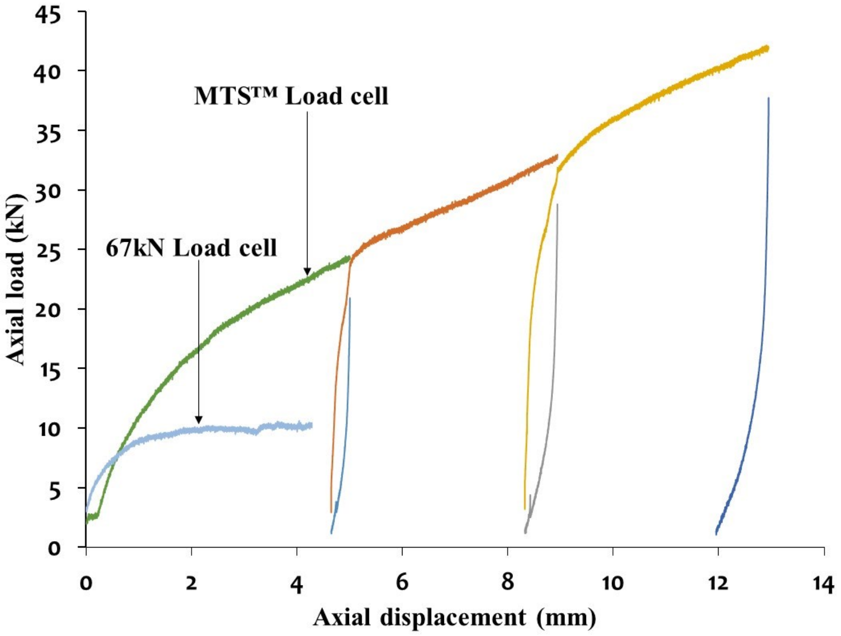

Figure 4.9: Axial load vs axial displacement in the MTS rock frame at 60 MPa radial stress; in order to move the stainless steel cylinder inside the modified Obert-Hoek cell by 4 mm the MTS™ load cell overestimates the axial load by 10 kN.

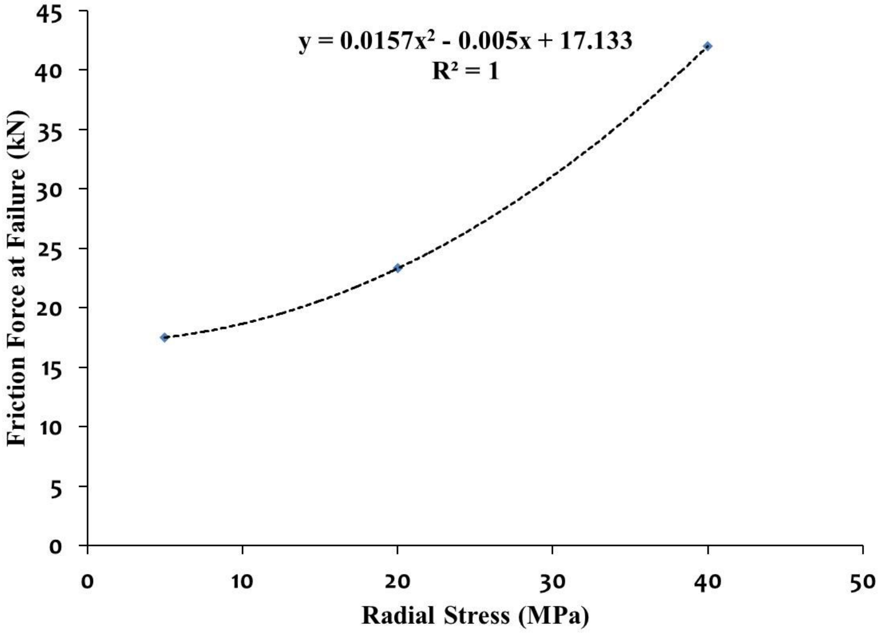

Figure 4.10: Force applied to overcome friction vs radial stress.

In order to minimize the influence of the friction force between the loading platens and the rubber membrane, the cylindrical surfaces of the loading platens were lubricated with crystalline silica powder (White lubricant by Panef™).

4.3 High Capacity Load Controlled Testing Facility

The testing facility used to perform the tests using the modified Obert-Hoek Cell was the High Capacity Load Controlled (HCLC) testing machine located in the EGL. The controlled radial stress was applied to the sample using the GDS Controller. The application of the axial loads required modifications that would allow the gross control of filling the 4448 kN hydraulic jack (see Figure 4.11), using the electric hydraulic pump and the fine control of loading was achieved using a second GDS Controller (see Figure 4.3). The electric hydraulic pump was used to lower the hydraulic jack and load cell such that it made contact with the upper loading platen of the modified Obert-Hoek Cell. In this function, GDS Controller 1 was used to maintain a specified axial stress compensating for temperature fluctuations during the permeability testing. The manual hydraulic pump was used to increase/decrease either the axial or radial stress. All components for the hydraulics are pressure-rated for 69 MPa. In such an arrangement the axial load was maintained within ±3 kN of the specified load.

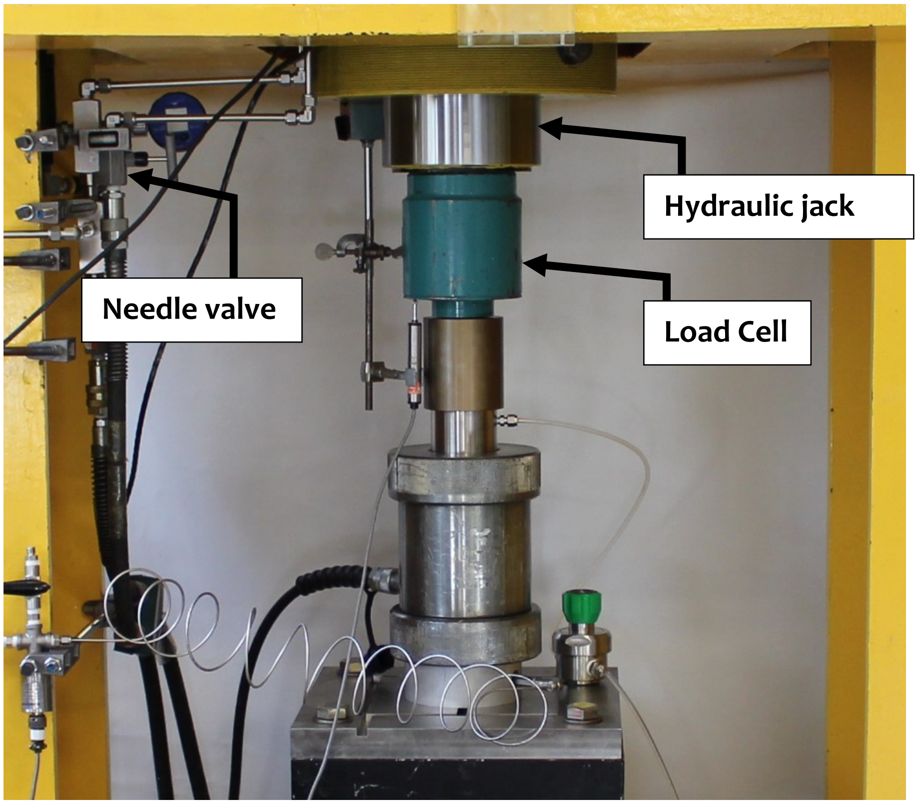

Figure 4.11: The High Capacity Load Controlled (HCLC) testing machine with the modified Obert-Hoek Cell.

The hydraulic hoses used in previous research (Selvadurai *et al*., 2005; Selvadurai *et al*., 2011) were reduced by replacing the fluid supply lines with stainless steel tubing (316L, Swagelok™: rated for 27 MPa). This achieved a better control of the applied stresses. It was necessary since the expansion of the hydraulic hoses during loading could not be compensated for by using the GDS Controller and the hydraulic hoses were prone to leakage. The solution was to separate the hydraulic hoses from the GDS™ Controller with the use of high pressure ball valves (Swagelok™, SS-H83PF4, rated 69 MPa) and needle valves (Enerpac™ V-82, rated 69 MPa) (see Appendix B for details: Figures 6 and 9). In so doing the electric hydraulic pump and the manual hydraulic pump were used only to prime the pressurizing fluids in the HCLC and the fine control of the stresses was provided through by the two GDS™ Controllers. Once the permeability testing at a specific stress state was complete, the hydraulic pumps were reconnected to the system and used to either increase or decrease the applied stresses.

A full operations manual with comprehensive explanations of the functionalities of the axial loading frame is given in the Appendix B.

4.4 Vacuum Saturation

The Indiana Limestone and Cobourg Limestone samples that were used in the research were in an air dried condition (1 year, at room temperature). Prior to vacuum saturation, the samples were measured and weighed using a digital scale accurate up to ± 0.01 g. The samples were saturated in a stainless steel container filled with distilled water (see Figure 4.12). The water level and sample submersion depth was systematically controlled in order to allow the air bubbles to escape from the porous matrix. The vacuum pressure was produced by a venturi pump (Vaccon™ JS-200-AA6) which was activated by a constant supply of compressed air. Once connected to the air supply it could achieve vacuum pressures between -80 kPa to -90 kPa. The sample mass was determined at specific time intervals (typically every 24 hours), and once the sample showed no increase in its mass (i.e. less than 0.01% variation between measurements) then the rock was considered to be saturated. In such setup, samples (diameter: 49 mm length: 122 mm) of Indiana Limestone took 70 hrs to saturate (see Figure 4.13). When a sample was removed from the vacuum container for weighing, its surfaces were dried using a cloth and weighed within the first 1.5 min in order to keep the procedure constant. This procedure cannot guarantee that the sample was 100% saturated and/or that all the occluding air bubbles in the flow channels have been successfully removed. Brace *et al*. (1968) noted that it is probably not possible to completely saturate the sample with water and that small differences in the degree of saturation might contribute to the variability in the estimation of permeability during testing.

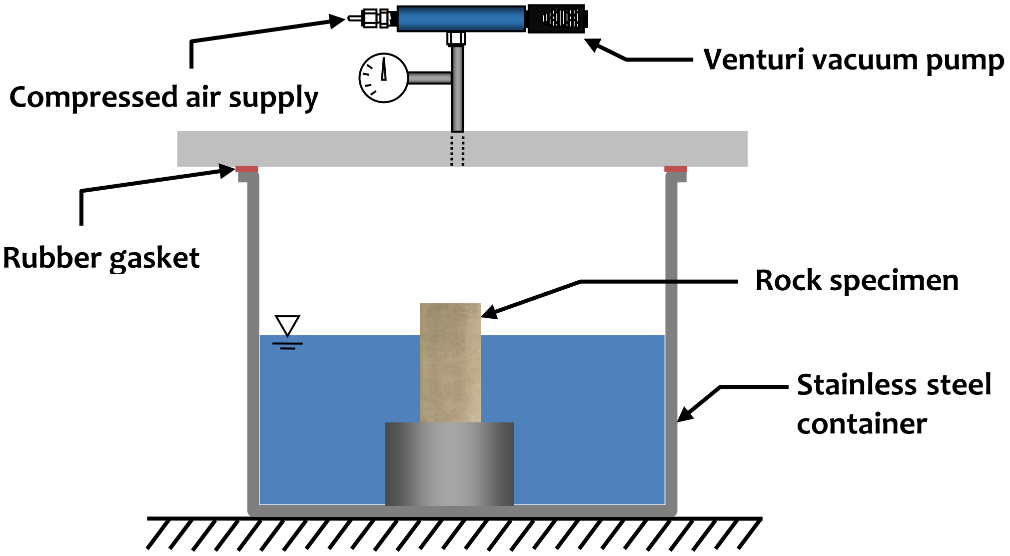

Figure 4.12: Schematic view of the vacuum saturation setup.

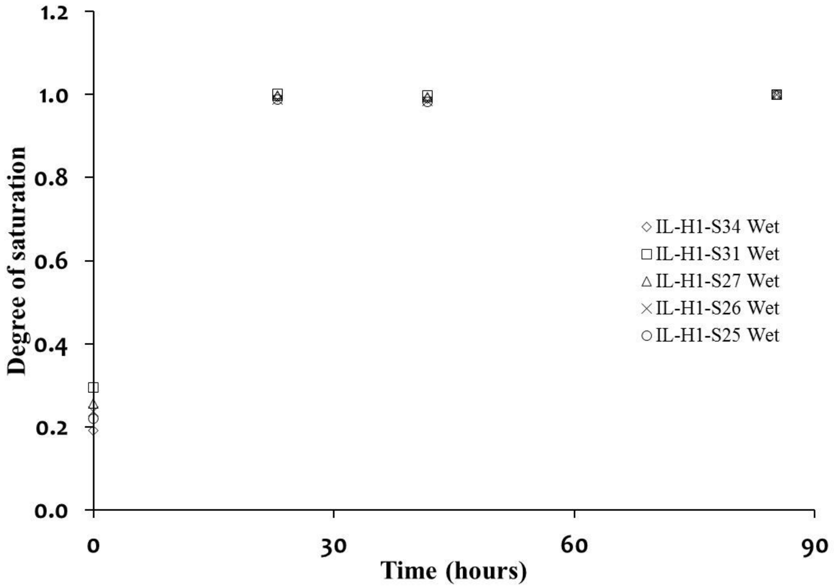

Figure 4.13: Degree of saturation vs number of hours that five Indiana Limestone samples were subject to vacuum saturation.

The vacuum saturation method was also utilized for the unstressed permeability tests involving the capped and cylindrical surface epoxied samples (see Chapter 5). For those tests, however, with the acrylic pucks and epoxy coatings, the vacuum saturation was done using a venturi pump and by submerging the prepared sample in a beaker (see Figure 4.14). The saturation was terminated when the water absorption, measured by periodic weighing, stabilized to within an incremental change of 1% between subsequent weighings.

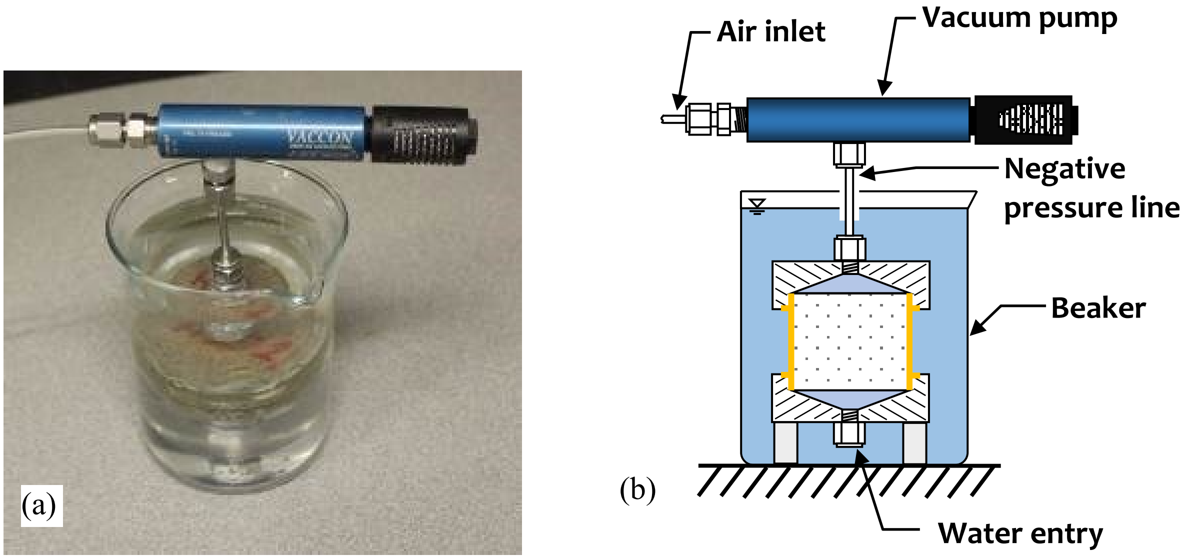

Figure 4.14: (a) The saturation arrangement, where the sample is subjected to negative pressure (-81 kPa) at the top using a venturi vacuum pump, (b) typical cross-section of the sample submerged in water.

4.5 De-aired Water System

A constant supply of de-aired water was needed for the experimental work performed in connection with this research. In order to have a continuous supply of de-aired water, two systems were available: helium de-airing system and Jasco™ degassing system (DG-2080-54). The use of de-aired water during permeability testing of porous media is known and used by researchers (Keaney *et al*., 1998; Selvadurai *et al*., 2005).

The helium de-airing system consisted of a water tank, helium gas tank, water diffuser and tubing. The helium (99.99% pure) was supplied at a flow rate of 10 mL/min from a pressurized gas tank at 250kPa and room temperature. This helium was diffused into the water tank with a diffuser, for at least 30 min prior to the commencement of the test in order to bring the Dissolved Oxygen Content (D.O.C.) from 8ppm to 2 ppm in a 10 liter water tank (see Figure 4.15). This produced an air deprived water which can be used to flush out pockets of air and remove them from the pressurizing system (tubing, pump head, fittings, etc.) and in the flow paths within the sample (Donaghe and Chaney, 1988). The (D.O.C.) of 2-3 ppm was verified with a dissolved oxygen probe (YSI 5000 and YSI 5010 BOD Probe). This procedure produced flow with a low air content water, which was then connected to the pump and used as the permeating water in the experiments. The helium de-airing system used in the experiments was an adaptation of the helium gas purging technique suggested by the Shimadzu Corporation (1991).

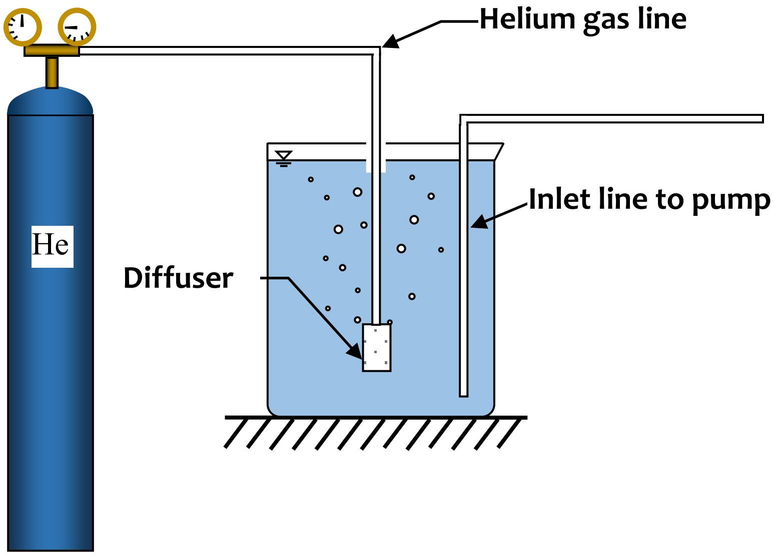

Figure 4.15: Schematic view of the helium degassing setup

In the second approach a Jasco™ degassing system was placed in series upstream of a pump. The degasser removes gaseous components such as O_2, N_2, and CO_2 from a fluid by passing this fluid through a special fluoropolymer hydrophobic membrane tube (which is porous to gas) with the pressure outside the tube kept at a lower value (Wikol *et al.*, 2007). This method is highly efficient and allows results to be similar to that of degassing by the helium de-airing method. Verification of the degasser with a dissolved oxygen probe showed that at a flow rates equal or less than 1 ml/min the unit was capable of maintaining a (D.O.C.) at 2 to 3 ppm.

4.5.1 Air bubbles in water

Special attention was given to water used in the experiments, in order to avoid any air bubble formation, which could affect the pump performance and the interpretation of permeability results; this is especially a concern for long duration tests (Fredlund, 1976). When air bubbles flow into the pump head where they can contract and expand with the plunger movement, they are effectively creating an erroneous volume of water being delivered to the sample (Shimadzu Corporation, 1991: Dolan, 1999). Hence, unless otherwise specified, the water used in experiments was distilled and de-aired before it entered the pump. Preliminary testing showed that using the de-aired water resulted in a steady signal in the measured inlet water pressures. Furthermore, to help control air bubble formation and dissolution in the permeating water, the outflow pressure was maintained above the atmospheric pressure at 100 kPa by using a backpressure regulator (Lee and Black 1972; Makhnenko and Labuz 2013).

4.6 Water Used in the Permeability Experiments

Unless otherwise specified in the test procedure distilled water was used in the experimental research,. The distilled water was made by a glass still (Lab Strong™: Fistreem III) and filter (Barnstead™: B-pure) obtained from the Environmental Laboratories, Department of Civil Engineering and Applied Mechanics, McGill University. During the experiments, the water supply was maintained at room temperature. However fluctuation of temperature did occur during prolonged tests and in such cases the permeabilities were estimated by using the respective dynamic viscosities of water. The pH of the water was 6.8 and was measured using an Oakton™ Waterproof Big Display pH Spear.

CHAPTER 5

THE EFFECT OF SATURATION AND FLOW REVERSAL ON PERMEABILITY ESTIMATION

5.0 Introduction

For Darcy's Law to be applicable in estimating the permeability of a porous medium, it is essential that the entire interconnected pore space should be fully saturated and that the flow velocities at the pore scale should be within the limits that ensure laminar flow (i.e. should satisfy a criterion based on the Reynolds Number, $\mathrm{Re} = \rho_f v d / \mu$, where ρ_f is the fluid density, v is the superficial flow velocity, d is the characteristic length of either the mean pore throat size or the mean grain size). With certain low permeability materials such as granite (Selvadurai *et al*. 2005; Selvadurai and Najari 2013 and 2015) and argillaceous limestones such as the Cobourg Limestone (Selvadurai *et al*. 2011; Selvadurai and Jenner, 2013, Selvadurai and Najari, 2016), the pore space needs to be saturated either through by prolonged application of a vacuum or flow through the specimen achieved with back-pressure control (Black and Lee 1973). When testing materials such as Indiana Limestone with high porosity the pore space can be saturated quite easily by vacuum saturation (Suri *et al*. 1997; Selvadurai and Głowacki 2008). Typically saturation is terminated when the saturated weight of the sample under vacuum stabilizes to within a change of less than 0.1%/day. However, there is limited information dealing with unsaturated intact rock permeability testing, although the results are important in the case of aquifers, dealing with water movement between ground surface and water table (Lewis *et al.*, 2006) as well as water movement through unsaturated weathered soft rock underneath a dam foundation (Shimoyama *et al.* 2012). In the development of the “Hot Dry Rock” concept (Hettkamp *et al.* 2004) permeability tests have been performed without prior saturation of the rock and, under these circumstances, occluded air pockets can influence the flow process, which can lead to erroneous interpretations of the permeability. Caputo *et al.* (2010) developed an infiltrometer (i.e. a large circular ring installed on the surface of the rock and filled with water) to measure the field-saturated hydraulic conductivity of outcrop rock (limestone) using the Green–Ampt method of infiltration estimation; although the surface of outcrop rock was initially dry. The influence of the degree of saturation on the development of steady pressures in one-dimensional flow in samples of Indiana Limestone was given by Selvadurai (2009) and Selvadurai and Selvadurai (2010). The manner in which occluded pockets of air in the rock can influence the estimation of permeability can also be governed by the length of the flow path and factors such as the viscosity of the water and temperature. A study of the influence of saturation, debris blockage of pore space, water composition and flow reversal on the development of stabilized inlet pressures is discussed in this chapter. The results of one-dimensional steady state flow experiments conducted on unstressed, initially dry and initially saturated samples of Indiana Limestone, Stanstead Granite and Rudna Sandstone, will be discussed. The experimental results obtained in this chapter were useful for the understanding and development of permeability testing procedures for rocks, described in subsequent chapters. Using the experimental results a relationship was developed to estimate the stable inlet pressure that would develop during steady state flow tests when dealing with initially unsaturated porous medium.

5.1 Samples and Preparation

The samples of rock (Indiana Limestone, Stanstead Granite and Rudna Sandstone) used in the experiments were recovered from block samples using a diamond core bit and cut to the required length using a circular diamond saw. Unless otherwise specified, for a particular sample, all the surfaces of the samples were cleaned with tap water using a stainless steel brush to remove coring and machining debris. Samples were air dried for 24hrs after tap water cleaning and before the application of the epoxy layers (Bondo™ Fibreglass Resin). Typically 3 layers of epoxy were applied to the cylindrical surface of the sample and each layer was allowed to dry for 24 hrs. The top and bottom acrylic caps were then glued to the ends of the sample (see Figure 5.1). The samples used in these tests measured 50 mm and 85 mm in diameter and 20 mm up to 170 mm in length. Microscopic analysis of thin sections of the interface between the rock and the epoxy indicated that the penetration of epoxy into the porous surface on Indiana Limestone varied between 0.30 mm to 0.76 mm (Luu, 2009). The details on the physical and mechanical properties of Indiana Limestone used in this segment of the research were discussed in Chapter 2. The Stanstead Granite used in this phase of the research is a medium to coarse-grained rock, typically found in the Beebe region of the Eastern Townships in Québec, Canada. The main minerals are: clear sharply defined quartz; feldspar laths, which are semi-transparent to milky white; muscovite flakes, in small amounts; sharply contrasting biotite in flakes and clusters and some chlorite flakes (Najari, 2013). The Rudna Sandstone samples come from Rudna copper mine in Poland (Cieślik, 2015). The XRD chemical analysis on the Rudna Sandstone revealed that it is primarily composed of quartz, dolomite and microcline. Summary of relevant physical and chemical properties of the rocks are provided in Table 5.1 and 5.2. The exact in-situ depth and location of all samples used in this research is unknown; therefore the in-situ stress state is also unknown. It can be assumed that all rocks would have been subjected to disturbance by extraction, transportation, handling and sample preparation.

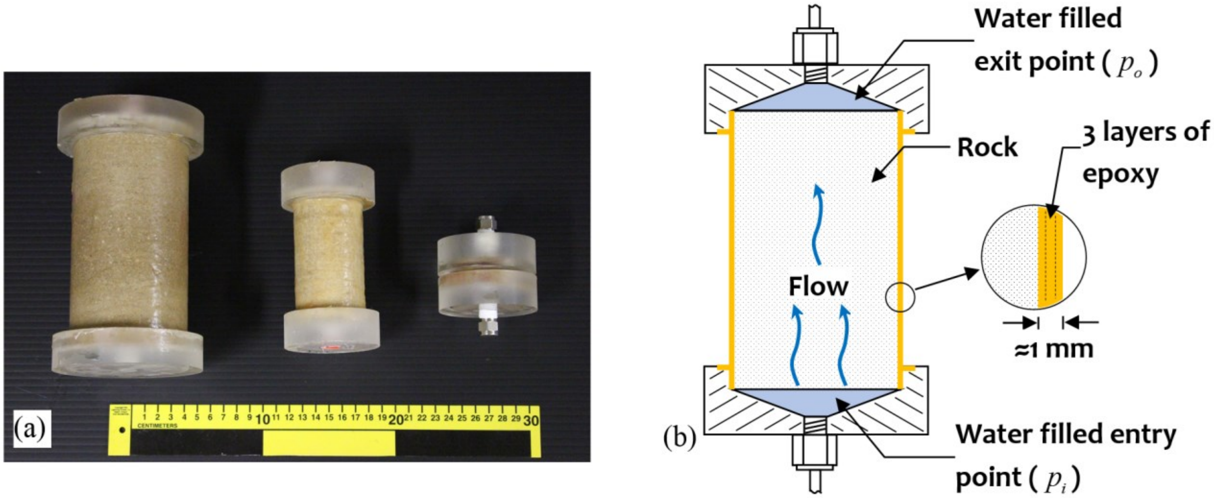

Figure 5.1: (a) Indiana Limestone samples epoxy coated and capped with acrylic caps; (b) typical cross-section of the caps, tapered to channel the water as well as to accommodate an NPT-threaded opening for connections.

Table 5.1: Physical and mechanical properties of tested rocks.

	Stanstead Granite	**Rudna Sandstone**	**Indiana Limestone**	**Units**
Porosity	0.002	0.023	0.161	-
Density	2607	2322	2210	kg/m^3
Tensile strenght	8.4[a]	6.0[b]	3.7	MPa
Permeablity	3.5E-18[a]	2.3E-17[c]	3.7E-14[d]	m^2

(a)Najari 2013; (b)Sheorey, 1997; Nad *et al.*, 2012; (c)Couture, 2016; (d)Mattar and Selvadurai, 2009; Selvadurai and Selvadurai, 2010

Table 5.2: Chemical properties of tested rocks.

Rudna Sandstone			**Indiana Limestone**			**Stanstead Granite****		
	Units			**Units**			**Units**	
	wt%*	**ppm**		**wt%***	**ppm**		**wt%***	**ppm**
SiO_2	76.650		SiO_2	0.553		SiO_2	69.500	
Al_2O_3	6.060		TiO_2	0.015		TiO_2	0.364	
Fe_2O_3	0.910		Al_2O_3	0.173		Al_2O_3	15.480	
CuO	0.87		Fe_2O_3	0.123		Fe_2O_3	2.829	
MgO	0.590		MnO	0.007		MnO	0.0386	
CaO	7.830		MgO	0.450		MgO	1.350	
Cl	0.110		CaO	54.087		CaO	2.740	
K_2O	1.820		Na_2O	0.013		Na_2O	4.339	
WO_3	0.210		K_2O	0.010		K_2O	2.690	
Ti		714	P_2O_5	0.013		P_2O_5	0.139	
Ba		639	BaO		-	BaO	-	884
Ce		170	Ce		-	Ce	-	15
Co		173	Co		-	Cr_2O_3	-	88.0
Cr		118.0	Cr_2O_3		23.0	Cu	-	2.0
Na		563.0	Cu		24.0	Ni	-	17
P		225	Ni		-	V	-	45.0
Mn		999	Sc		-	Zn	-	45.0
Yb		346.0	V		10.1	LOI	0.750	
NiO		240.0	Zn		23.0			
LOI	4.950		LOI	44.217				

* Expressed as weight percentage

** Results from Najari (2013)

Samples in their assembled condition (i.e. with the acrylic pucks and epoxy coating) were vacuum saturated using a venturi pump (see Section 4.4). The saturation was terminated when the water absorption, measured by periodic weighing, stabilized to within an incremental change of 1% between subsequent weighings.

5.2 Experimental Setup and Procedure

A prepared sample, in either a saturated or dry condition, was connected to the out-flow line from the pump (Jasco™; PU-2085 Semi-micro HPLC Pump) using Swagelok™ fittings. The inflow pressure was monitored via a pressure transducer (Honeywell™; TJE 300PSI) and the temperature was measured with a type-K thermocouple, which were installed on a pipe cross just before the sample (see Figure 5.2). The data was collected via a data acquisition system (InstruNet™ or Dataforth™) and stored on a computer (Dell™). The flow rate was adjusted according to the rock type in order to avoid delamination of the epoxy coating due to the development of high inlet pressures. The mass of the outflow of water was measured periodically in order to ensure that steady state conditions were applicable and that no leakage occurred. Unless otherwise specified, the samples were tested with distilled and de-aired/degassed water with a D.O. content at 2-3 ppm. Distilled and de-aired water is, however, not a commonly and naturally occurring fluid (for typical groundwater compositions see Abdelouas *et al.*, 1998; Malard and Hervant, 1999; Sykes, 2003) and the results of experiments that use such a fluid have to be treated with caution. Typically, a flow rate of 0.5 ml/min was applied to the 85 mm diameter samples while a flow rate of 0.1 ml/min to 0.01 ml/min was applied to the 50 mm diameter samples.

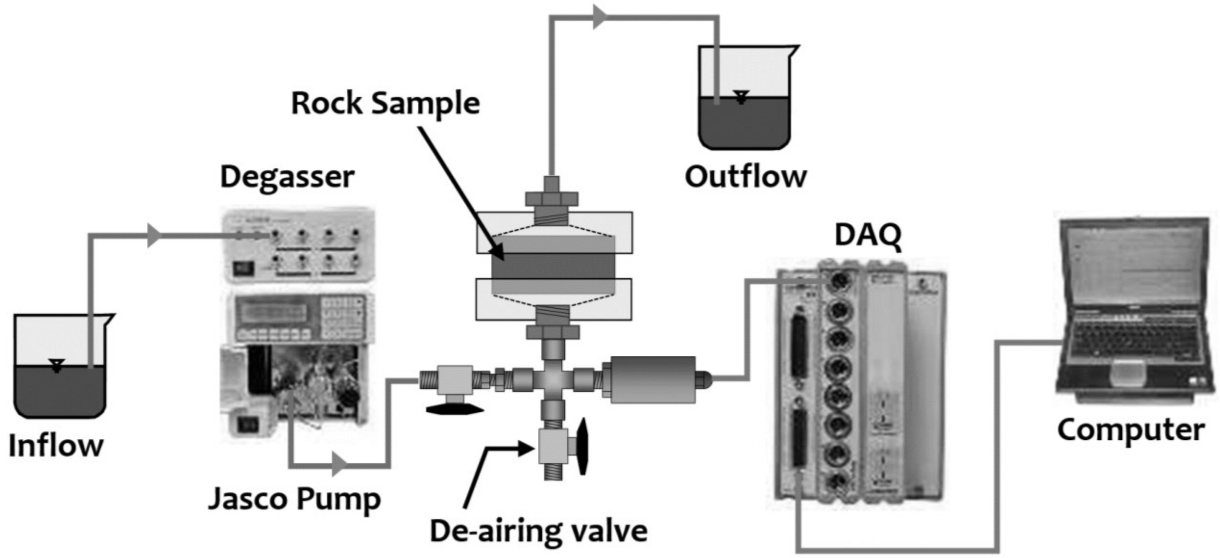

Figure 5.2: Schematic view of the experimental arrangement.

The accuracy of delivery of the flow rate by the pump used in the permeability tests was verified by independent testing of the flow measurement over long durations (i.e. 24hrs). The ambient air temperature in the laboratory can influence the viscosity of the permeating fluid; the laboratory tests were conducted at a room temperature of 23°C ±2°C. In this temperature range, the dynamic viscosity of the water can vary between $8.9\text{E}-4\text{Pa}\cdot\text{sec}$ to $9.8\text{E}-4\text{Pa}\cdot\text{sec}$, which was accounted in the permeability calculations.

The equation (3.12) was used to determine the permeability from experimental data.

5.2.1 Epoxy testing

The pressure required to either delaminate or puncture the epoxy layer was established by testing several samples of different rock types and different sizes, and running a step by step increase in pressure until a break through pressure loss was recorded and/or leakage observed. In general, the inflow pressure required to detach the 3-layers of epoxy coating was 600 kPa. Hence, the pressure of the inflow during the permeability testing was maintained at 50% of the epoxy delamination/puncture pressure. Furthermore, the inlet fluid pressures were adjusted to below 10% of the tensile strength of the rock in order to avoid the creation of micro-fissures or damage to the samples.

5.2.2 Chemically altered water for Indiana Limestone

The high calcium carbonate content implies that the Indiana Limestone is susceptible to dissolution during migration of chemically altered water. As an organic rock, limestones are known to exhibit very unpredictable results during permeability testing because they are dissolvable with flowing water, as argued by Bulnes and Fitting (1945). For example, laboratory wormhole development in Oxfordian crinoïdal limestone sample during flow of CO_2 acidized water is documented by Noiriel *et al*. (2004). Other manifestations of limestone dissolution are documented in the study of Karst formations (Hasenmueller *et al*. 2003, Dreybrodt, 1988). In this research permeability measurements were conducted using the distilled water as well as chemically altered water. This investigation also served as a preliminary verification of experimental concept for the testing of Indiana Limestone permeability evolution during application of triaxial stress states (see Chapter 7). A solution was prepared by combining disodium phosphate $\left(Na_2HPO_4\right)$ at 14 ppm, calcium carbonate $\left(CaCO_3\right)$ at 47 ppm (maximum solubility in water at normal atmospheric CO_2 partial pressure) with distilled water. Phosphate in concentrations ranging between 1.4 to 142 ppm has been shown to inhibit the dissolution rates of calcium carbonate (Svensson and Dreybrodt, 1992; Zhang and Spiers, 2005). Whereas the presence of calcium carbonate in the permeating water was to ensure a more representative groundwater found in the limestone formation (IDNR, 2016), hence more neutral to the porous matrix of the Indiana Limestone.

5.3 Results

5.3.1 Results of experiments on initially dry samples

A summary of permeabilities estimated from experiments conducted on Indiana Limestone air-dried samples (with relative humidity of 70%, obtained from Weather Canada: Montreal) are shown in Figure 5.3. In general, it was observed that, irrespective of the rock type (Indiana Limestone, Rudna Sandstone and Stanstead Granite), that the initially air-dry samples of all types of rock displayed an inlet water pressure that rose to a specific value followed by a decay and finally the attainment of a steady pressure (see Figures 5.4, 5.5, 5.6, 5.7, 5.9 and 5.11). For these dry samples, it is particularly important to ascertain whether the pressure gradient has stabilized, otherwise the result will lead to an erroneous interpretation of permeability, due to partial saturation of the sample (see Figure 5.3 and Figure 5.4 insert). If the "pseudo-stable" pressure of 90 kPa, Figure 5.4, is used to calculate the permeability instead of the plateau pressure (13 kPa), the error would be around 86%. Figure 5.3 shows the permeability for the dry samples which appears to be stable between 12 and 48 hours with the outflow of water being stable. However, this is misleading and can give erroneous permeability results, in part because: the flow paths of the sample were not fully saturated and due to the occlusion by air bubbles and particulates of flow paths which were not yet flushed out. Similarly, in Selvadurai *et al.* (2005), during steady state radial flow experiments of Barre granite using cylindrical hollow samples a gradual increase in pressure with time was noted. Whereas, steady state pressure experiments performed on hollow cylinders of Cobourg limestone by Selvadurai and Jenner (2013) showed a nominal "bump" followed by the attainment of a steady pressure.

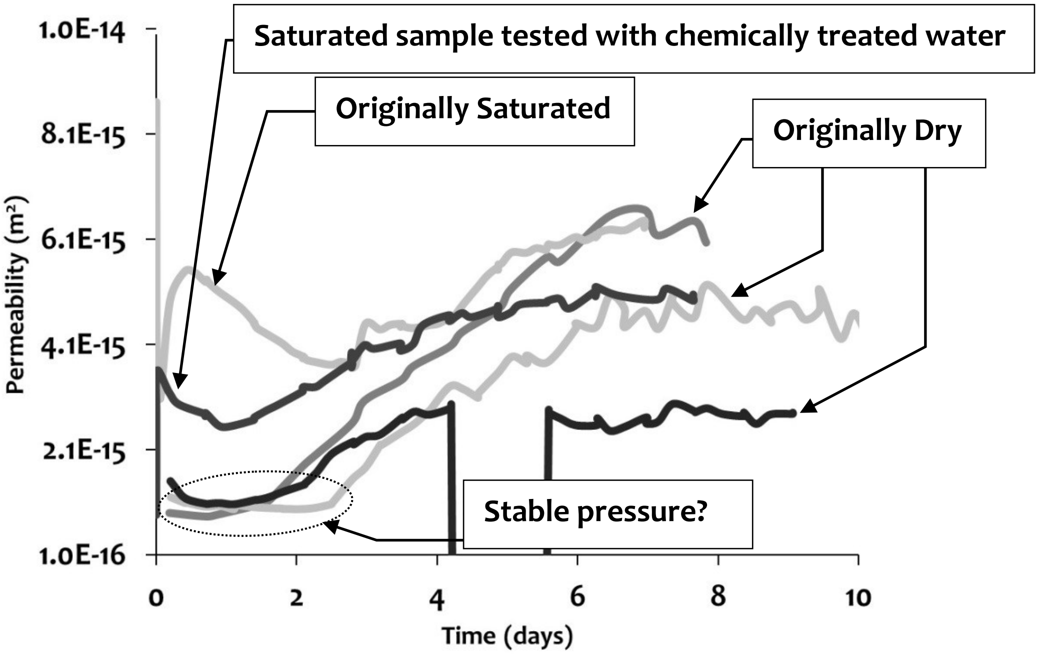

Figure 5.3: Permeability vs. time, samples of Indiana Limestone.

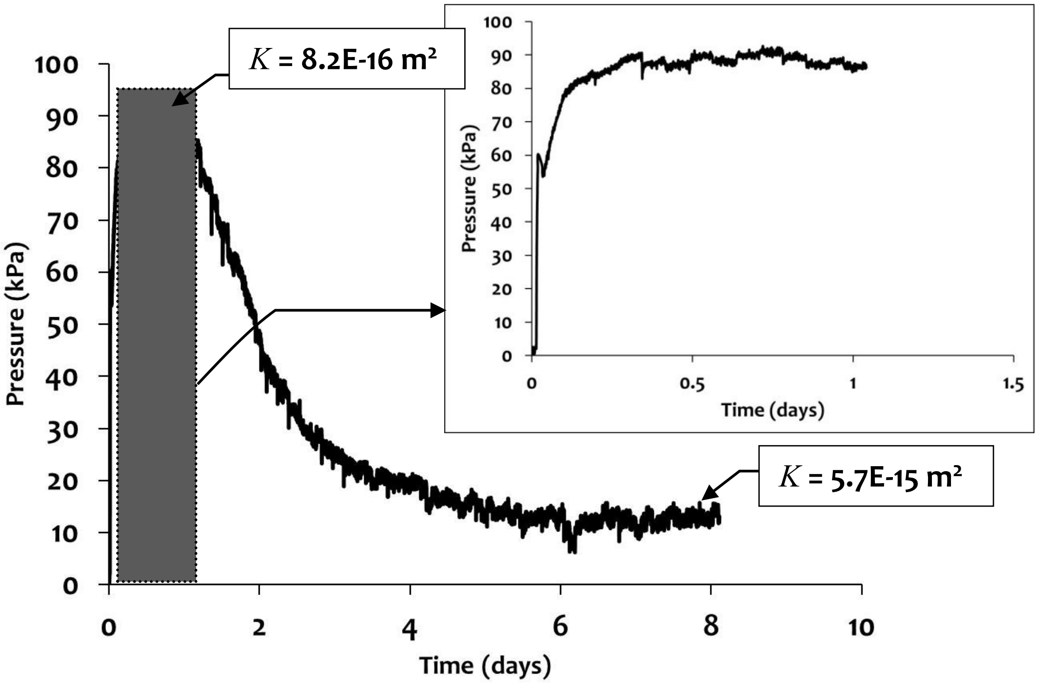

Figures 5.4: Tests on Indiana Limestone: time history of the inlet fluid pressure at the entry location [0.1ml/min flow rate, distilled and helium de-aired water, initially dry sample, ILH1SC (50.24 mm diam. 98.9 mm length)]. The insert graph shows the short-term pressure history from the highlighted grey rectangle.

5.3.2 Experiments on saturated samples

Samples that were saturated prior to permeability testing required between 2 and 4 days of continuous pumping to reach a plateau of stable pressure (see Figures 5.6, 5.8 and 5.11). In contrast, the initially dry rock samples did not reach a stable pressure plateau within the same time period, and, in some cases, it took 21 days to reach equilibrium (see Figure 5.6). Furthermore, the initial rise in the peak pressure, seen in the dry samples, was either non-existent or minimal for the saturated samples. The difficulties encountered during the saturation process for rocks and the time required to reach 100% saturation (or near 100%) is discussed in the work by Makhnenko and Labuz (2013). Some of the common procedures used by these authors include either the installation of a back pressure regulator on the outflow line to force air bubbles into solution or the use of de-aired water to trap and remove air bubbles from the sample.

5.3.3 The use of de-aired water

The inlet pressure spikes observed during steady state permeability testing are in part due to the functioning of the pump pistons as well as dissolved air bubble formation (see Figure 5.8). By employing helium purging or degassing techniques, the dissolved oxygen (D.O.) content in the permeating water drops from 8 ppm to 2 ppm and the number of pressure peaks decreases significantly (Shimadzu Corporation, 1991; Dolan, 1999). Since water can retain up to 2% per volume of dissolved air (Fredlund, 1976); the use of oxygen-deprived water during permeability testing allows the permeating water to absorb and flush out the air bubbles that maybe occluding the interconnected flow paths and promotes pore space saturation. During the experiments the air bubbles that were visible on the top surface of the acrylic cap dissolved into the de-aired water, confirming that this is an efficient method for removing air bubbles. Due to the low inflow pressures and the continuous flow of highly de-aired water (dissolved oxygen content ≈ 2 ppm), it was not necessary to install a back pressure regulator on the outflow line during the tests.

5.3.4 Results from experiments using disodium phosphate (Na_2HPO_4) and calcium carbonate ($CaCO_3$) saturated water

Phosphate is known to reduce the precipitation of calcite, thus inhibiting the build-up of intergranular pressure solution (Zhang and Spiers, 2005). Similarly, the research by Svensson and Dreybrodt (1992) showed that the presence of phosphate in a CO_2-H_2O solution inhibits the dissolution of calcite ($CaCO_3$). Hence, a solution of phosphate (14 ppm) and calcium carbonate-saturated (47 ppm) fluid was prepared to be tested on the Indiana Limestone. However, the results did not yield any conclusive evidence about the influence of the chemical composition of water on the stabilization of the inlet pressure (i.e. it did not eliminate the pressure response "spikes" nor did it significantly affect the estimated permeability of the rock (see Figures 5.3 and 5.8).

5.3.5 Results of chemical analysis of outflow

The outflow water collected during the testing of the Indiana Limestone and the Rudna Sandstone was analyzed using an ICP-OES (Atomic Absorption Spectrometer) apparatus to determine if there was dissolution of the limestone and sandstone matrix with distilled/de-aired water. The results show a concentration of elements that decays as the test progresses (see Figures 5.7 and 5.10) and generally follows the drop in fluid inlet pressure. These results confirm that the apparent dissolution had no significant impact on the estimated permeability of the rock; the results obtained being similar to those from tests conducted using either chemically treated water or untreated water.

5.3.6 Results of experiments with no flow for extended periods of time

Figure 5.5 presents data for experiments where pumping was stopped for about 36 hours, once the pressure had stabilized, in order to verify whether the attained pressures were stable and repeatable or whether any time-dependent chemical process could affect the inlet pressures. The sample was not allowed to dry out, and, once pumping resumed, the pressures stabilized quickly to the values previously recorded, confirming that such rest periods did not affect the inlet pressures and consequently the estimates of permeability.

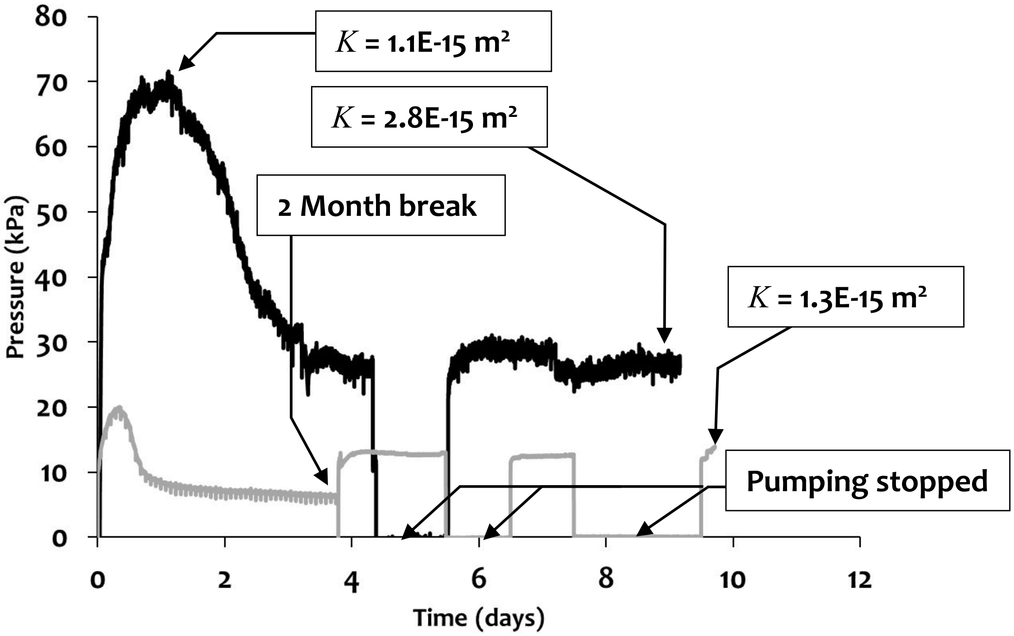

Figure 5.5: Tests on Indiana Limestone: time history of the inlet fluid pressure at the entry location [**grey curve** 0.1ml/min flow rate, sample surface was thoroughly brushed/washed to remove particulates remaining after sample preparation; is an initially dry sample subjected to venturi vacuum saturation with distilled helium de-aired water; after a two month break, a saturated sample with distilled Jasco degassed water, ILH1SP4 (49.0 mm diam. 19.9 mm length); **black curve** [0.1ml/min flow rate, distilled and helium de-aired water, initially dry sample, ILH1SA (50.2 mm diam. 98.9 mm height)].

5.3.7 Results of experiments conducted by reversing the flow direction

The effect of reversing the fluid flow direction on permeability (see Figure 5.10 and 5.12) was examined. For granite and sandstone, reversing the inflow had only a small effect on the inlet fluid pressures (see Figures 5.6 and 5.11). The observed small changes to the inlet pressure (-4% for sandstones, +12% for granites) indicate that there is some particulate movement within the flow channels even at the scale of the 20 mm long and 50 mm diameter samples. The results obtained from an Indiana Limestone sample with machining/coring debris on both entry and exit surfaces, indicate that there is evidence to support the clogging of pores, which results in discontinuities in the pressure time history, once a steady pressure was attained (see Figure 5.9). Chitty *et al.* (1994) hypothesized that the Indiana Limestone specimens used in their experiments were altered by the testing procedure; they pointed to the possibility that the pores of the intact material became clogged by particles that were either internal or external to the specimen.

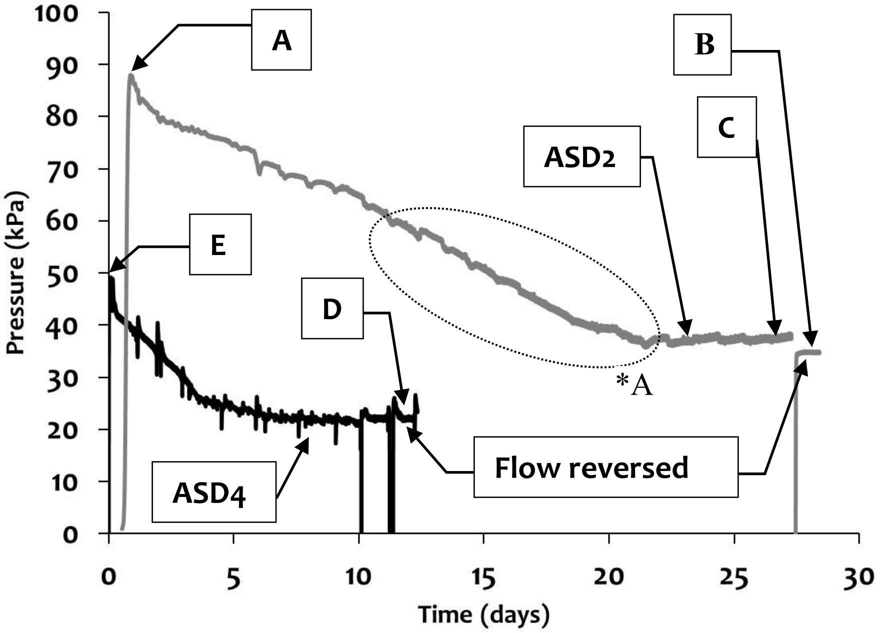

Figure 5.6: Tests on Rudna Sandstone: time history of the inlet fluid pressure at the entry location [0.01 ml/min flow rate, samples cleaned after machining by wire brushing under water, distilled /de-aired water; ASD2 sample, initially dry (51.03 mm diam. 27.15 mm length); ASD4 sample, 5 days vacuum (-81 kPa) saturated (51.1 mm diam. 18.87 mm length)]. Permeabilities at location: **A** $2.3\mathrm{E}-17\,\mathrm{m}^2$; **B** $5.8\mathrm{E}-17\,\mathrm{m}^2$; **C** $5.4\mathrm{E}-17\,\mathrm{m}^2$; **D** $6.3\mathrm{E}-17\,\mathrm{m}^2$; **E** $3.1\mathrm{E}-17\,\mathrm{m}^2$. Details of *A are shown in Figure 5.14.

5.3.8 A correlation between peak and residual steady state hydraulic gradients

An observation resulting from experiments performed in connection with this research is that the attainment of a steady hydraulic gradient necessary for the estimation of the permeability of different types of rock will be influenced by a number of factors with the initial degree of saturation exerting the greatest influence. With the initially dry samples, the inlet pressure develops a peak $\left(p_i^{\max}\right)$ and with progressive saturation reaches a stable threshold$\left(p_i^{\min}\right)$. It is inferred that $\left(p_i^{\max} - p_i^{\min}\right)$ is proportional to the length of the flow path $\left(L\right)$ (i.e. the longer the flow path the greater the differential threshold) and inversely proportional to the porosity $\left(\phi\right)$ of the rock (i.e. the lower the porosity the greater the differential threshold), which gives the following relationship:

$$\left(p_i^{\max} - p_i^{\min}\right) \propto \frac{L}{f(\phi)} \tag{5.1}$$

where $f(\phi)$ is an arbitrary function of the porosity. If we assume that each rock that was tested was an idealized porous medium and remained chemically uninfluenced by the permeating fluid; then the results obtained for the separate rocks can be regarded as being applicable to three separate porosity measures. Considering the experimental data, it can be shown that the non-dimensional pressure differential threshold Ω defined by

$$\Omega = \frac{\left(p_i^{\max} - p_i^{\min}\right)}{\gamma_w L} \tag{5.2}$$

And is related to the porosity according to the relationship

$$\Omega \simeq \frac{[illegible]}{\sqrt{\phi}} \tag{5.3}$$

This correlation is shown in Figure 5.13.

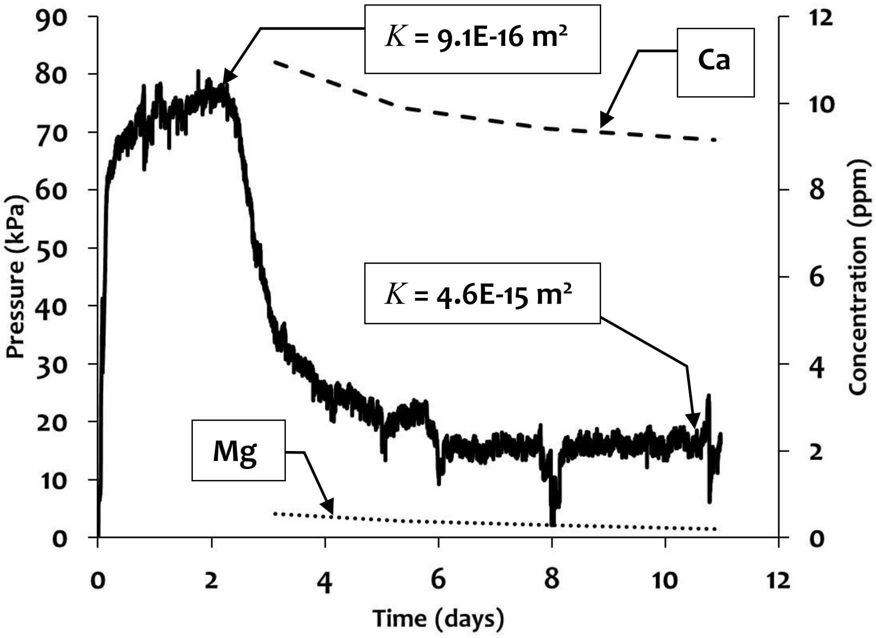

Figure 5.7: Tests on Indiana Limestone: time history of the inlet fluid pressure at the entry location vs. outflow concentration [0.1ml/min flow rate, distilled and helium de-aired water, initially dry sample, ILH1SB (50.6 mm diam. 98.8 mm length)].

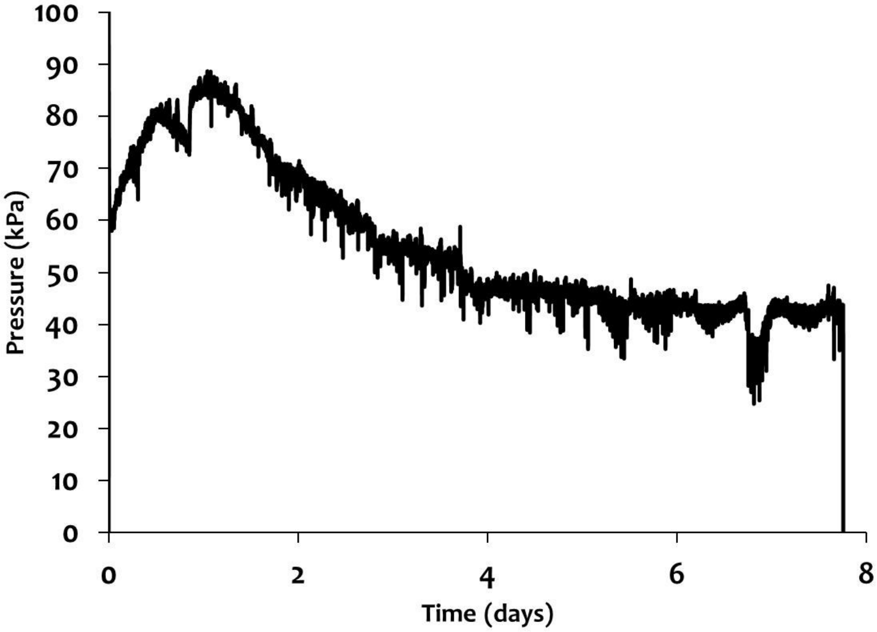

Figure 5.8: Tests on Indiana Limestone: time history of the inlet fluid pressure at the entry location [0.5ml/min flow rate, phosphorous and calcium carbonate saturated water, 1 day vacuum (-81 kPa) saturated sample, ILH2S24A (85.3 mm diam. 167.7 mm length)].

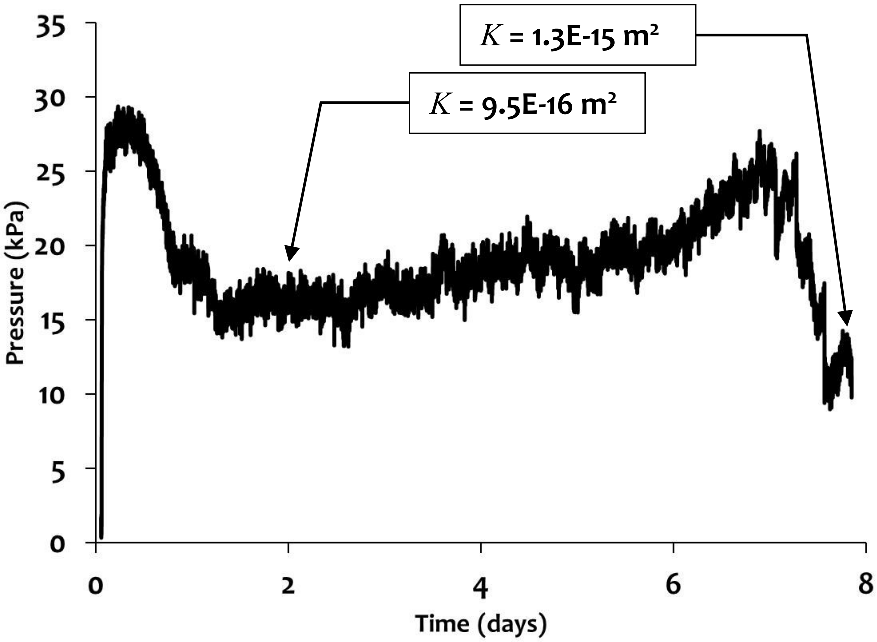

Figure 5.9: Tests on Indiana Limestone: time history of the inlet fluid pressure at the entry location [0.1ml/min flow rate, *sample was not cleaned of debris after machining*, distilled and helium de-aired water, initially dry sample, ILH1SP1 (49.0 mm diam. 20.0 mm height)].

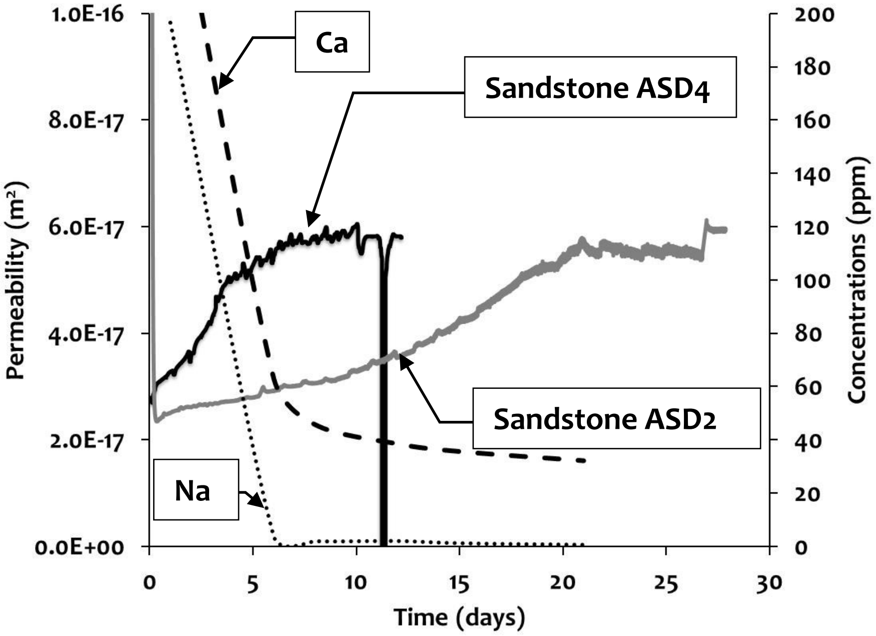

Figure 5.10: Permeability vs. time vs outflow concentration for Rudna Sandstone samples; chemical analysis of outflow for Ca and Na was done on the initially dry sample ASD2.

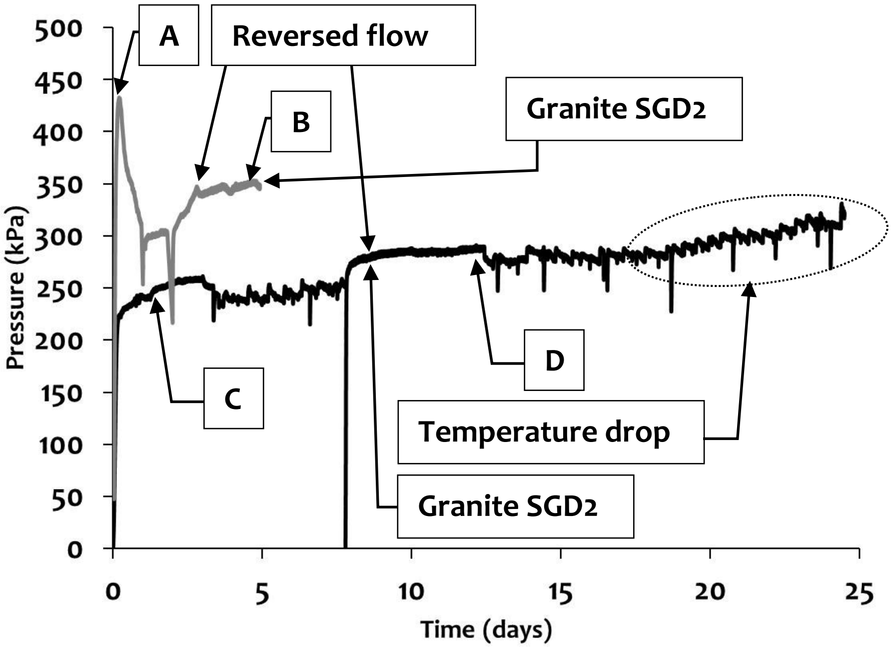

Figure 5.11: Tests on Stanstead Granite: time history of the inlet fluid pressure at the entry location [0.01 ml/min flow rate, samples were cleaned after machining by brushing under water, distilled and Jasco degassed water: SGD2 initially dry sample (50.2 mm diam. 20.04 mm length); SGD4, 7 days vacuum (-81 kPa) saturated sample (50.2 mm in diam. 18.8 mm length)]. Permeability at **A**: $3.5\mathrm{E}-18\,\mathrm{m}^2$, **B**: $4.3\mathrm{E}-18\,\mathrm{m}^2$, **C**: $5.0\mathrm{E}-18\,\mathrm{m}^2$ and **D**: $5.7\mathrm{E}-18\,\mathrm{m}^2$.

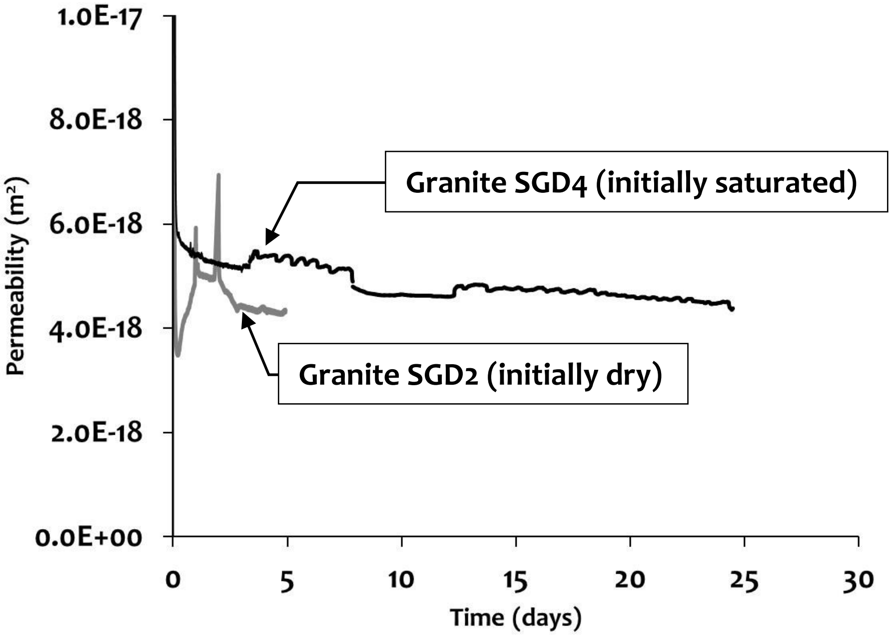

Figure 5.12: Permeability vs time, Stanstead Granite samples.

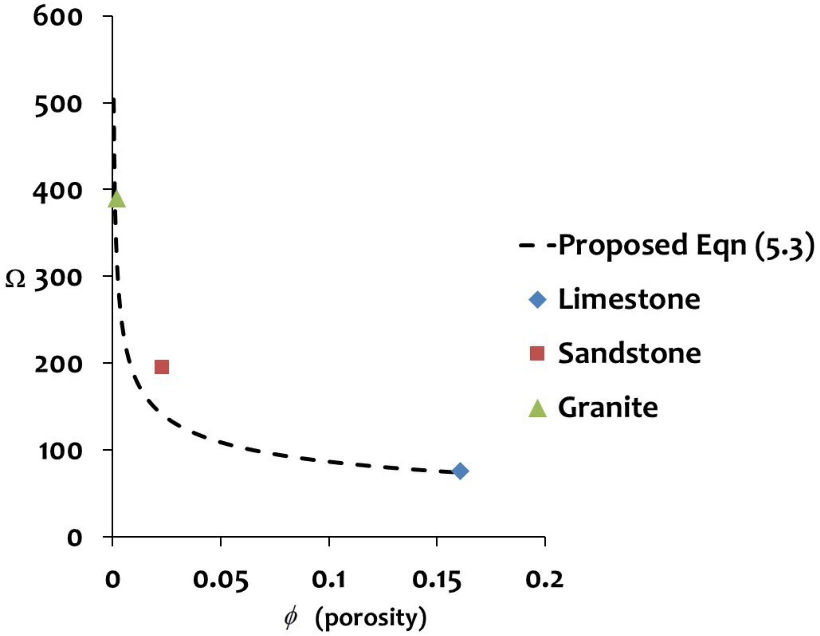

Figure 5.13: Pressure adjustment factor (Ω) vs. porosity (ϕ) showing the trend for three types of rock.

5.4 Summary

Currently there is no convenient way to remove all the trapped air in the pore system of a rock for laboratory testing of permeability. However, with a thorough understanding of the test objectives, an experimental setup and a procedure can be configured to minimize the influences of trapped air.

In this experimental research the common trend of air-dried specimens was an initial rise in the inlet pressure to a peak value followed by a steady and lengthy decay. This phenomenon was observed in samples of three different types of rock. Based on the results presented in this research, the initially dry Indiana Limestone showed the most unstable inlet pressure response during long periods of testing.

The results of this research raise the question as to the use of vacuum saturation method. Since, in the case of Indiana Limestone and Rudna Sandstone, the results show that the initial peak pressures were not avoided by vacuum saturating the samples.

Based on the results presented in this research, for the initially dry samples, an empirical relationship is proposed to predict the final steady state flow inflow pressure, which can be used to estimate the saturated permeability. The ability to predict the ultimate steady state inlet pressure at steady flow conditions can reduce the time and cost required to conduct steady state tests.

The use of a specific type of water (i.e.: de-aired, brine, distilled) is an important factor to be considered during permeability testing; in the case of the de-aired water, occluded air bubbles are absorbed, which increases the effective accessible flow paths and therefore increases the measured permeability of the rock. Also the de-aired water helps to control the pump performance during steady state flow experiments.

Temperature has a notable effect on the inflow pressure response (i.e. an increase in temperature decreases the inflow pressure, see Figure 5.14). Therefore, in order to minimize such effects, when the pressure gradient starts to stabilize and the pressure fluctuations occur due to temperature variations it is important to maintain the system at a controlled temperature, either by monitoring and maintaining the room temperature constant, ideally at ± 1°C, or by placing the permeability setup into a closed/sealed environment where the temperature is maintained constant, to within ± 1°C (i.e.; submersing the fittings and the sample in a water bath).

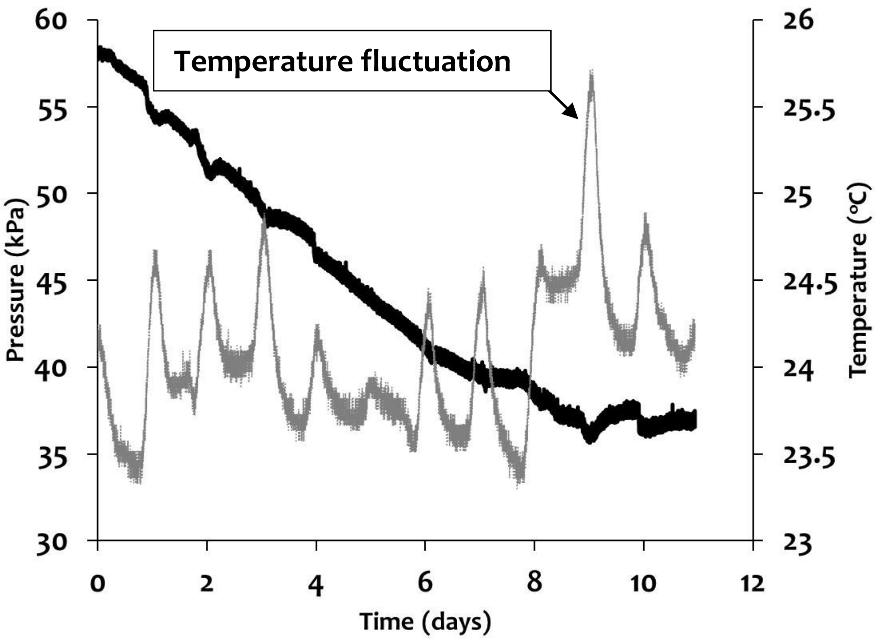

Figure 5.14: Tests on Rudna Sandstone: time history of the inlet fluid pressure at the entry location vs. temperature of water for ASD2; the black curve is the zoomed-in region *A shown in Figure 5.6; the grey curve is the temperature.

These studies demonstrate that interpretation of inlet fluid pressure with time is complex and requires reliable testing procedures that would enable correct estimations of the permeability during steady state constant flow conditions. The sample preparation can influence the results in terms of the presence of machining debris which can lead to clogging of the flow paths, which leads to unstable inlet pressures. The results from flow reversal demonstrate that there is a change in pressure gradients in sandstone and granite once a steady state conditions have occurred.

Long resting periods between tests on Indiana Limestone samples, had no significant effect on the inlet pressures.

In future research, the capillary rise should be examined to assess its influence on the determination of permeability, especially when low flow rates are applied and when dealing with a two phase fluid (air–water) medium (Pini and Benson, 2013).

CHAPTER 6

PERMEABILITY HETEROGENEITY IN THE COBOURG LIMESTONE

6.0 Introduction

The Cobourg Limestone is a heterogeneous argillaceous limestone composed of two distinctive phases: (i) light grey carbonate nodular material; (ii) dark grey argillaceous partings (see Figure 6.1). This particular limestone is found in the southern Ontario, in the Trenton group which is part of the middle Ordovician formation, at 650 m below the surface (OPG, 2011b). The presence of an observable heterogeneity would suggest that the physical, mechanical and fluid transport characteristics of the two phases could exhibit differences. In this research, experiments are conducted to determine the variability in the mechanical properties and the fluid transport characteristics between the two phases: the light grey carbonate phase and the dark grey argillaceous phase, which were characterized and defined in section 2.2.1.1.

In general, the micro-scale (ranging from centimeters to microns) testing of permeabilities in heterogeneous rock samples, such as the Cobourg Limestone, in a laboratory setting, are rare, partly because they have only limited potential use and are very difficult to perform. The intention of current study is to conduct experiments in order to determine the mechanical and fluid transport characteristics at the scale of the heterogeneity. The report by OPG (2011b) states that the unconfined compressive strength and the elastic modulus for the Cobourg formation is slightly anisotropic, whereas permeability results, obtained from borehole straddle-packer hydraulic tests, give average values for horizontal hydraulic conductivity $\mathrm{k_h} \approx 10^{-18}\mathrm{m}^2$; since these values were averaged, they are effectively averaging the effects of any existing heterogeneity. However, Vilks and Miller (2007) tested small cylindrical samples of Cobourg Limestone (i.e. diameter = 25 mm, length = 20 mm), under confining pressures (5 to 15 MPa), and found that the average permeability parallel to the nominal bedding plane $\left(K_h\right)$ is $1.1\times10^{-21}\,\mathrm{m}^2$ and perpendicular to the nominal bedding plane $\left(K_v\right)$ is $1.9\times10^{-22}\,\mathrm{m}^2$. These results would indicate that the Cobourg Limestone is transversely isotropic at that scale. This heterogeneity can be explained by sedimentary deposition that occurred throughout the Ordovician period (NWMO, 2011).

The spatial heterogeneity of permeability, its impact and importance on the development of a geological storage repository for radioactive waste in clayey rocks is discussed by Tsang *et al.* (2012). Tchelepi *et al.*, (1993) who investigated the heterogeneity of millstone and limestone using acoustic measurements and dispersion of acoustic waves; they were able to produce permeability maps by using acoustic measurements conducted on cubical samples (4.5x4.5x4.5cm). The estimation of permeability heterogeneity in a limestone (15x15x5cm) at the laboratory scale was investigated by Hadia et al. (2012) by adapting the water flooding method (i.e. a secondary oil recovery process involving oil displacement by water while maintaining the pore pressure) and continuous pressure monitoring of wells at various locations on the surface of the sample. The pore pressure results were matched with numerical simulations and finally the permeability distribution of the sample was obtained. Soltani *et al.* (2009) proposed a method to characterize core scale permeability profile of artificially man-made heterogeneous samples, limestone and sandstone along the axial flow direction by saturating the samples (38 mm in diameter and 80 mm in length) with low and high viscosity fluids and then using CT images; in so doing the moving front was captured in order to compute the permeability profiles along the flow axis. Soltani *et al*. (2009) provide a review of published articles from 1956 to 2005 that outline various techniques used to characterize permeability heterogeneity in the reservoirs as well as in laboratory cores. Research into a porous medium with heterogeneous permeability using numerical modeling techniques with a focus on mixing (i.e. of contaminants) of two fluids with different viscosities was investigated by Nicolaides *et al*., (2015). The numerical simulation has shown that it is the viscosity difference between the contaminant fluid and the ambient fluid that exerts the control on the spatial distribution of the contaminant plume. Selvadurai and Selvadurai (2010) used a surface permeameter to measure the permeability variation of the Indiana Limestone in a cube measuring 0.5x0.5x0.5m; a specially designed permeameter was placed on the surface of the cubic specimen at 54 different locations; variations in permeability (i.e. from $254\mathrm{E}-15\,\mathrm{m}^2$ to $11\mathrm{E}-15\,\mathrm{m}^2$) were observed in a visibly homogenous rock. The result of Selvadurai and Selvadurai (2010) research was the proposed geometric mean ($K_{eff}^{S} = \sqrt[3]{K_1 K_2 K_3}$ where K_1, K_2, K_3 are the principal values of the permeability tensor) to estimate the effective permeability for a heterogeneous rock.

The present research investigates the permeability variations at a macro scale (i.e. mm) in a sample of the Cobourg Limestone by testing the visually apparent heterogeneous phases (the carbonate light grey and the argillaceous dark grey) that make up the rock. Previous research (Selvadurai *et al*., 2011; Selvadurai and Jenner, 2013) examined the bulk permeability characteristics of the Cobourg Limestone when subjected to either an isotropic stress state or in an unstressed state, respectively. Nasseri *et al*. (2013) conducted a series of hydraulic pulse decay tests on Cobourg Limestone using a triaxial geophysical imaging cell; ultrasonic sensors were employed to determine the influence of the temperature (i.e. 25^{o}C up to 150^{o}C) and deviatoric stresses on the permeability. Other studies of the mechanical and physical properties of Cobourg Limestone were conducted by Raven *et al*. (1992), Golder Associates (2003), Mazurek (2004), Gartner Lee Ltd. (2008). A detailed technical summary of the geomechanical properties of the Cobourg Limestone can also be found in the report by OPG (2011b). The available research investigations point to the fact that when bulk permeability is evaluated, permeability orthotropy exists up to an order of magnitude (Vilks and Miller, 2007; Gartner Lee Ltd., 2008). The contributions of the separate phases to the generation of permeability of the Cobourg Limestone has not been investigated. An evaluation of the relative contributions of the two main phases (i.e light grey carbonate phase and dark grey argillaceous phase) to the permeability of the Cobourg Limestone can lead to a better estimation of the bulk permeability of Cobourg Limestone.

6.1 Sample Preparation

The Cobourg Limestone used in this experimental research was obtained from a block acquired from the Saint Mary's Quarry in Bowmanville, Ontario. The block was wet cored, perpendicular to the nominal bedding plane, using a diamond tipped corer. The cored sample was then cut to length using a diamond saw. Additionally, four flat surfaces were created in order to facilitate the installation of the fluid entry port connector. The prepared sample was approximately 150 mm in diameter and 185 mm in length, with no visible superficial cracks or defects. Although several 150 mm diameter samples were cored, it was decided to test a sample which clearly showed heterogeneous spatial distributions of the lighter carbonate phases and the darker argillaceous phases to facilitate the installation of the fluid entry port connector (see Figure 6.1).

Figure 6.1: Sample of Cobourg Limestone with cut flat surfaces and entry port connectors positioned on the specific phases.

6.2 Unconfined Compression Testing of the Phases

These tests were aimed at determining the bulk moduli of the light grey carbonate and the dark grey argillaceous phases of the Cobourg Limestone. This information was necessary because it was needed for calculating the storativity S_N in the equation (3.19) which was then used for pulse decay modeling in COMSOL™.

The following procedure was used to determine the Young's modulus and Poisson's ratio for the skeletal fabric of the rock, recovered from the separate regions of the heterogeneous Cobourg Limestone.

First, four samples were obtained by coring a Cobourg Limestone block (see Figure 6.2). The samples were then machined on a lathe to an average diameter of 24.2 mm and a height of 36.7 mm. The samples were then washed under tap water and surface brushed to remove machining and coring debris. Samples were then left to air dry for 24 hours. Following the drying period two coats of epoxy (cyanoacrylate) were applied over the surface where the stain gauges would be positioned, this was done to ensure proper bonding of the strain gauges. The gauges were epoxied normal to each other on the same type of phase (see Figure 6.3).

Following IRSM (2007) standard for compression testing, extension steel platens would be needed to move the radius of curvature from the base loading platen to the center of the sample if such arrangement was to be used. This was due to small dimensions of the sample. However, it was decided that two (rigid) plates on the load frame Sintech™ (MTS: 30/G, capacity 250kN, located in the Materials Laboratory) should be used instead.

Each sample was axially loaded up to 33% of the UCS (i.e. ≈44 MPa) and unloaded three times (see Figure 6.4). This was done by manually controlling the loading frame (Sintech™). A loading and unloading rate of 0.05 mm/min was used.

A total of 4 dry cylindrical samples were tested (2 light grey carbonate and 2 dark grey argillaceous) with an average moisture content of 0.1%. The axial strain, the circumferential strain and the axial load were recorded during each test of each sample and the results are summarized in Table 6.1:

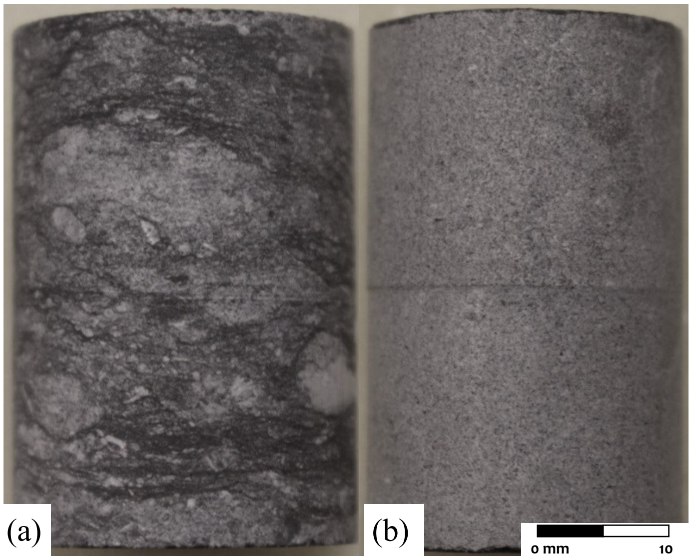

Figure 6.2: Typical machined cylindrical samples, representing (a) the dark grey argillaceous and (b) light gray carbonate phases of the Cobourg Limestone.

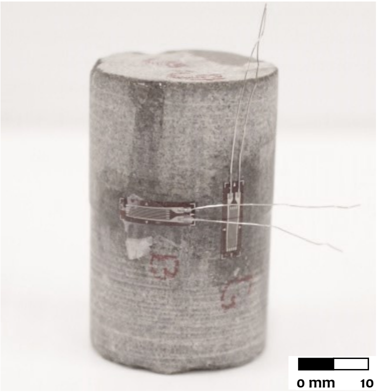

Figure 6.3: Cylindrical sample of the Cobourg Limestone, representing the light gray carbonate phase, with strain gauges attached octagonal to each other for determining the Young's modulus and Poisson's ratio.

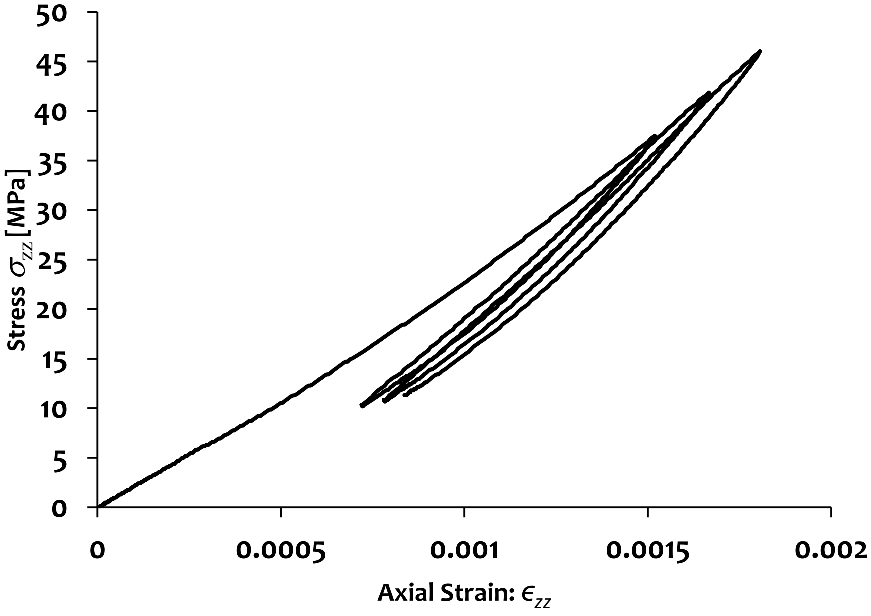

Figure 6.4: Results for axial stress vs. axial strain for Cobourg Limestone; sample C7.

Table 6.1: Phase specific mechanical properties of Cobourg Limestone

	Condition	**Phases**	**Dimensions**		E	v	C_{eff}
Sample			Dimeter [mm]	Length [mm]	[GPa]		[1/kPa]
C8	dry	Light grey carbonate	24.3	36.2	64.0	0.33	1.59E-08
C10	dry	Light grey carbonate	24.3	39.5	39.1	0.27	3.54E-08
C7	dry	Dark grey argillaceous	24.0	35.7	34.6	0.28	3.88E-08
C4	dry	Dark grey argillaceous	24.1	35.2	43.6	0.31	2.67E-08

These results did not show any significant difference, in terms of averaged compressibility, for the two phases; the results are comparable to the results from other studies (see Table 2.6). Hence, when solving for the permeability from the pressure decay results a bulk value was used for the compressibility of the porous skeleton C_{eff}.

6.3 Water Entry Port

In order to test permeability of the observable heterogeneous regions on the Cobourg Limestone, a special water entry port connector was developed. The entry port connector was fabricated by utilizing a Swagelok™ fitting (1/4 inch Tube OD x ¼ inch Male NPT fitting), a stainless steel disc and Hilti™ Hit-RE 500 epoxy (see Figure 6.5). The metal disk was machined to a 25.8 mm diameter and a ¼ inch NPT thread was made in the center. The ¼ inch NPT thread in the metal disk was coated with epoxy followed quickly (within one minute) with the Swagelok™ fitting being tightened into position. Having epoxy in the threads helped to create a better seal as well as prevented air pockets from being trapped in the threads. The stainless steel disk (25.8 mm in diameter) had machined circular grooves (0.5 mm deep and 1.5 mm apart) on the surface where the epoxy was applied (see Figure 6.5c) in order to increase the bond between the metal and epoxy. The assembled entry port connector was allowed to dry for 24 hrs before it was installed on the Cobourg Limestone. The epoxy (Hilti™) was selected on the basis of experiments performed with three commonly available epoxies (Bondo™ Fibreglass Resin, Hilti™ Hit-RE 500 and LePage™ Marine Epoxy, see 6.3.2 Epoxy tests).

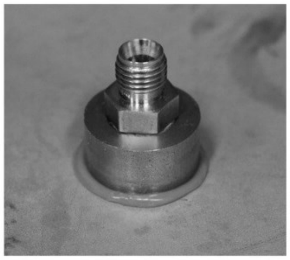

(a)

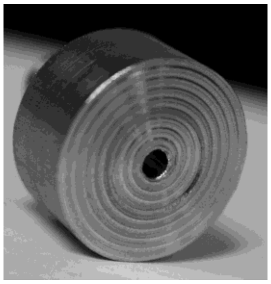

(c)

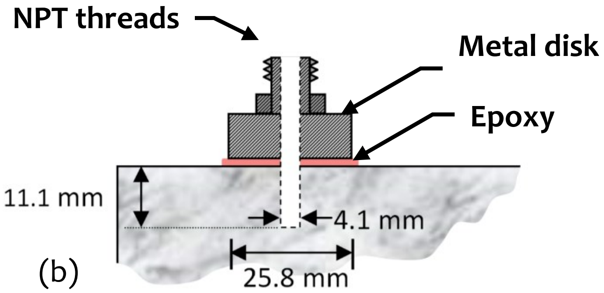

Figure 6.5: Details of the entry port connector: (a) entry port connector epoxied to a stainless steel plate to verify the pressure drop across the epoxy layer, (b) details of the cavity and entry port connector, (c) machined circular grooves on the entry port connector.

6.3.1 Sealing capabilities of the fittings

Prior to the permeability testing of the Cobourg Limestone light grey carbonate and dark grey argillaceous phases, a series of complementary tests were performed to assess the integrity of the seal between the water entry port connector bonded to the Cobourg Limestone. In this regard, the entry port connector was epoxied to a stainless steel plate (see Figure 6.5a) and a series of pressurization tests were performed to determine the decay in pressure of the pressurizing system and the effectiveness of epoxy sealing. This was confirmed by pressure rating all the components up to at least 600 kPa (three times the pulse pressure that will be applied when testing the Cobourg Limestone) and observing the pressure decay with time. The results indicated a less than 0.8% reduction in pressure during 5000 sec starting from 600kPa.

The results obtained for the entry port connector installed on the stainless steel plate demonstrated that the room temperature does have an influence on the pressure decay curves.

Hence, a stainless steel pipe cross with the epoxy filled fitting at one end was placed in a water tank (see Figure 6.6). The pressure within the pipe cross was increased to 300 kPa using the Quizix pump and locked-in by closing the inlet valve. The temperatures of the room and the tank water and the pressure within the pipe cross were monitored. A drop in water temperature clearly produces a drop in the pressure within the tightly sealed cross assembly and fittings; conversely, an increase in temperature results in an increase in pressure over the course of a day (see Figure 6.7). The peaks in pressure tend to occur every 24 hrs corresponding to the times when the laboratory was the warmest; therefore, as noted by Brace *et al*. (1968), it was necessary to minimize the temperature fluctuations as well as selecting the magnitudes of pressure pulses. These complementary experiments prompted the adoption of a more controlled system where the sample and fittings were submerged (see Figure 6.8) to minimize the temperature fluctuations. The laboratory was better sealed and temperature controlled with an air conditioner. Results showed that a variation in the room temperature of 1°C would cause, during the same time lapse, a change in the temperature in the water tank by 0.5°C. Hence, once the entry port connector was attached to the surface of the sample and the entire setup submerged in the water tank, the influence of temperature fluctuations of the water affecting the pressure decay curves was reduced, especially if the duration of the pressure pulse decay was kept short (i.e. 5000 sec).

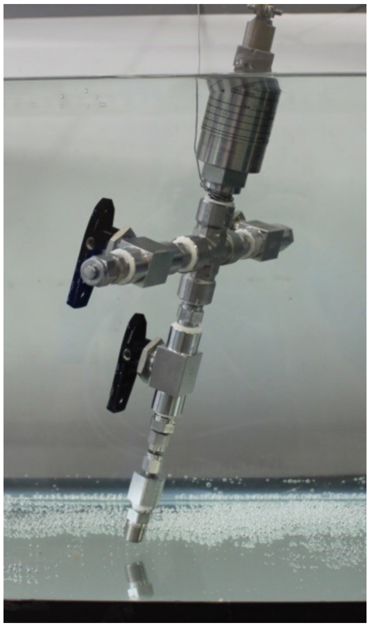

Figure 6.6: Stainless steel pipe cross assembly submerged in the water tank with the epoxy filled fitting.

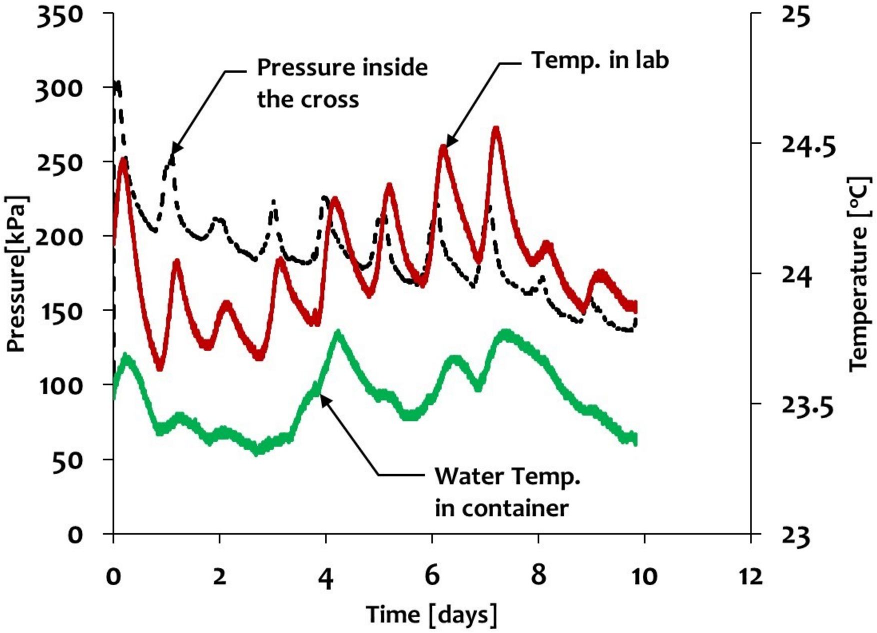

Figure 6.7: Pressure inside the pipe cross assembly submerged in the water tank [**doted-black**] vs Temperature in the lab [**red**] vs Temperature in the water tank [**green**] vs Time.

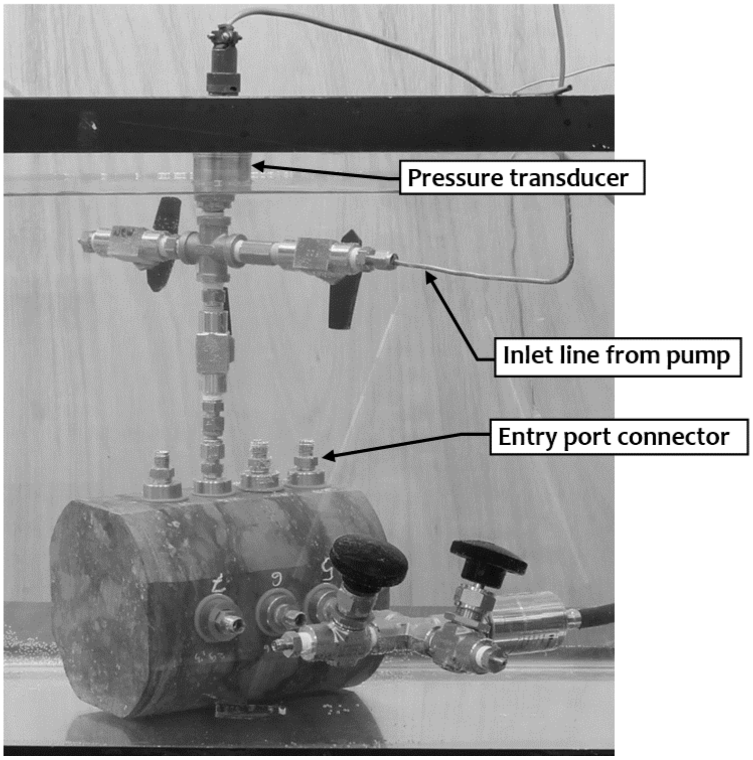

Figure 6.8: The experimental arrangement of the Cobourg Limestone sample inside the water tank.

6.3.2 Epoxy tests

The selection of epoxy (Hilti Hit-RE 500) was based on complementary testing of three commonly available epoxies (Bondo™ Fibreglass Resin, Hilti™ Hit-RE 500 and LePage™ Marine Epoxy, see Figure 6.9). The testing of epoxies was performed by attaching a pipe fitting filled with a particular epoxy to the pipe cross assembly and submerging the entire setup in the water tank (see Figure 6.6). The results of pressure decay tests (see Figure 6.10) on these epoxies show that, with time, the Hilti™ epoxy maintained the most stable sealing and was therefore selected to for this research. Furthermore, the possibility of a chemical reaction of the epoxy

(Hilti™ Hit-RE 500) with the Cobourg Limestone surface was tested on a cubical sample (see Figure 6.11). The results from 4 tests showed that a pressure build up to 200 kPa was possible with no signs of delamination of the entry port connector from the surface, as well as confirming that the method of installation was adequate.

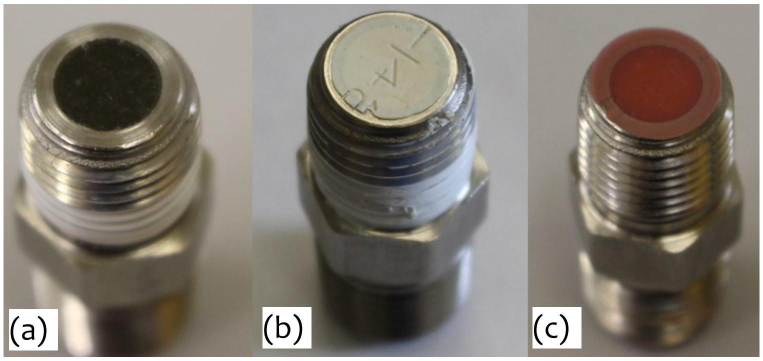

Figure 6.9: Details of complementary epoxy testing: (a) ¼ inch NPT fitting filled with Bondo™ Fibreglass resin (b) ¼ inch NPT fitting filled with LePage™ Marine epoxy (c) ¼ inch NPT fitting filled with Hilti™ Hit-RE 500 epoxy.

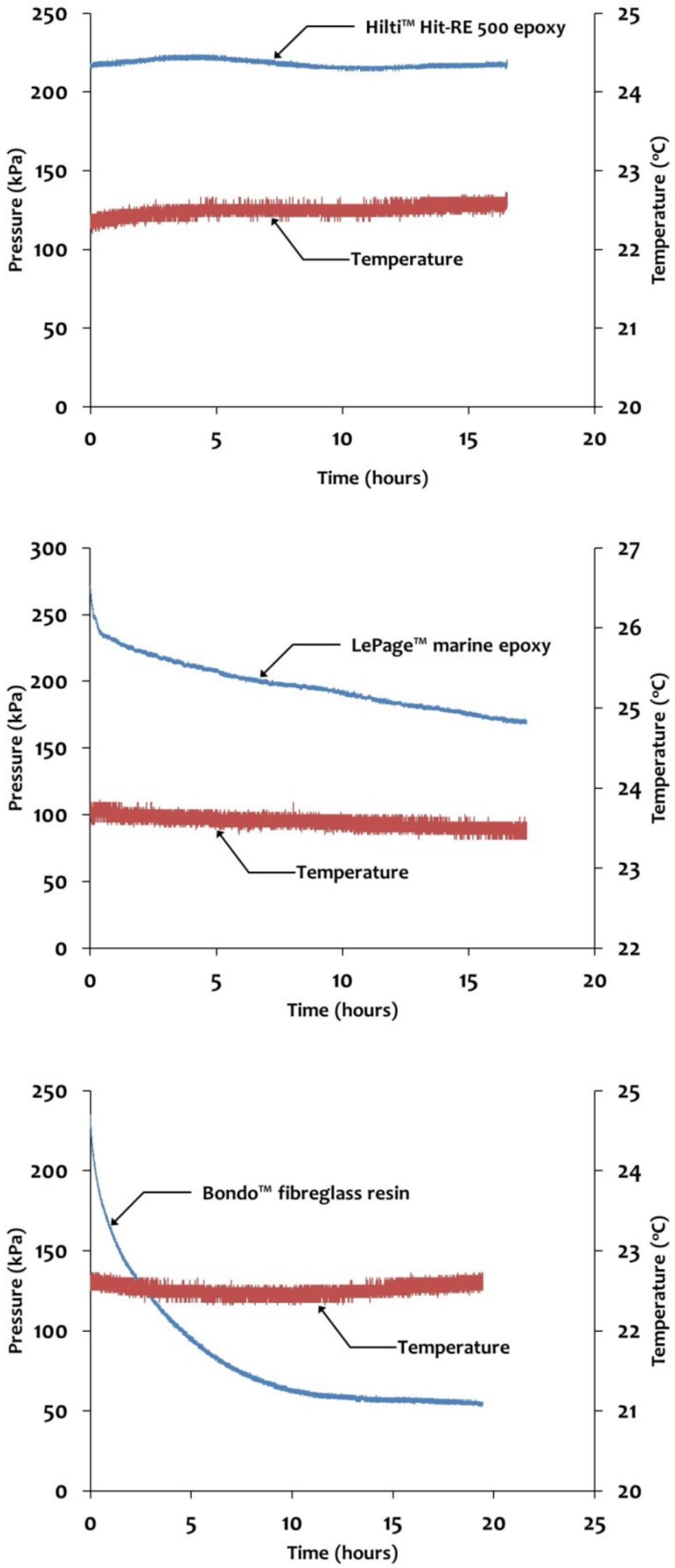

Figure 6.10: Evolution of pressure inside the cross assembly with the three types of epoxy. Blue thin curve shows the pressure.

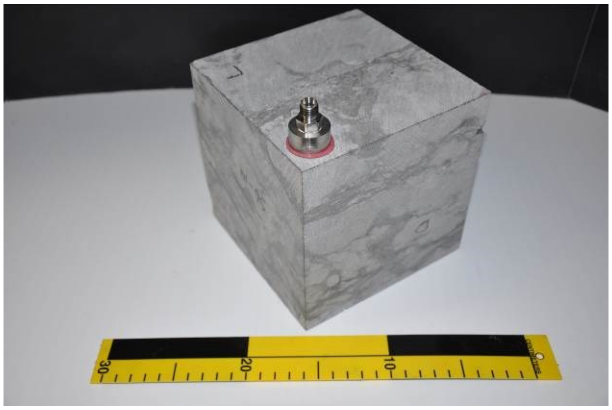

Figure 6.11: The entry port connector on the surface of the Cobourg Limestone cube.

6.4 Experimental Setup and Procedure

The location for installation of the entry port connector has to be clean, free of defects and grease. For the Cobourg Limestone an attempt was made to select exclusively either light grey carbonate or the dark grey argillaceous regions on the rock surface (see Figure 6.12a). The entry port connectors were epoxied to the selected locations and allowed to dry for 24 hours (see Figure 6.12b). Using a drill bit (4 mm in diameter) a hole was drilled through the epoxy and into the sample (see Figure 6.12c) to a depth of 11.1 mm. In order to remove any remaining debris inside the cavity, a vacuum venturi pump mounted with a long needle was used (see Figure 6.12d). The entry port connector was then attached to a cross assembly (see Figure 6.7).

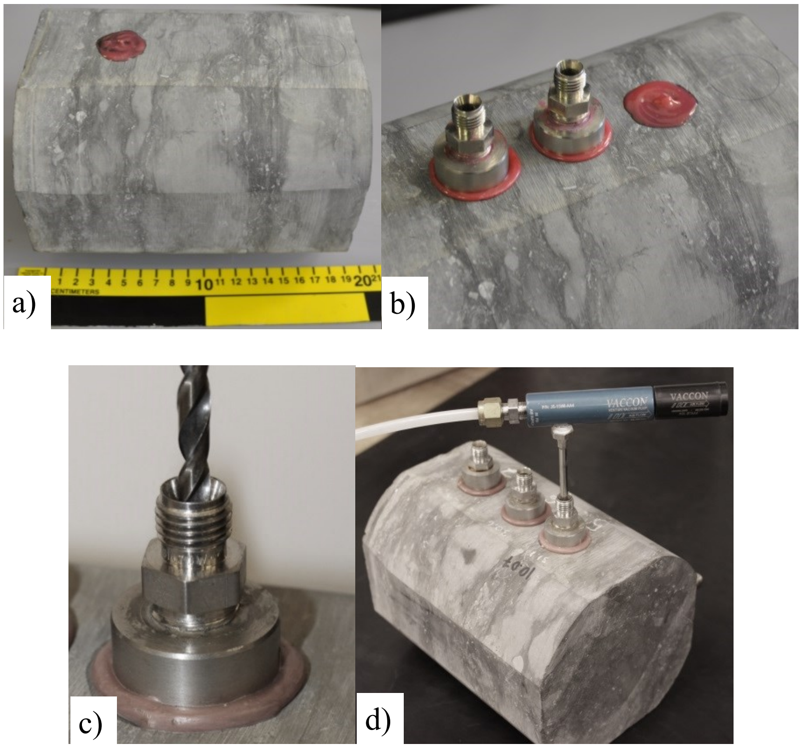

Figure 6.12: Sequential installation procedure of the entry port connector on the surface of the Cobourg Limestone sample: a) Applying a layer of epoxy to the specific phase for better adhesion; b) Placement of entry port connector on the surface of the layer epoxy, with a light nominal force of finger push; c) Drilling through the epoxy and into the sample; d) vacuuming the drilling debris with a vacuum Venturi pump and a coarse needle (diameter 2 mm).

6.4.1 Permeability estimation: pulse decay tests

Once all the entry port connectors were attached on the Cobourg Limestone sample, the entire setup was submerged in the water tank for two weeks to allow the temperature of the sample to reach the temperature of the water inside the tank. Each location to be tested was vacuumed at -75 kPa for 24 hours, followed by a 24 hour rest period to allow for dissipation of any residual negative pressure build up (Selvadurai, 2009). Using a high precision pump (Quizix™ QX-6000), a flow rate of 0.5 ml/min was applied to pressurize the lines, the pipe cross assembly and the entry port connector (see Figure 6.13). This pressure build up was recorded and used to estimate the air fraction in the system using numerical modeling discussed in Section 6.5.1. Once the desired pressure of 200 kPa was reached (on average 50 seconds) the inlet valve controlling the flow of water from the pump was shut closed and the pumping stopped. The ensuing pressure decay within the cavity was monitored using a pressure transducer (Honeywell™ TJE-200PSI) and the data acquired using the DAQ software (DASYLab™ v.13). The test was terminated by opening the de-airing valve for 15 seconds to release the remaining pressure. Any residual pressure in the sample was allowed to dissipate, and the rest period between subsequent tests varied between 15 and 30hrs. This rest period was based on complementary experimental testing on the Cobourg Limestone and showed that the residual cavity pressure (see Figure 6.14), after opening/closing the de-airing valve, would on average rise to 7.4 kPa. This residual build up pressure stabilizes within the rest period and represents 3.7 % of the applied pulse pressure. The tests on the Cobourg Limestone sample continued until repeatability in decay pressure was reached (on average 7 tests were required per location, see Figure 6.15).

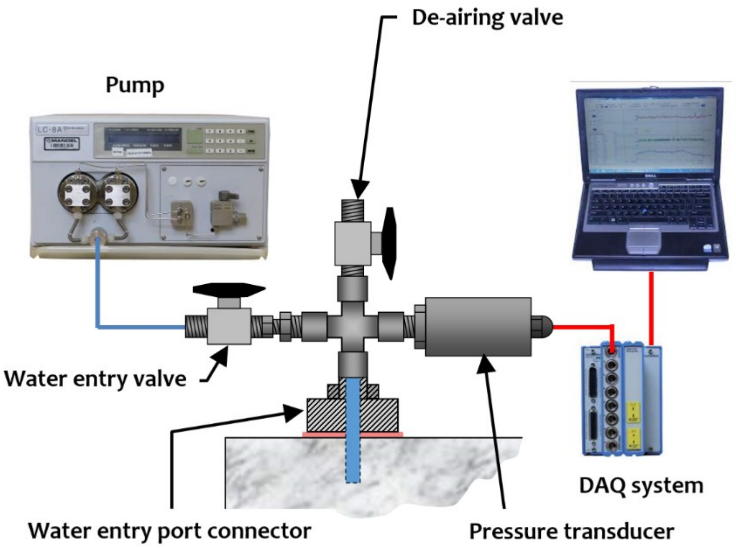

Figure 6.13: Schematic view of the typical experimental arrangements.

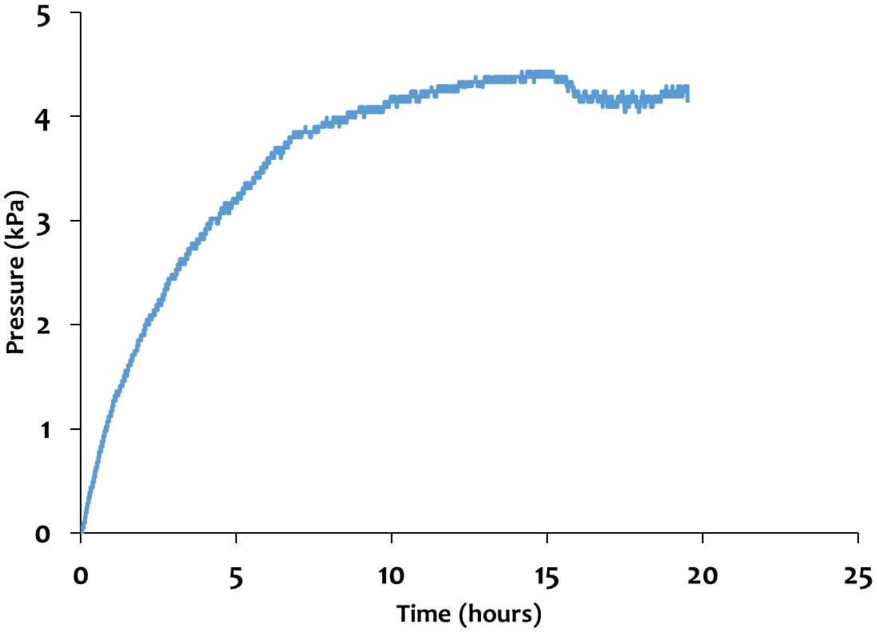

Figure 6.14: Residual pressure build up vs time, after pulse decay testing: location 4 on the Cobourg Limestone.

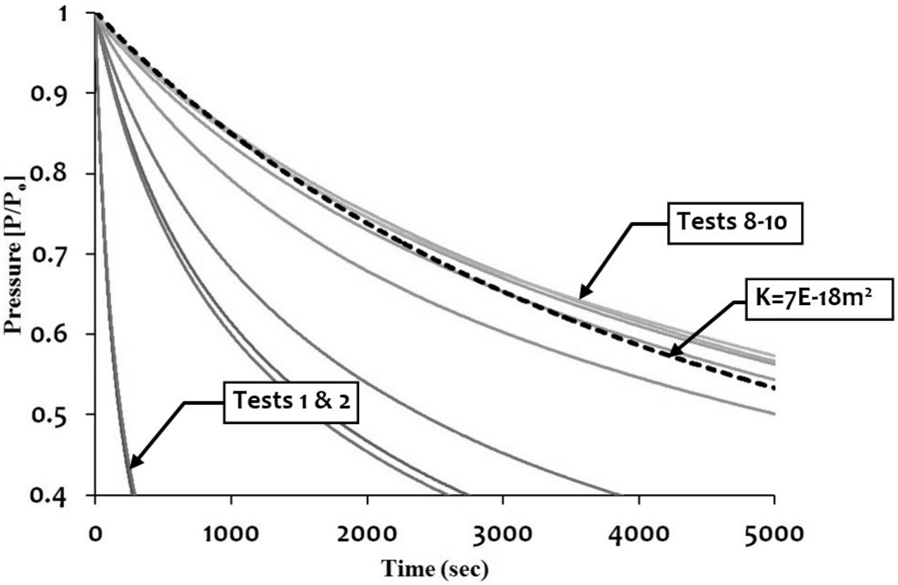

Figure 6.14: Pressure decay vs time for the Cobourg Limestone at location 1 (light grey carbonate phase); the dotted line represents the COMSOL™ model solution for permeability.

6.4.2 Permeability estimation: steady state flow tests

Cobourg Limestone sample was immersed in water and allowed to attain a reference state for a period of one month following a series of the pulse decay tests. Each testing location was then vacuumed for 24 hrs and allowed to stabilize for an additional week prior to steady state flow testing. Using a precision pump (Quizix™ QX-6000) a steady state pressure of 100 kPa was maintained continuously at a specific water entry port leaving the remaining entry ports open. The inflow pressure as well as the cumulative volume of water pumped into a specific location of the rock were monitored and recorded via the internal DAQ of the pump (PumpWorks™). This volume was then used to estimate the flow rate necessary to maintain a constant pressure of 100 kPa and the results were used in a computational model (COMSOL™) to estimate the permeability at that particular location. The details of the computational model are presented in section 6.5.2. The test was terminated once a steady flow rate was reached, taking on average 1.5 days per test (see Figure 6.16). After termination of a test the de-airing valve was opened to release any excess pressure. The pipe fitting cross assembly was then removed from that location and connected to an adjacent location, with a stabilization period of 24 hrs between tests. All experiments were performed with the sample assembly fully immersed in water in order to avoid the introduction of an air fraction into the testing assembly. The applicability of steady state tests was verified by calculating the Reynolds number for Cobourg Limestone ($\mathrm{Re} = 1.3\mathrm{E}\text{-}11$ to $\mathrm{Re} = 5.6\mathrm{E}-10$), based on the pore throat diameter of $7.7 \pm 1.6\,\mathrm{nm}$ (Vilks and Miller, 2007). This flow regime falls within the laminar flow since $\mathrm{Re} \ll$, where n is the porosity (i.e. $n = 0.006$), more details on the Reynolds number calculation can be found in the work by Selvadurai and Selvadurai (2010).

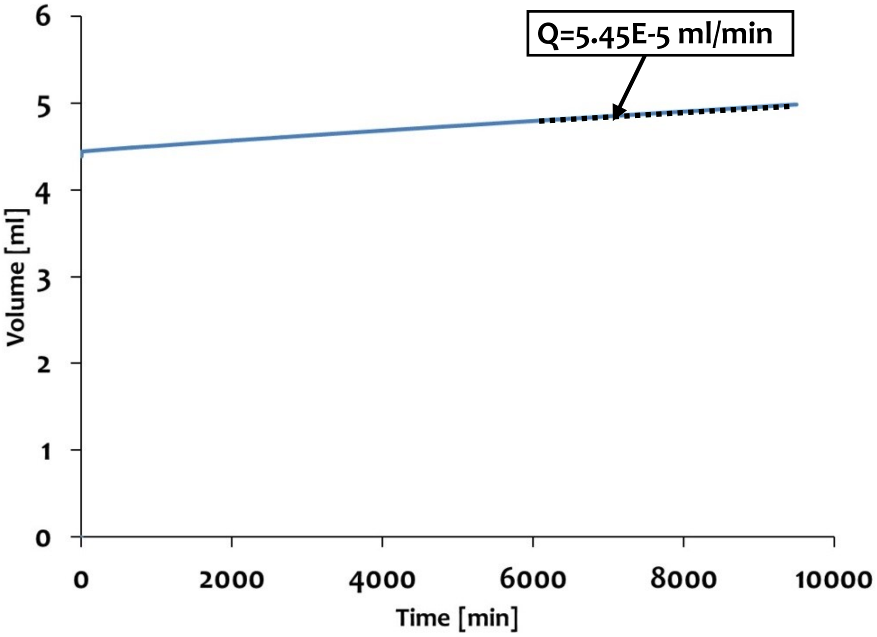

Figure 6.16: Volume inflow vs time for the Cobourg Limestone at location 5 (dark grey argillaceous phase); dotted line represents time span over which the flow rate was estimated.

6.5 Computational Modelling

The pulse decay pressures and the steady state tests were modelled using the finite element software COMSOL™; the previous experience of the research group at McGill and the applicability of this software for estimating permeability can be found in the articles by Selvadurai and Selvadurai (2010), Selvadurai and Jenner (2012); Selvadurai and Suvorov (2012, 2014) and Selvadurai and Najari (2013, 2015). The 2D finite element model used to simulate the hydraulic pulse decay and steady state experiments was axisymmetric (about the z -axis; for each location of the water entry port connector). The numerical model, along with the respective mesh and boundary conditions, are presented in Figure 6.17 for hydraulic pulse decay and Figure 6.21 for steady state respectively. The model consists of quadratic triangular elements (19 402) with Lagrangian shape function and 34 211 degrees of freedom. The finite element mesh used in the modeling needed to be refined on the boundary separating the fluid cavity and the rock matrix in order to avoid the Heaviside step function-type (pressure drop) during the initial stages of the modeling. The rock matrix in the vicinity of the cavity is assumed to be homogenous and isotropic for the purpose of modeling and parameter assignation (Selvadurai and Selvadurai, 2010). This assumption is based on the premise that the cavities were drilled into a particular phase of the Cobourg Limestone.

Additionally, a 3D model, where the entire cavity configuration was included (see Figure 6.18), was analyzed and the results verified against the presence and influence of neighboring cavities as well as the geometry; consisting of 79000 tetrahedral elements and 116000 degrees of freedom. All exterior surfaces of the Cobourg Limestone model, except the epoxied areas and cavities, were assigned a boundary condition of zero pressure (i.e. $p = 0$). The computed results show that modelling the exact experimental cavity pattern (i.e. $K = 5.21\text{E} - 20\,\text{m}^2$) in 3D differs from the reduced cavity axisymmetric model (i.e. $K = 5.00\text{E} - 20\,\text{m}^2$) by 4%, this was considered to be a minor influence when compared to the differences in results between adjacent locations. Furthermore, an axisymmetric model required less computational effort. Hence, the results presented in the following sections were computed on a 2D model.

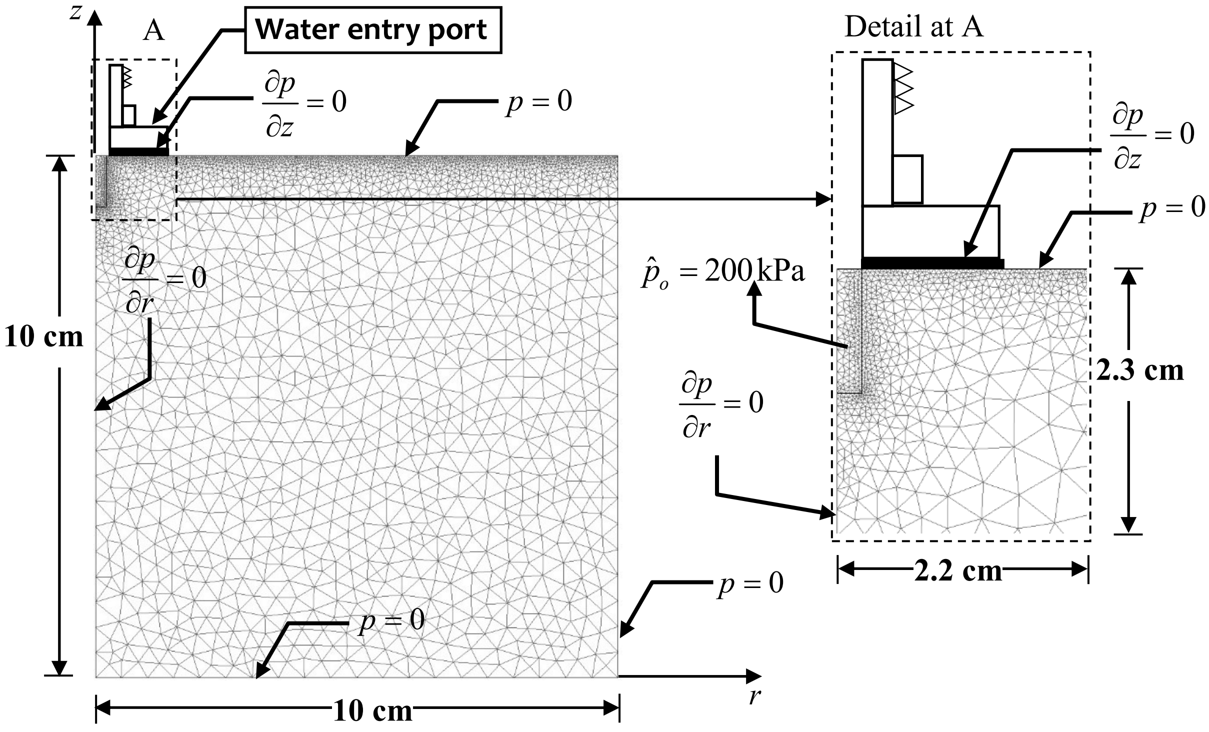

Figure 6.17: Schematic view of the simplified model with boundary conditions used to perform the pulse decay permeability estimations in COMSOL™.

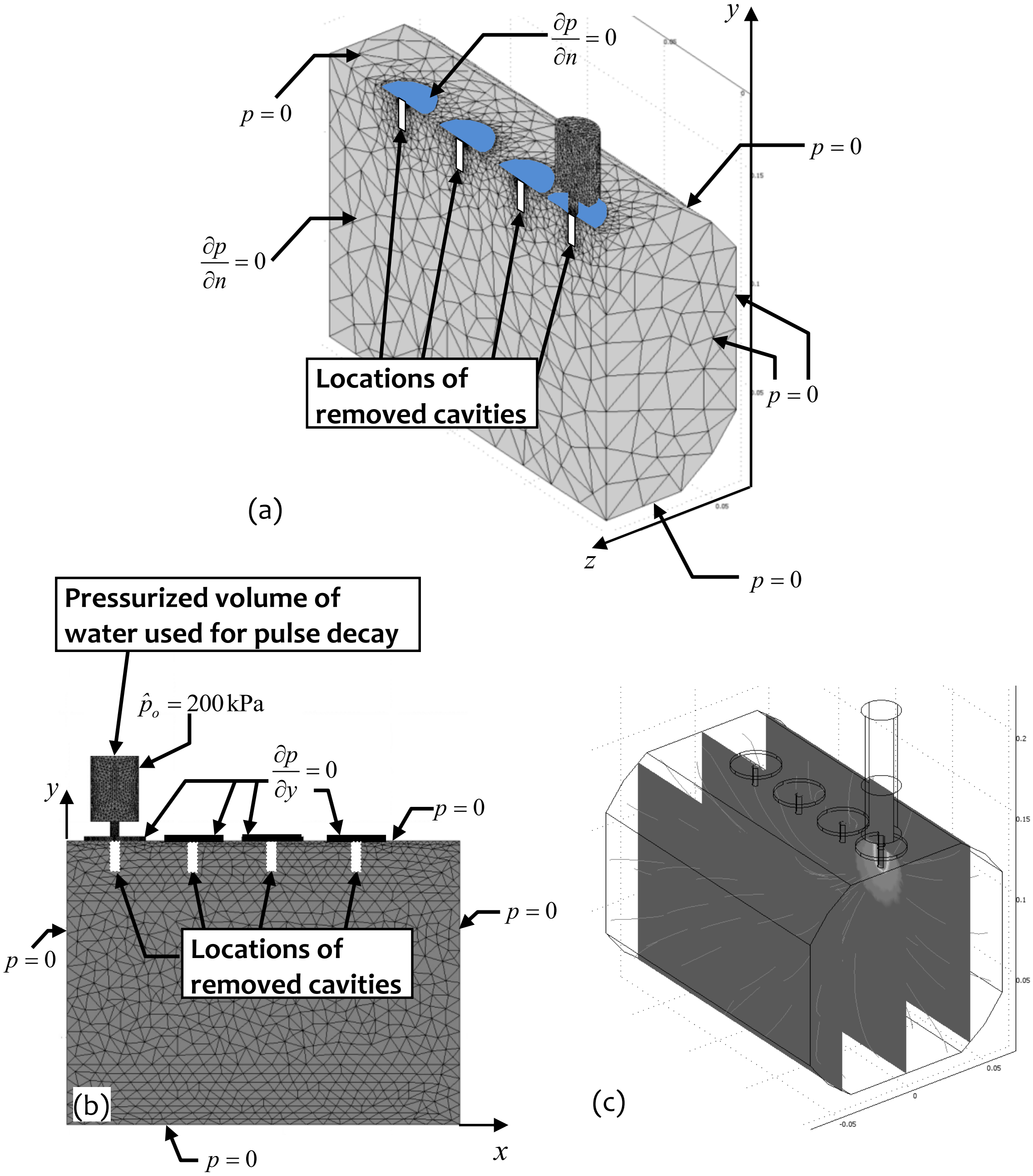

Figure 6.18: Computational model for the 3D experimental setup used to check the geometric influence of neighboring cavities on the pulse decay permeability estimations in COMSOL™;(a) cross-section view of assigned boundary conditions and mesh refinement to the model with removed cavities (b) assigned boundary conditions to the model with removed cavities; (c) modelling of pressure distribution and flow lines of an exact geometry with four cavities as used in the experimental setup.

6.5.1 Computational modelling of the hydraulic pulse tests

In order to estimate the permeability from the pulse decay curves, the piezo-conduction equation was used in the computational modelling, taking into account the compressibility of the solid grains and the air fraction in the pressurized fluid volume, adopting the procedure developed by Selvadurai and Najari (2015). First, the percentage of air fraction (ϕ) in the pressurized fluid volume and the connections was estimated using the pressure build up curves (see Figure 6.19). However, there is a difference in pressurizing volumes that needs to be accounted for when estimating the air fraction versus the permeability from the hydraulic pulse tests, because the water entry valve is open (see Figure 6.13). The total pressurized volume of 29.2 mL was used to estimate the air fraction; this volume accounted for the fluid in the fittings, the pump, the tubing and the valves. The percentage of air fraction used in the numerical models for pressure decay analysis was obtained iteratively by altering the compressibility of the fluid according to (3.27), which takes into account the air, till the results matched the experimental pressure build up curves. Once the pressurization, up to $\hat{p}_o = 200\,\text{kPa}$, was completed the water entry valve was closed, hence deducing the volume of pressurized fluid used in computing the pressure decay curves. The water reservoir, shown in Figure 6.18a, corresponds to the volume of pressurized water (V_w) in the entry port connector, piping and the cavity when the water inlet valve is closed (i.e. post pressure build up). This volume (V_w) of pressurized fluid used for pressure decay was on average 11.5 mL. The water parameters used in the model were the dynamic viscosity $\mu = 0.001\,\text{Pa}\bullet$, the compressibility of water $C_w = 4.54\text{E}-10\,\text{Pa}^{-1}$ and the density $\rho = 998\,\mathrm{kg/m^3}$ (values were adjusted for specific tests according to the measured temperature of water). Based on previously obtained estimates for bulk permeability of Cobourg Limestone, an initial value is selected for the model, i.e. $K = 1.0\mathrm{E}-22\,\mathrm{m}^2$ (Selvadurai *et al.*, 2011). Once the solution of the model is obtained, the pressure decay in the water reservoir (COMSOL™ solution) is compared to the experimental results (see Figure 6.15). If the results do not match, the permeability of the rock in the COMSOL™ model is adjusted. Additionally, the following parameters were used for the rock in COMSOL™:

Skeletal Young's modulus (E) = 35 (GPa)

Skeletal Poisson's ratio (ν) = 0.25

Porosity (n) = 0.006

Biot coefficient (α) = 0.7; (0.5 in OPG 2011c; 0.7 in Selvadurai and Najari, 2016)

In addition, the influence of adjacent cavities on the pressure decay results, in an axis-symmetric model, was verified by determining the distance the pressure front traveled over a specified time. Hence, in order to determine the radius of influence of the pulse decay front a pulse pressure of 200 kPa was applied to a single cavity and the distance this front reached in 5 000 sec was determined (see Figure 6.20). The results show that as long as a radius of 3 cm or more was kept between adjacent cavities the influence on the pressure decay results was negligible (less than 2% after 5000 sec).

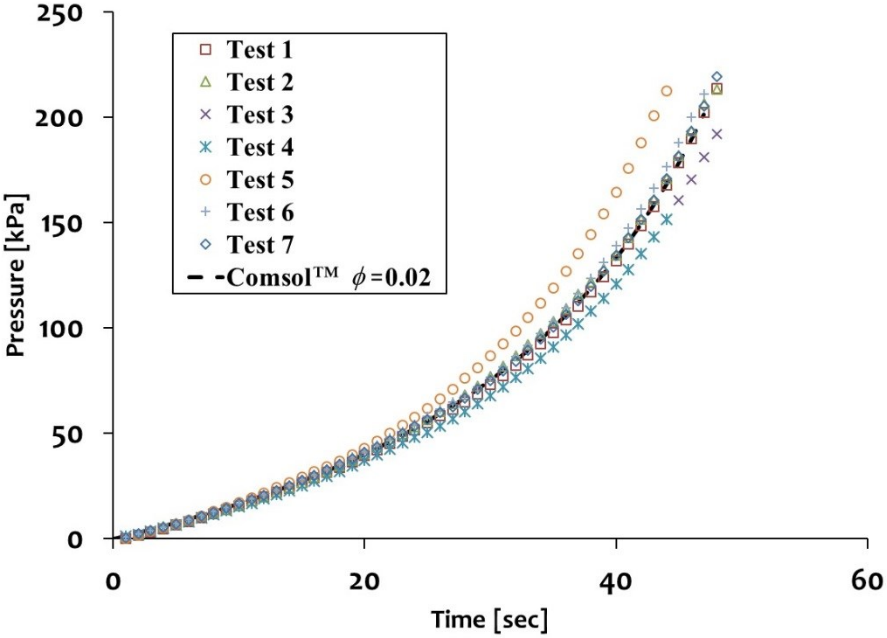

Figure 6.19: Pressure build up vs time for the Cobourg Limestone at location 4 (dark argillaceous phase); [ϕ is the air fraction (non-dimensional) defined as volume of air bubble fraction divided by the sum of volume of pure water and air bubble fraction].

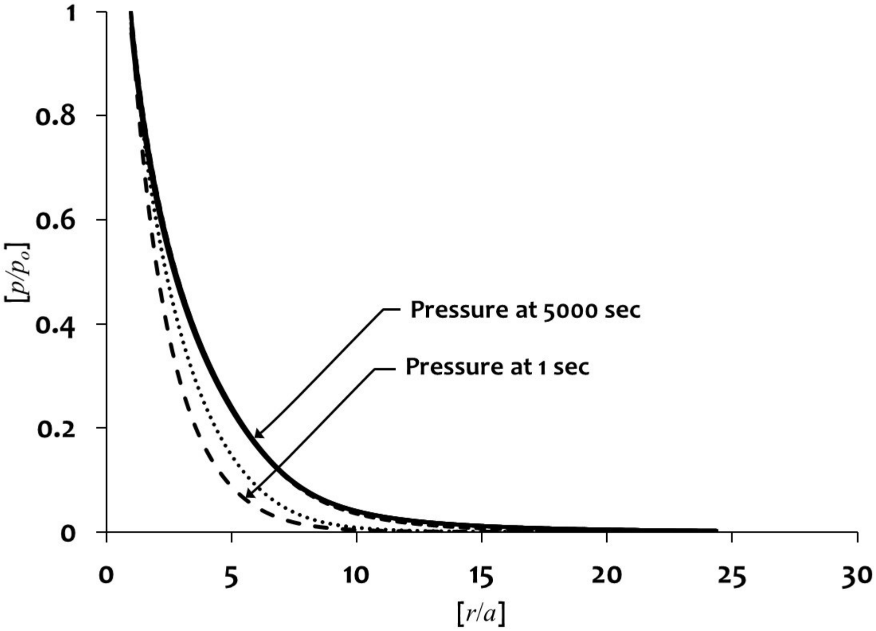

Figure 6.20: Numerical computation of the normalized pressure decay curves vs normalized radial distances for various times; selected pressure lines (1, 10, 100, 1000 to 5000 seconds) and the radius of influence r are shown, where a is the cavity radius (2.05 mm) and p_o is the initial cavity pressure (200 kPa); results computed at the mid-height of the cavity.

6.5.2 Computational modelling of the steady state tests

The computational code COMSOL™ was used to examine the steady state flow from a single entry port connector. The computational modelling of the steady state pressure at each location for the Cobourg Limestone was similar to that reported in Selvadurai and Najari (2016), where this procedure was successfully used to determine the permeability of a 150 mm diameter Cobourg Limestone with a pressurized fluid-filled cylindrical cavity of finite length. In this research, a constant pressure (100 kPa) was assigned to the surface of the fluid cavity along with a pre-assigned permeability for the rock from which a steady state flux on the boundaries of the cavity was calculated (see Figure 6.21). The iterations were repeated, by adjusting the permeability of the rock, until the computed flow rate matched the experimental results.

The process required to solve the problem of steady state pressure inside the cavity followed an iterative process:

1. The fluid cavity was assigned a 100 kPa constant pressure and the Cobourg Limestone was assigned a reasonable permeability.
2. The model was then solved for out flux through the boundaries of the cavity and converted to outflow rate.
3. This outflow rate was then compared to the outflow rate obtained from the experiments. If the results matched, then the assigned permeability in step 1 was the permeability for that particular location.
4. If the flow rates did not match the permeability was adjusted and the model solved again.

Additionally, the influence of the neighboring cavities on development of the steady state model was verified by performing additional computations. The most exaggerated model was the one for which the shortest distance (3.8 cm) between two adjacent entry port connectors served as the outer most boundary (see Figure 6.22). The results show that the change in estimated permeability between both models would be very insignificant and at most 1%. Additionally, the distance of pressure influence from the steady state computation model is shown in Figure 6.23. The results show that there is a 0.14% difference between the pressure at 3.8 cm away from the pressurized cavity between the numerical model without adjacent cavities and the numerical model with cavities.

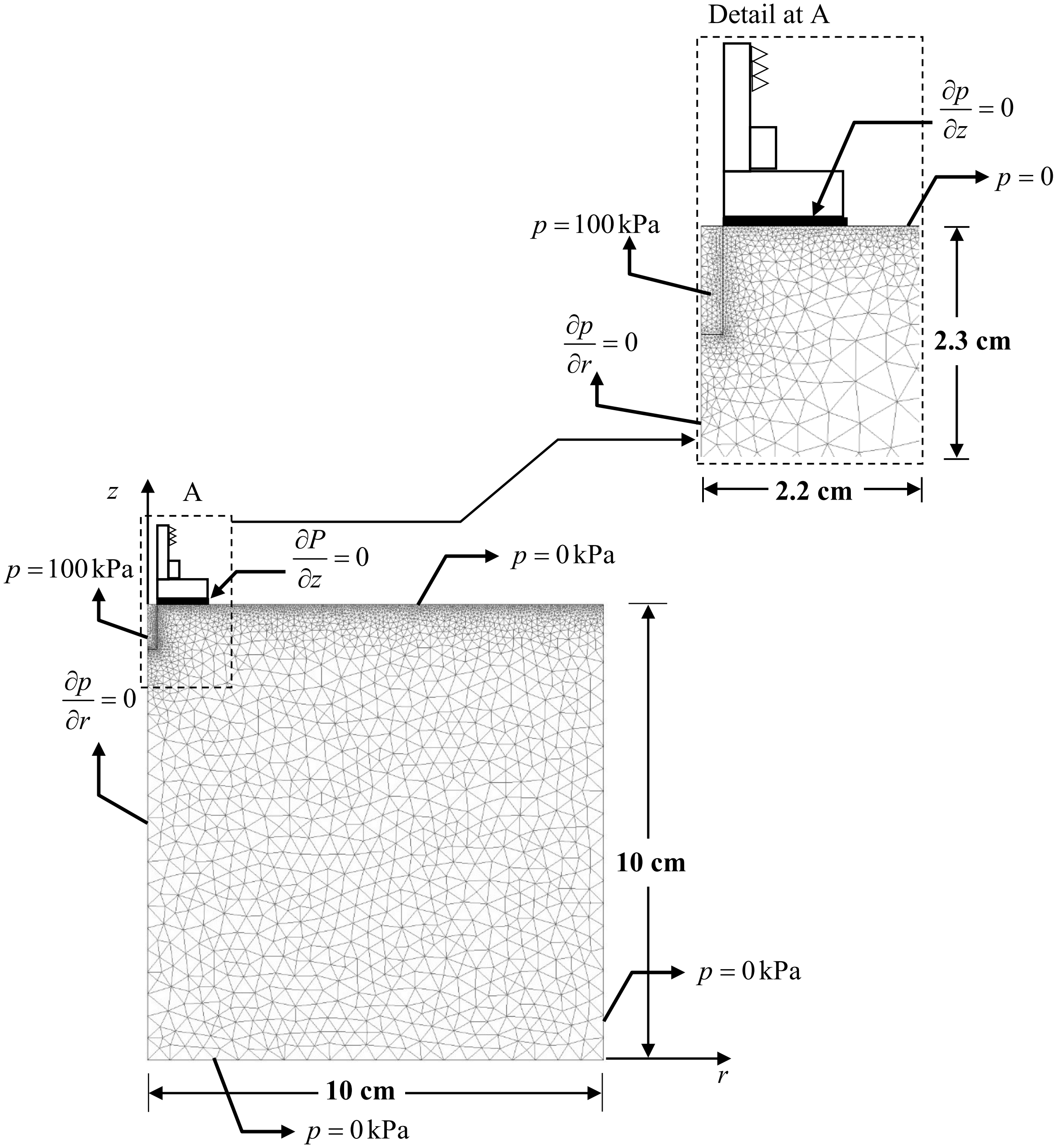

Figure 6.21: Schematic view of the simplified model with boundary conditions used to perform the steady state permeability estimations in COMSOL™.

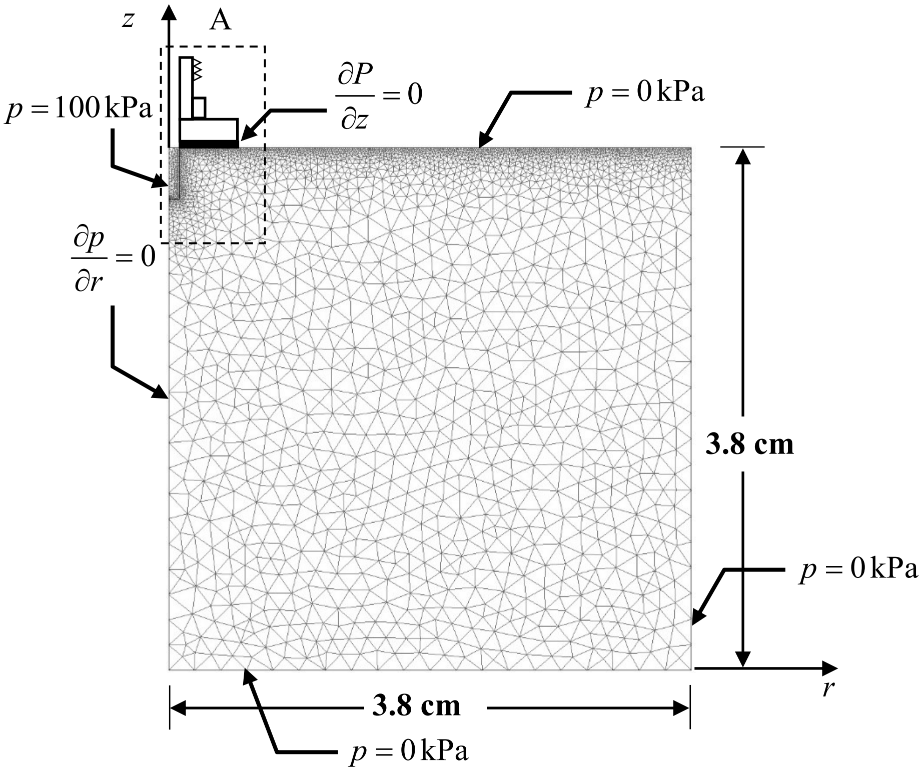

Figure 6.22: Schematic view of the steady state model with boundary conditions used to perform the check of the influence of the neighboring cavity (3.8 cm apart) on the permeability estimations in COMSOL™.

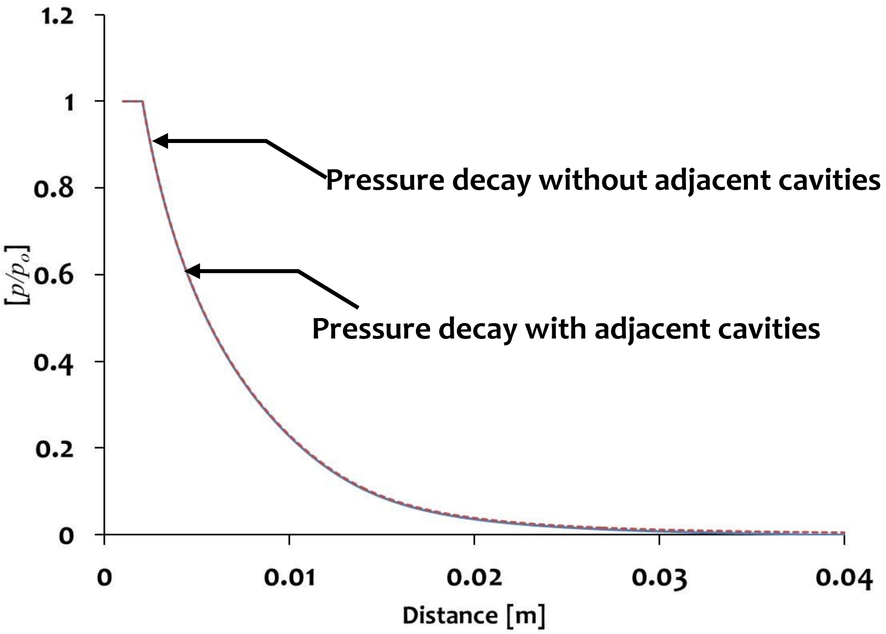

Figure 6.23: Numerical computation of the normalized pressure decay curves vs radial distances computed in COMSOL™; results computed at the mid-height of the cavity.

6.6 Results and Summary

The estimates for permeability obtained from both hydraulic pulse decay and steady state pressure tests are summarized in Figure 6.24. The results presented for the estimated permeability from the hydraulic pulse decay tests were calculated using the effective compressibility compressibility of the porous skeleton $\left(C_{eff}\right)$ defined in equation 3.17.

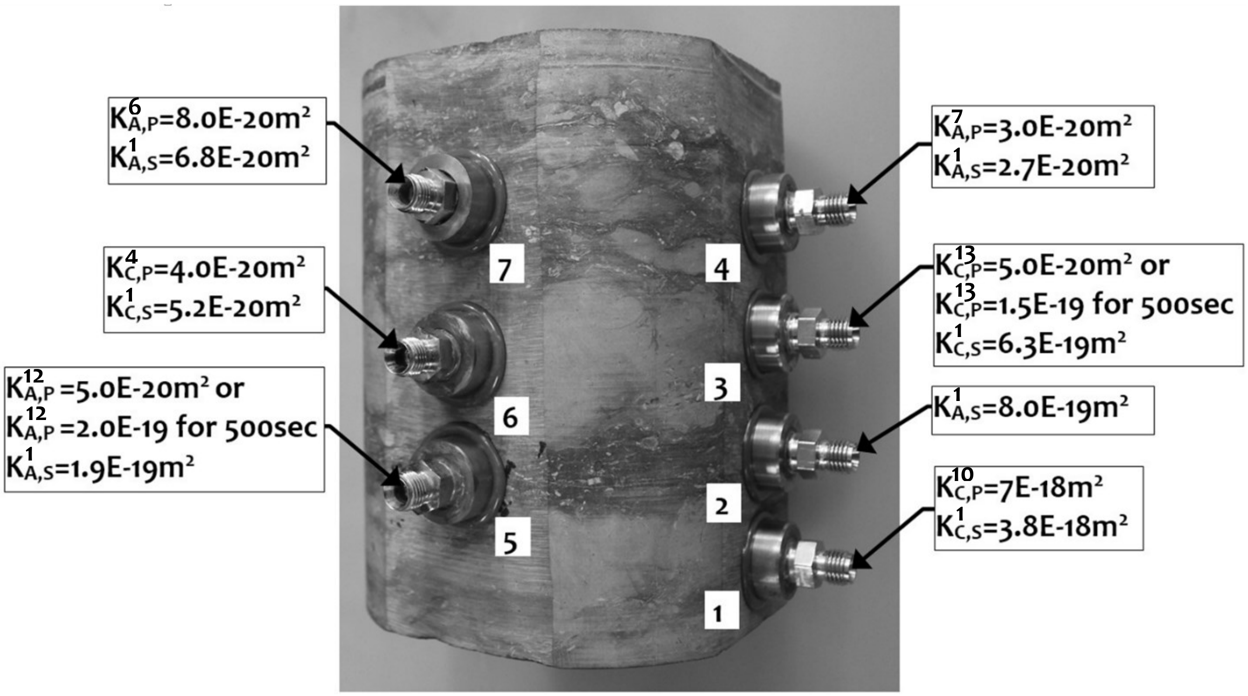

Figure 6.24. The Cobourg Limestone sample with water entry port connectors epoxied to specific limestone phases, numbering indicates the location. The permeabilities are based on pulse tests and steady state tests; where subscript C is for the light grey carbonate phase, A is for the dark grey argillaceous phase, S is for the steady state test and P is for the pulse decay test; whereas the superscript indicate the number of tests. The numbers located besides each port are there for referencing in the text and data results.

The pulse decay results from location 2 are not presented because the fitting at that location was damaged during the 3rd test. Also, since only 2 pulse tests were performed before the damage, the results were not considered to be representative. When the Cobourg Limestone sample was removed from the water tank a visible crack had formed close to the water entry port at location 1 (see Figure 6.25), which provides an explanation for the higher permeability values obtained at this location.

Figure 6.25: Close up view of the Location 1 on the Cobourg Limestone; the crack that had formed near the entry port connector was accentuated, for visual appreciation, by wetting the surface with water.

For purposes of comparison with the results obtained from pulse tests, a series of steady state permeability tests were performed. Although not a perfect match, the results are in general agreement and confirm that the proposed method, which consists of (i) using high precision pumps, (ii) an entry port connector and (iii) the steady state method, can provide permeability estimates as low as $2.7\mathrm{E}-20\,\mathrm{m}^2$.

In certain locations there was a significant lack of correlation between the results of hydraulic pulse and the steady state tests (i.e. locations 3 and 5). In these cases, by analyzing the pulse decay curve for a shorter time period, the estimated permeability gives values closer to the results obtained from steady state tests. This can be attributed to rapid increase in temperature in the water tank (i.e. +0.25°C in 5000 sec), which would impede the pulse decay, hence making the estimated permeability lower.

The results for the Young's modulus and the Poisson's ratios that were obtained from small cylindrical samples of the specific phases (i.e. light grey carbonate and dark grey argillaceous) of Cobourg Limestone were used in the computational modelling but these parameters did not affect the estimated permeabilities for the pulse decay calculations. On average the change in permeability was less than 0.3 %. Therefore, with such a low influence on the estimation of permeability the bulk effective Young's modulus and Poisson's ratio were used to determine the permeability of particular location on the sample.

The results of the current research is of importance to the assessment of fluid migration in the vicinity of the DGR. The results show that the permeability of the dominant phases composing the Cobourg Limestone fall within a range of $7.0\mathrm{E}-18\,\mathrm{m}^2$ to $2.7\mathrm{E}-20\,\mathrm{m}^2$. Based on the results there is nearly an order of magnitude difference in the permeability of the light grey carbonate phase and the dark grey argillaceous phase, with the argillaceous phase having the higher permeability. These results are supported by results on the estimation of permeability on Cobourg Limestone cylinder subject to triaxial failure stresses (Selvadurai and Głowacki, 2016), where it is observed that the darker argillaceous phase is the weaker material and forms pathways (cracks) for water flow. The accuracy of the current results in the estimation of the permeability can be improved by testing a larger sample with more water entry port connectors, as well as a knowledge of the exact phase into which the cavity is drilled; the latter is difficult as accurate CT-scanning is currently not feasible on large samples. The water entry port connector proposed in this study was quite effective, inexpensive to produce and larder versions of the arrangement can be easily installed, in situ, in areas where the testing surface areas are scarce or at precise locations on laboratory samples.

CHAPTER 7

STRESS-INDUCED PERMEABILITY EVOLUTION IN THE INDIANA LIMESTONE

7.0 Introduction

Permeability of rocks can be influenced by the alteration in the stress state; including stresses that can induce failure and damage to porous media due to engineering constructions (see Figure 7.1). In such situations it is important to correctly estimate the permeability evolution with stress in order to improve the design and construction of engineered facilities. The expectation is that as the stress state increases in the compressive range the accessible pore space will be reduced resulting in an overall decrease in the permeability. A literature review of stress-induced permeability evolution in rocks was also presented in Chapter 1. In this chapter the focus of literature review will be on research that was primarily focused on permeability estimation in Indiana Limestone. Leith *et al.* (1996) subjected cores (25 mm in diameter and 75 mm in length) of Salem Limestone (also known as: Indiana Limestone) to a net radial confining stress of 3.4 MPa and used air injection techniques to determine the absolute and relative permeabilities. They concluded that a large portion of the porosity is intragranular, since the carbonate grains hold static water, which contributes very little to fluid transport; additionally there is wetting and drying cycle hysteresis that affects the permeability measurements. Azeemuddin *et al.* (1995) used an oscillating pulse to estimate the permeability of Indiana Limestone under hydrostatic and deviatoric compression: at confining pressure (6.9 MPa), permeability decreased until the initiation of dilatancy after which it increased, whereas at higher confining pressures (20.7 MPa to 48.3 MPa) permeability decreased and this was associated with pore compression. Suri *et al.* (1997) and Dautriat *et al.* (2011) reported a reduction in permeability ranging from 25% to 80% for triaxial tests performed on Indiana Limestone and Estaillades Limestone, respectively, at effective confining pressures ranging between 6.9 MPa and 48.3 MPa. Selvadurai and Głowacki (2008) observed a permeability reduction with increasing isotropic compression of Indiana Limestone and permeability hysteresis during unloading and re-loading. Further examples of permeability studies on Indiana limestone can be found in Selvadurai and Selvadurai (2010 and 2014) who examined the fluid transport properties of a cuboidal block of Indiana Limestone measuring 0.5 m, in an unstressed state, by using a surface permeameter and developed a geometric mean formula to represent the effective permeability that was found to have spatial heterogeneity.

This research investigates the evolution of permeability in cylindrical samples of Indiana Limestone subjected to triaxial stress states including post-failure. This research culminates in the development of a "*State-Space Permeability Evolution Model*", which provides a simplified analytical result to describe the variation of permeability of the Indiana Limestone in the *compressive stress range* involving principal stresses (σ_1 and σ_3). The analytical results are implemented in a finite element-based computational procedure that accounts for stress-dependent permeability evolution and is used to examine an idealized problem of flow into an excavated circular cavity (tunnel) in an elastic geomaterial under geostatic stresses. The influence of the stress-induced permeability on the alteration on the flow rate into the cavity is estimated.

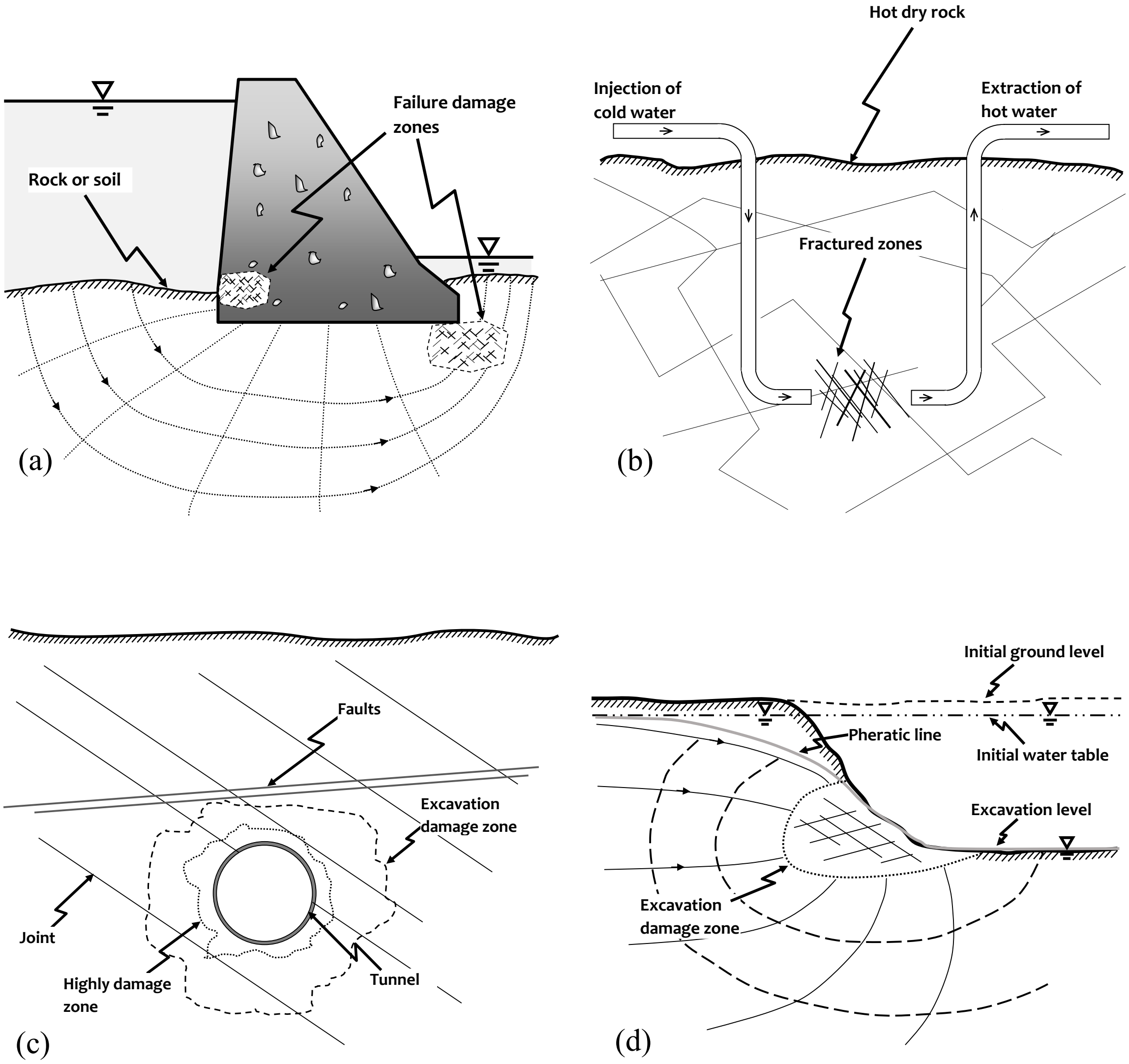

Figure 7.1: Damage to rocks induced by engineering activities leading to permeability alterations (a) gravity dams; (b) geothermal energy extraction; (c) pipelines and tunnels; (d) deep excavation

7.1 Sample Preparation

The eleven cylindrical samples of Indiana Limestone were wet cored from blocks measuring 35 cm x 47 cm x 91 cm, which were supplied by Les Carrières Ducharme Inc, Québec. The wet coring was done with a diamond tip coring bit supplied by Abrasifs Diamantés

North Star Ltée (87 mm inside diameter and 380 mm inside length). The rough cored samples were then cut to size with a diamond rotary saw and machined to a diameter of 85 mm using a lathe. The machined samples were washed to remove the machining/coring debris and brushed with a stainless steel soft brush under running tap water. All samples were precisely dimensioned, weighed and labeled. Each sample was placed in the vacuum saturation chamber (see Chapter 4.4) prior to testing, periodically weighed and removed for triaxial permeability testing when the measured weight stabilized to 0.1 % between readings.

7.2 Experimental Setup and Procedure

The Indiana Limestone was tested using the modified Obert-Hoek Triaxial Cell and the HCLC Testing facility (axial loading frame) described in Chapter 4.3. The modified Obert-Hoek cell was placed in the axial loading frame as shown on Figure 7.2. The setup procedure was refined after preliminary testing trials. In general, the process involved pre-assembling the modified Obert-Hoek Cell by filling the space between the membrane and the cell wall with hydraulic oil using a manual hydraulic pump. The pressure release port (Figure 7.2b) was opened to allow the release of trapped air. The assembled modified Obert-Hoek Cell was then positioned in the axial loading frame by resting it on the lower loading platen (85 mm in diameter and 140 mm in length) that contained a geotextile disk on the plane that will come into contact with the sample. This was done by placing an aluminum collar spacer which maintained the assembled cell in a precise vertical position and provided access to the water inlet fitting. A sample of Indiana Limestone was then inserted into position and a geotextile disk was placed on the upper plane of the Indiana Limestone sample. These geotextile disks (Texel™: F-200) served to distribute the water as well as to reduce friction between the sample and the loading platen. The upper loading platen (85 mm in diameter and 140 mm in length) was placed to complete the assembly procedure. The geotextiles disks were saturated prior to the placement in the modified Obert-Hoek Cell. The geotextile experiences compression that leads to a reduction in its permeability; however, this reduced permeability is significantly higher ($2.3\text{x}10^{-7}$ m^2) than the permeability of the intact Indiana Limestone ($1.6\text{x}10^{-14}$ m^2) at a reference confining pressure of 5 MPa (Selvadurai and Głowacki, 2008). In order to flush out trapped air bubbles a nominal axial stress of 200 kPa was applied to the sample, followed by a constant pumping of fluid through the base at 1 ml/min, until water emerged from around the upper loading platen.

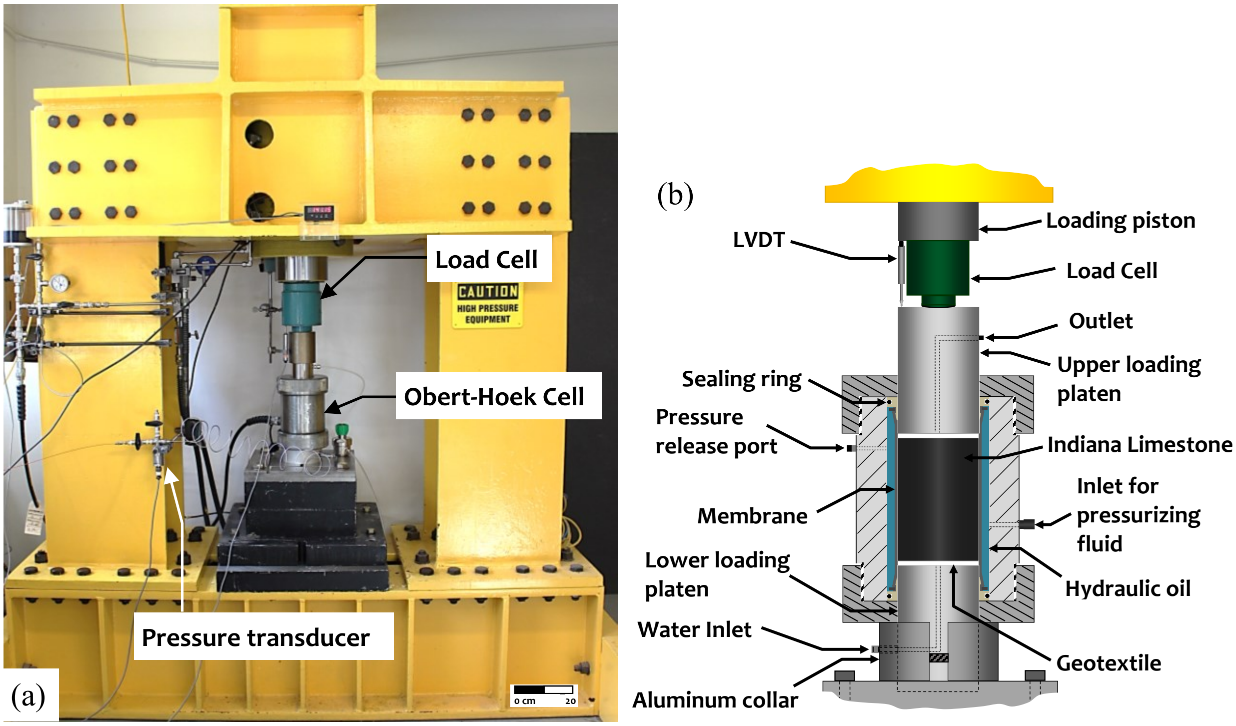

Figure 7.2: (a) View of the testing facility (b) Cross-sectional detail of Obert-Hoek Cell

After flushing air from the system a back pressure regulator was attached to the outflow line creating a known hydraulic gradient when a steady state condition was reached and preventing air bubbles being released from solution. An initial isotropic stress level of 5 MPa was used in all the tests. To achieve this stress state, axial and radial stresses were increased, in stages, simultaneously. Before application of the axial stress, the loading piston had to be lowered using the electric hydraulic pump in order to initiate contact between the load cell and the upper loading platen. The fine control of the axial stress was performed using the manual hydraulic pump and maintained using a digitally controlled servo-hydraulic system (GDS™ Controller 1). The radial stress was also applied using a manual hydraulic pump and maintained by using a separate digitally controlled servo-hydraulic system (GDS™ Controller 2). The entire schematic view of the experimental setup was presented in Figure 4.3. The fluid flow through the pressurized Indiana Limestone sample was supplied at flow rates as low as 0.5 mL/min which were verified to be well within the laminar flow regime. The validity of the Darcy flow regime for conducting steady state flow tests on Indiana Limestone was discussed in the research conducted by Selvadurai and Selvadurai (2010). Based on the assumptions used by Selvadurai and Selavdurai (2010) for calculating the Reynolds number and the average pore diameter from MIP test (see Appendix D), the flow rates used in the current tests fall well within the Darcy flow range with $\mathrm{Re} = 3.4 \times 10^{-9}$ when compared to the limit $\left(\mathrm{Re} \ll\right.$ given by Philips (1991) where n is the porosity (i.e. 0.16). Furthermore, based on criterion presented by Zeng and Grigg (2006) the Forchheimer number (Fo = 0.000003) falls below the non-Darcian flow regime criterion (Fo = 0.005 to 0.2). The pressure gradient induced during the attainment of a steady flow rate was monitored on the inlet side, using a pressure transducer (Honeywell™, TJE-1500PSI) attached to the water supply line. Both the cell pressure and the fluid pressure were monitored throughout the test as well as the temperature of the permeating water and the axial load. All the results were recorded using TracerDAQ™ Pro software by Measurement Computing™ and saved on a computer via a data acquisition system (USB-1408FS by Measurement Computing™).

Water temperature was maintained to be within 23°C to 25°C during the testing sequence. Each test commenced by subjecting the Indiana Limestone sample to a specified combination of equal axial and radial stresses. Once permeability was determined at that isotropic stress state, the axial stress $\left(\sigma_1\right)$ was increased using the manual hydraulic pump to the desired level and maintained by the GDS™ controller 1. The stress sequence used during permeability measurements, which followed that same stress paths as the compressive strength tests (see Figure 2.2), (where σ_f is the total failure stress for a specific confining stress state determined from triaxial tests, see Figure 2.3) was as follows:

(a) Attainment of an isotropic stress state: the axial stress σ_1 and the radial stress σ_3 (see Figure 7.3) were increased continuously until the desired isotropic stress state was reached (e.g. $\sigma_1 = \sigma_3 = 15\,\mathrm{MPa}$) and the permeability was measured.

(b) Application of deviatoric stress state: the radial stress was maintained at the value attained in (a) and the axial stress was increased continuously until the $0.5\sigma_\mathrm{f}$ and $4/5\,\sigma_\mathrm{f}$ axial stresses were reached and maintained during permeability testing (i.e. $\sigma_3 = 15\,\mathrm{MPa}$, $\sigma_1 = 0.5\sigma_\mathrm{f} = 43\,\mathrm{MPa}$).

(c) Application of a failure stress state: the radial stress was maintained at the value attained in (a) and the axial stress is allowed to reduce past the peak failure value (e.g. $\sigma_3 = 15\,\text{MPa}, \sigma_1 < \sigma_f$) and maintained constant during permeability testing.

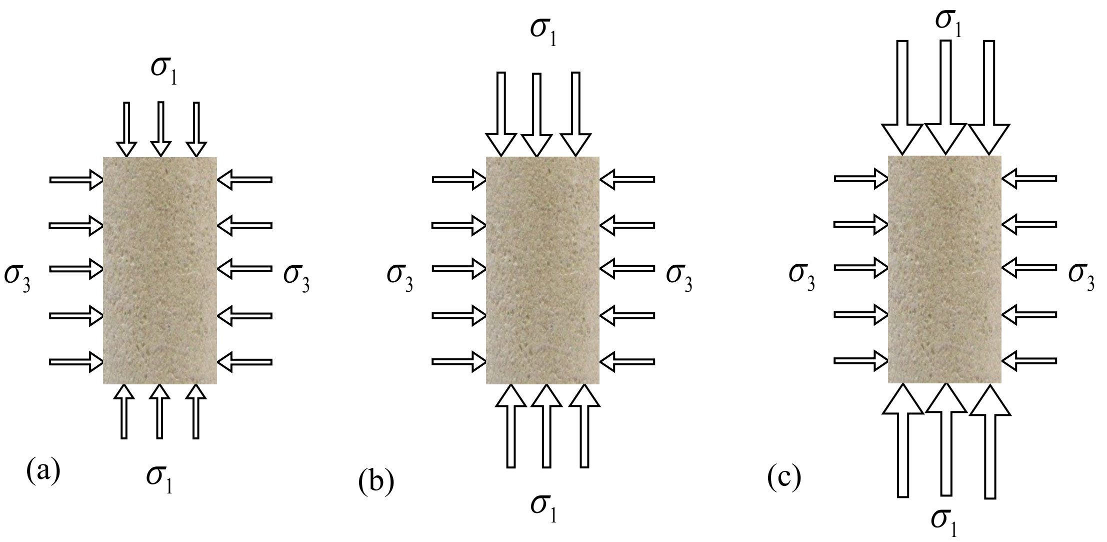

Figure 7.3: Sequence of stresses applied to samples tested in the modified Obert-Hoek Cell: a) isotropic stress state (i.e. $\sigma_1 = \sigma_3 = 15\,\text{MPa}$); b) deviatoric stress state (i.e. $\sigma_3 = 15\,\text{MPa}$, $\sigma_1 = 0.5\sigma_f = 43\,\text{MPa}$); c) deviatoric stress state post-failure (i.e. $\sigma_3 = 15\,\text{MPa}, \sigma_1 < \sigma_f = 85\,\text{MPa}$).

7.3 Results

Steady state permeability tests were performed at confining stress states that were limited to (5, 10, 15, 20 and 30) MPa. The minimum fluid pressures needed to initiate one-dimensional flow through the sample can vary with the radial and axial stress states. For example, (i) when the isotropic stress was 5 MPa, the inlet water pressure was 114 kPa (i.e. 2.3% of the radial stress) and when failure was initiated at a radial stress of 5 MPa and an axial post-failure stress of

38 MPa, the inlet water pressure was 6.2% of the radial stress; and (ii) when the isotropic stress was 30 MPa, the inlet water pressure required for steady flow was 0.9% of the radial stress and at a post-failure stress of 97 MPa, the inlet water pressure was 3.9 % of the radial stress. Considering the relative magnitudes of the minimum radial principal stress and the maximum pore fluid pressures in the permeability tests, it can be concluded that within the range of accuracy of the measurements, the externally applied radial stresses and the axial stresses can be regarded as being equivalent to the effective stresses that are applied to the Indiana Limestone sample. The calculated minimum and maximum permeabilities were $1.1\mathrm{E}-16\,\mathrm{m}^2$ and $4.4\mathrm{E}-15\,\mathrm{m}^2$ respectively. The stress range over which the permeability was tested covered the brittle, transitional and the ductile failure regime of the Indiana Limestone.

The results show a decrease in permeability for all samples loaded up to 80% of the failure load. Post-failure, the permeability increased only slightly (on average 7% with respect to pre-failure stress states) and a distinct crack (see Figure 7.4) was formed when tests were carried out at isotropic stresses between 5 MPa and 15 MPa. However, the permeability determined from steady state tests remained constant for post-failure at confining stress states of 20 MPa and 30 MPa.

Figure 7.4: Indiana Limestone post failure subjected to confining stress of 15 MPa.

7.4 Analysis of Experiments on Indiana Limestone

The results of permeability estimates obtained from the eleven samples [31 experimental data points] were used to develop a stress state $\left(\sigma_1, \sigma_3\right)$ dependent permeability evolution model for the tested Indiana Limestone. The experimental data was analyzed and several empirical relationships were investigated. A requirement was that the relationship should be capable of incorporating either the *tensile* or *compressive* nature of the axial and radial stresses. Since the relationship is to be derived from triaxial stress states applicable to the *compressive stress range*, the relationship *should not contain quadratic terms* in σ_1 and σ_3 but should include non-linear dependencies. The exclusion of quadratic terms would allow the use of the relationships to approximately account for permeability changes in the tensile stress range (i.e. the permeability can increase with a tensile stress state and decrease with a compressive stress state.). Considering this constraint and recognizing the type of relationships that have been established for variations of permeability during isotropic compression of Indiana Limestone (Selvadurai and Głowacki 2008) the relationship is restricted to the exponential dependence of permeability with linear arguments in σ_1 and σ_3, i.e.:

$$\frac{K(\sigma_1,\sigma_3)}{K_0}=\exp\left\{-\lambda_1\frac{\sigma_1}{\sigma_{\mathrm{T}}}\right\}\exp\left\{-\lambda_2\frac{\sigma_3}{\sigma_{\mathrm{T}}}\right\} \tag{7.1}$$

where σ_1 is the major principal stress and σ_3 is the minor principal stress (in MPa); $\sigma_{\mathrm{T}}(=3.7\,\mathrm{MPa})$ is the average tensile strength; $K_0=4.0\times10^{-15}\,\mathrm{m}^2$ is the average initial permeability in the unstressed state and λ_1 and λ_2 are constants to be determined from a statistical analysis of the data.

When the complete set of experimental data was used to evaluate the constants λ_1 and λ_2 in (7.1), the coefficient of determination was approximately $\mathrm{R}^2 \in (0.6493)$. In order to examine the sensitivity of the developments to the data set, certain experimental data points that clearly could be classified as ***outliers*** were systematically excluded by considering the residuals with respect to the proposed model. Referring to Figure 7.5, the identified ***outliers*** are shown with squares. When these outliers were removed in succession, the values of the coefficient of determination improved from $\mathrm{R}^2=0.65$ to $\mathrm{R}^2=0.80$. Referring to Figure 7.5, the results of the analysis indicates that the *four outlier points* $(2.7,2.7,0.07)$; $(5.4,5.4,0.05)$; $(8.1,4.1,0.52)$ and $(10.3,2.7,0.06)$ have a significant influence on the parameter identification exercise as well as on capturing the general trend of what could be realistically expected in permeability evolution with stress, in a relatively homogeneous rock.

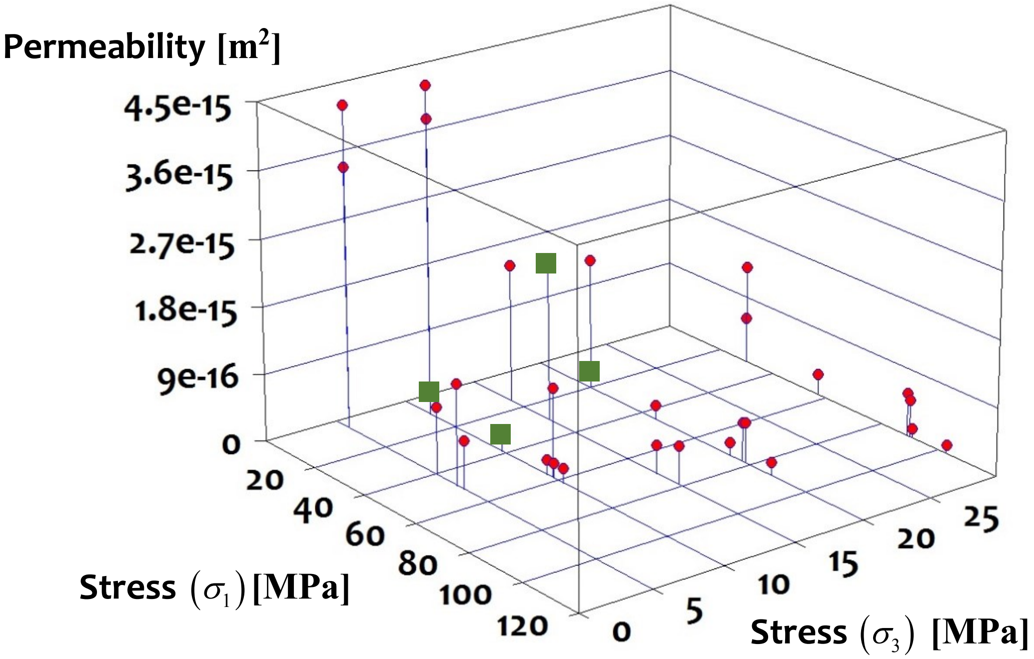

Figure 7.5: Permeability evolution with stress state, where σ_1 is the maximum principal stress and σ_3 is the minimum principal stress. Data points shown in 3D space with selected 4 outliers points (boxed in squares) based on residual analysis of the data.

The empirical expression (7.1) which gave the **highest coefficient** of determination was selected as a plausible expression for modelling the state space surface, ***including the four data points described as outliers***. The surface presented in Figure 7.6 can be described by equation (7.1), with the following parameters: $\lambda_1 = 0.12$; $\lambda_2 = 0.05$; $\sigma_\mathrm{T} = 3.7\,\mathrm{MPa}$; $K_0 = 4.0 \times 10^{-15}\,\mathrm{m}^2$. The outlier points are presented in Figure 7.6 for purpose of reference.

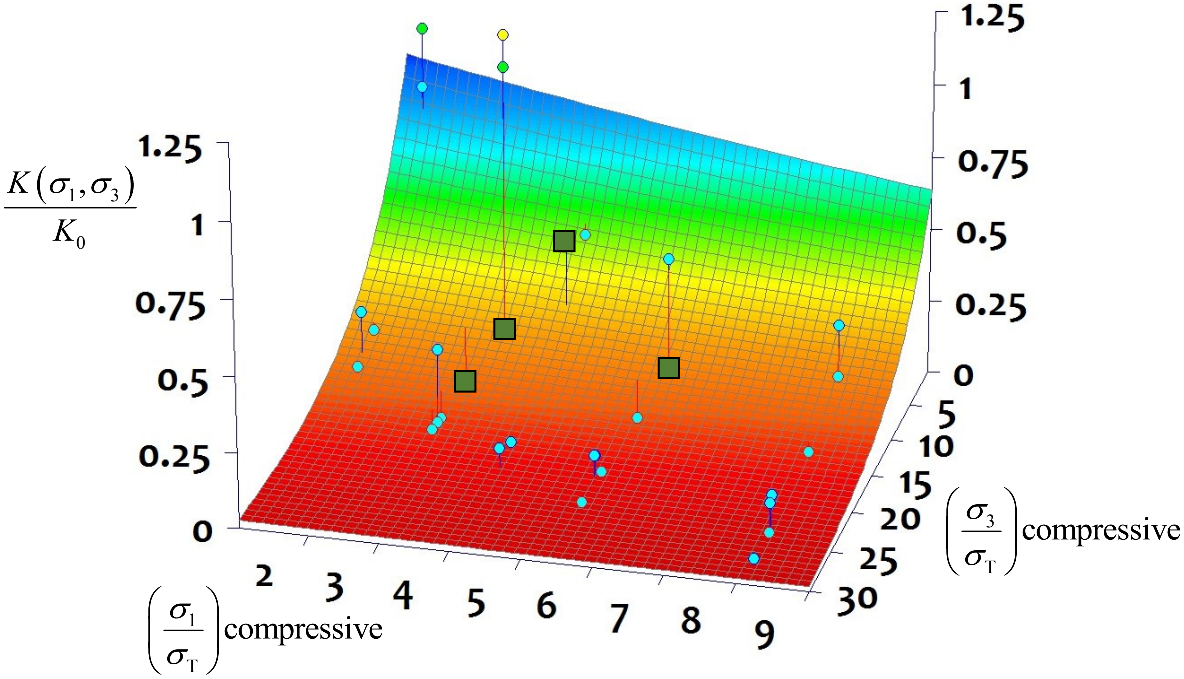

Figure 7.6: Permeability evolution with stress state, where σ_1 is the maximum principal stress and σ_3 is the minimum principal stress (all stresses normalized with respect to the tensile strength of the Indiana Limestone). Data points shown in 3D space with vertical lines (error) connecting to the surface, including selected 4 outliers points (boxed in squares).

7.5 Computational Application of Results to Tunnels

The developed empirical model (equation 7.1) was used to analyze an idealized problem where seepage occurs into an unlined circular tunnel constructed in an elastic rock mass. The in-situ stress state in the rock is geostatic with a bulk unit weight of the rock $\gamma = 22\,\text{kN/m}^3$. The unlined cylindrical cavity has a diameter $2a = 3.0\,\text{m}$ and is located at a depth of 1300 m; the rock mass is assumed to be isotropic elastic with $E = 33.0\,\text{GPa}$ and $\nu = 0.3$ (see Figure 7.7). The ground water level is considered to be at the upper surface of the problem domain and the DATUM on the lower surface. For purposes of illustration we assume that both the *elasticity* *problem* and the *fluid flow problem* can be modelled by considering symmetry of the domain. The computations are performed using the multiphysics code COMSOL™. First, the fluid inflow rate to the tunnel is calculated by assuming that the permeability of the rock is at the unaltered value of $K_0 = 4.0\times10^{-15}\ \mathrm{m}^2$. In the second modelling exercise, alterations in the stress state due to the construction of the tunnel are established from an elastic analysis of the unlined tunnel problem (see Figure 7.8). The spatial distribution of permeability in the elastic material is now estimated from the relationship (7.1) and the fluid flow into the cavity is calculated with the revised spatial distribution of permeability. The computed distribution of the altered permeability is shown in Figure 7.9**.** The calculated values of fluid flow rates are as follows:

(i) Fluid flow into the cylindrical cavity *without any stress-induced alteration of permeability* is $4.12\ \ \mathrm{m}^3/\mathrm{day}/\mathrm{m}$ of the tunnel. The average fluid velocity at the boundary of the opening is $5.1\times10^{-4}\,\mathrm{cm}/\mathrm{sec}$.

(ii) Fluid flow into the cylindrical cavity *taking into consideration stress-induced alteration* in the permeability of the rock is $2.02\ \ \mathrm{m}^3/\mathrm{day}/\mathrm{m}$ of tunnel. The average fluid velocity at the boundary of the opening is $2.5\times10^{-4}\,\mathrm{cm}/\mathrm{sec}$. The permeability varied from $K_0 = 4.0\times10^{-15}\,\mathrm{m}^2$ up to $K = 8.3\times10^{-16}\,\mathrm{m}^2$ in the most compressed region in the vicinity of the tunnel.

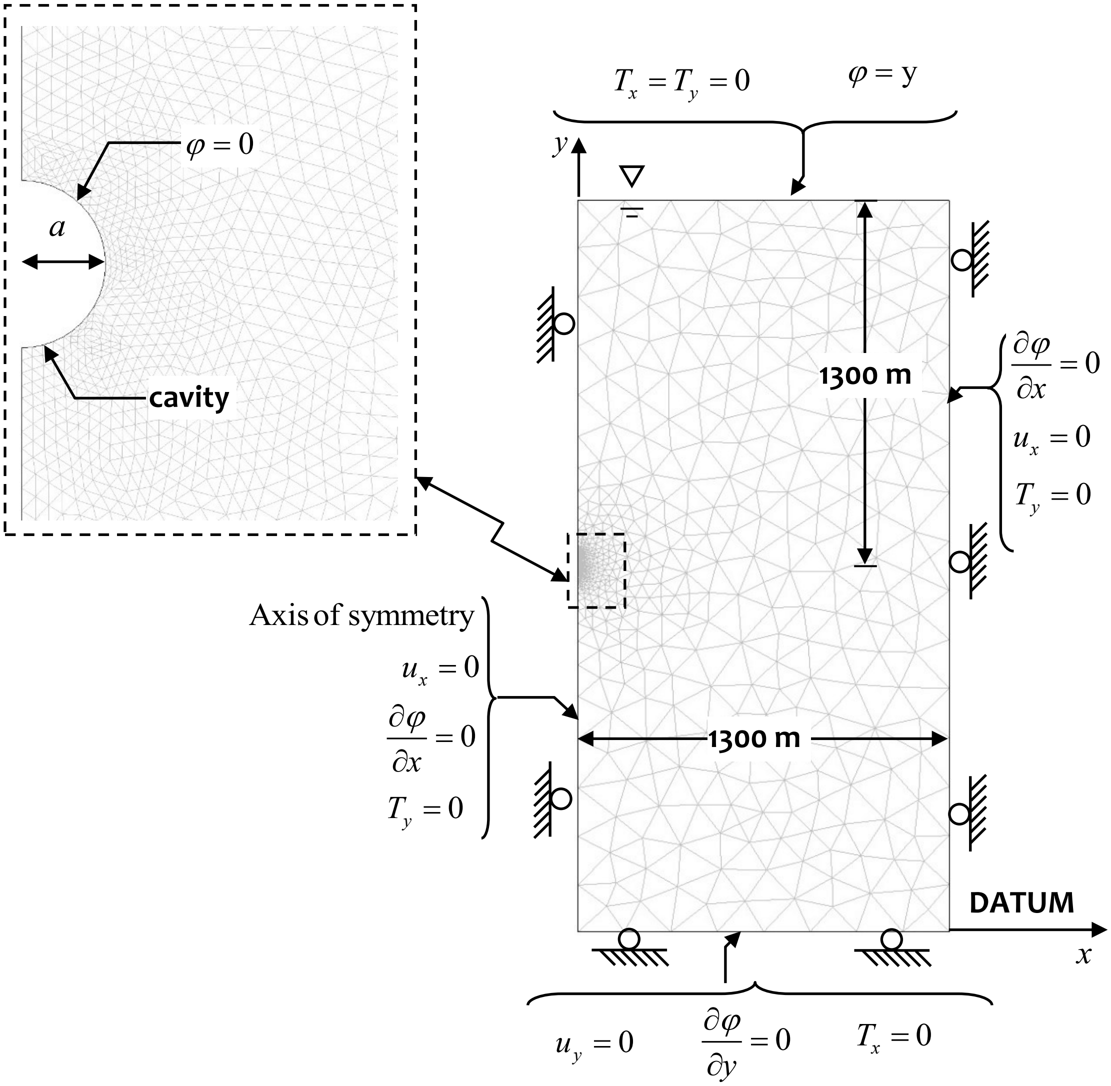

Figure 7.7: Computational representation, with COMSOL™, of an underground tunnel subjected to compressive stresses: mesh refinement and boundary conditions for modeling.

7.6 Summary

The proposed state space description of permeability evolution with principal stresses (σ_1 and σ_3) is a convenient representation that is suitable for adaptation in geomechanics problems where the stress state is expected to change due to engineering activities, such as deep excavations and underground construction. The results of permeability alteration with stress can be used in computational codes that can model the influences of stress states and permeability evolution either in an independent or coupled approach in order to examine the influence of permeability alterations on groundwater flow and seepage. The experimental results show that there is a slight increase in permeability, in the brittle failure regime; however, this can be attributed to the stress reduction after failure (i.e. the sample is subjected to an axial stress state lower than the failure stress). In the ductile failure regime the sample experienced irreversible changes in the fabric of the rock and compression of the pore space, similar to the development of compaction bands that can act as barriers to fluid flow; as a result, the estimated permeability decreased. These processes materialized without significant alterations in the overall dimensions of the rock sample. Also, the stress states applied to the samples do not lead to the development of failure planes that had significantly higher permeabilities in comparison to the parent material. Even in such situations, the method of permeability testing should be capable of capturing the fluid flow through the failure region; however, one-dimensional fluid flow arrangements are incapable of addressing this issue unless the failure plane forms a direct path through the tested sample between the end planes.

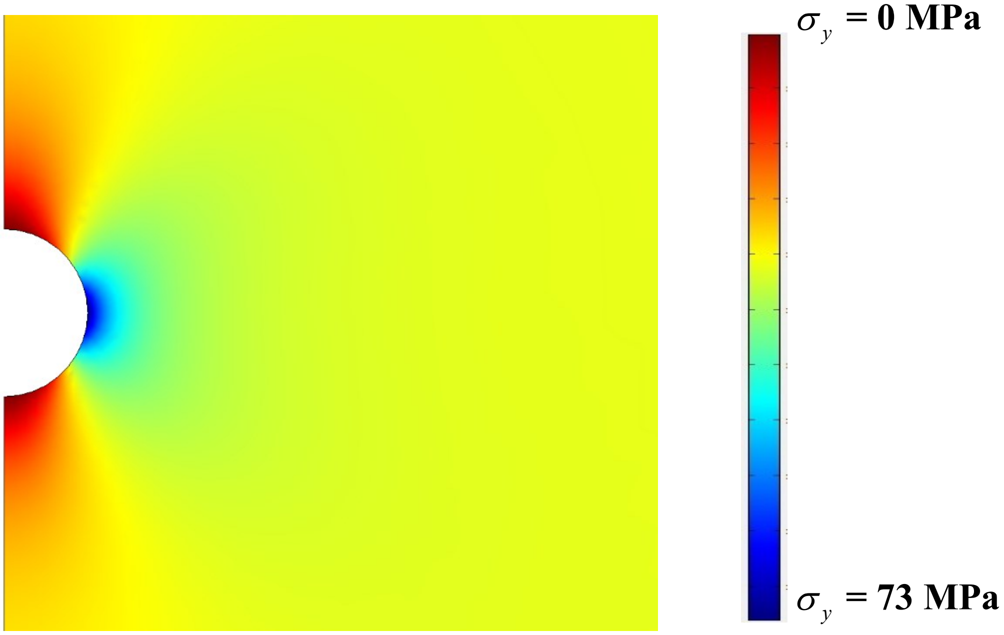

Figure 7.8: Computational representation, with COMSOL™, of an underground unlined tunnel subjected to compressive stresses: the vertical stress distribution is shown.

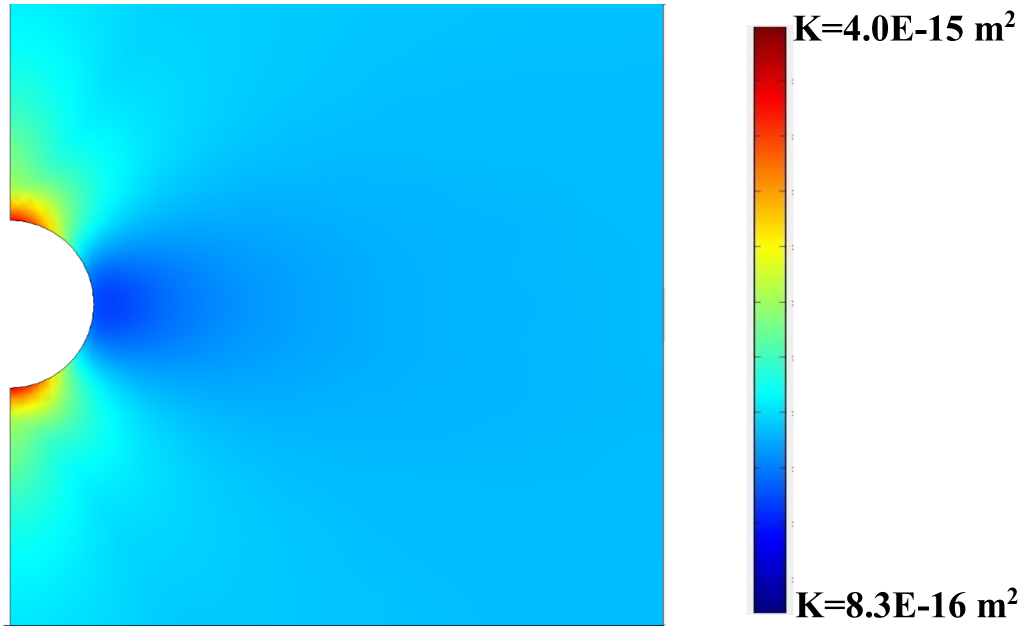

Figure 7.9: Computational representation, with COMSOL™, of an underground unlined tunnel subjected to compressive stresses: permeability distribution.

CHAPTER 8

STRESS-INDUCED PERMEABILITY EVOLUTION IN THE COBOURG LIMESTONE

8.0 Introduction

This chapter describes the results of a series of permeability tests that were performed on cylindrical samples of Cobourg Limestone subjected to triaxial stress states, using the modified Obert-Hoek Cell. Samples were subjected to stress states with magnitudes that are to be expected at the depth of the proposed DGR for storing the low to intermediate-level nuclear waste at the Bruce Nuclear Site in Kincardine, Ontario. The permeability was estimated either by the pulse decay method (pre-failure) or the steady state method (post-failure). Furthermore, it was intended in the current research to simulate the EDZ (post-failure) that can occur in the vicinity of a tunnel constructed at the proposed DGR location and estimate the effective permeability. Previous laboratory experimental work on this Cobourg Limestone, with small samples (50 mm in diameter and 125 mm in height), was done by Nassari et al. (2013) using a Hoek-type triaxial cell and the pulse decay method to measure permeability up to failure under variable temperatures (from 25ºC up to 150ºC), with a radial stress of 12.5 MPa. The results show that during the initial stages of axial loading the permeability *decreases* with an increase in temperature, followed by an *increase* in permeability with increased axial loading up to failure. In contrast this chapter deals with experiments conducted at room temperature and post-failure permeability estimates using larger (85 mm diameter) samples of Cobourg Limestone under varying radial stress conditions ($\sigma_r \in 0\,\mathrm{to}\,30\,\mathrm{MPa}$). Based on conducted tests by Montazer and Hustrulid (1983) on unsaturated fractured (EDZ) metamorphic rocks (quartz monzonite migmatite) in a mine laboratory using steady state and pulse decay methods with air and water injections directly into boreholes using a packer system; their results show that for post–failure the factures, normal to the maximum principal stress axis, closed due to high stress concentrations around the opening hence that fracture permeability decreased. The report by Lanyon (2001) for NWMO looks into the development of EDZ, in particular from engineering activities related to construction of underground laboratories and repositories at various location around the world; it summarizes the current methods used to characterize the hydraulic properties of EDZ zones and discusses the difficulties in obtaining experimental data for permeability in the EDZ. The report states that in general the permeability decreases with distance away from the tunnel and the EDZ; and that the results are influenced by local conditions such as saturation. With heterogeneous geological media, the external application of isotropic compression can also lead to the development of non-uniform stress states in the internal fabric of the geological medium that can result in an *increase* in permeability. An increase in permeability in the argillaceous Cobourg Limestone under isotropic compression is reported by Selvadurai *et al*. (2011), which results are shown in Figure 1.7.

Cobourg Limestone has been investigated by the McGill Environmental Geomechanical group for a number of years, with research focusing on the permeability of the rock under isotropic stress states, thermal effects and radial flow with normal and parallel orientations to the bedding plane (Selvadurai *et al.*, 2011; Selvadurai and Jenner, 2013; Selvadurai and Najari, 2016). The current research builds on the experience and extends the experimental work by exploring the permeability evolution with deviatoric stress states, including post-failure conditions. This allows the development of empirical equations for the stress state permeability evolution with triaxial stresses, which will aid in the studies related to a future DGR.

8.1 Sample Preparation

The presence of a nominal bedding plane with differences in permeability either normal to or along the phases sets some restrictions on the selection of samples of the Cobourg Limestone for laboratory testing. In the current experimental research, the samples were cored normal to the nominal bedding plane. The cored samples were machined and ground to size (long samples 85±1mm in diameter and 125±5mm in length and short samples 85.4±0.1mm in diameter and 84.4±1.6mm in length). In total, 12 samples were prepared for permeability evolution with changing stress states testing. One sample was selected for investigation of permeability evolution with the pre-failure stress states (see Section 8.2). This particular sample (CL1H) was saturated for 79 days prior to testing, using the vacuum saturation method described in Section 4.4. The remaining samples that were tested to failure and were initially air-dry. It is assumed that the formation of EDZ during construction would produce fractures in the rock around the tunnel and that those fractures will not be saturated (Lanyon, 2001).

8.2 Experimental Setup and Procedure: Pulse Decay Pre-failure

In this research permeability estimations were obtained using the modified Obert-Hoek Cell with the sealing rings and black rubber (Nitrile) tubing used to apply triaxial stress states (see Sections 4.1 and 4.2 and Figure 4.5). Due to the number of permeability tests performed (pre-failure) and time required to conduct all the tests at various stress states, the modified Obert-Hoek Cell was setup in the axial loading frame (HCLC Testing facility) located in the EGL (see Figure 8.1). The application of axial and confining stresses was presented in detail in Chapter 4 and in Appendix B. The test specimen was contained between upper and lower stainless steel loading platens. Both platens contained entry ports to provide water inflow and outflow. The interfaces between the plane ends of the platens and the sample were fitted with a stainless steel porous discs (see Figure 4.4) and geotextile which served to distribute the inflow evenly to the surface of the sample. A rubber membrane (Nitrile; thickness 2.4 mm) was used to seal the cylindrical surface of the sample; this membrane was capable of withstanding the applied peak confining cell pressures (up to 30 MPa) without rupture. From preliminary testing (see Chapter 4.1) and previous research (Selvadurai and Głowacki 2008; Selvadurai *et al*. 2011) it was established that a minimum radial stress of 5 MPa was sufficient to provide an adequate seal between the rubber (Nitrile) membrane and the sample to prevent interface flow during the experiment.

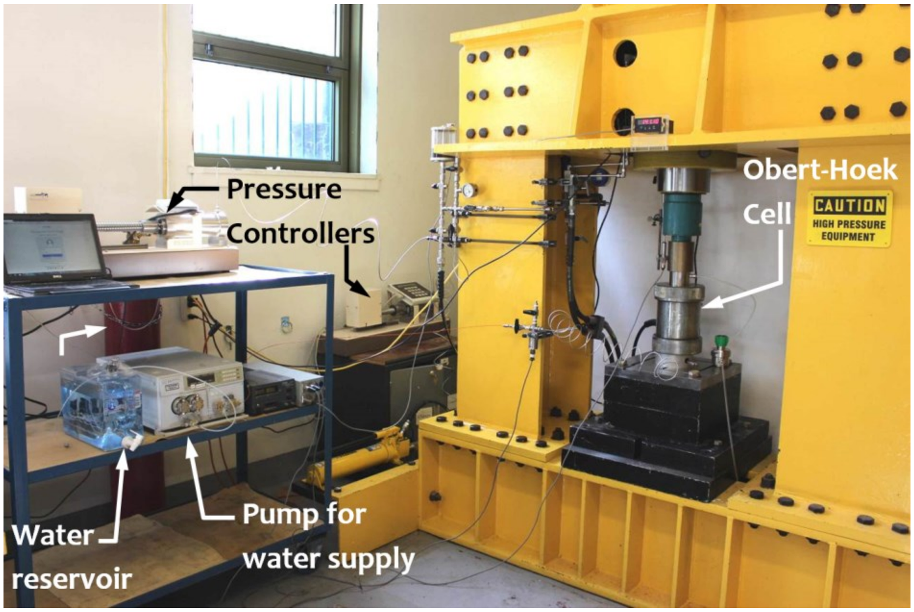

Figure 8.1: The High Capacity Load Controlled (HCLC) testing frame system with the modified Obert-Hoek Cell setup for pre-failure permeability estimation tests.

For these tests it was particularly important to ensure that the sample was fully saturated prior to testing. Selvadurai (2009) examined the influence of residual hydraulic gradients on the response of the 1-D hydraulic pulse test as well as the degree of saturation on the performance of the axial flow pulse test. In this regard, the sample was placed in a vacuum chamber (-78 kPa) for a period of 79 days prior to testing. The gain in mass was measured until it stabilized with a variance ±0.005% between measurements, at which point the sample was deemed to be saturated. The sample was then left in the chamber to depressurize (i.e. evacuate residual negative pressures) for a further 25 days before the first pulse decay test. The temperature of the water used in the permeability experiments varied between 23^{o}C and 31^{o}C (0.4 to 4.1 ^{o}C/test) during the extended period of testing over serval months. The permeating fluid used for testing was de-aired tap water and its pH, measured using an Oakton™ Waterproof Big Display pH Spear, was 6.8. During the sample installation inside of the modified Obert-Hoek Cell following with the setup in the axial loading frame, there was introduction of air into the system. This air was detected by analyzing the pressurizing curves which showed that initially, on average, 475 sec was needed to pressurize the system up to 200 kPa using 1.0 ml/min flow rates. From experience, this time was considered too long and several steps were taken to reduce the air content in the system and remove as much as possible the occluding air bubbles:

1) In order to remove the air pockets from the system, helium de-aired water was pumped through at 0.7 ml/min for 18 hrs. The flow of de-aired water through the pump, tubing and the unconfined sample, would flush out occluding air bubbles stuck to the wall of the flow path and carry them out of the system via the de-airing valve.

2) Additionally, the pressure inside the fittings, excluding the modified Hoek Cell, was raised twice up to 600 kPa and released in order to flush out air bubbles via the de-airing valve.

The above two processes decreased the pressurizing time to 180 seconds, which was still deemed unsatisfactory. Hence, in order to improve the pressurizing time the following additional steps were taken:

3) A vacuum venturi (-78 kPa) was attached to the pressurizing lines in order to de-air the water inside the lines and the pump.

4) The pump was purged of air using manufacturer’s recommended method, which involved a syringe and the application of negative pressure to the purging valve of the pump.

5) In order to purge air from the modified Obert-Hoek Cell, the porous disk and around the sample membrane interface, the confining pressure was reduced to 200 kPa and the inlet was pressurized to 200 kPa. The purging was stopped when the purging water emerged from

around the upper loading platen.

By performing all of the above processes the pressurizing time was reduced to 68 sec on average. Furthermore, the system (pump, tubing, fittings, excluding the modified Obert-Hoek Cell) was checked to assess the time it required to pressurize up to 200 kPa. This was done after the purging of the air content and the time was established at 24 sec; this time was determined to be due to the intrinsic flexibility of the experimental setup. This was the main reason why the analysis of the results was done by excluding the influence of the air content (see Section 3.2.1). The 5 MPa isotropic stress state served as the starting point for the stress-path sequence to test the permeability evolution, which can be summarized as follows:

Table 8.1: Sequence of stress states stages at which permeability of the Cobourg Limestone was tested.

Loading Isotropic Compression			**Unloading Deviatoric Stress States**			**Re-Loading Deviatoric Stress States**		
Stage	σ_1 [MPa]	σ_3 [MPa]	**Stage**	σ_1 [MPa]	σ_3 [MPa]	**Stage**	σ_1 [MPa]	σ_3 [MPa]
1	5	5	4	25	30	10	30	15
2	15	15	5	30	25	11	30	30
3	30	30	6	30	20			
			7	30	15			
			8	30	10			
			9	30	5			

Upon reaching a particular stress state, the stresses were stabilized using the GDS™ controllers for one hour before the permeability testing began. Fluid flows were supplied at flow rates of 1.0 mL/min using a liquid chromatography pump (Shimadzu™, LC-8A) for the pulse decay tests. The inlet fluid pressure was monitored using a pressure transducer (Honeywell™, TJE-300PSI) attached to the water supply line. The radial stress (σ_3) and the inlet fluid pressure, the temperature of the permeating water and the axial stress (σ_1), were monitored throughout the tests. All acquired data was saved to a computer using a data acquisition system (TracerDAQ™ Pro and USB-1408FS by Measurement Computing Corporation).

8.2.1 Permeability measurement pre-failure: hydraulic pulse decay

Taking into the account the magnitude of the applied stresses and the fluid pressures used in performing the permeability tests, all stresses mentioned below are total stresses. Based on preliminary testing it was observed that a period of 8 hours was needed to dissipate the residual pressure from a previous pulse decay test. However, a minimum period of 17 hours was allowed between two successive tests. At each stress state the number of pulse decay tests varied from 3 to 12 depending upon whether repeatability was achieved (see Figure 8.2). The process of testing was as follows:

1. The sample was confined at an initial stress of $\sigma_1 = \sigma_2 = \sigma_3 = 5\,\text{MPa}$
2. Pressure build up, at a specific stress state, was obtained by opening the inlet valve and allowing fluid inflow (1 ml/min) to pressurize the base of the sample up to 200 kPa.
3. At 200 kPa the inlet valve was closed and the pump immediately turned off.
4. Pressure was allowed to decay for a minimum of 3 hours.
5. To release the remaining pressure the inlet valve and the de-airing valve were opened for 15 seconds. This opening/closing of valves prevented air from infiltrating the pressurizing fittings and tubing.
6. The rock sample was allowed to stabilize for 17 hours which dissipated the pore pressure before the next pressure build up test.
7. A minimum of 3 repeatable pulse decay tests were performed at each stress state.

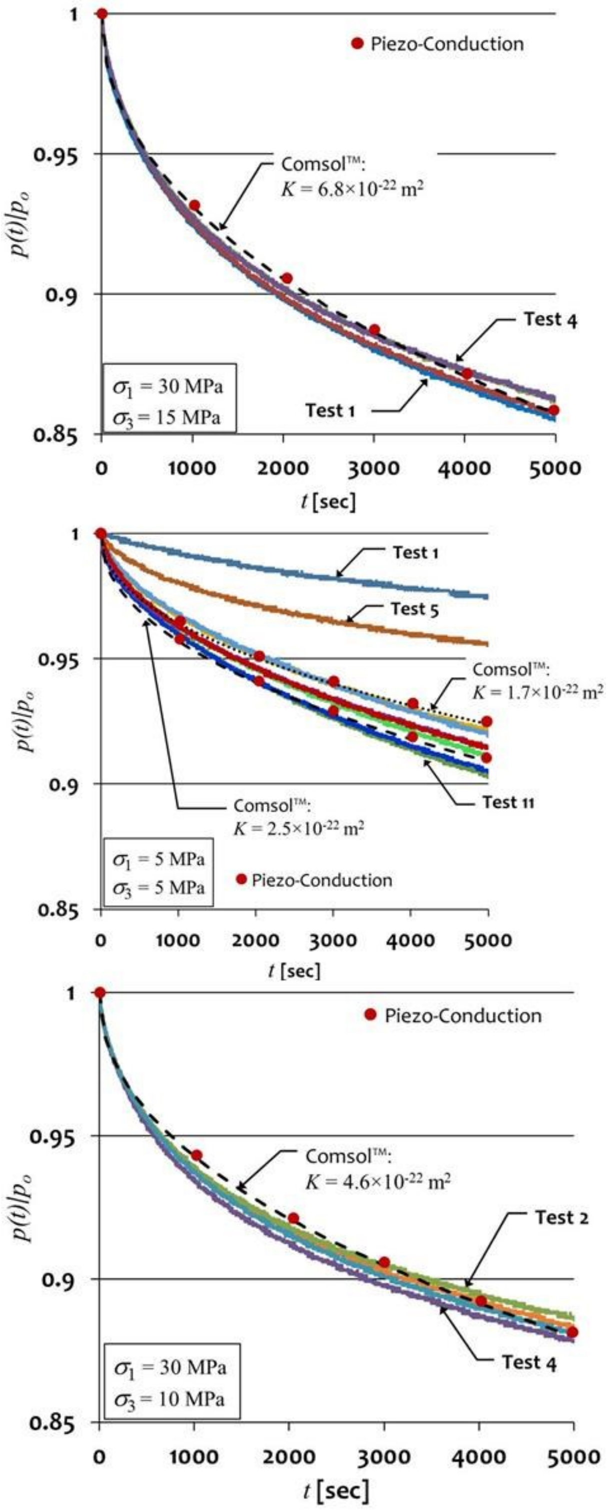

Figure 8.2: Hydraulic pressure decay curves vs time for varying stress states.

8.2.1.1 Computational model for hydraulic pulse decay tests

Governing equation used to solve this pulse decay problem was presented in Chapter 3 as the piezo-conduction equation (3.15). The numerical modeling of hydraulic pulse decay in COMSOL™ was described in Chapter 6 (see section 6.5). The boundary between the water cavity and the rock surface required a more refined mesh (see Figure 8.3) in order to account for the Heaviside step function-type discontinuous pressure gradients. These pressure gradients can develop in the computational model during the initial stages of the test, when the pore fluid pressure within the saturated rock is set to zero on one side but the adjacent water cavity has a high pressure. The following parameters were used in the numerical modelling to estimate the permeability using the COMSOL™ finite element code.

Skeletal Young's modulus (E) = 35 (GPa)

Skeletal Poisson's ratio (v) = 0.25

Porosity (n) = 0.006

Dynamic viscosity of water at 25 ºC (μ) = 0.000890 (Pa·s)

Density of water at 25 ºC (ρ) = 997 (kg/m3)

Compressibility of water (C_w) = 4.541×10^{-10} (Pa^{-1})

Compressibility of the solid grains (C_s) = 1.29×10^{-11} (Pa^{-1}) from equation (3.18)

Compressibility of the porous skeleton (C_{eff}) = 4.29×10^{-11} (Pa^{-1})

Estimated Biot coefficient (α) = 0.7; {in literature: 0.5 in OPG, (2011c) and 0.7 in Selvadurai and Najari, (2016)}

Sample dimensions: Diameter 84.62 mm; Height 129.83 mm

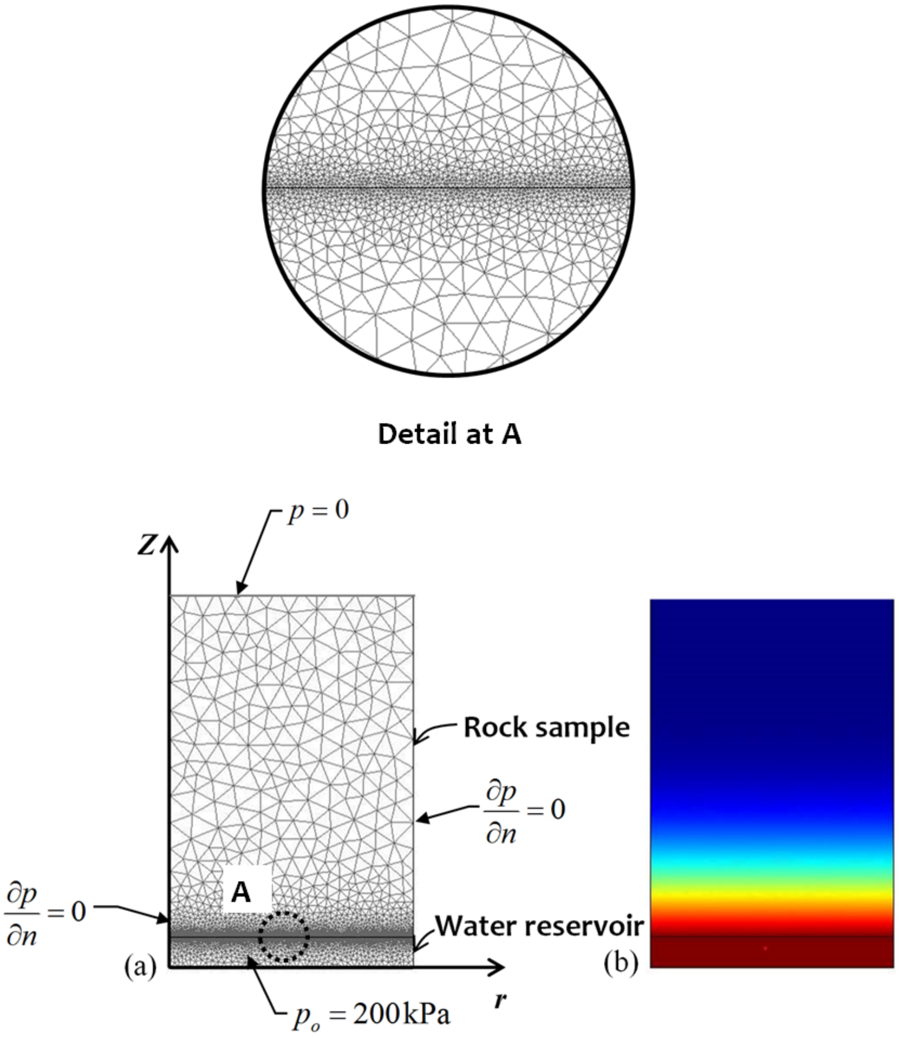

Figure 8.3: Finite element model for the hydraulic pulse decay permeability estimations: a) the boundary conditions and mesh; b) the pressure distribution after 5000 seconds.

8.3 Experimental Setup and Procedure: Steady State Post-Failure

During these tests there where a total of 12 samples tested to failure. All samples were tested using the modified Obert-Hoek Cell and the MTS™ rock frame (see Figure 8.4). The samples were subjected to 3 different confining stresses (10, 20 and 30 MPa) and allowed to fail in compression. The maximum confining stress (i.e. 30 MPa) was selected based on the knowledge of in-situ stresses that are to be expected (i.e. 18 MPa to 42 MPa; OPG, 2011b) at the Bruce Nuclear Site of the future DGR. Due to laboratory time constraint, all tests had an allocated total time of 8 hours from start to finish.

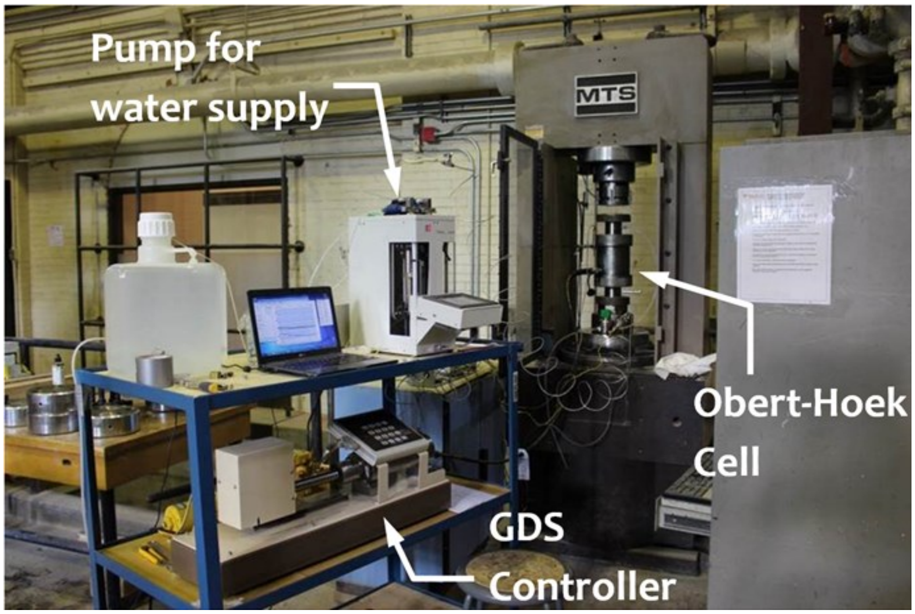

Figure 8.4: The MTS rock frame system with the Obert-Hoek Cell setup for post-failure permeability estimation tests.

One day prior to testing, the sample was positioned inside the fully assembled modified Obert-Hoek Cell and a confining stress of 300 kPa was applied in order to hold all components tightly connected inside the modified Obert-Hoek Cell during lifting and transport. The Cell was then lifted with the fork lift into the MTS rock frame and all the hydraulic lines, electrical lines and tubing were connected. When everything was in place, the confining stress was reduced to 0 MPa and the purging of air from the tubing and around the sample begun (see similar purging method in Section 7.2). Once the purging was finished, the sample was resealed with a nominal confining stress of 300 kPa and valves closed to isolate the sample and to prevent air re-entering the system.

The following day the test debuted with the loading sequence which involved simultaneously increasing the confining stress and axial stress to the initial isotropic stress state (i.e 10 or 20 or 30 MPa). The confining stress was increased using the manual hydraulic pump and then maintained with the GDS™ controller, wheras the axial load was increased and maintained with the MTS™ rock frame loading system. Once the confining stress was attained a constant pore pressure of 100 kPa was applied using a high precision pump (Quizix™ QX-6000). This constant pore pressure was maintained until post failure and the pore pressure was monitored using a pressure transducer. The main idea behind the constant pore pressure was to observe if, at any point around the peak failure stresses, there was a sudden drop in pore pressure, which would most likely be due to crack formation. The axial load was increased at a rate of 0.2 mm/min, which typically caused failure within the first 10 min. After failure, the axial load was unloaded (i.e. unloading at 0.4 mm/min) to the initial confining stress and reloaded (allowing 1.5 mm stroke displacement between each cycle of unloading and reloading). This was repeated 2 to 3 times on each failed sample (see Figure 8.5). Once the load cycling was finished, the MTS™ rock frame was put on hold which maintained a fixed position for the axial loading piston (i.e. axial displacement was kept constant) and allowed the axial load to decay to a constant value. At this point the steady state permeability testing was initiated (see Figure 8.6).

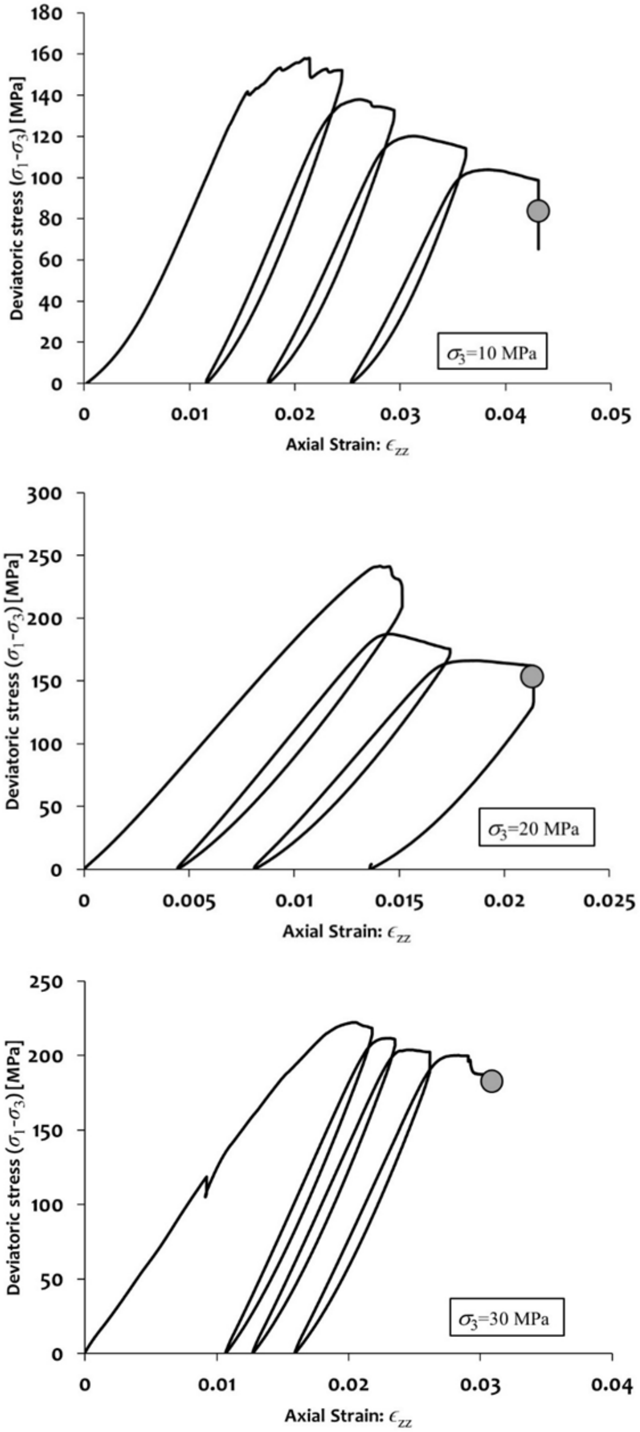

Figure 8.5: Typical results for the variation of deviatoric stress applied to the sample with axial strain [● Indicates the deviatoric stress level at which permeability tests were performed]

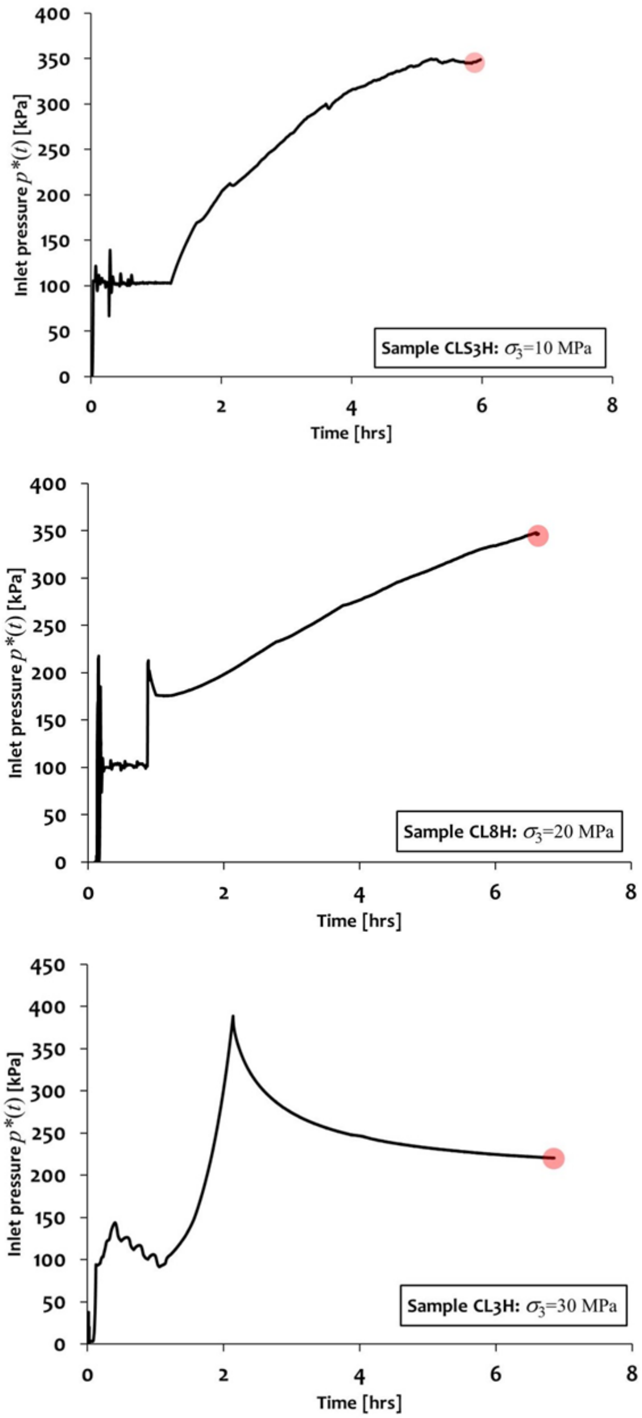

Figure 8.6: Time history of the entry point fluid pressure during steady state permeability tests of failed samples. [● Indicates the inlet pressure at which steady state permeability tests were performed].

8.3.1 Permeability measurement post-failure: steady state tests

The permeability testing of a failed sample was conducted when a stable stress state plateau was attained. Some axial load creep (i.e. 1 to 13 MPa in 5 hrs) was observed when the stress plateau (see Table 8.2) was reached. At this stress plateau a steady flow was initiated from the base of the failed sample to determine the effective permeability. Each test was completed within 5 hours.

Table 8.2: Estimated permeabilities from the post-failure tests on Cobourg Limestone cylindrical samples.

	Sample dimensions [mm]		**Total Stresses [MPa]**		**Estimated permeability [m^2]**	
Sample	Diameter	Length	σ_1	σ_3	**Steady state**	**Pulse decay**
CL4H	85.0	120.4	84 to 81	10	1.6E-16	-
CL5H	85.5	120.3	66 to 65	10	2.5E-18	6.8E-20
CL6H	85.3	121.4	86 to 73	10	2.0E-17	1.4E-19
CLSH1	85.4	86.0	90 to 77	10	2.4E-17	-
CLSH2	85.3	84.4	83 to 79	10	5.9E-17	-
CLSH3	85.5	82.9	86 to 75	10	3.5E-17	-
CL7H	85.6	121.1	134 to 129	20	-	2.3E-20
CLB1H	84.6	129.8	142 to 135	20	3.8E-18	1.5E-21
CL8H	85.6	122.0	165 to 154	20	5.7E-18	-
CL1H	85.6	132.0	183 to 179	30	-	3.5E-22
CL2H	85.2	134.8	159 to 147	30	3.7E-18	-
CL3H	85.4	119.8	190 to 185	30	2.0E-18	-

For each steady state permeability test the proviso was to select an appropriate flow rate, taking into consideration the likely extent of damage to the sample at near failure stresses, the inflow pressure build up, equipment pressure limits, and completing the test within a fixed timeframe. Typically the inflow rates ranged between 0.01 mL/min to 0.001 mL/min.

Due to the very low flow rates and the possibility of leakage, one sample was tested with water dosed with a tracer (Tri Tex inc: Triactive Red™ DF-6BL) applied at the inflow. Once the permeability test was completed and the sample removed from the modified Obert-Hoek Cell, it was visually inspected, photographed and the sample was separated along the visible planes of failure. Observations of the two fragments confirmed that the tracer was distributed throughout the entire height of the sample, with higher concentrations, as expected, on the inlet side and there was no evidence of leakage of tracer along the cylindrical surface. All failed samples were carefully removed from the confining membrane allowing little or no disturbance and photographed (panoramic views). The surfaces were lightly wetted in order to enhance the location of fractures and cracks, which were enhanced by overlay of red color to further highlight the cracks patterns (see Figures 8.7 and 8.8). The location of the failure cracks tend to be predominately located in the darker grey argillaceous phase.

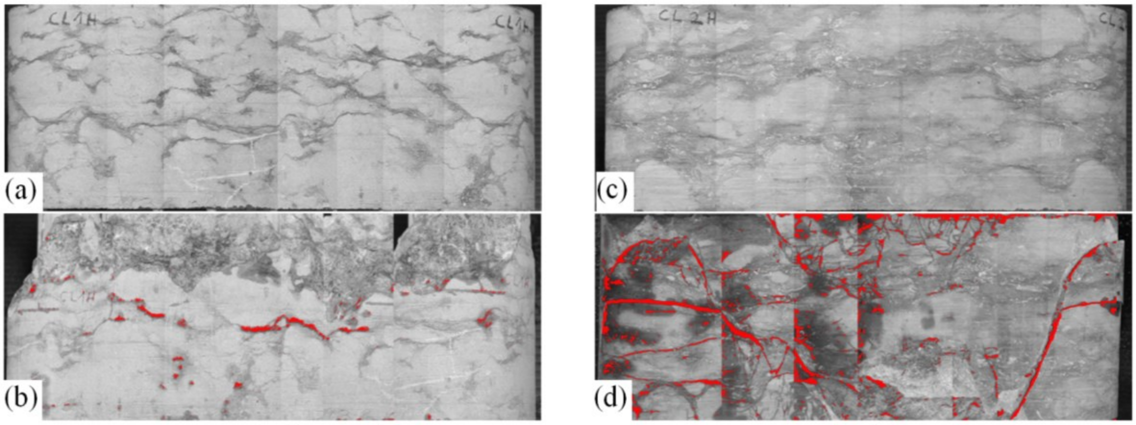

CL1H: $K_{PD} = 3.5\text{E}-22\,\text{m}^2$; $(\sigma_1 - \sigma_3)_{\max} = 205$ MPa

CL2H: $K_{SS} = 3.7\text{E}-18\,\text{m}^2$; $(\sigma_1 - \sigma_3)_{\max} = 220$ MPa

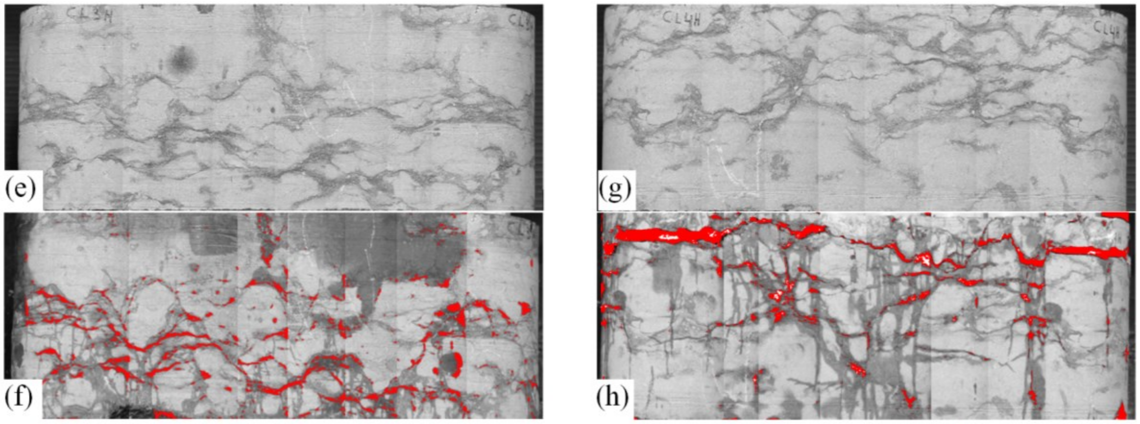

CL3H: $K_{SS} = 2.0\text{E}-18\text{m}^2$; $\left(\sigma_1 - \sigma_3\right)_{\max} = 222$ MPa CL4H: $K_{SS} = 1.6\text{E}-16\text{m}^2$; $\left(\sigma_1 - \sigma_3\right)_{\max} = 141$ MPa

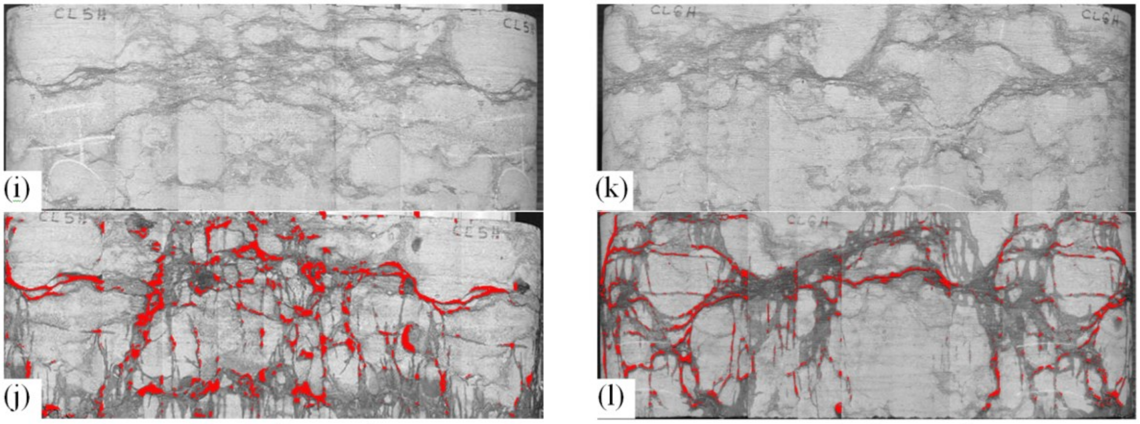

CL5H: $K_{SS} = 2.5\text{E}-18\text{m}^2$; $\left(\sigma_1 - \sigma_3\right)_{\max} = 128$ MPa CL6H: $K_{SS} = 2.0\text{E}-17\text{m}^2$; $\left(\sigma_1 - \sigma_3\right)_{\max} = 157$ MPa

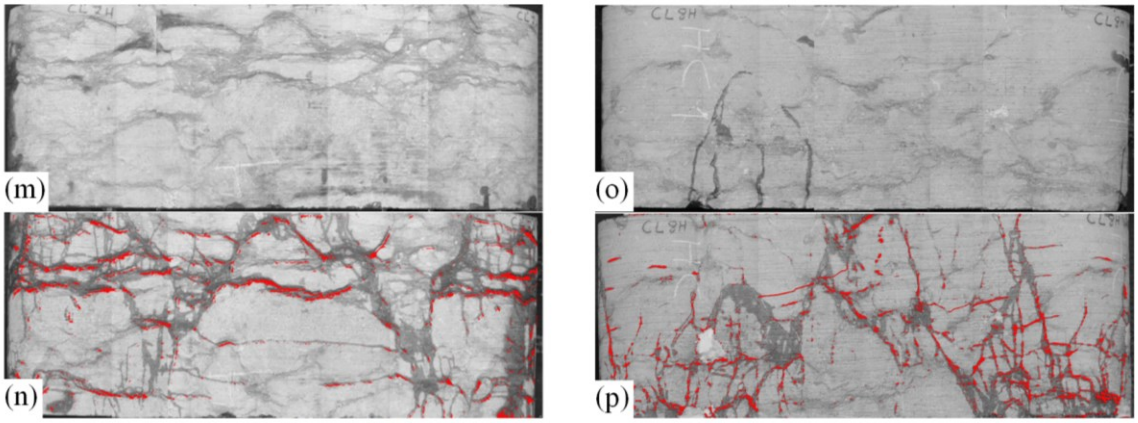

CL7H: $K_{PD} = 2.3\text{E}-20\text{m}^2$; $\left(\sigma_1 - \sigma_3\right)_{\max} = 197$ MPa CL8H: $K_{SS} = 5.7\text{E}-18\text{m}^2$; $\left(\sigma_1 - \sigma_3\right)_{\max} = 242$ MPa

Figure 8.7: Panoramic views of failure patterns observed on the cylindrical surface of the Cobourg Limestone samples measuring ~85mm diameter and ~120mm to 132mm long. [K_{SS} and K_{PD} are the permeabilities measured using the steady state or pulse decay method, respectively].

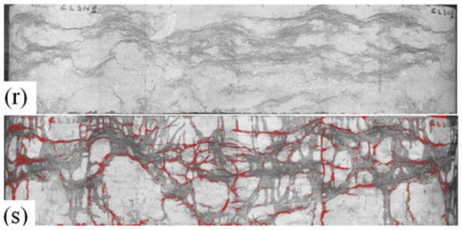

CLSH1: $K_{SS} = 2.7\mathrm{E}-17\mathrm{m}^2$; $(\sigma_1 - \sigma_3)_{\max} = 167$ MPa

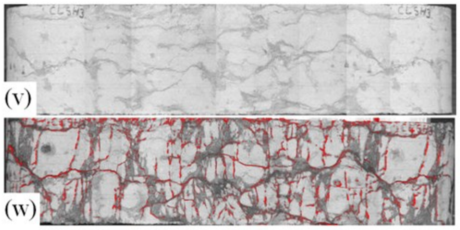

CLSH3: $K_{SS} = 3.5\mathrm{E}-17\mathrm{m}^2$; $(\sigma_1 - \sigma_3)_{\max} = 158$ MPa

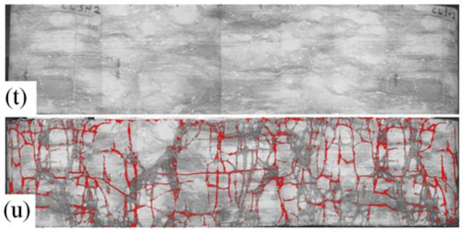

CLSH2: $K_{SS} = 5.9\mathrm{E}-17\mathrm{m}^2$; $(\sigma_1 - \sigma_3)_{\max} = 171$MPa

Figure 8.8: Panoramic views of failure patterns observed on the cylindrical surface of the short Cobourg Limestone samples measuring ~85mm diameter and ~85mm long. [K_{SS} is the permeability measured using the steady state method].

8.4 Analysis and Results

Results from pre-failure permeability tests were obtained by analyzing the decay curves and the results were plotted along with (i) the results of computational modelling and (ii) the results obtained from the analytical solution based on the piezo-conduction modelling. In certain instances the experimental results were bounded by the two computed decay curves in order to correctly assess the permeability range at a specific stress state (see Figure 8.2).

The averaged values of the computed permeabilities for the pre-failure tests were used to create a 3D representation of all the results at various stress states (see Figure 8.9). The results point to a trend of an increase in permeability as the compressive stresses increase.

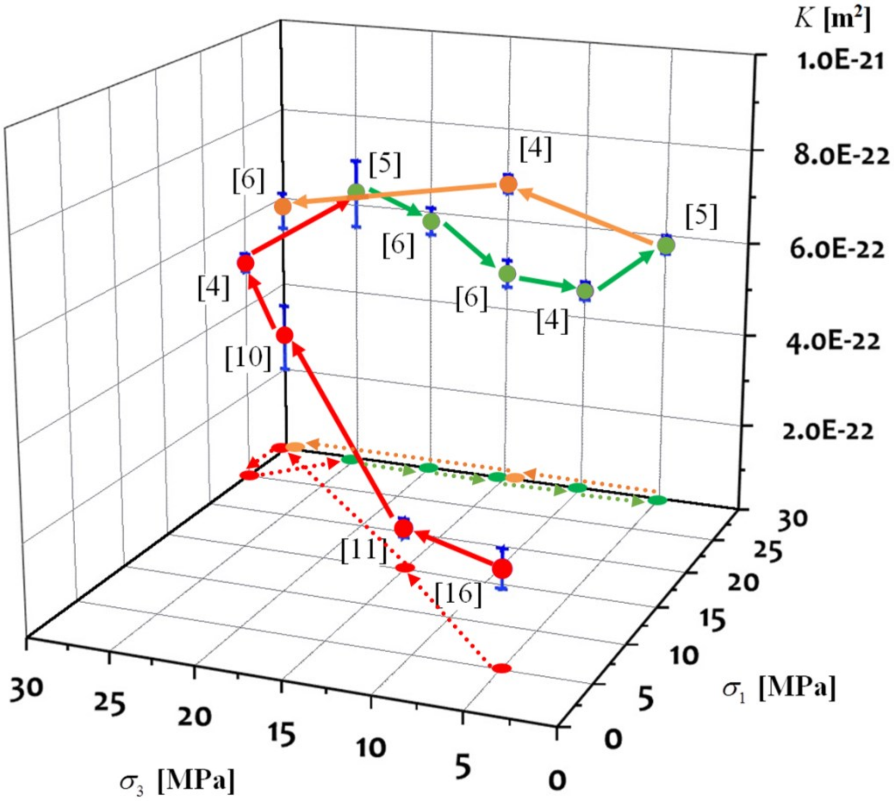

Figure 8.9: Stress state vs estimated permeability; loading sequence is indicated by arrows: **red** loading path, **green** unloading path and **orange** re-loading path; [n] indicates the number of tests per point; ellipses on the σ_1 and σ_3 planes are projections of the permeability stress state.

A summary of all permeability results (i.e. pre-failure and post failure) were plotted on a *p* vs *q* graph (see Figure 8.10) to give an overview of the permeabilities determined in the current study in relation to the stress state. The results show that post-failure the Cobourg Limestone permeability increases by *four orders* of magnitude in relation to the pre-failure permeability. Furthermore, the effective permeabilities obtained from post-failed samples at varying confining stresses, there is a two order of magnitude decrease in effective permeability as the confining stresses increase from 10 to 30 MPa.

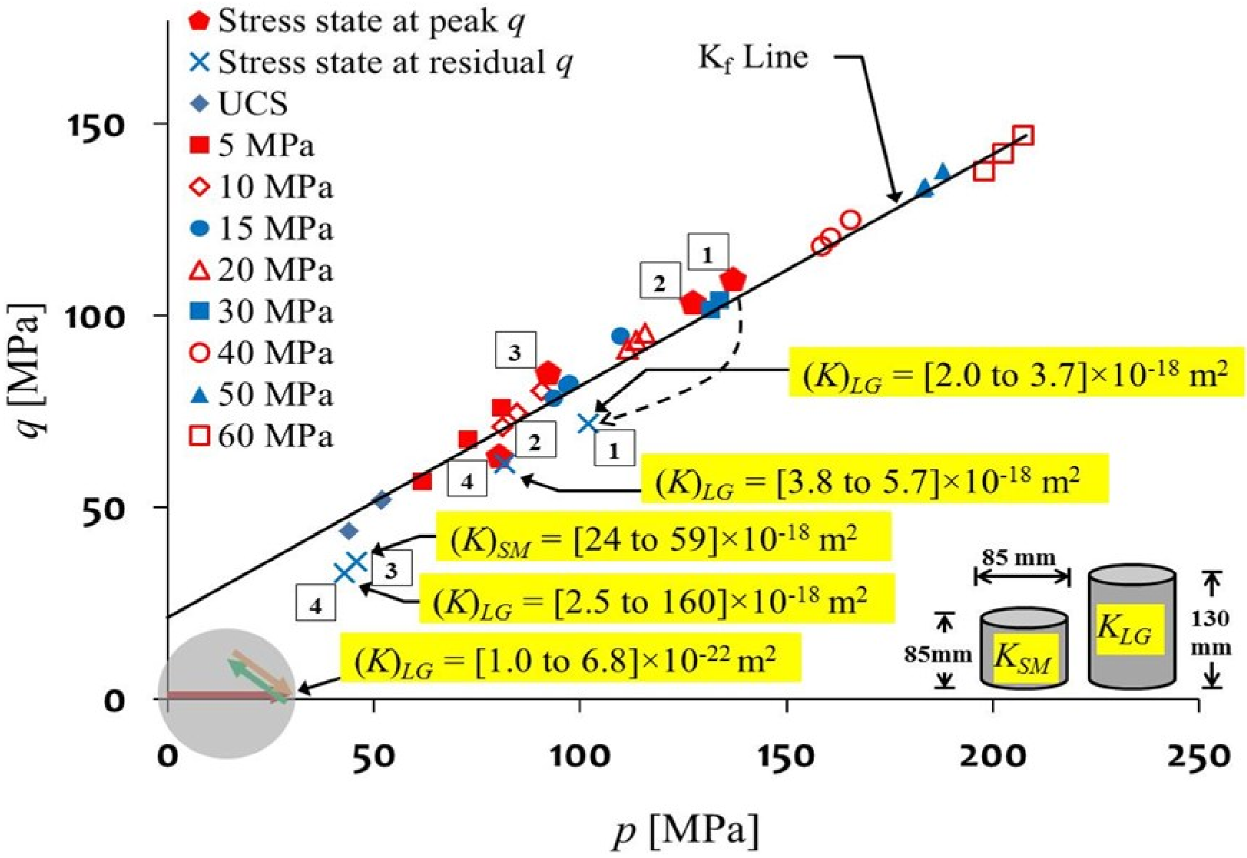

Figure 8.10: *p* vs *q* graph with results from the current study superimposed on results from unpublished previous studies.

8.5 Proposed Models for Permeability Evolution in Pre-Failure

Based on the results from the current study, two models are proposed to account for the evolution of permeability with stress state. The results can be represented in several ways, but a convenient representation is to illustrate the evolution of permeability in relation to the combination of total principal stresses σ_1 and σ_3. Since the permeability was evaluated during the application of isotropic stress states, the variation of permeability during the loading path can be expressed as a function of the mean applied stress $\sigma_m = \left(\sigma_1 + 2\sigma_3\right)/3$. Figure 8.11 illustrates the variation of the permeability with mean stress during loading. The approximate relationship (model 1) that can be developed for this loading path with a coefficient of determination of 0.84 is:

$$\frac{K\left(\sigma_1, \sigma_3\right)}{K_0} = \exp\left(\lambda_1^m \frac{\sigma_1}{\sigma_0}\right) \exp\left(\lambda_3^m \frac{\sigma_3}{\sigma_0}\right) \qquad (8.1)$$

where $\lambda_0^m \simeq$; $\lambda_1^m \simeq$; K_0 is the reference permeability ($1\mathrm{E}-22\,\mathrm{m}^2$) and σ_0 is the initial isotropic stress state of 5 MPa.

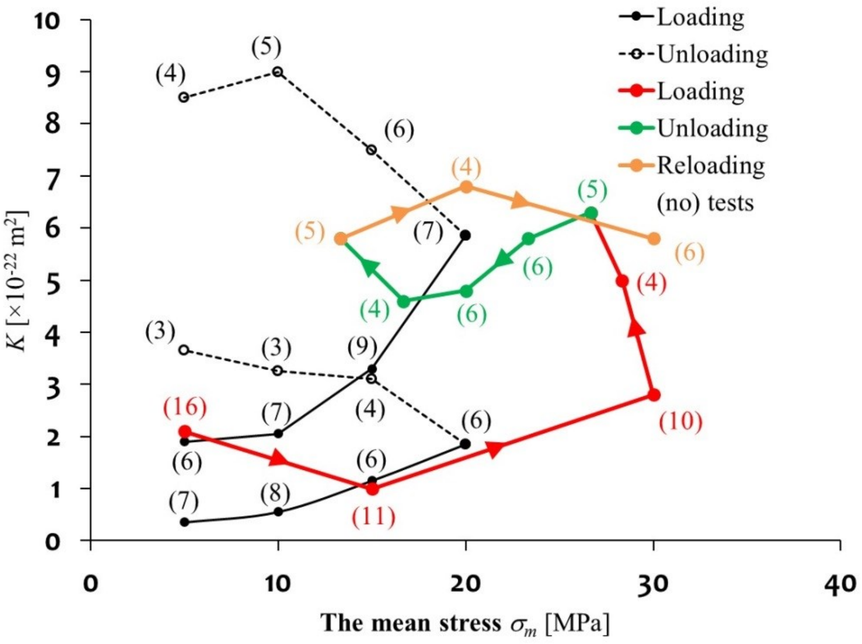

Figure 8.11: Permeability evolution of the Cobourg Limestone in the pre-failure stress states as a function of the mean stress $\sigma_m = \left(\sigma_1 + 2\sigma_3\right)/3$ [The solid and dotted black lines with no arrows refer to the results obtained by Selvadurai *et al*. (2011)].

The development of a general relationship for the evolution of permeability during a reduction in the minor principal stress σ_3 was not feasible since the unloading experiments were conducted only at a specific value (30 MPa) of the major principal stress. In this study, stress states were chosen to examine the evolution of permeability when stresses were varied orthogonal to the flow direction. An approximate relationship was developed by constructing a state space surface between the isotropic loading path (model 8.1) and the unloading path at a constant value of σ_1. The corresponding relationship (model 2) can be represented in the following form:

$$\frac{K\left(\sigma_1, \sigma_3\right)}{K_0} = \exp\left(\lambda_1^u \frac{\sigma_1}{\sigma_0}\right) + \exp\left(\lambda_3^u \frac{\sigma_3}{\sigma_0}\right) + \lambda_0^u \qquad (8.2)$$

where $\lambda_0^u \simeq \quad ; \lambda_1^u \simeq \quad ; \lambda_1^u = 0.20$.

The state space evolution of permeability with principal stresses between the isotropic loading and unloading path is shown in Figure 8.12. Such a proposed model (8.2) is useful in the context of DGR excavation studies. An example of such loading behavior would be during the excavation of an underground opening followed by the installation of a stiff liner as support.

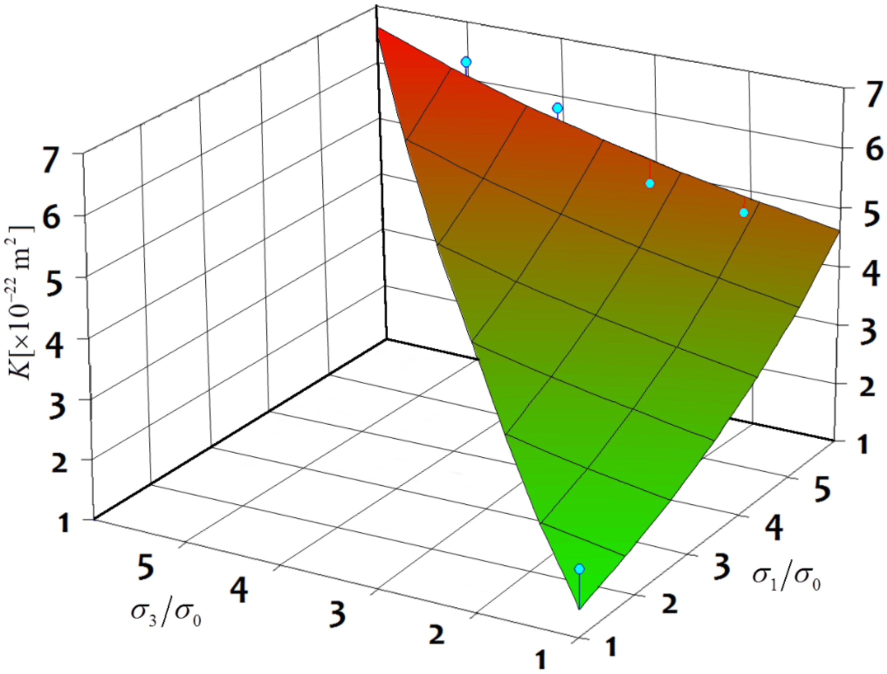

Figure 8.12: Proposed permeability evolution with stress state, where σ_1 is the maximum principal stress, σ_3 is the minimum principal stress (all normalized with respect to the initial confining stress $\sigma_0 = 5\,\mathrm{MPa}$).

8.6 Summary

The typical expected behavior for a rock subjected to an isotropic compressive stress state would be a decrease in the permeability as the compressive stresses increase. This decrease in permeability can be explained by pore collapse and/or closure of micro fractures resulting in a decrease in the void ratio. However, the results from the current research, conducted on the

Cobourg Limestone, differ from this typical trend. The results show an increase in permeability with increasing stresses (see Figures 8.9 and 8.11) in the pre-failure stress states. Furthermore, the unloading and reloading sequences, at a constant axial stress of 30 MPa, produced a higher permeability then the initial permeability at the onset of the loading sequence. This hysteresis in permeability represents a 140% increase in permeability when $\sigma_1 = \sigma_3 = 30\,\mathrm{MPa}$.

The darker grey argillaceous phase in a wet static state, when compared to dry unstressed state, was significantly weakened by the triaxial loading (post-failure). The material became fragile and finger nail scratching of this particular phases was able to remove particulates, something that was not possible before the tests were conducted on this material.

For visual enhancement, the cracks of the failure regions of the samples were accentuated by wetting the surface (see Figures 8.7 and 8.8) and an over-layer of red was placed on regions where the cracks were visible. The predominant trend among all failed samples is that the cracks were located in the darker grey argillaceous material. Some samples did not exhibit any visible surface cracks that connected the plane ends of the sample, which explains their lower permeability estimates (see e.g. CL1H and CL7H in Figure 8.7). The samples that exhibited interconnected cracking between upper and lower surfaces showed an increase of effective estimated permeability up to 4 orders of magnitude (see Table 8.1).

The constant pore pressure (100 kPa) that was applied to the base of the samples up to failure did not yield any conclusive results as to the detection of cracks connecting the upper and lower surfaces of the sample. There were reductions in the pore pressure (i.e. 0 to 25 kPa) in certain tested samples after failure, which lasted for 1 to 3 min, however these pressure drops were quickly re-established by the pump. The reasons of the drops could be attributed to localized crack formation on the bottom surface. The results, from the constant pressure monitoring, however, did not support crack dilatancy formation and crack opening which, would have reduced the pressure due to an increase in the effective permeability of the failed sample.

Two empirical state-space models are proposed for the permeability evolution, in the pre-failure sequence, with isotropic loading and deviatoric unloading of principal stresses in the 5 MPa to 30 MPa range.

CHAPTER 9

CONCLUSIONS

9.0 Summary and Conclusions

Two limestones (Indiana and Cobourg) were studied in a laboratory setting in order to determine the evolution of their permeabilities with triaxial stresses. The experimental facilities that allowed the testing of large samples (85 mm in diameter and 170 mm in length). The results were complementary to the ongoing research into geomechanical characterization of the strata encountered at the proposed nuclear waste repository at the Bruce Nuclear Site, Ontario. The following are the major highlights of the current research:

1. The factors affecting the determination of permeability evolution with triaxial stresses in rocks in the pre-failure regime were examined in detail. The main source of error when estimating permeability is the presence of air bubbles in the rock and in the testing equipment. The presence of air in the permeating water can significantly affect pulse decay pressures as well as the flow rate delivered by the pump during steady state flow tests. These effects can be mitigated by utilizing a de-airing system, which will remove air from the permeating fluid and flush out the air bubbles that are present in the pressurizing system. Additionally, proper saturation of the system and the rock sample and removal of air bubbles from the testing equipment by vacuuming will greatly improve the estimation of permeability.
2. The study of permeability evolution in Indiana Limestone subjected to triaxial stress states, using the steady state constant flow method, indicated that the permeability constantly

decreases as the confining stresses are increased and compressive axial loads are applied. Furthermore, the permeability is either unchanged or decreases slightly after failure in the confining stress range of 5 MPa up to 30 MPa; these stress states include the brittle, transitional and ductile failure regimes. In all eleven samples were tested to post-failure and by measuring the permeability change are various stress states this allowed the development of an empirical model using the acquired data. The proposed empirical relationship is based on the initial permeability, tensile strength and principal stresses. The empirical relationship was successfully used in a computational model that simulates permeability evolution due to stress state variation around a circular underground tunnel. The proposed empirical relationship enabled the determination of the influx of water to the tunnel. The computational model showed that by accounting for the changes in permeability around the circular opening, the influx into the tunnel was reduced by a factor of 2.

3. The permeability results obtained using an entry port connector on the light grey carbonate phase and the dark grey argillaceous phase of the Cobourg Limestone were within a range of $7.0\mathrm{E}-18\,\mathrm{m}^2$ to $2.7\mathrm{E}-20\,\mathrm{m}^2$. These results were confirmed with the steady state constant pressure method and are in good agreement with the hydraulic pulse decay results. Furthermore, the results show that there is one order of magnitude difference between the two phases with the darker phase being more conductive. This is supported by results of the estimation of permeability on cylindrical samples of Cobourg Limestone subjected to triaxial failure stresses, where it was found that the darker grey argillaceous phase is the weaker material and forms pathways (cracks) for water flow (Selvadurai and Głowacki, 2016). The water entry port connector proposed in this study was quite effective, inexpensive to produce and can be easily installed in situ or on samples in areas where the testing surface area is

scarce. Additionally, the results obtained validate the proposed testing method, which consists of using a high precision pump, an entry port connector and the steady state constant pressure method to conduct experiments on tight rocks with permeabilities as low as $2.7\mathrm{E}-20\,\mathrm{m}^2$.

In certain locations there was a lack of correlation between the pulse tests and the steady state tests (i.e. locations 3 and 5). In these cases, by analyzing the pulse decay curves for a shorter time period, the estimated permeability was better correlated to the results obtained from steady state tests. This was attributed to a rapid increase in the water tank temperature (i.e. +0.25°C in 5000 sec).

4. The typical behavior for a rock subjected to a compressive stress state would be a decrease in the estimated permeability as the compressive triaxial stresses increase. This decrease in permeability would be attributed to pore collapse and/or closure of micro fractures, which would decrease the void ratio. However, the results in the pre-failure stress states obtained from the tests on the Cobourg Limestone differ from the typical trend in the range of 5 to 30 MPa confining stresses. The results show an increase in permeability with increasing stresses. Furthermore, the unloading and reloading sequences, at a constant axial stress of 30 MPa, produced a hysteresis in estimated permeability. This hysteresis represents a 50% increase in permeability when compared to results at the stress state of $\sigma_1 = \sigma_3 = 30\,\mathrm{MPa}$. In a post-failure sequence of testing, the dark grey argillaceous phase, when compared to the dry unstressed state, was significantly weakened by the testing sequence. The material became frail; and finger nail scratching of this particular phase could remove particulates, which was not possible on the same material before testing. The predominant trend among all failed samples was that the cracks were located in the dark grey argillaceous phase. In summary, the effective permeability of the failed samples increased by up to 4 orders of magnitude when

compared to the pre-failure estimated permeability. Furthermore, the results obtained from the post-failure tests show that the increase in confining stress from 10 MPa to 30 MPa resulted in a decrease in two orders in magnitude for the effective permeability. Additionally, two empirical models for the permeability evolution, in the pre-failure sequence, with isotropic loading and unloading of principal stresses were proposed.

5. A summary of average estimates for permeability obtained in the current research using different testing method is presented in Table 9.1. The results in Table 9.1 exclude the permeabilities obtained on samples in the post-failure stress states; since such permeabilities are stress state dependent and have a large range of values.

Table 9.1: Summary of permeabilities from different rock types

Rock type	**Permeability** [m^2]	**Stress state** Axial stress σ_1 [MPa]	Radial stress σ_3 [MPa]	**Testing method**
Indiana Limestone	4.0E-15	0	0	Constant flow
	3.0E-15	5	5	Constant flow
	4.0E-16	30	30	Constant flow
Cobourg Limesotne	2.0E-19	0	0	Pulse decay and constant perssure
	2.0E-22	5	5	Pulse decay
	7.0E-22	30	30	Pulse decay
Rudna Sandstone	6.0E-17	0	0	Constant flow
Stanstead Granite	5.0E-18	0	0	Constant flow

The main contribution of this research is that it adds knowledge to the understanding of permeability evolution with compressive triaxial stresses of relatively large samples of limestone with different porosities. The innovation includes the development of experimental facilities and procedures, which enabled the determination of permeability evolution with triaxial stress states for both Indiana Limestone and Cobourg Limestone.

9.1 Future Research

In order to fully understand the effect of water dissolution of the matrix of limestones, any future research should incorporate pre- and post-experimental imaging (CT-scans, optical microscope) of the samples. This would confirm that the amounts of dissolved minerals that are found in the outflow are due to matrix dissolution or the transport of residual material (i.e. from machining and coring) found in the pores. It would also permit the assessment of any micro-damage before and after testing the samples.

In the steady state experiments, especially for the low flow rates, it would be an improvement and a helpful confirmation if an experimental setup could be designed to accurately monitor the outflow rates, perhaps with the use of high precision pump. In so doing, it would further confirm that a steady state is established and that the sample in question is not being saturated.

In order to develop a more realistic model for the evolution of permeability in the Indiana Limestone subjected to triaxial compressive stress states, it would be necessary to conduct experimental research based on in-situ pore pressures. These pore pressures can be determined either from the literature or borehole investigations. Hence, the experimental method of determining permeability would be based on steady state constant pressure gradients, in contrast to the steady state constant flow experiments that were performed here.

When testing rock with low permeabilities it is important to have precise control of several factors, including room and permeating fluid temperature. In this research it was observed that such factors can alter the results and cause unwanted pressure build up inside the experimental setup.

In steady state tests the capillary rise should be examined to assess its influence on the determination of permeability, especially when low flow rates are applied and when dealing with a two phase fluid (air–water) medium.

The current research has examined the evolution of permeability in a porous material with varying stress states. However, the permeability evolution is dependent on the state of microstructure parameters such as porosity, cracks interconnectivity and cracks dimensions. Hence, future research could examine the influence of stress state on microstructural parameters and link them to permeability evolution. Although, such endeavor would require substantial upgrading to the laboratory equipment as well as new experimental procedures would have to be developed to capture the necessary microstructural parameters at a particular stress state during permeability testing.

REFERENCES

Abdelouas, A., Lu, Y., Lutze, W. and Nuttall, H.E. 1998. Reduction of U(VI) to U(IV) by indigenous bacteria in contaminated ground water, *Journal of Contaminant Hydrology* **35**: 217-233.

Akbarnejad-Nesheli, B. and Ghassemi, A. 2009. Undrained poroelastic response of Berea Sandstone and Indiana Limestone to confining and deviatoric stress change, *American Tock Mechanics Association*: 43rd US Rock Mechanics Symposium and 4th US-Canada Rock Mechanics Symposium in Asheville, North Carolina.

Alsayed, M.I. 2002. Utilising the Hoek triaxial cell for multiaxial testing of hollow rock cylinders, *International Journal of Rock Mechanics and Mining Sciences* **39**(3): 355–366.

Auzerais, F. M., Dunsmuir, J., Ferreol, B. B., Martys, N., Olson, J., Ramakrishnan, T. S., Rothman, D. H. and Schwartz, L. M. 1996. Transport in sandstone: A study based on three dimensional microtomography, *Geophysical Research Letters* **23**(7): 705–708.

Azeemuddin, M., Roegiers, J.-C., Suri, P., Zaman, M. and Kukreti, A. R. 1995. Stress-dependent permeability measurement of rocks in a triaxial cell, The 35th U.S. Symposium on Rock Mechanics, University of Nevada, A. A. Balkema, Rotterdam: 645–650.

Bachu, S., Brulotte, M., Grobe, M. and Stewart. S. 2000. Suitability of the Alberta subsurface for carbon-dioxide sequestration in geological media, *Alberta Energy and Utilities Board: Alberta Geological Survey,* Earth Sciences Report 2000-11.

Bear, J. 1972. *Dynamics of Fluids in Porous Media*, American Elsevier Publishing Company, New York, London, Amsterdam.

Bernabe, Y. 1986. The effective pressure law for permeability in Chelmsford Granite and Barre Granite, *International Journal of Rock Mechanics and Mining Science* **23**: 267–275.

Bernaix, J. 1969. New laboratory methods of studying the mechanical properties of rocks, *International Journal of Rock Mechanics and Mining Sciences* **6**(1): 43–90.

Biot, M.A. (1941), General theory of three-dimensional consolidation. *Journal of Applied Physics* **12**: 155-164.

Black, D.K. and Lee, K.L. 1973. Saturating laboratory samples by back pressure, *Journal of the Soil Mechanics and Foundations Division*, American Society of Civil Engineers **99**: 75-93.

Boulin, P.F., Bretonnier, P., Gland, N. and Lombard, J.M. 2012. Contribution of the steady state method to water permeability measurement in very low permeability porous media, *Oil and Gas Science and Technology-Revue d'IFP Energies nouvelles* **67**(3): 387–401.

Bouwer, H. 2000. Integrated water management: emerging issues and challenges. *Agricultural Water Management,* **45**, 217-228. DOI: 10.1016/S0378-3774(00)00092-5.

Boyer, C., Kieschnick, J., Suarez-Rivera, R., Lewis, R.E. and Waters. G. 2006. Producing gas from its source. *Oilfields Review* **18**(3): 36–49.

Brace W, Walsh, J., and Frangos, W.T. 1968. Permeability of granite under high pressure. *Journal of Geophysical Research* **73**(6): 2225–36.

Bredehoeft, J.D., England, A.W., Stewart, D.B., Trask, N.J. and Winograd, I.J. 1978. Geologic disposal of high-level radioactive wastes–Earth-Science Perspectives, *U.S. Geological Survey Circular* 779, Washington, D.C.: U.S. Government Printing Office: 1–15

Bulnes, A.C. and Fitting, R.U. jr. 1945. An introductory discussion of the reservoir performance of limestone formations, *Society of Petroleum Engineers* **160**(01): 179–201.

Caputo, M.C., De Carlo, L., Masciopinto, C., and Nimmo, J.R., 2010, "Measurement of field-saturated hydraulic conductivity on fractured rock outcrops near Altamura (Southern Italy) with an adjustable large ring infiltrometer." *Environmental Earth Sciences,* **60**(3), pp. 583–590.

Cieślik, J. 2015. Stress drop as a result of splitting brittle and transitional faulting of rock samples in uniaxial and triaxial compression tests, *Studia Geotechnica et Mechanica* **37**(1): 17–23.

Chitty, D.E., Blouin, S.E., Sun, X. and Kim, K.J. 1994. Laboratory investigation and analysis of the strength and deformation of joints and fluid flow in Salem limestone, *Technical Report for Defense Nuclear Agency*, 6801 Telegraph Road, Alexandria, VA 22310–3398.

Couture, B.C. 2016. *The development of wormholes in Indiana Limestone during carbon dioxide-acidized water flow*, Masters Thesis, McGill University.

Darcy, H. 1856. Les Fontaines Publiques de la Ville de Dijon, éditeur Victor Dalmont, Successeur de Carilian- Gœury et Vor Dalmont, Libraire Des Corps Impériaux Des Ponts Et Chaussées Et Des Mines, Qual des Augustins 49, Paris.

Dautriat, J., Gland, N., Dimanov, A. and Raphanel. J. 2011. Hydromechanical behavior of heterogeneous carbonate rock under proportional triaxial loadings, *Journal of Geophysical Research* **116**(B1): DOI: 10.1029/2009JB000830.

Davis, J.A. and Curtis G.P. 2007. Consideration of geochemical issues in groundwater restoration at uranium in-situ leach mining facilities. Division of Fuel, Engineering, and Radiological Research; Office of Nuclear Regulatory Research: U.S. Nuclear Regulatory Commission Washington. DC 20555-0001, NUREG/CR-6870.

Dolan, J.W. 1999. Mobile-phase degassing – Why, when, and how.” *Chromatographyonline.com LCGC* **17**(10): 908–912.

Donaghe, R.T. and Chaney, R.C. 1988. *Advanced Triaxial Testing of Soil and Rock*, Issue 977, ASTM International.

Dreybrodt, W. 1988. *Processes in Karst systems: physics, chemistry, and geology*, Berlin; New York: Springer-Verlag.

Fatt, I. 1953. The effect of overburden pressure on relative permeability, *Journal of Petroleum Technology* **5**: 15–16.

Fatt, I., and Davis, D.H. 1952. Reductions in permeability with overburden pressure, *Transactions of the American Institute of Mining Engineers* **195**: 329.

Ford, D.C., and Williams, P.W. 2007. Karst Hydrogeology and Geomorphology, John Wiley & Sons Ltd, West Sussex, England.

Fredlund, D.G. 1976. Density and compressibility characteristics of air-water mixtures, *Canadian Geotechnical Journal*, **13**(4): 386–396.

Gangi, A.F. 1978. Variation of whole and fractured porous rock permeability with confining pressure, *International Journal of Rock Mechanics and Mining Science and Geomechanics Abstract* **15**(5): 249–257.

Gartner Lee Limited. 2008. Phase I Geosynthesis; Supporting Technical Report Prepared for Ontario Power Generation: OPG 00216-REP-01300-00010-R00.

Géraud, Y. and Gaviglio, P. 2000. Reconstitution du réseau poreux d'un échantillon décomprimé. Mise en évidence d'une anisotropie de connectivité, *Comptes Rendus de l'Académie des Sciences - Series IIA - Earth and Planetary Science* **331(**5): Pages 339–344.

Ghabezloo, S., Sulem, J., Guédon, S. and Martineau, F. 2008. Effective stress law for the permeability of a limestone, *International Journal of Rock Mechanics and Mining Science* **46**(2): 297–306. DOI 10.1016/j.ijrmms.2008.05.006.

Giot, R., Giraud, A., Auvray, C., Homand, F. and Guillon, T. 2011. Fully coupled poromechanical back analysis of the pulse test by inverse method, *International Journal for Numerical and Analytical Methods in Geomechanics* **35**: 329–359; doi:10.1002/nag.897.

Głowacki, A. 2006. The permeability hysteresis of Indiana Limestone during isotropic compression. Masters Thesis, McGill University.

Gnirk, P. 1993. OECD/NEA International Stripa project overview. *Natural Barriers*, Sweden: SKB: Stockholm.

Golder Associates Ltd. 2003. LLW Geotechnical Feasibility Study Western Waste Management Facility Bruce site Tiverton, Ontario. *Report submitted to municipality of Kincardine and Ontario Power Generation*. Report No. 021–1570.

Grader, A.S., Clarck, A.B.S., Al-Dayyani, T. and Nur, A. 2009. Computations of porosity and permeability of sparic carbonate using multi-scale CT images, *International Symposium of the Society of Core Analysts*, Noordwijk aan Zee, Netherlands.

Gregory, K.B., Vidic, R.D. and Dzombak D.A. 2011. Water Management Challenges Associated with the Production of Shale Gas by Hydraulic Fracturing, *Mineralogical Society of America* **7**(3) 181–186.

Guéguen, Y., Gavrilenko, R. and Le Ravalec, M. 1996. Scales of rock permeability, *Surveys in Geophysics* **17**: 245–263.

Hadia, N.J., Mitra, S.K. and Vinjamur, M. 2012. Estimation of permeability heterogeneity in limestone outcrop by pressure measurements: Experiments and numerical simulation, *Experimental Thermal and Fluid Science* **40**: 177-184.

Harvey R.D. 1968. Thermal expansion of certain Illinois Limestones and Dolomites, *Illinois State Geological Survey*, Circular 415.

Harrison, S.S. 1983. Evaluating system for ground-water contamination hazards due to gas-well drilling on the glaciated Appalachian Plateau. *Ground Water* **21**(6): 689–700.

Hasenmueller, N. R., Rexroad, C. B., Powell, R. L., Buehler, M. A., Bassett, J. L. Hasenmueller, N.R., Rexroad, C.B., Powell, R.L., Buehler, M.A. and Bassett, J.L. 2003. Karst geology and hydrology of the Spring Mill Lake and Lost River drainage basins in southern Indiana: Indiana Geological Survey Guidebook.

Healy, J. H., Rubey, W. W., Griggs, D. T. and Raleigh, C. B. (1968). The Denver Earthquakes, *Science* **161**: 1301–1310.

Hekimi, B. 2012. The Physical and Mechanical Properties of an Argillaceous Limestone, Masters Thesis, McGill University.

Heystee, R. and Roegiers J.-C. 1981. The effect of stress on the primary permeability of rock cores – a facet of hydraulic fracturing, *Canadian Geotechnical Journal* **18**(2): 195–204.

Hettkamp, T., Baumgärtner, J., Baria, R., Gérard, A., Gandy, T., Michelet, S. and Teza, D. 2004. Electricity production from hot rocks. Proceedings, Twenty-Ninth Workshop on Geothermal Reservoir Engineering, Stanford University, Stanford, California, January 26-28, SGP-TR-175.

Hoek, E. and J.A. Franklin. 1968. A simple triaxial cell for field and laboratory testing of rock, *Transactions of the Institute of Mining and Metallurgy* **77**: A22–A26.

Hsieh, P.A., Tracy, J.V., Neuzil, C.E., Bredehoeft, J.D. and Silliman, S.E. 1981. A transient laboratory method for determining the hydraulic properties of tight rocks – I. Theory. *International Journal of Rock Mechanics and Mining Sciences & Geomechanics Abstracts* **18**(3): 245–252.

IDNR. 2016. Ground-Water Quality, *Indiana Department of Natural Resources*, accessed on 15th of November, 2016: https://www.in.gov/dnr/water/files/WFWR_web50-119.pdf

ILIA. 2007. *Indiana Limestone Handbook*, 22nd Edition, Indiana Limestone Institute of America Inc., Bedford, IN.

INTERA. 2011. Descriptive Geosphere Site Model. Prepared by: Intera Engineering Ltd. NWMO DGR-TR-2011-24.

ISRM. 2007. The Complete ISRM Suggested Methods for Rock Characterization, Testing and Monitoring:1974-2006, Edited by R. Ulusay and J.A. Hudson, International Society for Rock Mechanics.

Jackson, R.B., Osborn, S.G., Vengosh, A. and Warner, N.R. 2011. Reply to Davies: Hydraulic fracturing remains a possible mechanism for observed methane contamination of drinking water. *Proceedings of the National Academy of Sciences of the USA* **108**(43): E872–E872.

Keaney, G.M.J., Meredith, P. and Murrell, S.A.F. 1998. Laboratory study of permeability evolution in a tight sandstone under non-hydrostatic stress conditions, *Society of Petroleum Engineers Conference Proceedings*, SPE **47265**: 329–335.

Kiyama T., Kita, H., Ishijima, Y., Yanagidani, T., Akoi, K. and Sato, T. 1996. Permeability in anisotropic granite under hydrostatic compression and tri-axial compression including post-failure region, *Proceedings of the 2nd North American Rock Mechanics Symposium*: 1643–1650.

Knackstedt, M.A., Latham, S., Madadi, M., Sheppard, A., Varslot, T. and Arns. C. 2009. 3D imaging of core material and correlations to acoustic and flow properties, *Society of Exploration Geophysicists* **35**(11): 28–33.

Kowallis, B.J and Wang, H.F. 1983. Microcrack study of granitic cores from Illinois deep borehole UPH 3, *Journal of Geophysical Research: Solid Earth* **88**(B9): 7373–7380.

Kranz, R.L., Saltzman, J.S. and J.D. Blacic, J.D. 1990. Hydraulic diffusivity measurements on laboratory rock samples using an oscillating pore pressure method, *International Journal of Rock Mechanics and Mining Sciences & Geomechanics Abstracts* **27**(5): 345–352.

Lanyon, G.W. 2011 Excavation damaged zones assessment, *NWMO 1080 DGR-TR 2011-21* report prepared by Fracture Systems Ltd.

Lee, K.L. and Black, D.K. 1972. Time to dissolve air bubble in drain line, *Journal of the Soil Mechanics and Foundations Division*, American Society of Civil Engineers, **98**(2): 181–194.

Leith, S.D., Reddy, M.M., Fred Ramirez, W. and Heymans, M.J. 1996. Limestone characterization to model damage from acidic precipitation: Effect of pore structure on mass transfer, *Environmental Science and Technology* **30**(7): 2202–2210.

Lemieux, J-M. 2011. Review: The potential impact of underground geological storage of carbon dioxide in deep saline aquifers on shallow groundwater resources, *Hydrogeology Journal* **19**(4): 757–778.

Lewis, M.A., Cheney, C.S. and Ódochartaigh, B.É. 2006. Guide to Permeability Indices. British Geological Survey, Open Report CR/06/160N.

Lin, W. (1977). Compressible fluid flow through rocks of variable permeability, Rep. UCRL-52304, Lawrence Livermore Lab. Univ. of Calif., Livermore.

Liu, J., C. Zheng, L. Zheng, and Y. Lei. 2008. Ground water sustainability: methodology and application to the North China Plain, *Ground Water* **46**(6): 897–909.

Luu, T. 2009. Anisotropic permeability characteristics of Indiana Limestone: experimental and computational studies, Master's Thesis, McGill University.

Makhnenko, R.Y. and Labuz, J.F. 2013. Saturation of porous rock and measurement of the B coefficient. American Rock Mechanics Association, *47th Rock Mechanics/Geomechanics Symposium*, San Francisco, USA: 679-684.

Malard, F. and Hervant, F. 1999. Oxygen supply and adaptations of animals in groundwater, *Freshwater Biology* **41**: 1-30.

Massart, T.J. and Selvadurai. A.P.S. 2012. Stress-induced permeability evolution in a quasi-brittle geomaterial, *Journal of Geophysical Research* **117**(B07207): DOI: 10.1029/2012JB009251.

Mattar, P. 2009. Permeability of intact and fractured Indiana Limestone, Master's Thesis, McGill University.

Mattar, P. and Selvadurai, A.P.S. 2009 Radial flow testing of Indiana Limestone, *Proceedings of the 3rd CANUS Rock Mechanics Symposium,* May, (Ed: M. Diederichs and G. Grasselli), Toronto, Ontario, Paper **4119**: 1–7.

Mazurek, M. 2004. Long-term used nuclear fuel waste management – Geoscientific review of the sedimentary sequence in southern Ontario; prepared for Ontario Power Generation, Technical Report TR 04–01.

McClure, N.W. and Horne, R.N. (2011) Pressure transient analysis of fracture zone permeability at Soultz-sous-Forêts, *Geothermal Resources Council Transactions* **35**: 1487–1498.

Meier, P.M., Trick, T., Blümling, P. and Volckaert, G. 2002. Self-healing of fractures within the EDZ at the Mont Terri rock laboratory: Results after one year of experimental work, *Proceedings of International Workshop on Geomechanics, Hydromechanical and Thermohydro-mechanical Behaviour of Deep Argillaceous Rocks: Theory and Experiment*, 11-12 October, Andra, Paris.

Micro-Measurements (2010) Measurement of the thermal expansion coefficient using strain gages. Strain gages and Instruments: Tech Note TN-513-1, Vishay, Precision Group.

Montazer, P.M. and Hustrulid, W. A. 1983. An investigation of fracture around an underground opening in metamorphic rocks, *Technical Report prepared for Office of Crystalline Repository Development*, BMI/OCRD-4(5).

Morrow, C.A. and Lockner, D.A. 1997. Permeability and porosity of the Illinois UPH3 drillhole granite and a comparison with other deep drillhole rocks. Journal of Geophysical Research **102**: 3067–3075.

Nad, A., Brożek, M. and Naziemiec, Z. 2012. The tensile strength properties of lithological variety of Polish copper ores, AGH *Journal of Mining and Geoengineering* **36**(4): 101–108.

Najari, M. 2013. *A computational and experimental modelling of Thermo-Hydro-Mechanical processes in a low permeability granite,* PhD Thesis, McGill University.

Nasseri, M.H.B., Goodfellow, S.D., Wanne, T.S., Young, R.P. 2013. Coupled Thermo-Hydro-Mechanical properties of Cobourg, *International Journal of Rock Mechanics and Mining Sciences* **61**: 212–222.

Neuman, S.P. 1994. Generalized scaling of permeabilities: validation and effect of support scale, *Geophysical Research Letters* **21**(5): 349–352.

Neuzil, C.E., Cooley, C., Silliman, S.E., Bredehoeft, J.D. and Hsieh, P.A. 1981. A transient laboratory method for determining the hydraulic properties of ‘tight’ rocks—II. Application, *International Journal of Rock Mechanics and Mining Sciences and Geomechanics Abstracts* **18**: 253–258.

Nicolaides, C., Jha, B., Cueto-Felgueroso, L. and Juanes, R. 2015. Impact of viscous fingering and permeability heterogeneity on fluid mixing in porous media, *Water Resources Research* **51**: doi:10.1002/2014WR015811.

Noiriel, C., Gouze, P. and Bernard, D. 2004. Investigation of porosity and permeability effects from microstructure changes during limestone dissolution, *Geophysical Research Letters* **31**(24), L24603.

NWMO (Nuclear Waste Management Organization). 2011. Regional Geology – Southern Ontario, prepared by AECOM Canada Ltd. and Itasca Consulting Canada, Inc, NWMO DGR-TR-2011-15

NWMO (Nuclear Waste Management Organization). 2015a. Inter-University Geomechanics Research Laboratory Comparison Report: UCS Test Results for Indiana Limestone. By Nasseri M.H.B., Young R.P., Diederichs M., Labre D., Selvadurai A.P.S., Głowacki A, and Hekimi B. To be published.

NWMO (Nuclear Waste Management Organization). 2015b. An update to the Canadian Shield stress database. By Salina Yong and Sean Maloney, NWMO-TR-2015-18.

Obert, L. 1963. An Inexpensive Triaxial Apparatus for Testing Mine Rock, U.S. Dept. of Interior, Bureau of Mines, Report of investigations 6332.

OPG. 2011a. Ontario power generation's deep geologic repository for low and intermediate level waste. *Postclosure Safety Assessment*: NWMO DGR-TR-2011-25.

OPG. 2011b. Ontario power generation's deep geologic repository for low and intermediate level waste. *Geosynthesis*: NWMO DGR-TR-2011-11.

OPG. 2011c. Ontario power generation's deep geologic repository for low and intermediate level waste. *Hydrogeologic Modelling*: NWMO DGR-TR-2011-16.

OPG. 2016. Ontario power generation's deep geologic repository for low and intermediate level waste: *DGR: Protecting Lake Huron*: NWMO 228-DGR Lake Huron Report; accessed 2016: www.opg.com/dgr.

Osborn, S.G., Vengosh, A., Warner, N.R. and Jackson. R.B. 2011. Methane contamination of drinking water accompanying gas-well drilling and hydraulic fracturing. *Proceedings of the National Academy of Sciences of the USA* **108**(20): 8172–8176.

Pearson, C. 1981. The relationship between microseismicity and high pore pressures during hydraulic stimulation experiments in low permeability granitic rocks, *Journal of Geophysical Research: Solid Earth* **86**(B9): 7855–7864

Pedretti, D., Barahona-Palomo, M., Bolster, D., Fernàndez-Garcia, D., Sanchez-Vila, X. and Tartakovsky, D.M. 2012. Probabilistic analysis of maintenance and operation of artificial recharge ponds, *Advances in Water Resources* **36**: 23–35

Philips, O. M. 1991. *Flow and reactions in permeable rocks*. Cambridge, UK: Cambridge University Press.

Raven, K.G., Novakowski, K.S., Yager, R.M. and Heystee, R.J. 1992. Supernormal fluid pressures in sedimentary rocks of southern Onatrio – western New York State, *Canadian Geotechnical Journal* **29**: 80–93.

Rubinstein, J.L. and Mahani, A.B. 2015. Myths and facts on wastewater injection, hydraulic fracturing, enhanced oil recovery, and induced seismicity, *Seismological Research Letters* **86**(4):

Selvadurai, A.P.S. 2000. *Partial Differential Equations in Mechanics Vol. 1: Fundamentals, Laplace's Equation, the Diffusion Equation, the Wave Equation*, Springer-Verlag, Berlin.

Selvadurai, A.P.S. 2004. Stationary damage modelling of poroelastic contact, *International Journal of Solids and Structures* **41**(8): 2043–2064.

Selvadurai, A.P.S. 2006. Gravity-driven advective transport during deep geological disposal of contaminants, *Geophysical Research Letters* **33**(8)L0840: 1–4.

Selvadurai, A.P.S. 2009. Influence of residual hydraulic gradients on decay curves for one-dimensional hydraulic pulse tests, *Geophysical Journal International* **177**: 1357–1365.

Selvadurai, A.P.S. 2011. On the hydraulic intake shape factor for a circular opening located at an impervious boundary: Influence of inclined stratification, *International Journal for numerical and analytical methods in geomechanics* **35**: 639–651.

Selvadurai, A.P.S. 2012. Fluid leakage through fractures in an impervious caprock embedded between two geologic aquifers. *Advances in Water Resources* **41**: 76–83.

Selvadurai, A.P.S. and Benson, P.M. 2011. An elastic plug compression test for estimating the tensile strength of a brittle rock, Environmental Geomechanics Laboratory (EGL), McGill University. [Unpublished].

Selvadurai, A.P.S. and Carnaffan, P. 1997. A transient pressure pulse method for the measurement of permeability of a cement grout, *Canadian Journal of Civil Engineering* **24**(3): 489–502.

Selvadurai, A.P.S. and Głowacki, A. 2008. Permeability hysterisis of limestone during isotropic compression, Groundwater 46(1): 113–119.

Selvadurai, A.P.S. and Głowacki, A. 2016. Stress-induced permeability alterations in an argillaceous limestone. Rock Mechanics and Rock Engineering. [Accepted for publication]

Selvadurai, A.P.S. and Ichikawa, Y. 2013. Some aspects of air-entrainment on decay rates in hydraulic pulse tests, *Engineering Geology* **165**: 38–45.

Selvadurai, A.P.S. and Jenner, L. 2013. Radial flow permeability testing of an argillaceous limestone, *Ground Water* **51**(1): 100–107.

Selvadurai, A.P.S. and Najari, M. 2013. On the interpretation of hydraulic pulse tests on rock specimens, *Advances in Water Resources* **53**: 139–149.

Selvadurai, A.P.S. and Najari, M. 2015. Laboratory-scale hydraulic pulse testing: influence of air fraction in cavity on estimation of permeability, *Géotechnique* **65**(2): 126–134.

Selvadurai, A.P.S. and Najari, M. 2016. Isothermal permeability of the argillaceous Cobourg Limestone, *Oil and Gas Science and Technology – Revue d'IFP Energies nouvelles, Special Issue on Low Permeability Geomaterials* **71**(53): 1–16.

Selvadurai, A.P.S. and Nguyen, T.S. 1996. Scoping analysis of the coupled thermal-hydrological-mechanical behaviour. *Engineering Geology* **47**(4): 379–400.

Selvadurai, A.P.S. and Selvadurai, P.A. 2010. Surface permeability test; experiments and modeling for estimating effective permeability, *Proceedings of the Royal Society A*, **466**: 2819–2846. DOI: 10.1098/rspa.2009.0475

Selvadurai, A.P.S. and Suvorov, A.P. 2012. Boundary heating of poroelastic and poro-elastoplastic spheres, *Proceedings of the Royal Society A: Mathematical, Physical and Engineering Sciences* **468**(2145): 2779–2806.

Selvadurai, A.P.S. and Suvorov, A.P. 2014. Thermo-poromechanics of a fluid-filled cavity in a fluid-saturated geomaterial, *Proceedings of the Royal Society, Mathematical and Physical Sciences Series A* **470**: 20130634.

Selvadurai, A.P.S., Boulon, M.J. and Nguyen, T.S. 2005. The permeability of an intact granite, *Pure and Applied Geophysics* 162(2): 373–407.

Selvadurai, A.P.S., Letendre, A. and Hekimi, B. 2011. Axial flow hydraulic pulse testing of an argillaceous limestone. *Environmental Earth Sciences* **64**: 2047–2058.

Selvadurai, P.A. 2010. Permeability of Indiana Limestone: Experiments and theoretical concepts for interpretation of results. Master's Thesis, McGill University.

Selvadurai, P.A. and Selvadurai, A.P.S. 2014. On the effective permeability of a heterogeneous porous medium: the role of the geometric mean, *Philosophical Magazine* **94**(20): 2318–2338.

Shao, J. F., Zhou, H. and Chau, K. T., P.A. 2005. Coupling between anisotropic damage and permeability variation in brittle rocks, *International Journal for Numerical and Analytical Methods in Geomechanics* **29**: 1231–1247.

Sheorey, P.R. (1997) *Empirical Rock Failure Criteria*, A.A. Balkema, Rotterdam, Netherlands.

Shimadzu Corporation. 1991. Degassing Mobile Phase Solvents, *LC talk Special Issue* **5**. Accessed on July 24th, 2014) <*http://www.shimadzu.com/an/hplc/support/lib/lctalk/s5/055.html*>.

Shimoyama, K., Yamaguchi, Y. and Sakamoto, H. 2012. Rapid Evaluation Method of Saturated Permeability in Unsaturated Foundations, *Journal of Japan Society of Dam Engineers* **22**(4): 226–243. [In Japanese]

Shepherd, R.G. 1989. Correlations of permeability and grain size, *Ground Water* **27**(5), 633–638

Shiping, L., Yushou, L., Yi, L., Zhenye, W. and Gang, Z. 1994. Permeability-strain equations corresponding to the complete stress–strain path of Yinzhuang Sandstone. *International Journal of Rock Mechanics and Mining Sciences and Geomechanics Abstracts* **31**(4): 383–391.

Soltani, A., Le Ravalec-Dupin, M. and Fourar, M. 2009. An experimental method for one dimensional permeability characterization of heterogeneous porous media at the core scale. *Transport in Porous Media* **77**: 1–16.

Souley, M., Homand, F., Pepa, S. and Hoxha, D. 2001. Damage-induced permeability changes in granite: A case example at the URL in Canada, *International Journal of Rock Mechanics and Mining Sciences* **38**(2): 297–310.

Suri, P., M. Azeemuddin, M., M. Zaman, M., Kukreti, A.R. and Roegiers, J.-C. 1997. Stress-dependent permeability measurement using the oscillating pulse technique, *Journal of Petroleum Science and Engineering* **17**: 247-264.

Svensson, U. and Dreybrodt W. 1992. Dissolution kinetics of natural calcite minerals in COT-water systems approaching calcite equilibrium, *Chemical Geology* **100**: 129–145.

Sykes, J.F. 2003. Characterizing the geosphere in the high-level radioactive waste management, *NWMO Background Papers: 4. Science and Environment*.

Tchelepi, H.A., Orr Jr, F.M., Rakotomalala, N., Salin, D and Wouméni R. 1993. Dispersion, permeability heterogeneity, and viscous fingering: Acoustic experimental observations and particle-tracking simulations, *Physics of Fluids A* **5**(7): 1558–1574.

TEAL. 2015. The Elemental Analysis laboratories at McGill University, Accessed on 22nd of September, 2016: https://www.mcgill.ca/eps/research/facilities

Timoshenko, S and Goodier, J.N. 1951. *Theory of Elasticity*, McGraw-Hill Inc. New York Toronto London.

Tsang, C.F., Birkholzer, J. and Rutqvist, J. 2008. A comparative review of hydrologic issues involved in geologic storage of CO_2 and injection disposal of liquid waste, *Journal of Environmental Geology* **54**(8): 1723 –1737. doi:10.1007/s00254-007-0949-6.

Tsang, C.F., Barnichon, J.D., Birkholzer, J., Li. X.L, Liu, H.H. and Sillen, X. 2012. Coupled thermo-hydro-mechanical processes in the near field of a high-level Radioactive waste repository in clay formations, *International Journal of Rock Mechanics & Mining Sciences* **49**: 31–44.

Vajdova, V., Baud, P., Wu, L. and Wong, T.-f., 2012. Micromechanics of inelastic compaction in two allochemical limestones. *Journal of Structural Geology* **43**: 100–117.

Vilks, P. and Miller N.H. 2007. Evaluation of experimental protocols for characterizing diffusion in sedimentary rocks, *Nuclear Waste Management Organization*, NWMO TR-2007-11.

Wikol, M., Hartmann, B., Brendle, J., Crane, M., Beuscher, U., Brake, J. and Shickel, T. 2007. Expanded polytetrafluoroethylene membranes and their applications, *Filtration and*

Purification in the Biopharmaceutical Industry, Second Edition, Edited by Maik W . Jornitz and Theodore H . Meltzer: 619–640.

Wright, M., Dillon, P., Pavelic, P., Peter, P. and Nefiodovas, A. 2002. Measurement of 3-D hydraulic conductivity in aquifer cores at in situ effective stress, *Ground Water* **40**(5): 509–517.

Wyble, D.O. 1958. Effect of applied pressure on the conductivity, porosity and permeability of sandstones, *Transactions of the American Institute of Mining Engineers* **213**(3): 430–432.

Yang, Y. and Aplin, A.C. 1998. Influence of lithology and compaction on the pore size distribution and modelled permeability of some mudstones from the Norwegian margin, *Marine and Petroleum Geology* **15**: 163–175.

Zeng, Z. and Grigg, R. 2006. A criterion for non-Darcy flow in porous media, *Transport in Porous Media* **63**: 57–69; doi:10.1007/s11242-005-2720-3.

Zhang, X. and Spiers, C.J. 2005. Effects of phosphate ions on intergranular pressure solution in calcite: An experimental study, *Geochimica et Cosmochimica Acta* **69**(24): 5681–5691.

Zhu, W. and Wong. T-F. 1997. The transition from brittle faulting to cataclastic flow: Permeability evolution, *Journal of Geophysical Research* **102**(B2): 3027–3041.

Zoback, M.D. and Byerlee, J.D. 1975. The effect of micro-crack dilatancy on the permeability of Westerly Granite, *Journal of Geophysical Research* **80**(5): 752–755.

APPENDIX A

Chemical Analysis

Objectives:

Determine the chemical composition of the visually apparent light and dark grey phases of Cobourg Limestone.

Quantify de minerals and elements composing these phases

Testing facilities:

XRF analysis: S4 Pioneer (UQAM)

XRD analysis: D8 Advance Da Vinci design de Bruker, Cu tube (UQAM); Siemens D5000 X-ray Powder Diffraction (XRD) System (UQAM)

JEOL Electron Probe X-Ray Microanalyzer (JXA-8900)

Chemical dissolution:

Whenever there is mention of HCl, it's the hydrochloric acid with a concentration of 10%. This acid was used on the Cobourg Limestone sample to dissolve the carbonates, which form a coating around clay minerals and make the XRD analysis difficult.

Samples details:

Several Cobourg Limestone samples were prepared: powder, fragments, and disks.

Although great care was taken to select precisely light and dark grey phases, it was a daunting task and required numerous attempts and samples.

For the powder samples, visually apparent light and dark grey phases were etched from the surface of large Cobourg Limestone cubes with a harden steel (hook) and about 1 g of material was collected.

For the fragmented samples, visually apparent light and dark grey phases were selected and impacted with a hammer in order to delaminate that particular phase.

From core samples (25 mm diameter), section were cut out to selected a particular phase. Then the cut section was machined on a lathe to a disk section (2-3 mm in height, 25 mm diameter), which allowed it to be analyzed directly in the XRD apparatus (see Figure 1).

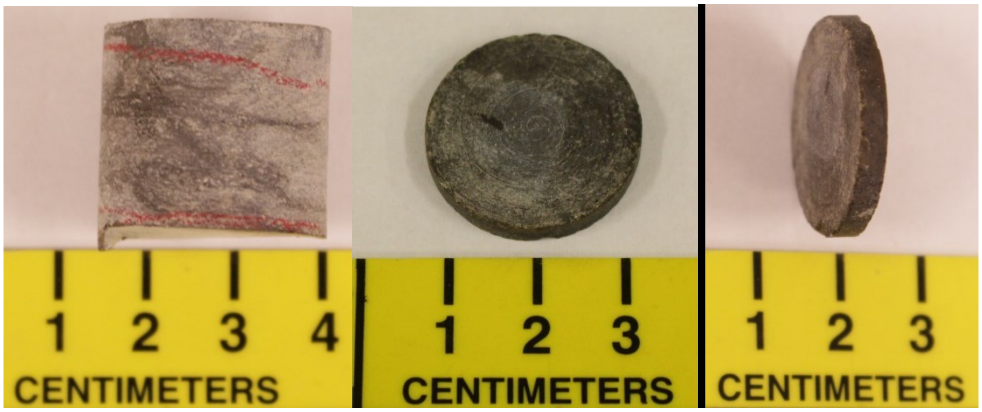

Figure 1: Disk preparation and final sample

Experimental procedure:

Samples (Roche 2, 3 and 4) of Cobourg Limestone dark grey phase were placed in a water beaker for 3 weeks. This process was used to clearly identify the clay minerals in the sample. The general idea is that water gets absorbed by the clay minerals which will re-orient the clay mineral structure, making it more visible during the XRD analysis.

Additionally, by heating (heat treatment) the powder, other clays such as: chlorite/kaolinite can be differentiated. Furthermore, saturation with glycol (marked as "Ed" on the Counts vs d – Scale graphs) allows to determine interstratified clays like smectite-illite or chlorite-smectite (i.e. montmorillonite, beidellite, nontronite, saponite and hectorite).

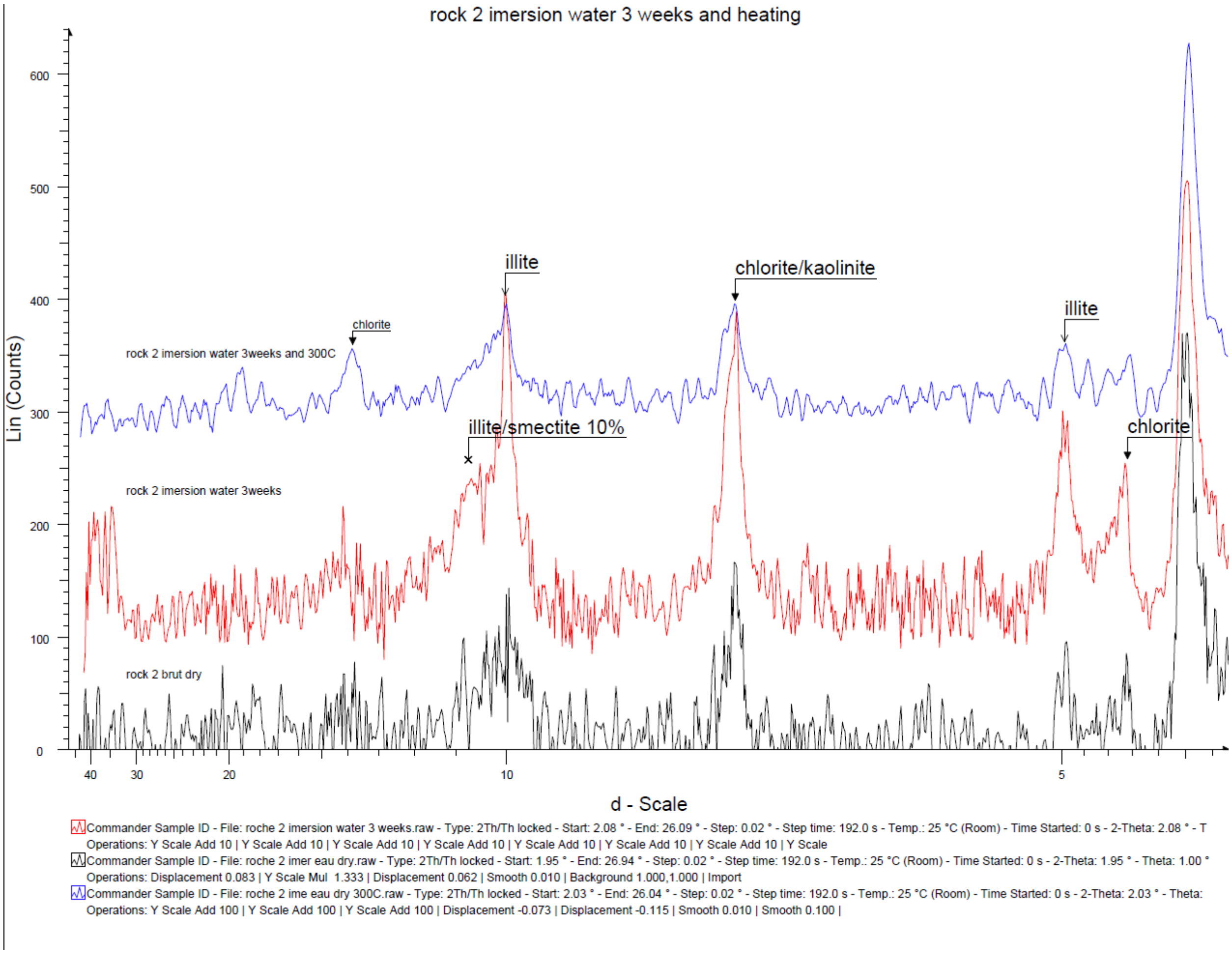

Figure 2: Sample Roche 2, the red curve (post immersion in water) clearly shows a peak for the illite, which was less apparent when the sample was dry analyzed.

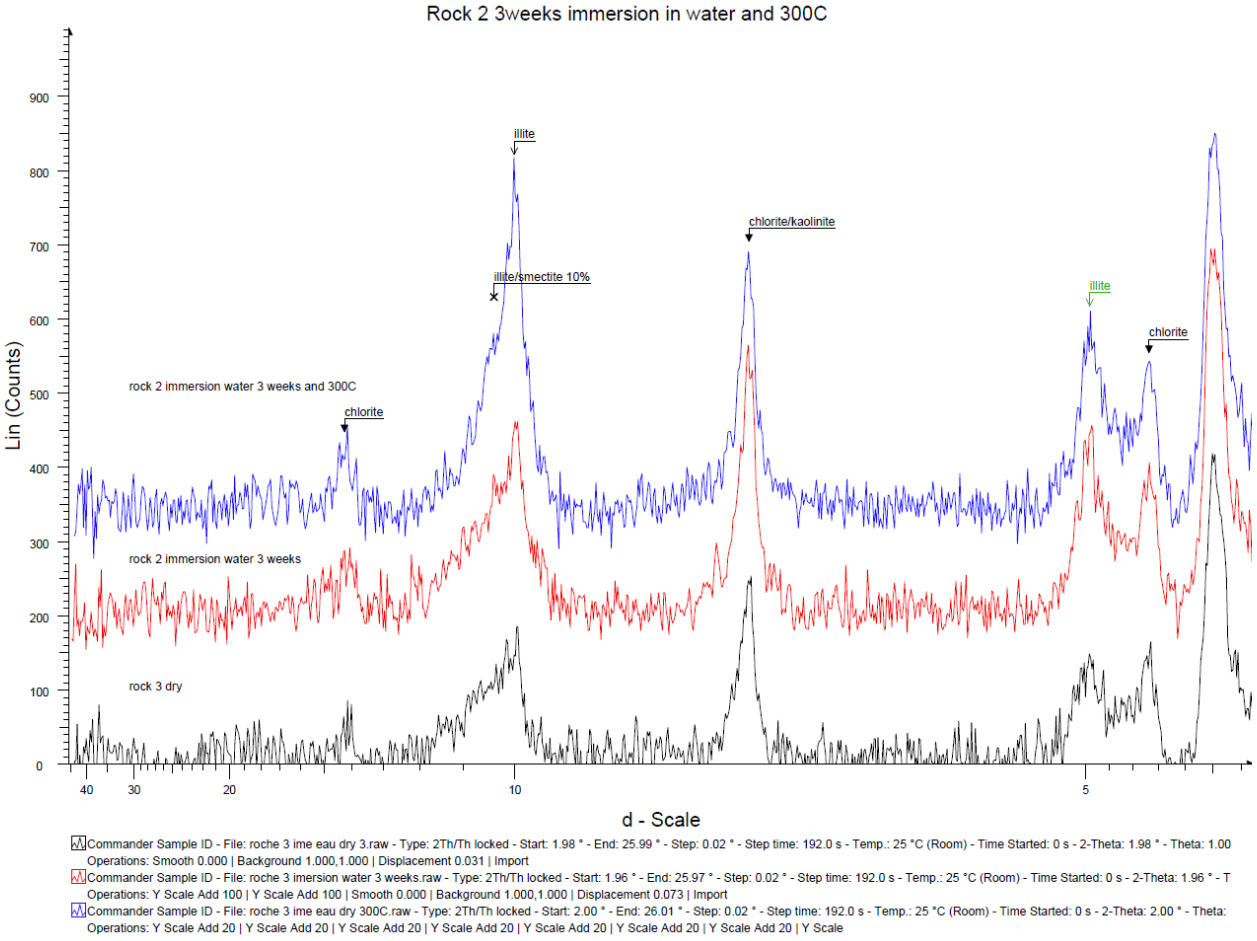

Figure 3: Sample Roche 3, the red curve (post immersion in water) clearly shows a peak for the illite, which was less apparent when the sample was dry analyzed.

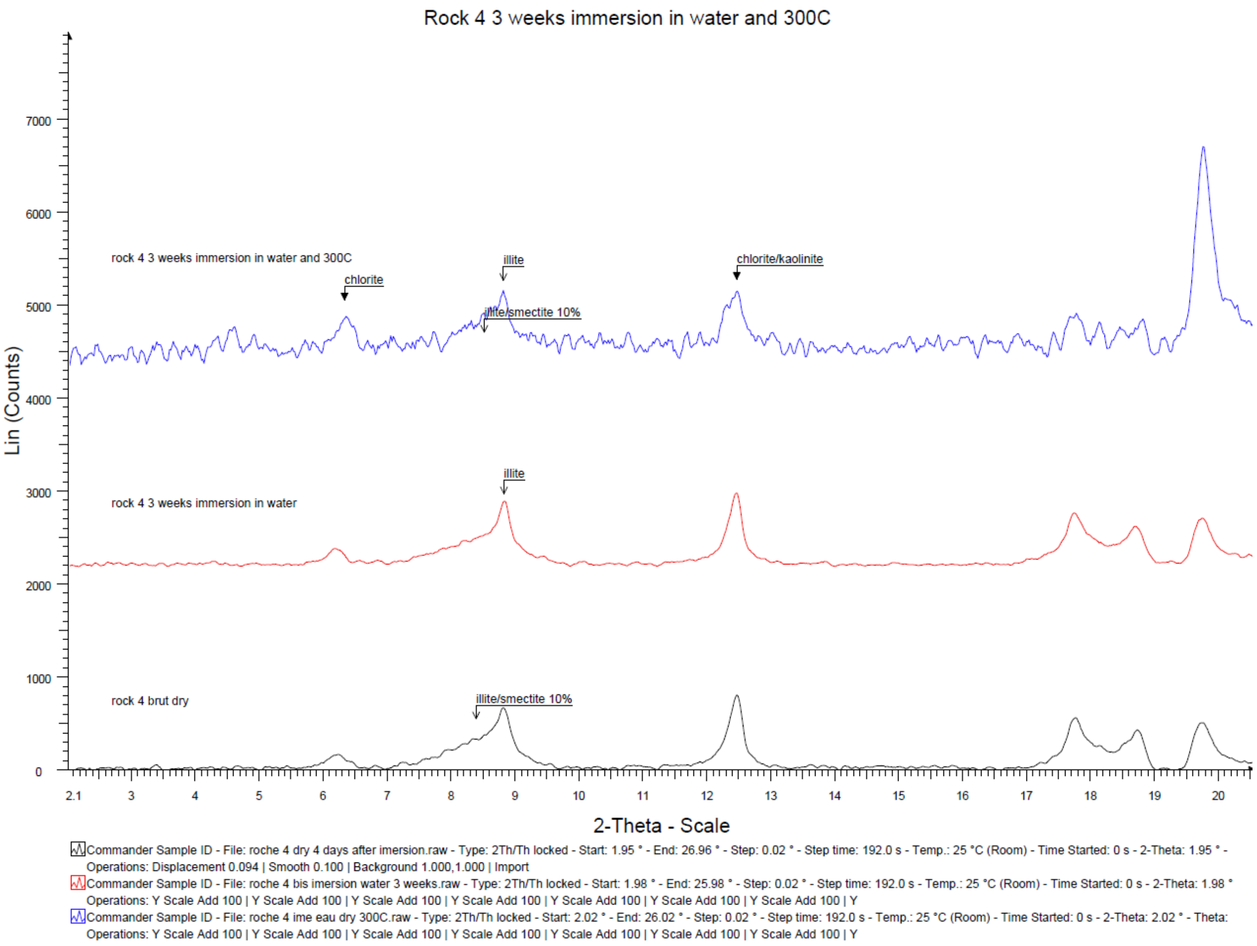

Figure 4: Sample Roche 4, the analysis of the results was smoothed to reduce the noisy signal; illite was present from the initial dry state with layers of smectite (montmorillonite); chlorite appears after immersion and heat treatment.

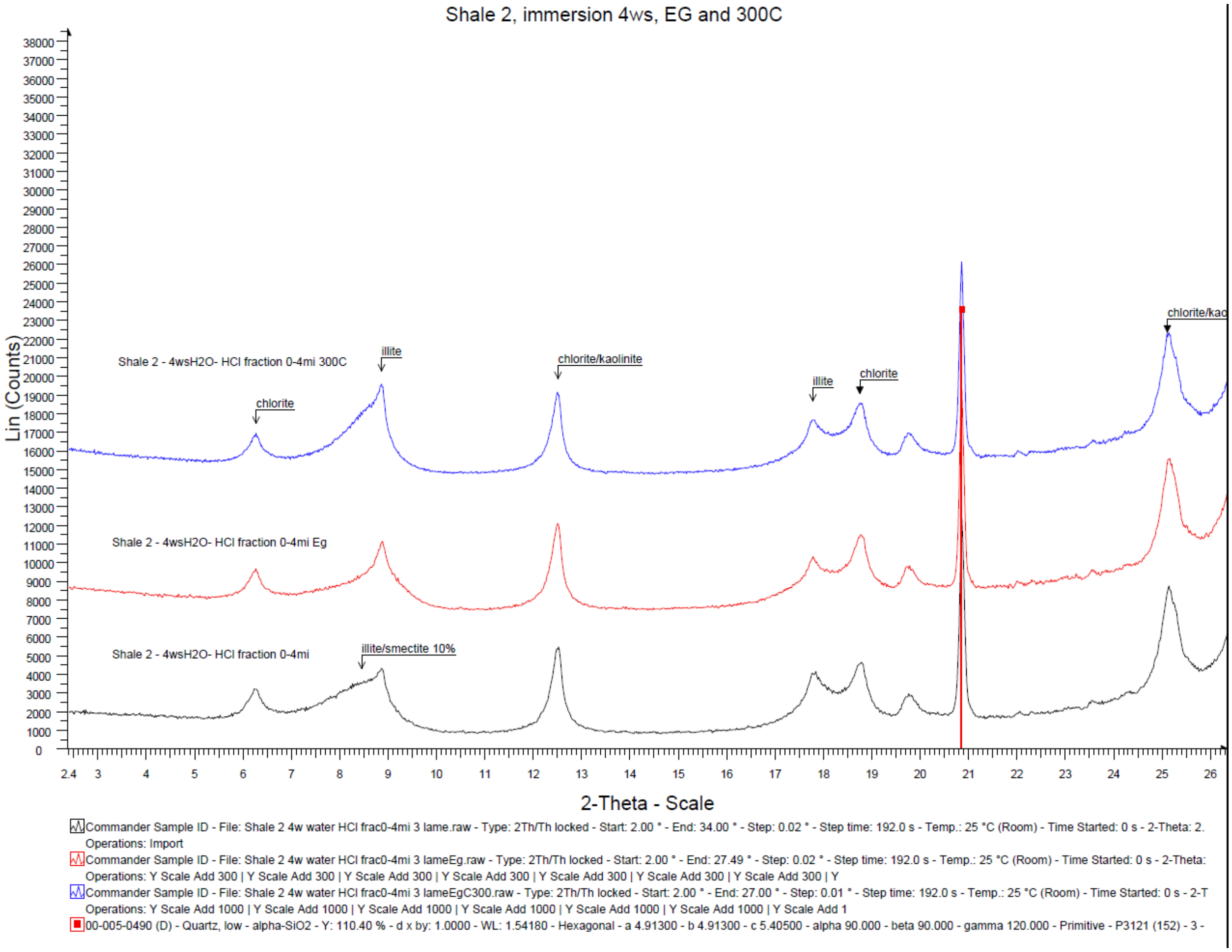

Figure 5: Sample Shale 2 (dark phase) was analyzed by following a particular set process:

1. Sample was immersed in water for 4 weeks after which a powder sample was created. It was then subjected to chemical treatment (HCl) following with the pipette method (sedimentation); by settling velocity (Stoke's law) we obtain the 0-4 microns fraction; this fraction was sedimented on a glass slide with a pipette to obtain an oriented preparation (black curve).

2. The powder sample was then subjected to ethylene glycol solvation to further distinguish between various non-swelling and swelling clay minerals (red curve).

3. The heat treatment was then used to further refine the analysis (blue curve): this heating is used to see the behavior of illite-smectite and to differentiate chlorite from kaolinite

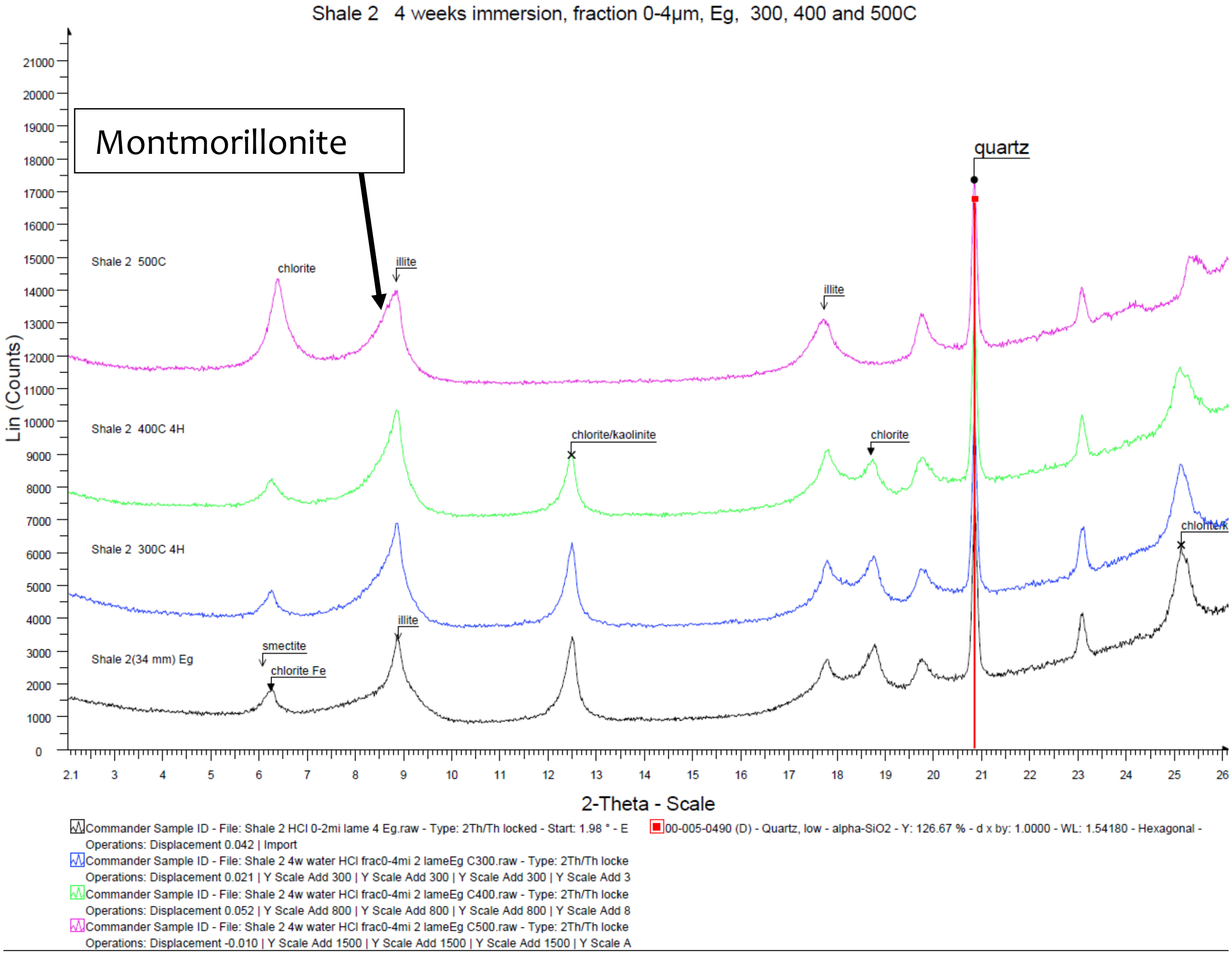

Figure 6: Sample Shale 2, dark phase powder analysis, trace/presence of montmorillonite. Chlorite/kaolinite disappear at 500ºC; kaolinite disappear as well as chlorite if it is Fe-chlorite (peak at 12.5 or 7A); there is an increase of intensity from 400 ºC to 500ºC.

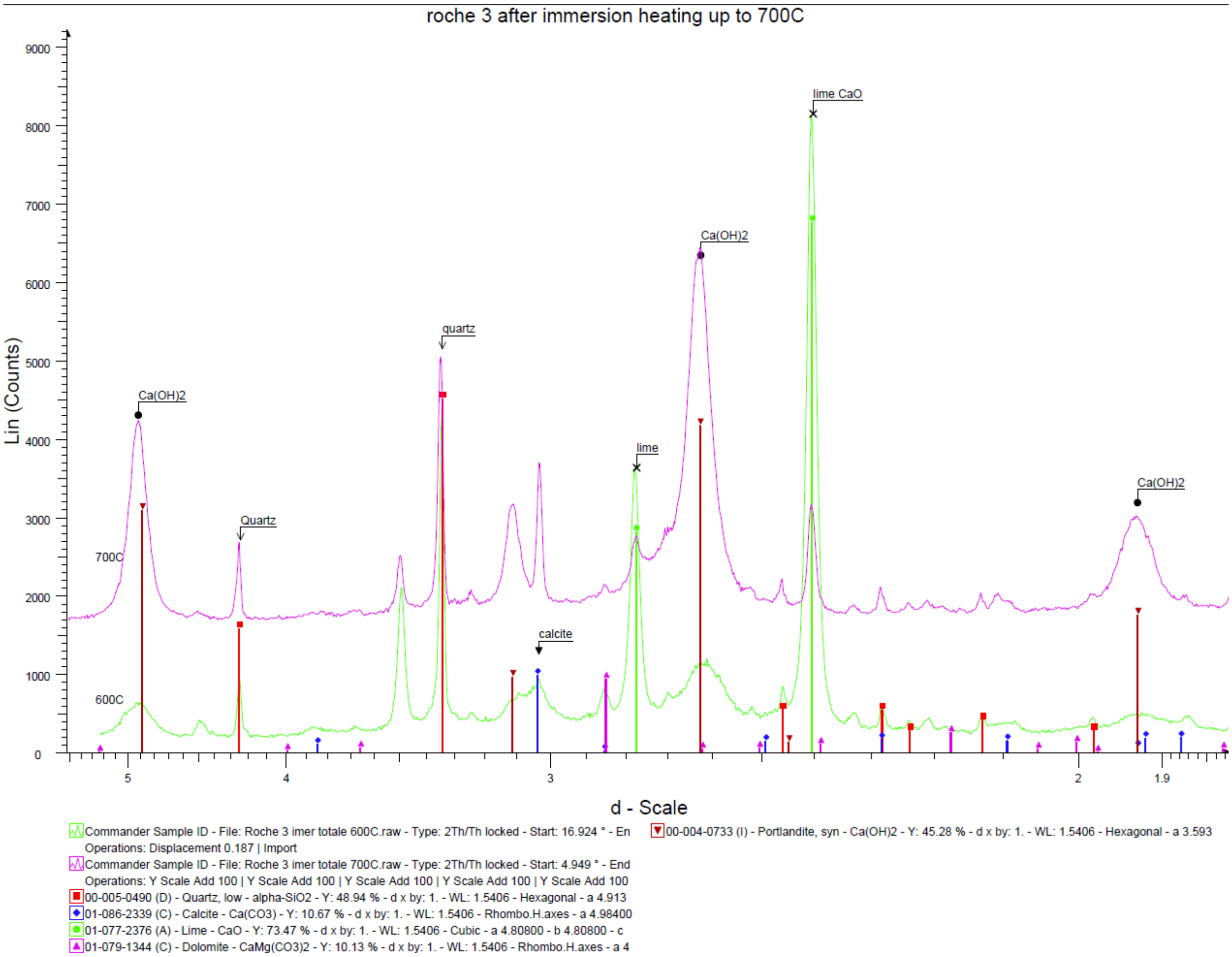

Figure 7: Sample Roche 3, heat treatment of dark phase up to 700ºC.

Upon heating the sample (Roche 3) of Cobourg Limestone to 700ºC, the disk fragmented.

The sample (Roche 3) was cooled after each heat treatment before the XRD analysis. The analysis has shown that once Cobourg Limestone was heated to 600ºC the Calcite ($CaCO_3$) thermally decomposed into Calcium oxide (CaO - Lime), then at 700ºC (cement kiln 1500ºC) Calcium Hydroxide ($Ca(OH)_2$) was formed after hydration with ambient air moisture when the sample was cooling.

Table 1: XRF analysis at UQAM of the fragmented and etched samples of light and dark grey phases.

Sample CLF1-L		**Sample CLF2-L**		**Sample CLP1-D**		**Sample CLP1-D**	
Light grey	**powder**	**Light grey**	**powder**	**Dark grey**	**powder**	**Dark grey**	**HCl/filtered**
Elements	**%**	**Elements**	**%**	**Elements**	**%**	**Elements**	**%**
C	6.24%	C	6.43%	C	3.46%	C	0.00%
O	41.84%	O	40.89%	O	43.77%	O	47.55%
Na	0.10%	Na	727 PPM	Na	0.23%	Na	0.22%
Mg	0.80%	Mg	0.54%	Mg	1.99%	Mg	2.10%
[redacted]	[redacted]	[redacted]	[redacted]	[redacted]	[redacted]	[redacted]	[redacted]
[redacted]	[redacted]	[redacted]	[redacted]	[redacted]	[redacted]	[redacted]	[redacted]
P	431 PPM	P	285 PPM	P	433 PPM	P	ND
S	0.23%	S	0.13%	S	0.61%	S	1.33%
Cl	402 PPM	Cl	337 PPM	Cl	0.11%	Cl	310 PPM
[redacted]	[redacted]	[redacted]	[redacted]	[redacted]	[redacted]	[redacted]	[redacted]
[redacted]	[redacted]	[redacted]	[redacted]	[redacted]	[redacted]	[redacted]	[redacted]
Ti	0.12%	Ti	413 PPM	Ti	0.27%	Ti	0.65%
V	trace	V	trace	V	31 PPM	V	57 PPM
Cr	132 PPM	Cr	115 PPM	Cr	181 PPM	Cr	262 PPM
Mn	334 PPM	Mn	396 PPM	Mn	331 PPM	Mn	181 PPM
[redacted]	[redacted]	[redacted]	[redacted]	[redacted]	[redacted]	[redacted]	[redacted]
Co	ND	Co	ND	Co	174 PPM	Co	ND
Ni	210 PPM	Ni	215 PPM	Ni	223 PPM	Ni	0.21%
Cu	77 PPM	Cu	79 PPM	Cu	115 PPM	Cu	120 PPM
Rb	29 PPM	Rb	trace	Rb	69 PPM	Rb	151 PPM
Sr	569 PPM	Sr	494 PPM	Sr	369 PPM	Sr	73 PPM
Zr	45 PPM	Zr	20 PPM	Zr	88 PPM	Zr	256 PPM
Mo	trace	Mo	trace	Mo	85 PPM	Mo	trace
Ba	ND	Ba	ND	Ba	216 PPM	Ba	384 PPM
Sb	569 PPM	Sb	739 PPM	Sb	102 PPM	Sb	ND
Te	650 PPM	Te	823 PPM	Te	215 PPM	Te	ND
Yb	219 PPM	Yb	224 PPM	Yb	370 PPM	Yb	ND
Ta	trace	Ta	trace	Ta	129 PPM	Ta	57 PPM
W	ND	W	ND	W	463 PPM	W	71 PPM
Total	**99.62%**		**99.60%**		**99.60%**		**99.29%**

The results in Table 1 show a higher content of iron the in the dark grey phase. Also there is a 20% reduction in the Calcium content from the light to the dark phase. There is a significant increase in Si in the dark grey phase confirming the presence of quartz. The presence of Al in the dark grey phase confirms the existence of clays and feldspar (microcline). Potassium (K) indicates the presence of illite and/or alkali feldspar (microcline). Fe is a sign that there could be Pyrite (FeS_2).

Two disks (34 mm in diameter) of Cobourg Limestone were prepared with a 50/50 portions representing the light and dark grey phases for analysis with JEOL Electron Probe X-Ray Microanalyzer (see Figure 8).

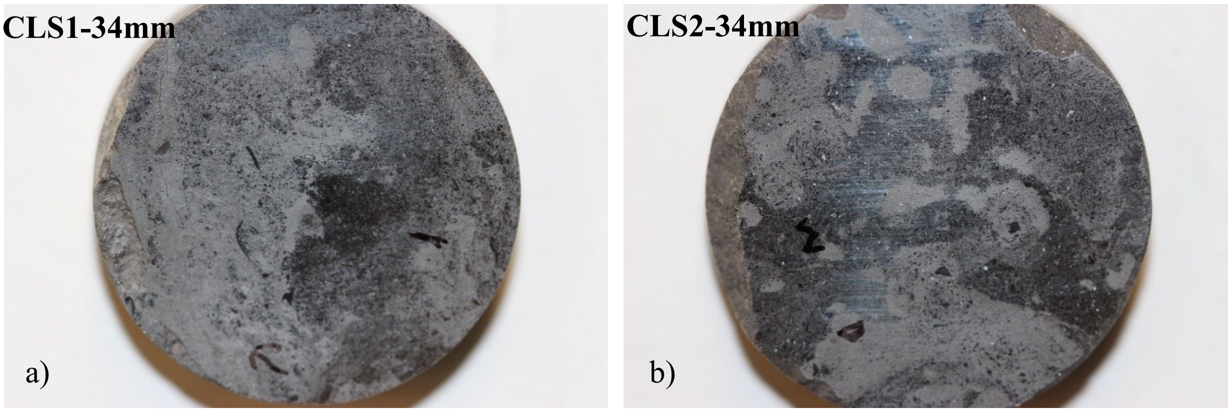

Figure 8: Cobourg limestone samples (34 mm in diameter) that were surface polished for the analysis using a JEOL Electron Probe X-Ray Microanalyzer (JXA-8900), the white/grey regions represent the originally dark phase. The CLS1 sample is more heterogeneous where the dark phase is on the left and the light on the right side, whereas the CLS2 is more evenly mixed with nodules of dark phase distributed on the surface

Table 2: XRF analysis at UQAM of the polished 34 mm samples

Water immersion	**CLS1-34 mm 3 weeks**		**CLS2-34 mm 4 weeks**
Elements	**%**	**Elements**	**%**
O	49.600%	O	41.60%
Ca	35.900%	Ca	45.83%
C	5.650%	C	7.31%
Si	4.090%	Si	2.45%
Al	1.380%	Al	0.71%
Fe	1.230%	Fe	0.77%
Mg	0.828%	Mg	0.66%
K	0.495%	K	0.29%
S	0.220%	S	0.15%
Ni	0.010%	Ni	0.02%
Cl	144 PPM	Cl	149 PPM
Ti	0.083%	Ti	337 PPM
Na	0.063%	Na	442 PPM
Te	0.056%	Te	749 PPM
Sr	0.049%	Sr	494 PPM
Sb	0.045%	Sb	663 PPM
P	0.041%	P	329 PPM
Mn	0.025%	Mn	348 PPM
Cl	0.015%	Cl	0.012%
Cr	0.011%	Cr	105 PPM
Cu	0.007%	Cu	103 PPM
Rb	0.003%	Rb	0.003%
Zr	0.002%	Zr	0.002%
Ta	30 PPM	Ta	31 PPM
Total	**99.80%**		**99.82%**

$CaCO_3$ %	**70.60%**	**91.44%**	**XRF Calculated**
$CaCO_3$ %	**68.30%**	**89.70%**	**HCl treatement**

Table 3: XRD analysis at UQAM of the polished 34 mm samples

Minerals	**CLS1-34 mm** **%**	**CLS1-34 mm** **%**
Calcite	79.3	85.5
Quartz	14.8	9.5
[redacted]	[redacted]	[redacted]
Chlorite	1.1	0.5
Pyrite	0.3	0.3
Microcline	0.4	0.5
Albite	0.3	0.3

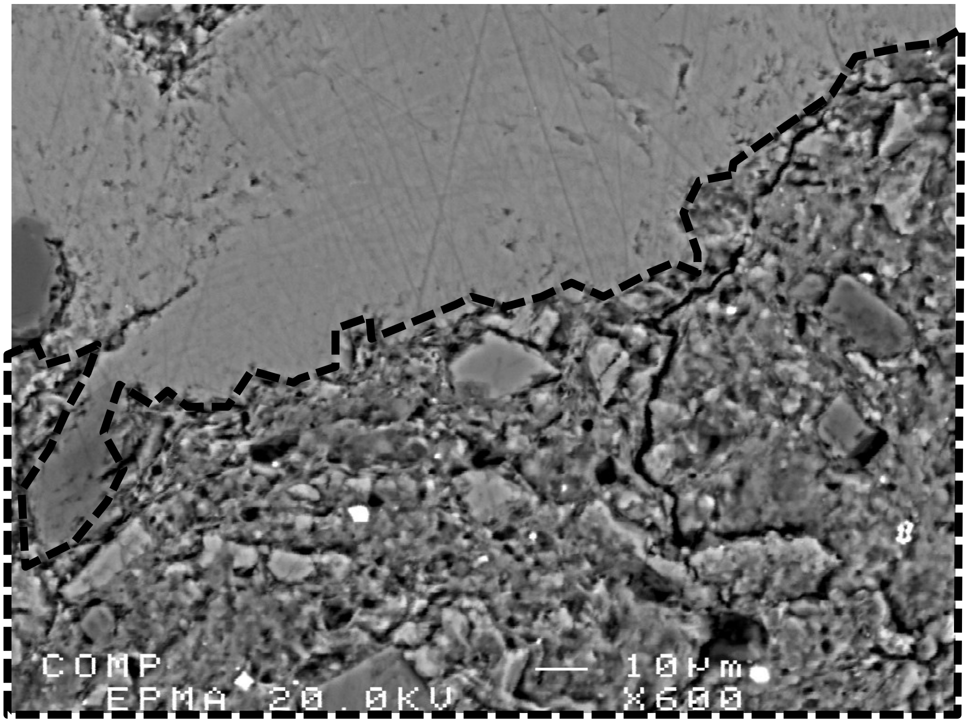

Figure 9: Zoomed picture of the CLS1-34 mm sample; the interface delimited by dotted line is between light grey (calcite) and dark grey (argillaceous) phase. The black areas represent the micro-pores/channels, which are located predominately in the dark phase.

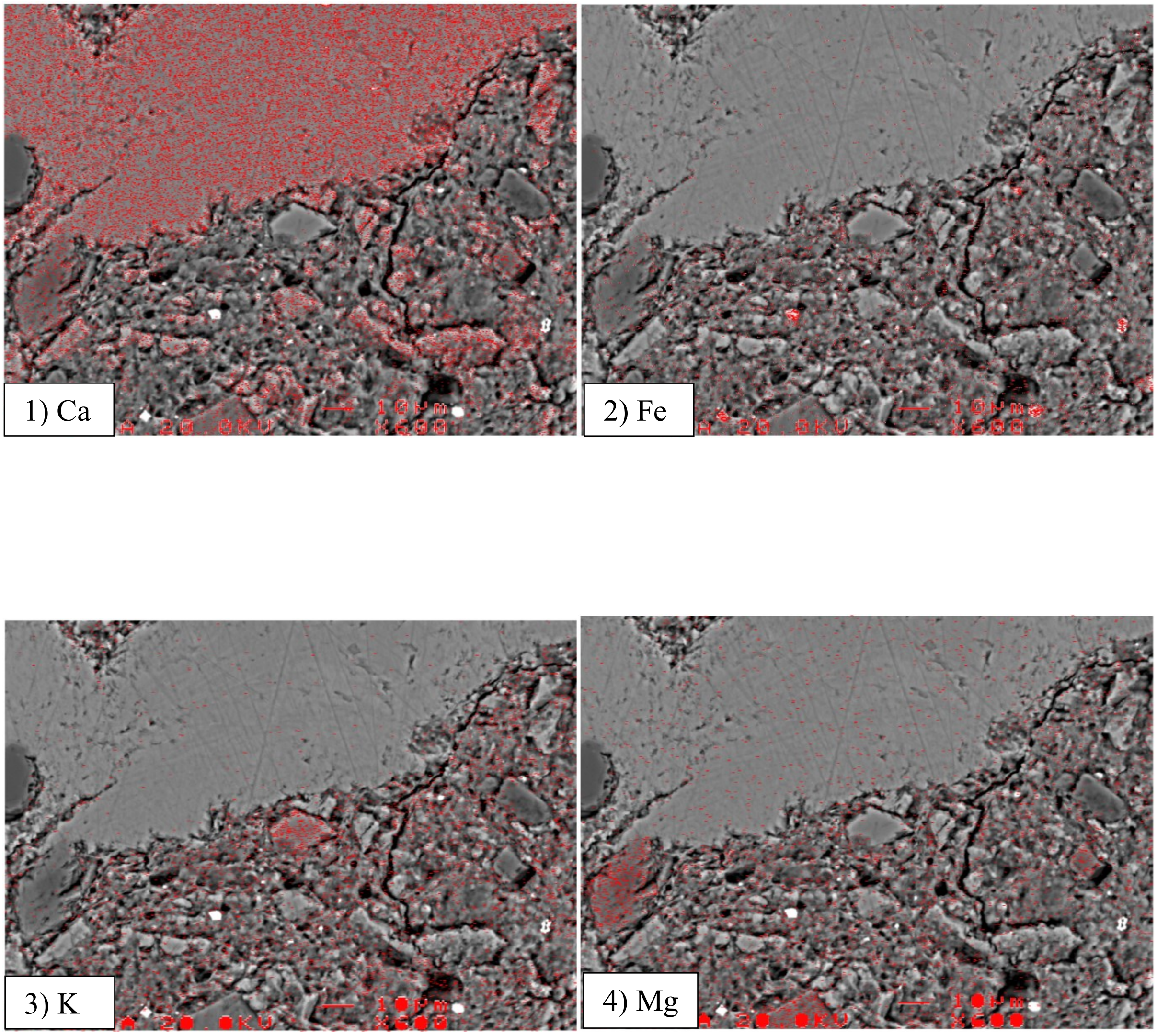

1) Ca

2) Fe

3) K

4) Mg

Figure 10: The following figures indicate the elements and their distribution on the CLS1-34 mm sample

Table 4: Powder analysis of the particular phases (Mixed: light and dark phases and Dark Grey: predominately on dark material), using the XRD, allowed to determine the dominating minerals in each:

Dark Grey

Minerals	%	varience
Quartz	22.00	± 5.9
Calcite	51.45	± 13.3
Dolomite	15.85	± 6.6
Albite	3.25	± 1.1
Microcline	3.00	± 0.2
Pyrite	1.45	± 0.8
Hematite	0.65	± 0.2

Mixed

Minerals	%
Quartz	8.01
Calcite	85.4
Dolomite	5.3
Albite	0.73
Microcline	0.25
Pyrite	0.08
Hematite	0.03

Highlighted in yellow is the clay content in each phase. It can be concluded that the dark phase contains around 2.4 % of clay minerals versus 0.3% in the light grey phase.

APPENDIX B

Triaxial Testing Facility using the Yellow frame and Obert-Hoek Cell

This report describes the testing of the facility, as developed up to June 1st 2014. It gives potential users a brief introduction to the operational steps in relation to the application of a triaxial stress state to a cylindrical sample measuring 85mm in diameter and a maximum height of 170 mm.

Prepared by: Adrian Głowacki

Approved by: Prof. A.P.S. Selvadurai

Date: 6 September 2014

Table of Contents:

PART 1: Setup

1.1 List of hardware

Load Cell: Capacity 200 000 lbs (890 kN), by Intertechnology, C693A200K-IOPI (see Figure 1)

Digital Display: Hoskins Scientific, Digital Space Meter Panel, Micro P. (see Figure 19)

LVDT: MPE LSC Transducer, Full-bridge 350Ω (see Figures 2 and 15)

Obert-Hoek Cell: Radial pressure capacity 10 000 psi (69 MPa), S/N: 011F11003, by Roctest (see Figures 1, 2 and 3)

Pressure Transducer: Capacity 200 PSI (1.4 kPa), Honeywell (see Figures 16 and 17)

Pump: Quizix, QX 6000SS-0-0-C-L-0, maximum pressure 6,000 psi (41 MPa), maximum flow rate 50 mL/min, minimum flow rate 0.001 mL/min (see Figures 7 and 8)

DAQ (Data Acquisition): Data logger, by Measurement Computing (see Figure 14)

DAQ: Isolation module mounting rack for eight 5B type isolation modules, by DATAFORTH (see Figure 13)

GDS Controller #1: Serial no 15624, Maximum pressure 64 MPa, maximum fluid volume 200 cc, flow rates: 100mm^3 per second under pressure control and 200mm^3 per second on volume control (see Figure 11)

GDS Controller #2: Serial no 000939, Maximum pressure 64 MPa, maximum fluid volume 200 cc, flow rates: 50mm^3 per second under pressure control and 100mm^3 per second on volume control (see Figure 12)

Electric Hydraulic Pump: Enerpac, C6K 17EZ8F (see Figure 4 and 5)

Hydraulic Hand Pump: Enerpac P84-SPVL maximum pressure 10,000 psi (see Figure 10)

High Pressure Hydraulic Hoses: pressure rated for 10 000 psi (69 MPa) (see Figures 5 and 6)

Yellow Frame: Rated for 1 000 000 lbs (4448 kN) in compression (see Figures 18 and 19)

Thermocouple: Type K connected to DAQ USB-TEMP (see Figure 8)

1.2 Experimental setup figures

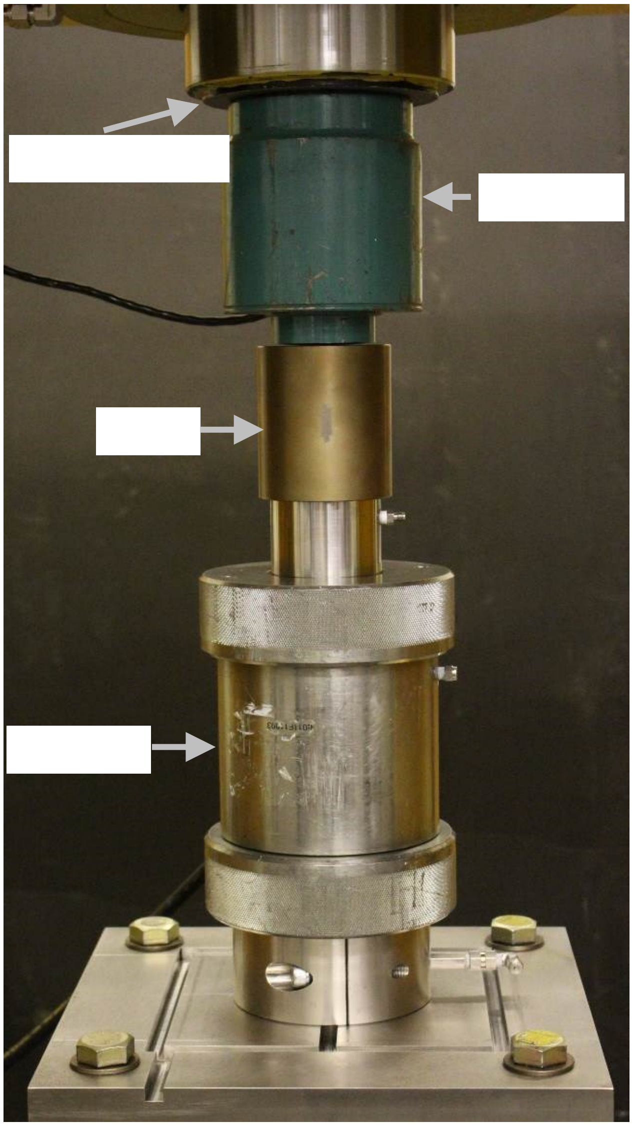

Fig. 1: Setup of Obert-Hoek Cell inside the Yellow Frame

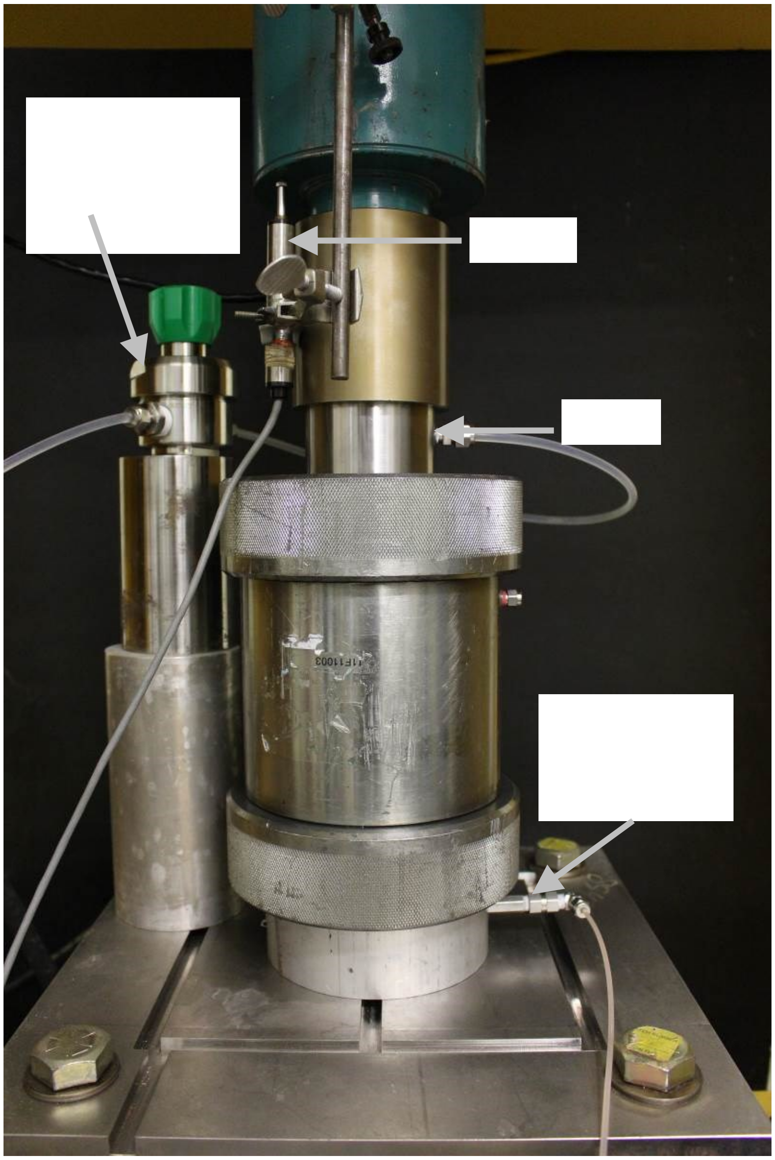

Fig. 2: Obert-Hoek Cell setup with all necessary connections

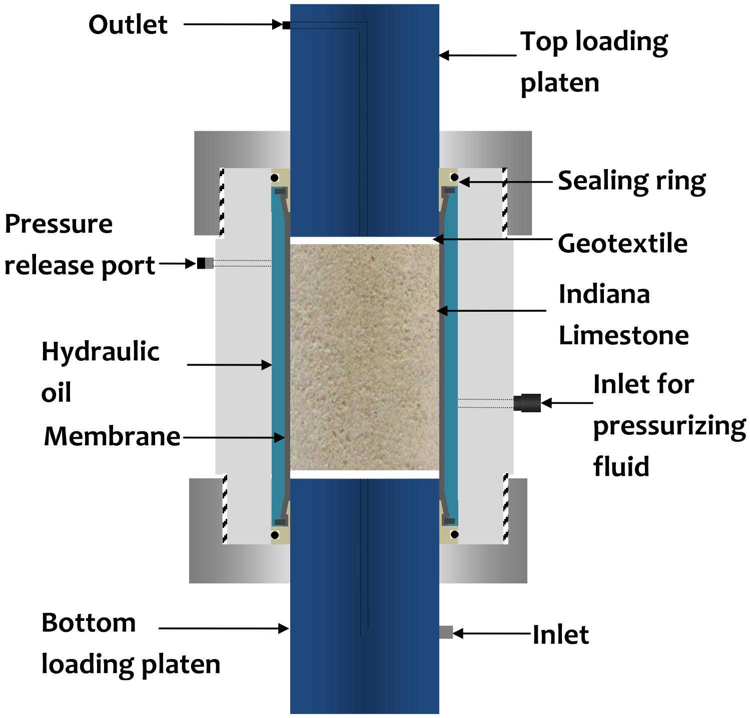

Fig. 3: Obert-Hoek Cell cross-section

Fig 4: Electric Hydraulic Pump used for large piston movements

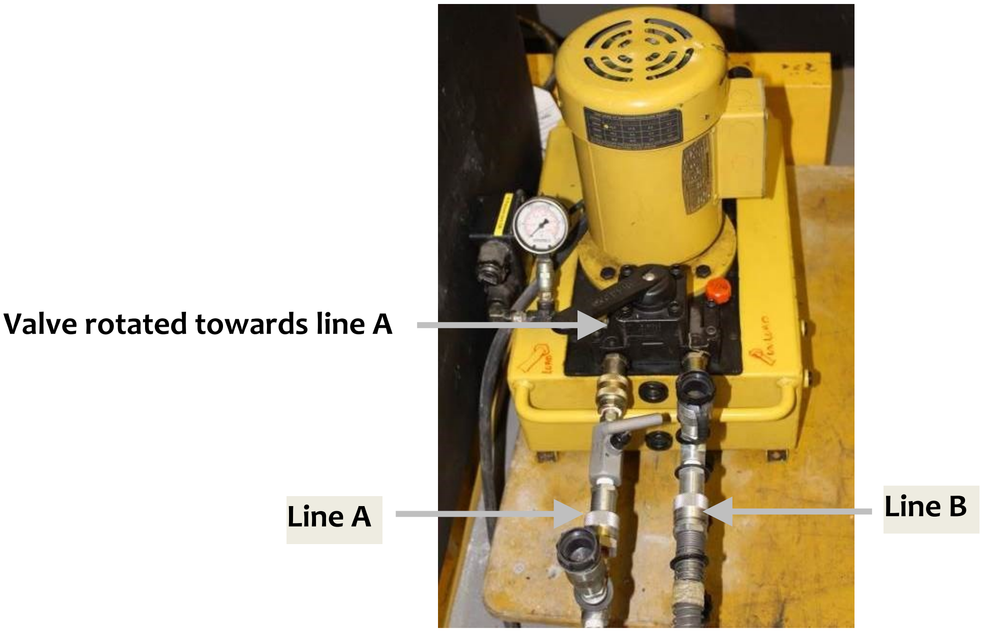

Fig 5: Front View showing the Electric Hydraulic Pump and High Pressure Hydraulic Hoses

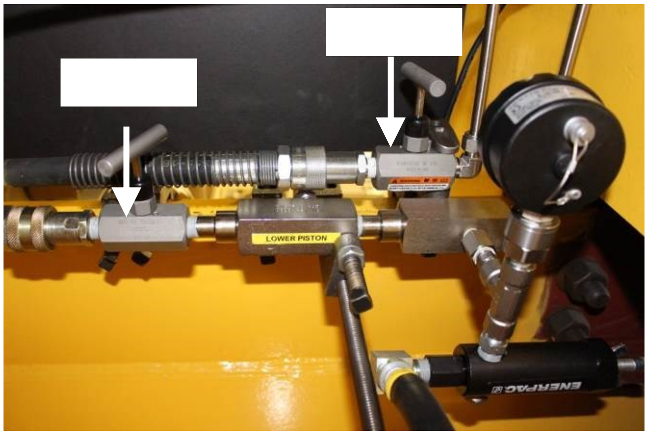

Fig 6: Side view showing the High Pressure Hydraulic Hoses and Valves

Fig. 7: Quizix used to pump water at a specified flow rate through the sample

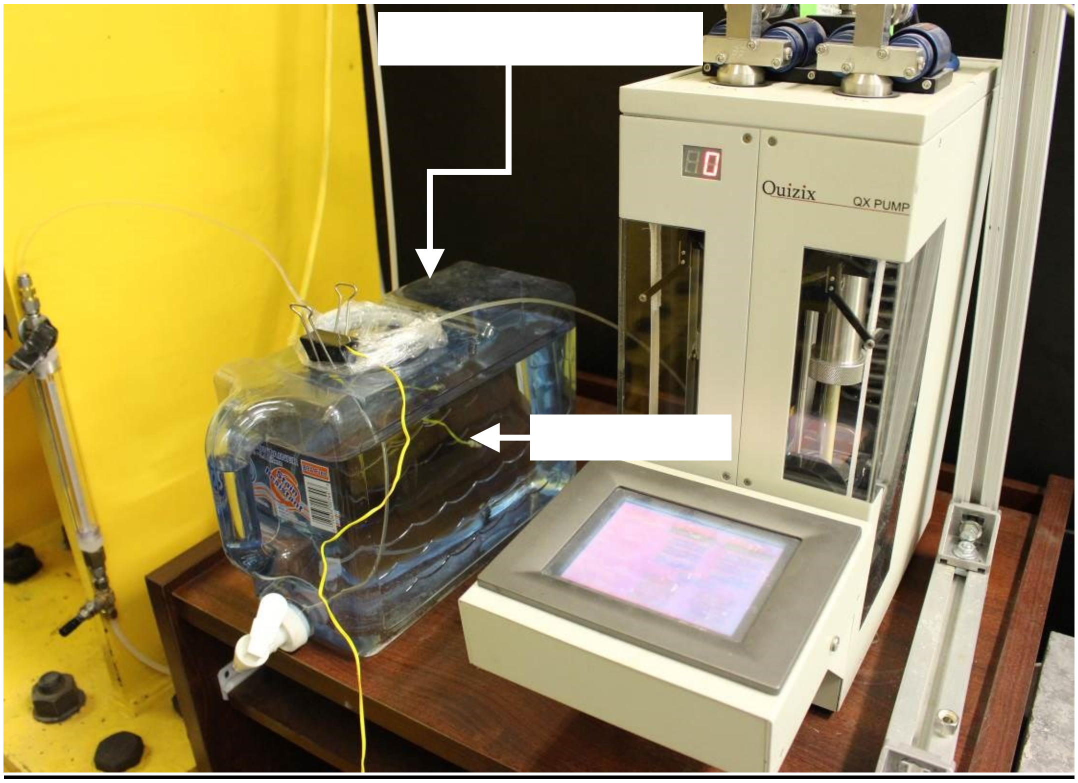

Fig. 8: The Quizix Pump and de-airing arrangement (using helium addition)

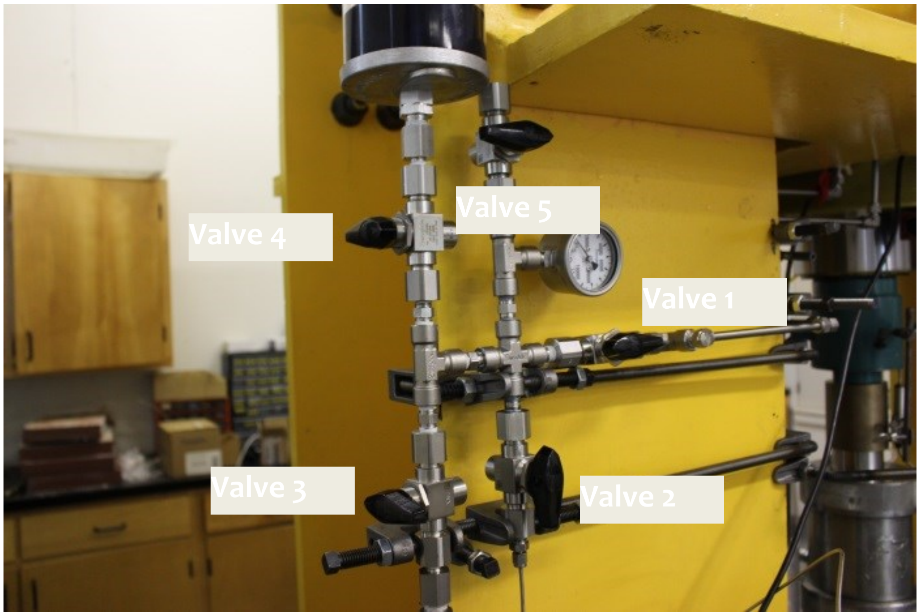

Fig. 9: From center right and clockwise: valves 1, 2, 3, 4 and 5 are used to control axial movement of the piston

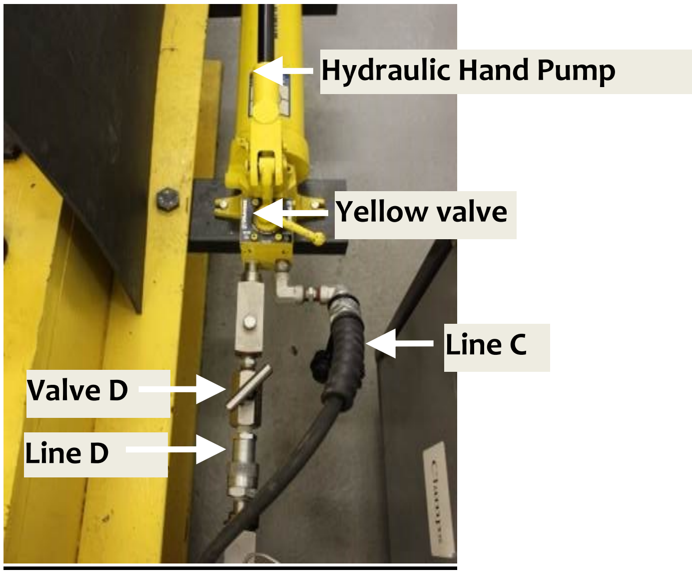

Fig. 10: The High Pressure Hydraulic Hand Pump used for precision control of the axial piston displacement, as well as the radial pressure

Fig 11: GDS Controller #1, which controls the axial load

Fig. 12: GDS Controller #2, which controls the radial pressure inside the Obert-Hoek Cell

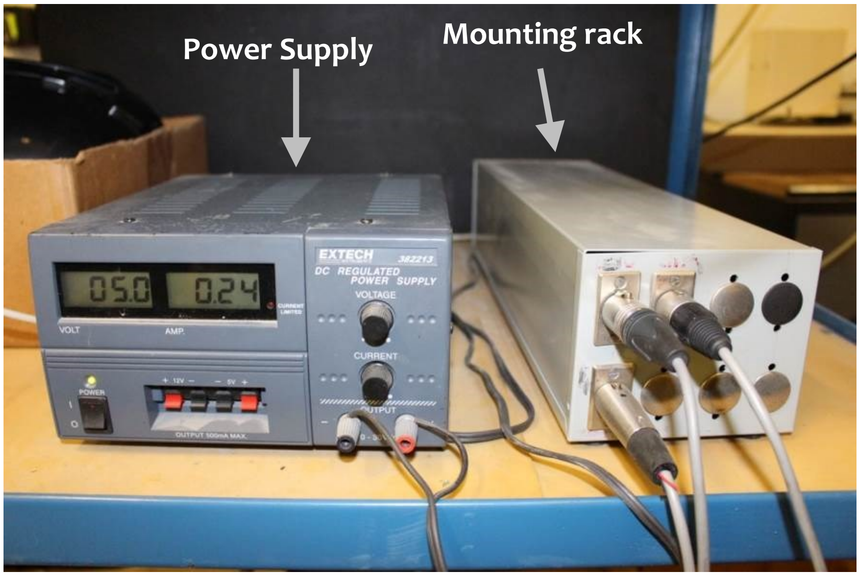

Fig. 13: Power Supply and DAQ

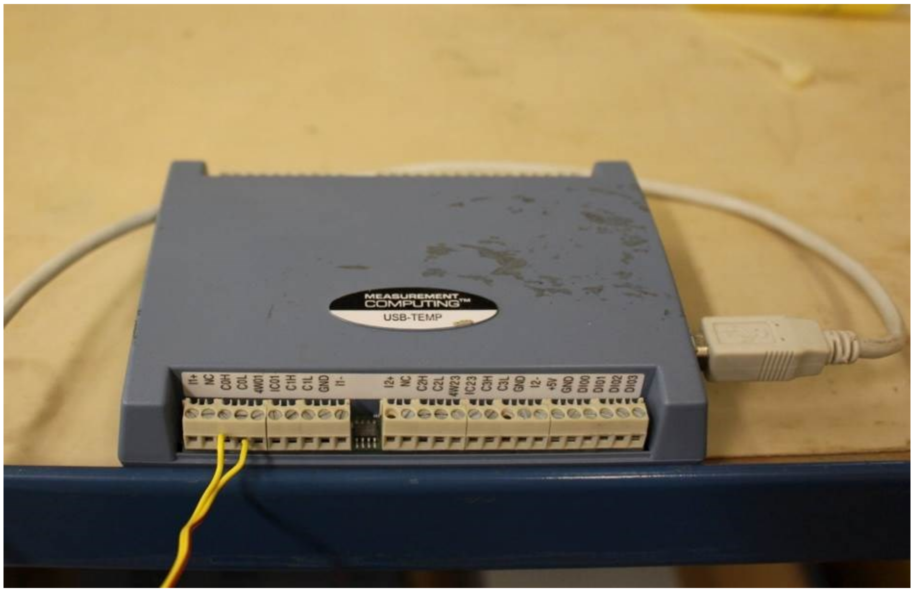

Fig. 14. The DAQ system, USB-TEMP, connected to thermocouple Type K

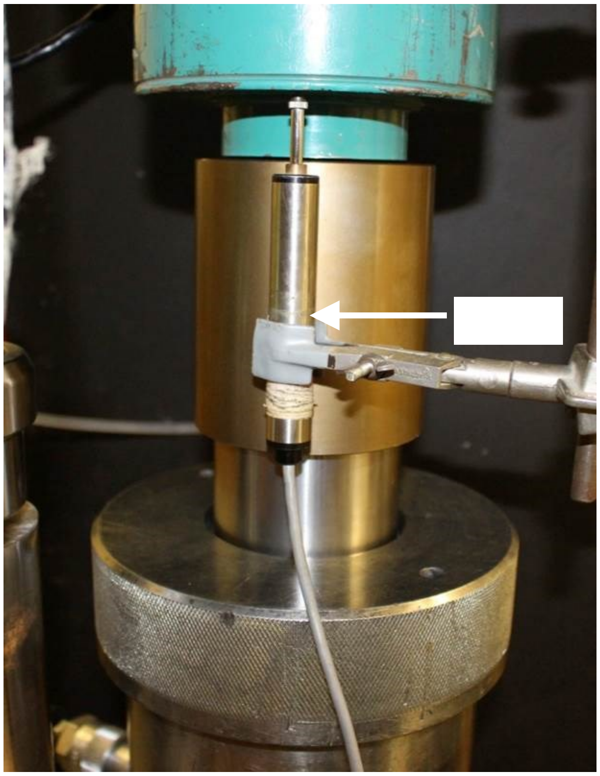

Fig. 15: The LVDT, measures displacement of the piston

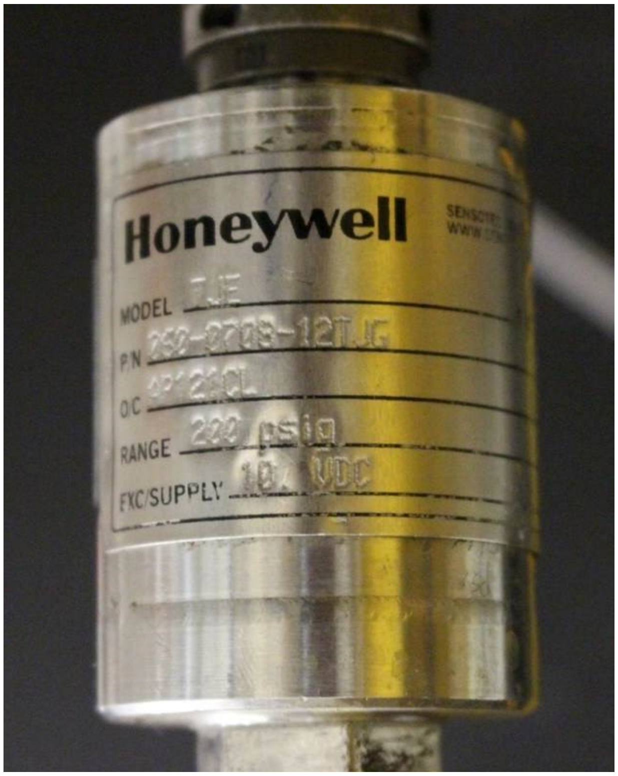

Fig. 16: A Close-up of Pressure Transducer

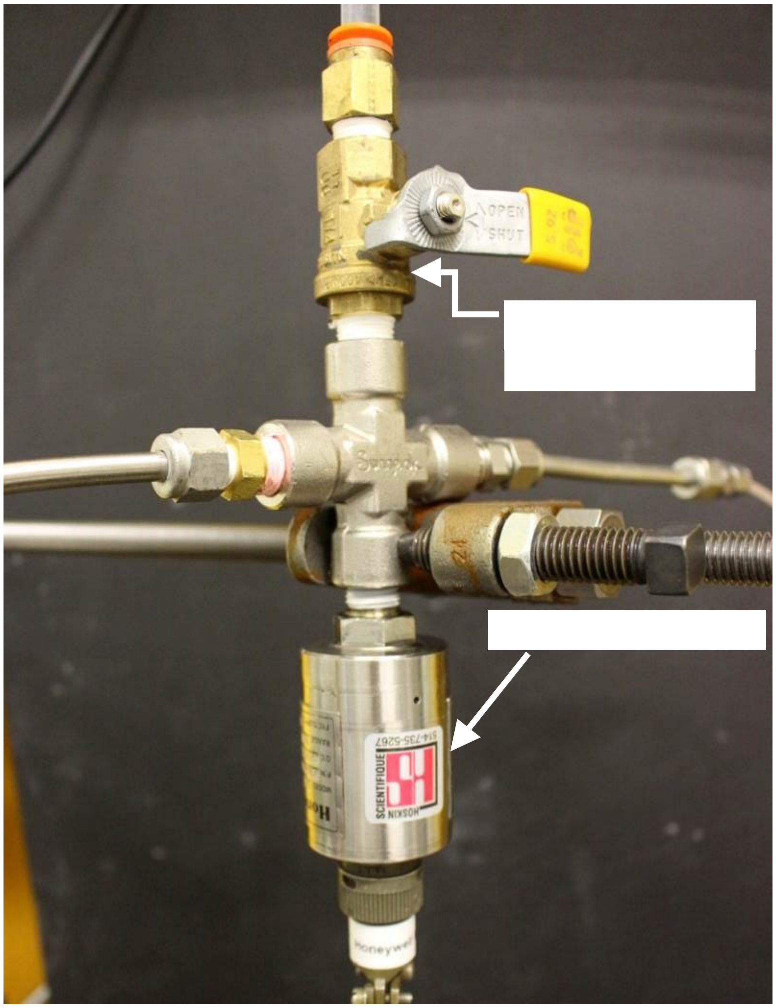

Fig. 17: The Connection of Pressure Transducer and de-airing valve

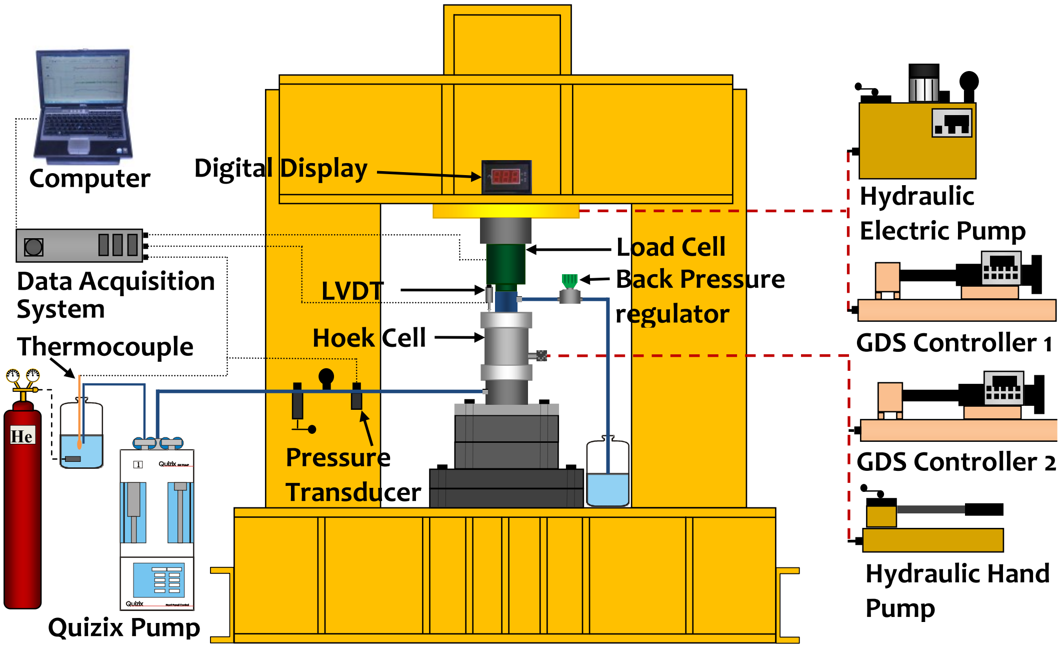

Figure 18: Experimental setup: The Yellow Frame with the Obert-Hoek Cell

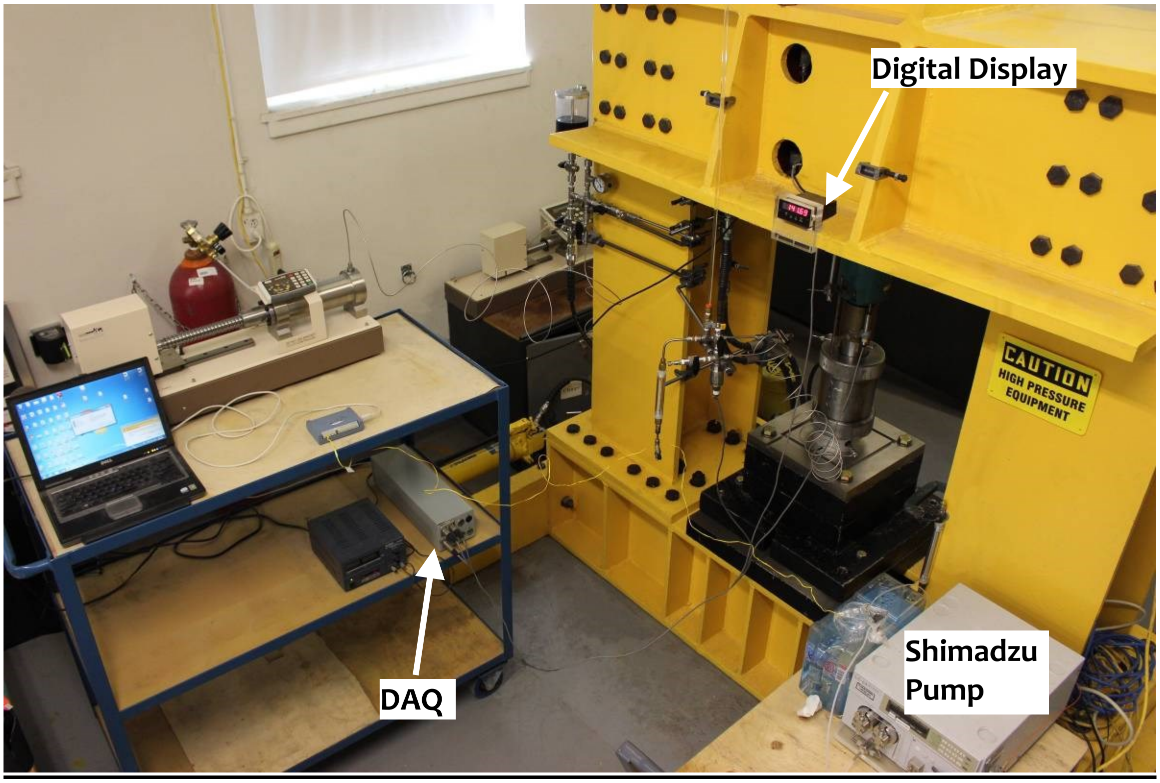

Figure 19: Experimental setup: The Yellow Frame with the Obert-Hoek Cell

Part 2: Software

2.1 Programs used

- TracerDAQ® Pro by Measurement Computing (http://www.mccdaq.com)
- Open Strip Chart and setup up 4 analogue channels (calibration factors + offsets)
- Channel 0: Pressure in the inflow line measure by Honeywell Pressure transducer (kPa)
- Channel 1: Displacement of the axial loading piston measured by LVDT (mm)
- Channel 2: Axial Load measured by 200 000 lbs load cell (kN)
- Channel 3: Temperature measured by Type K thermocouple (^{o}C)

Part 3: Usage

Warnings

- **All work should be approved by the supervisor and lab technician.**
- **Any work in the laboratory can ONLY be done while there are TWO people present.**
- **The Green Load Cell has a capacity of 200 000 pounds (890 kN), which limits the applicable axial load that can be applied to the sample.**
- **The Obert-Hoek Cell is a triaxial pressure chamber, rated for 10 000 psi (69 MPa) in radial pressure: however the supplier did not specify the amount of axial load that can be applied safely.**
- **The Yellow Frame and the hydraulic actuator have a capacity of 1 million pounds (4448 kN) in compression. The piston of the hydraulic actuator has a travel of 6 inches.**
- **The Digital Display shows the current axial load applied by the hydraulic actuator in kN and sends the signal to the DAQ system.**
- **There is no direct correlation between the load shown on the Digital Display and the pressure shown on the GDS Controller #1 due to many unknown factors such as: losses due to friction, temperature, viscosity, etc.**
- **The Quizix pump or similar pump is used to supply distilled de-aired water. The water enters the sample at its base at a desired flow rate or as a specified pressure history.**
- **Pumping helium gas through water at a rate of 10 ml/min removes dissolved oxygen in water effectively from approximately 8 ppm to approximately 2 ppm.**

3.1 Hydraulic piston large movement

Objective: To reduce the gap between the piston and the upper loading platen on of the Obert-Hoek Cell.

WARNING: the Hydraulic Electric Pump requires 20 amps to move the piston either up or down, therefore precautions must be taken to ensure that sufficient amperage is available and connected to the right power outlet.

1) Open (turn counter-clockwise) the three **Valves A, B** and **C** (see Figure 4,6) on High Pressure Hydraulic Hoses before operating the Electric Hydraulic Pump. Operating *needle valves* is a sensitive task, do not over-tighten them.
2) Make sure **Valve 1** is closed; this prevents any pressure build up from going into the sensitive apparatus.
3) Turn the valve on the Electric Hydraulic Pump to the load position (clock wise) to be able to move the piston down.
4) Switch the Electric Hydraulic Pump to “On”, keep the piston moving downwards until it is barely touching the Obert-Hoek Cell’s top loading platen.
5) The value recorded by the Digital Display should be close to zero and not more than 5 kN.
6) Once this is achieved, close **Valves A** and **B** and leave **Valve C** open. This prevents oil leakage back to the Electric Hydraulic Pump but still allows movement of the piston.
7) Open **Valve 1**.

3.2 Fine movement

WARNING: To avoid failure of the sample prematurely, apply axial and radial loads alternately. Do not apply high axial loads if you do not have the supporting radial pressure.

1) Valves' arrangement can be seen on Figure 9. **Valve 4** and **5** remain closed at all times (they are there to remove air and attach supplemental equipment).
2) Open **Valve 1, 2** and **3**.
3) Rotate the *yellow valve* on the Hydraulic Hand Pump towards Hydraulic Hose **Line C** (see Figure 10) to apply the fine movement to the loading piston.
4) WARNING: If you don't want to lose any applied load (pressure) then before you open **Valve 3**, lower the Hydraulic Hand Pump lever 1/3 of the way and then open **Valve 3**.
5) Maintain your pumping rate constant on the Hydraulic Hand Pump until you reach the desired load value on the Digital Display.
6) Convert this load value to axial stress for the specific area being loaded (have a conversion chart prepared in advance).
7) Once the desired load is reached, stop pumping and close **Valve 3**.
8) Read the pressure on GDS Controller #1 and set it up to maintain the pressure.

3.3 Applying radial pressure

1) Close **Valve 3** (see figure 9).
2) Make sure that **Valve D** is open (see Figure 10).
3) The *yellow valve* on the Hydraulic Hand Pump is rotated towards **Line D**, (see Figure 10).
4) Set GDS Controller #2 to a desired pressure (in kPa).
5) Start increasing the radial pressure with the Hydraulic Hand Pump until the desired pressure is reached.
6) Close **Valve D.**
7) Allow the GDS Controller #2 to stabilize the radial pressure.
   [NOTE: at this point the radial pressure will be maintained. If the radial pressure needs to be increased; then the GDS Controller #2 needs to be re-set to a new pressure (see step 4) and the process described above is repeated.]

3.4 Releasing the pressure

1) Start by gradually releasing the axial stress in order to reach isotropic stress conditions (the axial and radial stresses applied on the surface of the sample inside the Obert-Hoek Cell should be the same).
2) The release of excess axial stress can be used to refill GDS Controller #1. Set GDS Controller to FILL mode and wait for the axial load to drop to the confining stress level. Do not fill over 90% of the GDS Controller #1.
3) Stop the fill once the amount of oil has reached approximately 90%.
4) To release further the excess of pressure and decrease the axial load, direct the oil to the Hydraulic Hand Pump by closing **Valve D**, rotating *yellow valve* towards **Line D** and opening **Valve 3** ***very slowly***. This task requires experience and understanding of the mechanical properties of the sample. If axial load drops too low compared to the radial pressure, it will split the sample in half and probably puncture the membrane.
5) To reduce the radial pressures inside the Obert-Hoek Cell use the GDS Controller #2. Refer to *Section 3.3* and instead of increasing pressure in step 4, set GDS Controller #2 to a lower pressure.
6) Do not overfill the GDS Controller #2.
7) If GDS Controller #2 is at 90% filled, direct the excess radial pressure towards the Hydraulic Hand Pump by opening **Valve D**, rotating *yellow valve* towards Hydraulic Hose **Line C** *(if the system is properly sealed this step should not occur during normal operation of the Obert-Hoek Cell and only GDS Controller #2 should be used to reduce pressure)*.
8) NOTE: It is handy that the last step, in reducing the pressure, is to reduce radial pressure to zero; this is will help during the removal of a barrel shaped sample.

3.5: Decommissioning

1) Ensure that all pressures in all lines, GDS Controllers and Hydraulic pumps are reduced to zero.
2) All **Valves** (1 to 5) are closed.
3) All **Valves** on Hydraulic hoses are closed.
4) Open **Valves 4** and **5** to remove air.
5) Close **Valves 4** and **5**.
6) Remove the Obert-Hoek Cell, dismantle and clean it (soap water and methanol).
7) Turn off GDS Controllers, power supply and Quizix pump.
8) Disconnect power cords.
9) Clean all areas and moving parts, namely:
    a. Loading shaft on the GDS Controllers.
    b. Loading hydraulic piston.
    c. Stainless steel platen on which the Obert-Hoek Cell was installed.
    d. Obert-Hoek Cell.
    e. Refer to Quizix manual on how to store the pump for an extended period of time.
10) Cover all sensitive components of the apparatus to protect them from dust.

Part 4: Resources and Contacts

Mr. Jerry Sutton

Technical Director

jerry@gdsinstruments.com

GDS Instruments a division of Global Digital Systems Limited

Unit 32 Murrell Green Business Park,

London Road, Hook, Hampshire, RG27 9GR

Tel: +44 (0)1256 382450

Fax: +44 (0)1256 382451

www.gdsinstruments.com

Dr. William Cook

Systems Manager, Research Associate, McGill University

514-398-8176

bill.cook@mcgill.ca

Mr. John Bartczak

Technician, McGill University

514-398-6680

514-922-6785

john.bartczak@mcgill.ca

Prof. A.P.S. Selvadurai

Professor, Docteur h.c, PhD, DSc, FRSC, PEng, Cmath

William Scott Professor *and* James McGill Professor

patrick.selvadurai@mcgill.ca

McGill University

Macdonald Engineering Building

817 Sherbrooke Street West

Montreal, Quebec H3A 0C3

Tel: 514-398-6672

Fax: 514-398-7361

http://www.mcgill.ca/civil/people/selvadurai

Mr. Scott Vermeer

Product Manager, Quizix Precision Pumps

scott.vermeer@ametek.com

AMETEK Chandler Engineering

2001 North Indianwood Ave

Broken Arrow, OK 74012, USA

Main: +US 918-250-7200

Direct: +US 918-459-7115

Mobil: +US 918-605-5897

Fax: +US 918-459-0165

www.chandlerengineering.com

Enerpac products, Instruments ISS inc.

6059 de Maisonneuve Ouest, Montréal

Tel: 514-481-8111

Fax: 514-482-1640

Acknowledgements

The assistance of Mr. John Bartczak in the modification to the testing setup as well as the assistance of undergraduate students Ms. Julia Bond and Ms. Xiaoyu Yang.

Emergency / First Aid

For all emergencies call **911** immediately. Then inform campus security services at:

- 514-398-**3000**

APPENDIX C

ADIPRENE® LF 950A

TDI-terminated polyether based prepolymer

Urethane Prepolymers

PRODUCT DATA

ADIPRENE® LF 950A is a TDI-terminated polyether prepolymer with extremely low free TDI content. Curing with 4,4'-methylene-bis-(o-chloroaniline), MBCA, yields a high performance 95 Shore A polyurethane elastomer suitable for many high-performance applications.

Features of Adiprene LF 950A include:

- Low free TDI content
- Low viscosity
- Long pot life
- Excellent High Temperature Dynamic Properties

Adiprene LF prepolymers, including Adiprene LF 950A, offer cast polyurethane processors important advantages in three areas:

Hygiene

All TDI based prepolymers contain unreacted TDI monomer. The level of monomer can vary from 0.1% to 5.0% by weight, with high hardness materials generally having the highest level of free TDI. Adiprene LF 950A has less than 0.1% free TDI, which can be beneficial in the management and control of worker exposure to TDI.

Processing

Relative to conventional TDI based prepolymers of equal hardness, Adiprene LF 950A has the processing advantages of longer pot life and lower viscosity. These qualities can improve the performance of a casting operation by reducing scrap while increasing the variety of products that may be made via the casting process.

End-Use Performance

A third advantage of Adiprene LF 950A is excellent end-use dynamic performance. This material has low heat build-up due to hysteresis in high speed, high load-bearing applications such as rolls, tires and wheels. Therefore, it may be possible to expand the use of polyurethane into more dynamically demanding applications that require a 95 Shore A hardness elastomer.

UNIROYAL CHEMICAL
A Crompton Business

ADIPRENE® LF 950A
TYPICAL PROCESSING CHARACTERISTICS

Liquid Prepolymer Specifications:

% NCO	5.9 - 6.3
AE	667 - 712
Viscosity, Centipoise (Pa·s)	
@ 86°F (30°C)	6000 (6.0)
@ 140°F (52°C)	1000 (1.0)
@ 158°F (70°C)	500 (0.5)
@ 212°F (100°C)	150 (0.15)
Specific Gravity	
@ 86°F (30°C)	1.07
@ 158°F (70°C)	1.03
@ 212°F (100°C)	1.01

Processing Conditions:

Adiprene LF 950A temp, °F (°C)	150 (66)
MBCA, °F (°C)	240 (116)
pph MBCA, 95% theory, AE= 576	18.4
Mold Temperature, °F (°C)	212 (100)
Pot Life (time to 200 poise), Mins.	7.3
Demold Time, Mins.	25
Recommended Cure Cycle: Hrs/°F (°C)	16/212-230 (100-110)

*Room temperature molds may also be used. Longer demold times will be required.

ADIPRENE® LF 950A
TYPICAL PHYSICAL PROPERTIES

Physical Properties

Hardness, Shore A	95 - 97
Hardness, Shore D	48 - 52
Tensile, psi (MPa)	5500 (37.9)
Elongation, %	350
100% Modulus, psi (MPa)	2200 (15.2)
300% Modulus, psi (MPa)	4100 (28.3)
D-470 Split Tear, pli (kN/m)	125 (21.9)
Die C Tear, pli (kN/m)	500 (87.6)
Bashore Rebound, %	42
Compression Set, Method B	
22 Hrs. @ 158°F (70°C)	32
Compressive Modulus, psi (MPa)	
@ 5%	500 (3.4)
@ 10%	840 (5.8)
@ 15%	1200 (8.3)
@ 20%	1650 (11.4)
@ 25%	2100 (14.5)
Specific Gravity	1.13

Rev. 4/01 ljs/9/28/01/jbk

APPENDIX D

The MIP (Mercury Intrusion Porosimetry) test on Indiana Limestone was performed at Concordia University laboratories.

The average pore diameter was calculated from the collected data and was estimated to be 0.368 microns.

Additionally the cumulative porosity versus pore diameter for Indiana Limestone is presented in Figure 1. The pore diameter values were calculated with a contact angle of 141 Degrees.

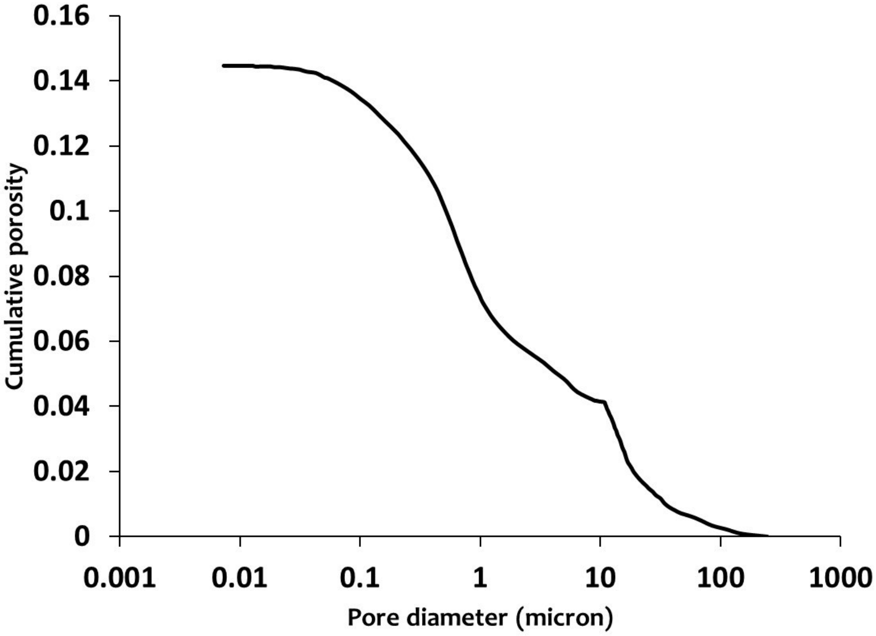

Figure 1: Cumulative porosity change versus pore diameter for Indiana Limestone